GENERAL ATOMIC

GA-A13975
UC-77

GAS-COOLED FAST BREEDER REACTOR

QUARTERLY PROGRESS REPORT
FOR THE PERIOD MAY 1, 1976 THROUGH July 31, 1976

by

Project Staff

Prepared under
Contract E(04-3)-167
Project Agreement No. 23
for the
San Francisco Operations Office
U.S. Energy Research and Development Administration

General Atomic Project 3228
Date Published: August 31, 1976

PROGRESS REPORT SERIES

GA-5537	November 1, 1963 through July 31, 1964
GA-6667	August 1, 1964 through July 31, 1965
GA-7645	August 1, 1965 through July 31, 1966
GA-8107	August 1, 1966 through July 31, 1967
GA-8787	August 1, 1967 through July 31, 1968
GA-8895	August 1, 1968 through October 31, 1968
GA-9229	November 1, 1968 through January 31, 1969
GA-9359	February 1, 1969 through April 30, 1969
GA-9639	May 1, 1969 through July 31, 1969
GA-9811	August 1, 1969 through October 31, 1969
GA-9838	November 1, 1969 through January 31, 1970
GA-10517	February 1, 1970 through January 31, 1971
GA-10645	February 1, 1971 through April 30, 1971
GA-A10803	May 1, 1971 through July 31, 1971
GA-A10906	August 1, 1971 through October 31, 1971
GA-A12003	November 1, 1971 through January 31, 1972
GA-A12252	May 1, 1972 through July 31, 1972
GA-A12421	August 1, 1972 through October 31, 1972
GA-A12530	November 1, 1972 through January 31, 1973
GA-A12635	February 1, 1973 through April 30, 1973
GA-A12728	May 1, 1973 through July 31, 1973
GA-A12824	August 1, 1973 through October 31, 1973
GA-A12894	November 1, 1973 through January 31, 1974
GA-A13021	February 1, 1974 through April 30, 1974
GA-A13148	May 1, 1974 through July 31, 1974
GA-A13238	August 1, 1974 through October 31, 1974
GA-A13379	November 1, 1974 through January 31, 1975
GA-A13458	February 1, 1975 through April 30, 1975
GA-A13565	May 1, 1975 through July 31, 1975
GA-A13766	August 1, 1975 through October 31, 1975
GA-A13815	November 1, 1975 through January 31, 1976
GA-A13868	February 1, 1976 through April 30, 1976

ABSTRACT

The tasks of the gas-cooled fast breeder reactor (GCFR) program that are supported by the U.S. Energy Research and Development Administration include development of GCFR fuel, blanket, and control elements; development of the pressure equalization system for GCFR fuel; out-of-pile loop facility test program planning; fuels and materials development; fuel, blanket, and control rod analyses and development; nuclear analysis and reactor physics for GCFR core design; shielding requirements for the GCFR; reactor engineering to assess the thermal, hydraulic, and structural performance of the core and the core support structure; plant systems control; development of reactor components, including reactor vessel, control and locking mechanisms, fuel handling equipment, core support structure, shielding assemblies, main helium circulator, steam generator, and auxiliary circulator; development of a helium circulator test facility; and reactor safety, including an in-pile safety evaluation program.

CONTENTS

FIGURES

FIGURES (Continued)

FIGURES (Continued)

FIGURES (Continued)

TABLES

TABLES (Continued)

1. INTRODUCTION

The various tasks of the gas-cooled fast breeder reactor (GCFR) program for the period May 1, 1976 through July 31, 1976 sponsored by the U.S. Energy Research and Development Administration (ERDA) are discussed in this quarterly progress report. The GCFR utility program, which is supported by a large number of electric utility companies, rural electric cooperatives, and General Atomic (GA), is primarily directed toward the development of a GCFR demonstration plant. The utility-sponsored work and the ERDA-sponsored work are complementary.

Analytical, experimental, and fabrication development is being accomplished under the core element development task to establish the basis for the design of GCFR fuel, blanket, and control element assemblies. Analytical methods development for structural and thermal-hydraulic analyses is discussed, and the results of structural analysis of the fuel assembly components and thermal-hydraulic analysis of the blanket element during low power are presented. Current progress on rod spacer interaction tests, fuel element seismic and vibration test planning, and development of assembly fabrication techniques is also presented. The various subtasks of core element development and the work accomplished during this reporting period are discussed in Section 2.

The technology to support the design and construction of the pressure equalization system for GCFR fuel is being developed. This includes (1) the development of analytical models and computer codes that will be verified by test programs and testing of materials and seals and (2) the development of fabrication processes for the pressure equalization system. These are discussed in Section 3.

To demonstrate the ability of GCFR fuel, control, and blanket assembly designs to meet design goals and verify predictions of analytical models, a series of out-of-pile simulation tests will be performed. The emphasis of the tests will be on obtaining thermal-structural data for steady-state, transient, and margin conditions using electrically heated rod bundles in a dynamic helium loop. These are discussed in Section 4.

In the fuels and materials development program, thermal flux and fast flux irradiation programs are being conducted to establish conditions and design features specific to GCFR fuel rods, such as vented fuel, fission product traps, and surface-roughened cladding. In addition, a test program of smooth and surface-roughened GCFR cladding specimens is being conducted to determine how materials behave under irradiation. The fuels and materials tests, the analytical studies, and the results to date are presented in Section 5.

Under the fuel rod engineering task, performance of the fuel and blanket rods under steady-state and transient conditions is being evaluated to determine performance characteristics, operating limits, and design criteria. In addition, surveillance of the fuel rod and blanket rod technology of other programs is being carried out. These studies are presented in Section 6.

The objectives of the nuclear analysis and reactor physics task are to verify and validate the nuclear design methods which will be applied to the GCFR core design. A critical assembly experimental program is being carried out on the ZPR-9 facility at Argonne National Laboratory (ANL) for this purpose. Critical assembly design, analysis, and methods development are discussed in Section 7.

Verification of the physics and engineering analytical methods and the data for design of the GCFR shields is being conducted under the shielding requirements task along with an evaluation of the effectiveness of various shield configurations. The results of radial shield analyses and the work being done on structural analysis are presented in Section 8.

To assess the thermal-hydraulic performance of the GCFR reactor core, analytical methods and models are being developed and utilized to define operating strategies. These, together with the development of GCFR plant control systems and an evaluation of the capability of the PCRV internal structures to provide postaccident fuel containment, are discussed in Section 9.

Section 10 presents the evaluation and development of the main components of the GCFR which are currently in progress, including reactor vessel, control and locking mechanisms, fuel handling, core support structure, shielding assemblies, main helium circulator, steam generator, and auxiliary circulator.

Development of a test facility for qualification testing of the main helium circulator is discussed in Section 11. This task includes the responsibility for (1) evaluation studies of alternative test facility concepts, (2) preparation of specifications for the selected facility, and (3) final design, construction, and checkout of the facility.

The objective of the reactor safety task, which is discussed in Section 12, is to study the safety aspects of the GCFR using logical probabilistic methods to determine the probabilities associated with accident initiation and progression sequences.

The gas reactor in-pile safety test (GRIST) program is being studied as a potential follow-on to the analytical and experimental programs covering design basis accidents. The objective of the GRIST program is to provide information related to beyond-design-basis accidents, particularly the behavior of melted cladding and fuel. Progress in test assembly analysis and design is discussed in Section 13.

2. CORE ELEMENT DEVELOPMENT (189a No. SU006)

2.1. FUEL AND CONTROL ASSEMBLY ANALYSIS

2.1.1. Introduction

Through the evaluation of experimental data, the analytical basis for the design and development of the GCFR fuel and control assemblies is being developed. Because complete prototype in-pile tests cannot be conducted, a strong analytical base supported by development tests is required to design the core assemblies. The current effort is devoted to the development of an adequate steady-state and transient analysis capability in the areas of thermal-hydraulic and structural analyses to provide a basis for assembly design criteria and specific test requirements.

During the previous quarter, the subroutine for calculating the first-order outer flow rates in FLOMAX was developed, with some debugging still in progress. The chopped cosine power distribution was incorporated in the code, and preparations were begun for programming the inner solutions. The thermal-hydraulic analysis for that period concentrated on a more accurate determination of the effect of the rod-to-duct spacing of the fuel assembly. Using the rough-rod data from the Swiss Federal Institute (EIR) as a basis, a calculational scheme was developed, but further analysis is required for this complicated problem.

During this quarter, the outer solutions in FLOMAX were checked for several sample problems. Special techniques were developed to handle surface transitions and abrupt changes in heat flux. Preliminary comparisons with COBRA calculations indicate excellent agreement. The COBRA code has been modified (1) to permit the analysis of carbon-dioxide-cooled fuel bundles in order to perform analysis of the EIR experiments and (2) to increase the maximum number of types of subchannels, i.e., the number of friction factor and Stanton number correlations, which may be applied to a problem. Based on annulus test data, a correlation of the friction factor as a function of the Reynolds number and the relative roughness has been developed.

2.1.2. Analytical Methods Development

2.1.2.1. The FLOMAX Thermal Analysis Code. During this quarter, work continued on the development of the thermal-hydraulic subchannel analysis code FLOMAX. The mathematical problem of rod bundle codes is to determine for each subchannel i, and as a function of the axial coordinate x, the mass velocities $G_i(x)$, the temperatures $T_i(x)$, and the pressures $P_i(x)$. In FLOMAX, this is done by expanding these variables into the asymptotic series

$$G_i(x) \sim G_{oi} + \sigma G_{1i}(x) + \sigma g_i(\xi) + 0(\sigma^2) \quad ,$$

$$T_i(x) \sim T_o(x) + \sigma T_{1i}(x) + \sigma t_i(\xi) + 0(\sigma^2) \quad ,$$

$$P_i(x) \sim P_o(x) + \sigma P_1(x) + \sigma p_i(\xi) + 0(\sigma^2) \quad ,$$

Where the upper case letters denote outer variables which are valid away from the inlet and geometry transitions, the lower case letters denote inner variables which are valid near the inlet and transitions, σ is a small parameter, and the stretched inner coordinate is $\xi = x/\sigma$.

The outer solutions were previously programmed and have been checked for several problems. Some debugging is still in progress for problems with surface transitions and abrupt changes in heat flux. These changes required a piecewise integration of the power profile for the acceleration effect on the pressure drop. The formulas for the integration were completed and programmed and are now being checked with sample calculations. Preliminary results indicate excellent agreement with the COBRA code.

In the previous quarterly (Ref. 2-1), it was shown that the inner temperatures $t_i(\xi)$ were to be determined from the linear equation

$$\frac{dt_i}{d\xi} + A_{ij}t_j = 0 \quad , \tag{2-1}$$

where A_{ij} are the elements of a matrix containing axial flows and turbulent mixing and there is implied summation on the repeated subscript j. Formally, Eq. 2-1 can be solved as an eigenvalue problem by taking

$$t_i(\xi) = \sum_{\nu=1}^{n} c_\nu b_{i\nu} e^{-\lambda_\nu \xi} \quad , \tag{2-2}$$

where $b_{i\nu}e^{-\lambda_\nu \xi}$ are the eigenvectors, λ_ν are the eigenvalues, and c_ν are the coefficients to be determined from the initial conditions $t_i(0) = t_i^*$. However, the computation of eigenvectors for large systems is very cumbersome (the number of subchannels n in Eq. 2-2 could be as large as 1000); therefore, an approximate solution was developed for Eq. 2-1. The solution was obtained using the method of weighted residuals in which the average error of the approximation with respect to the weighting functions $W_i(\xi)$ is formed:

$$E = \int_D W_i R_i d\xi \quad ,$$

where D is the domain of integration and E is minimized using the free parameters in the trial functions. In the Galerkin method, which was used, the W_i values were taken as the trial functions themselves. Since the exact solution is made up of exponentials, the following trial functions were taken:

$$t_i(\xi) = b_i e^{-\alpha\xi} \quad ,$$

where $b_i = t_i(0)$ satisfies the initial conditions, and α is the free parameter. Substituting this into Eq. 2-1 gave the residual

$$R_i(\xi) = (A_{ij}b_j - \alpha b_i)e^{-\alpha\xi}$$

and the average error

$$E = b_i\ (A_{ij}b_j - \alpha b_i) \int_0^\infty e^{-2\alpha\xi}d\xi \quad .$$

Then, setting E = 0, and since the integral is nonvanishing, the following expression was obtained for the parameter α:

$$\alpha = \frac{b_i A_{ij} b_j}{b_k b_k} \quad . \tag{2-3}$$

Equation 2-3 is convenient in numerical computations because it does not involve the inverses of any matrices. In the case of a two-channel example, Eq. 2-3 gave an α within 1/2% of the exact eigenvalue. The above approximate solution is being programmed. Similarly, an approximate solution was obtained for the inner flow rates $g_i(\xi)$, but programming has not yet been initiated. With the successful programming and debugging of the $t_i(\xi)$ and $g_i(\xi)$ solutions, the FLOMAX code will be completed in its first version.

2.1.2.2. <u>The COBRA Thermal Analysis Code.</u> Additional development work was done on the COBRA subchannel analysis code. The present version of the code is capable of handling only helium as the working fluid and permits the use of a maximum of only four types of subchannels with respect to the specification of friction factor and Nusselt number correlations. With the modifications, the code analyzes carbon dioxide flow systems and accepts up to 50 different subchannel types, i.e., 50 separate friction factor and Stanton number (substituted for Nusselt number) correlations.

The AGATHE HEX fuel rod bundle tests performed by EIR utilize CO_2 rather than helium as the coolant. To participate in the design of the test section and the analysis of the test data, the second version of the COBRA code was developed and included the properties of CO_2. Correlations were developed for specific heat, density, viscosity, and thermal conductivity over the temperature range of interest. The corresponding correlations for helium in the code were replaced with these equations, and several checkout runs were made. Some minor problems in balancing the fluid enthalpy rise with the total heat generation have been encountered; these problems are apparently due to the variable specific heat of CO_2 and are currently being resolved.

2.1.2.3. Correlation of Rough-Surface Friction Factors.

Subchannel thermal-hydraulic analysis computer codes such as FLOMAX and COBRA use correlations of f and St (or Nusselt number) to calculate channel pressure drops and rod temperature. These correlations are developed external to the code in the form described in Section 2.1.2.2 and are input as a table of constants. Although the codes assume only a Reynolds number (Re) dependence of f and St, these parameters are also functions of the subchannel relative roughness ε_1 (roughness rib height/hydraulic diameter), the roughness rib configuration, and the ratio of rod wall temperature to local coolant temperature. These additional parameters must be taken into account when assigning values to A, B, C, A', B', and C'.

To develop correlations for f and St, data from tests of single heated rods in tubes are used. These tests, performed by EIR and used by GA under a private information exchange agreement, cover a wide range of Re, tube-to-rod diameter ratios, and roughness configurations. Data from rod 19, which has ribs similar in shape to the GCFR design and is tested at similar temperature ratios, are being used to express f and St in terms of Re. Annulus test data must first be "transformed," a procedure which essentially separates the effects of the smooth outer tube wall from those of the rough rod. The resulting EIR rod 19 transformed friction factor (f_1) and relative roughness (ε_1) data are plotted in Figs. 2-1 and 2-2, respectively, as functions of the transformed Re (Re_1). Data for the smaller 14-mm-diameter tube have higher values of f_1 and ε_1, as would be expected.

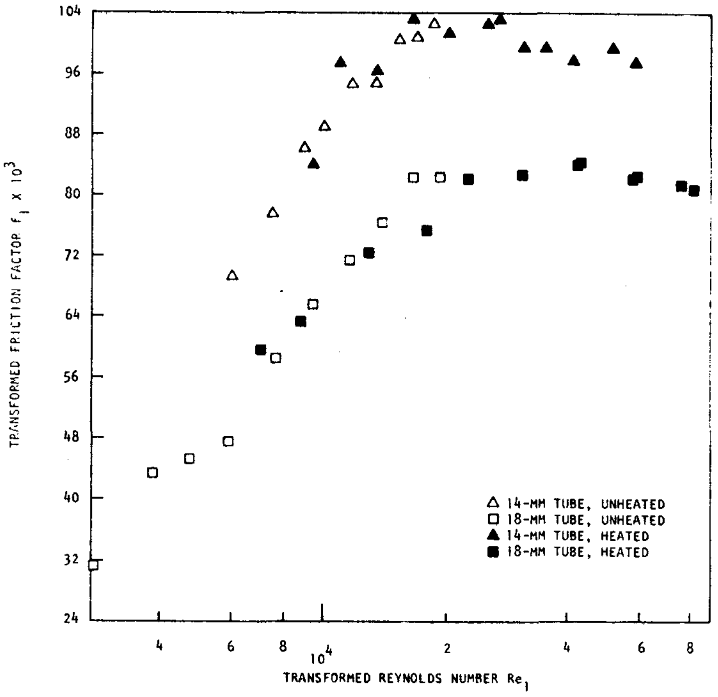

Fig. 2-1. Transformed friction factor for rod 19

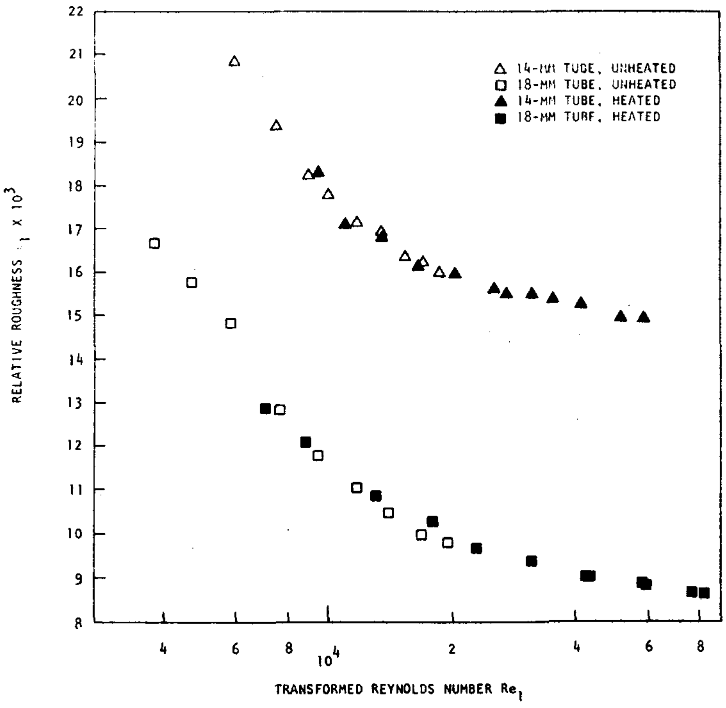

Fig. 2-2. Relative roughness for rod 19

The f_1 data level off in the transformed Re range 20,000 to 40,000, followed by a slight decline with increasing Re_1. The relative roughnesses decrease with increasing Re_1 since the hydraulic diameter is also increasing.

To be able to correlate f_1 as a function of Re_1 and ε_1, the effects of the two parameters on f_1 must be separated. This interpolation procedure is schematically shown in Fig. 2-3. Figure 2-3(a) represents Figs. 2-1 and 2-2. For a given value of Re_1^* and outer tube diameter d_2, values of ε_1 and f_1 (points a, b, c, d) can be read from Figs. 2-1 and 2-2 and plotted on Fig. 2-3(b), which relates f_1 to ε_1 for constant values of Re_1^*. To arrive at the desired form of the relationship between the parameters, an additional step is required. For a given value of relative roughness ε_1^*, corresponding values of Re_1^* and f_1 are read from Fig. 2-3(b) and plotted as shown in Fig. 2-3(c). This step inverts the positions of Re_1^* and ε_1^* and results in the final form desired for curve fitting.

Using functional forms derived from Fig. 2-3(c), curve fits were then made of the original f_1, Re_1, ε_1 data to permit the calculation of f_1 for a wide range of Re_1 and ε_1 values. No single equation was found which would fit these data over the required ranges of $0 \leq \varepsilon_1 \leq 0.05$ and $1000 \leq Re_1 \leq 100,000$. Therefore, the data were fitted in a piecewise fashion using quadratic and cubic spline equations and matching the point and the slope at the points of intersection. Using this procedure, a function subprogram was developed which calculates f_1, given Re_1, and ε_1 over the ranges given above. The data of Fig. 2-3 and the corresponding calculated values of f_1 are plotted together in Fig. 2-4. Using the subprogram, parametric values of f_1 were generated for the laminar, transition, and turbulent Re_1 regimes for various values of ε_1; these are plotted in Fig. 2-5. The transformed f was assumed to be invariant with transformed Re above a value of 10^5.

Work has been initiated to develop a similar correlation for the transformed St. These correlations will then be used for subsequent COBRA and FLOMAX analyses of the GCFR fuel elements.

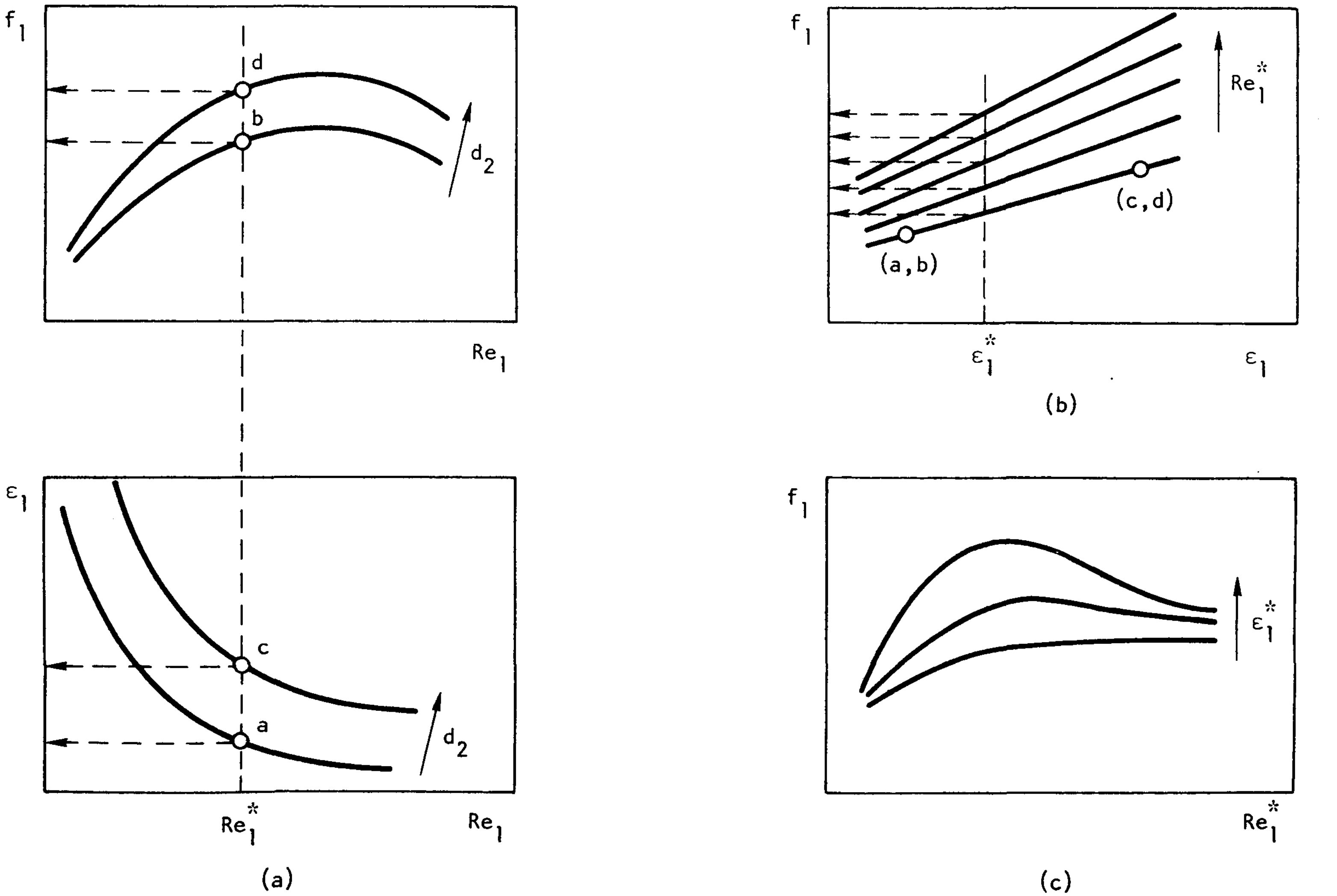

(a)

(b)

(c)

Fig. 2-3. Separation of parameters

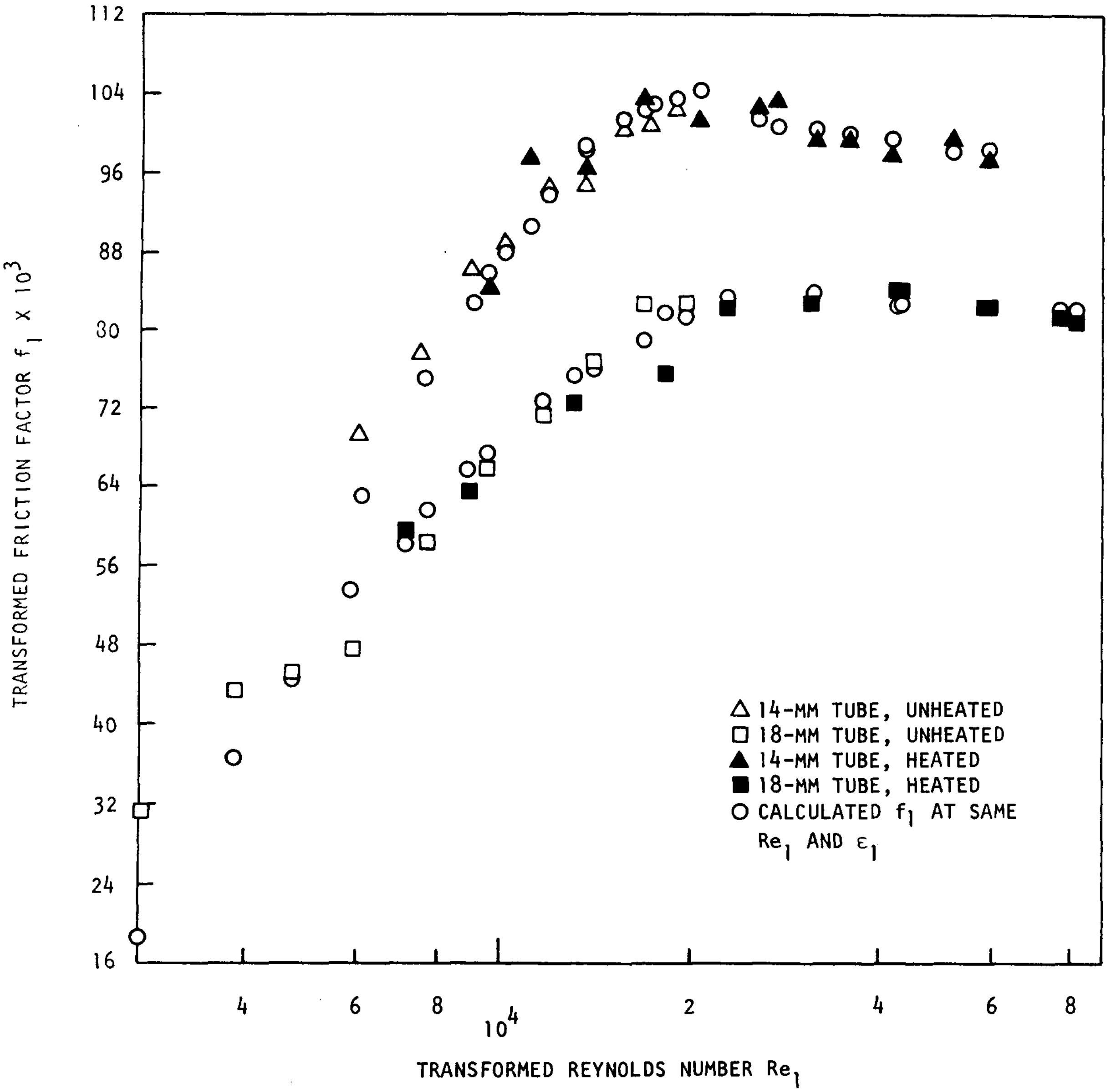

Fig. 2-4. Calculated and actual values of f_1 vs Re_1

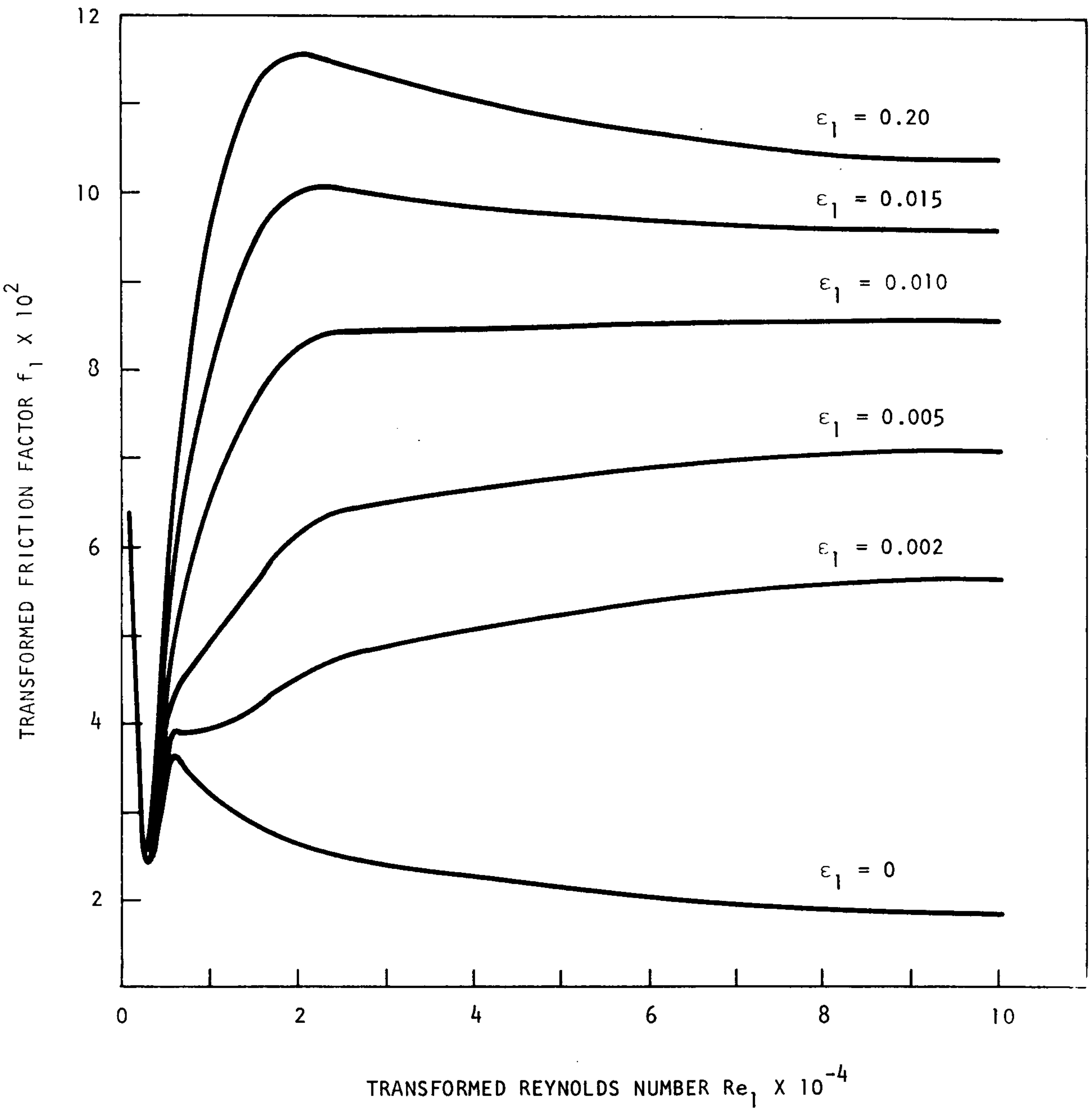

Fig. 2-5. Transformed friction factor values calculated by function subprogram

2.2. BLANKET ASSEMBLY ANALYSIS

The purpose of this task is to develop and verify the analytical techniques for blanket assembly analysis. These analytical techniques will be applied to obtain preliminary and final designs of the blanket assembly and to determine the design margin requirements. This task includes the thermal-hydraulic, structural, and dynamic analyses and the evaluation of handling and shipping of the blanket assembly.

During the previous quarter, some aspects of the thermal-hydraulics of the new reference design (61 rods per assembly and wire-wrap spacers) were reported. During this quarter, methods of obtaining the hot spot factors for the GCFR radial blanket assembly were reviewed, and a list of subfactors relevant to blanket assembly hot spot analysis was prepared.

2.2.1. Methods of Hot Spot Factor Analysis

One of the first and simplest methods of evaluating the hot spot factor is the deterministic or cumulative method (Ref. 2-2). In this method, it is assumed that all the uncertainties have the most unfavorable values at the same location and the same time. This method is very conservative and gives too high a value for the hot spot factors.

Since the probability of simultaneous occurrence of all uncertainties with the most unfavorable values at a location is very small, a statistical approach was introduced (Refs. 2-3 and 2-4). This method treats all uncertainties statistically and was used in the hot spot analysis of the Enrico Fermi Reactor (Ref. 2-5). This method is too optimistic because all variables entering the hot spot analysis are not subject to statistical (i.e., random) variations.

One of the most accurate methods of evaluating hot spot factors is the Monte Carlo method suggested by Antognetti (Ref. 2-6) and Businardo, et al. (Ref. 2-7). In this method, the hot spot temperature is obtained by randomly drawing a set of values of the variables affecting the hot spot factor and performing the calculations according to the functional relationship between the temperature of interest and the variables. The calculation is repeated until a reasonably accurate temperature distribution (statistical) is obtained. This method has a number of advantages but is very expensive in terms of computer usage.

A computational procedure restricted to continuous axial and radial temperature profiles, but dealing with the entire core rather than the hottest spot, has been suggested by a number of authors (Refs. 2-8 through 2-10). This procedure (synthesis method) is not applicable to GCFR core or blanket assemblies because no core-wide continuity in temperature profile exists in the GCFR.

In addition to the four basic methods discussed above, two other methods which are combinations of the above methods have been suggested for computation of hot spot factors. The first of these is the semistatistical method. In this method, all the uncertainties are divided into two groups, the total hot spot factor is calculated by cumulatively treating uncertainties of systematic order and statistically treating uncertainties of statistical origin. Figure 2-6 illustrates this procedure (Refs. 2-11, 2-12).

An improvement over the semistatistical procedure was suggested by Arnaberger and Mazumdar (Ref. 2-13) by combining the Monte Carlo procedure with the semistatistical method. The additional accuracy obtained by the method is offset by the more complicated computational scheme required in the procedure.

2.2.2. Selected Method for GCFR Radial Blanket Hot Spot Analysis

Of the methods discussed above, the semistatistical method of hot spot analysis is the most straightforward and gives results which agree with experiments. This is the method selected for fast flux test facility (FFTF) analysis and preliminary safety analysis of the Clinch River breeder reactor (Ref. 2-12).

The semistatistical method consists of separation of the variables which cause hot spot temperatures into categories of statistical and nonstatistical. Variables which have a random frequency of distribution are statistically treated. Variables of this kind are rod diameter, property data, heat transfer correlations, etc. A nonstatistical variable is not subject to random occurrence.

Figure 2-6 illustrates the procedure for application of the semistatistical method. A nominal temperature difference ΔT_{NOM} is first increased by nonstatistical uncertainty to ΔT_{CUM}, which represents the mean value of the hot spot temperature difference. The temperature difference $(\Delta T)_{3\sigma}$ then represents the hot spot temperature difference with 99.86% certainty.

2.2.3. Uncertainties in GCFR Radial Blanket Temperatures

The uncertainties influencing the hot spot factors of the GCFR radial blanket are given in Table 2-1. These subfactors will be divided into statistical and nonstatistical categories, their individual values will be obtained, and hot spot factors for the GCFR radial blanket will be evaluated by the semistatistical method. The following six components of the hot spot factors will be evaluated:

1. F_B: hot spot factor for coolant temperature rise.
2. F_f: hot spot factor for film temperature drop.
3. $F_{c\ell}$: hot spot factor for cladding temperature drop.
4. F_g: hot spot factor for temperature difference between cladding and fuel surface.
5. F_r: hot spot factor for blanket pellet.
6. F_e: hot spot factor for mixed mean assembly exit temperatures.

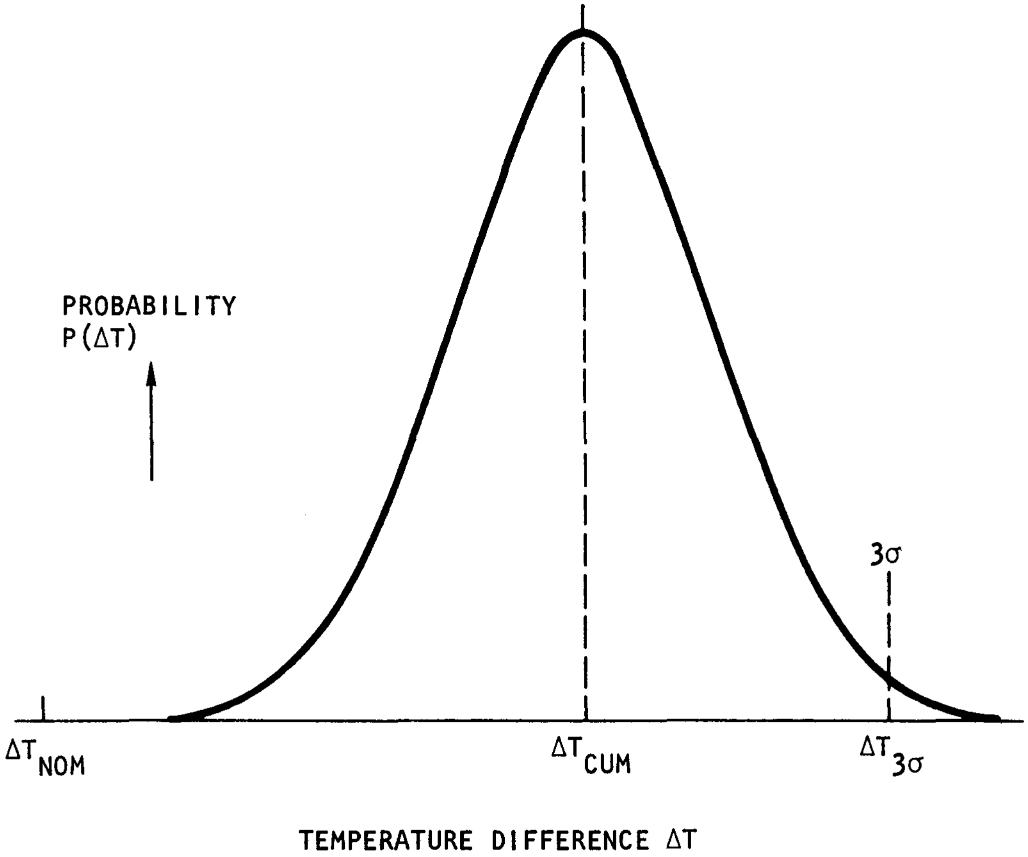

Fig. 2-6. Illustration of semistatistical method

TABLE 2-1
HOT SPOT FACTORS FOR GCFR BLANKET ELEMENT

	Coolant	Film	Cladding	Gap	Fuel	Mixed Mean Assembly Exit Coolant
Power measurement and control system dead band	X	X	X	X	X	X
Inlet (plenum) flow maldistribution (static pressure profile)	X	X				X
Assembly flow calculational uncertainties	X	X				X
Cladding circumferential temperature variation		X				
Nuclear data	X	X	X	X	X	X
Physics methods	X	X	X	X	X	X
Coolant properties: density, conductivity, viscosity	X	X				X
Cladding conductivity			X			
Cladding thickness			X			
Subchannel flow area: wire diameter, rod bowing, cladding outside diameter, cladding and duct thermal expansion, cladding and duct swelling	X	X				X
Heat transfer correlation		X				
Friction factor correlation	X	X				X
Flow sweeping correlation	X					
Gap conductance correlation				X		
Wire wrap orientation	X					
Cladding pellet eccentricity		X		X		
Pellet diameter	X	X	X	X	X	
Coolant inlet temperature(a) (plenum temperature distribution)	X					
Orifice (or assembly flow rate) tolerance	X	X				X

(a) In addition, the inlet coolant temperature will be increased to account for primary loop temperature control uncertainty.

Table 2-1 shows which uncertainties influence the above hot spot factors.

2.3. ASSEMBLY MECHANICAL TESTING

The objective of this task is to conduct mechanical tests of core element assembly components and assemblies to simulate the mechanical loads expected during normal and abnormal reactor operating conditions. The current phase of the assembly mechanical testing program involves testing of fuel element assembly components. The fuel rod/spacer interaction test is the initial long-term component test. Additional tests are being planned for FY 77.

2.3.1. Fuel Rod/Spacer Interaction Test

The purpose of the rod/spacer interaction test is to evaluate the effect of interacting forces between the fuel rod and the spacers under the operating conditions expected in the GCFR reactor. The interacting forces between rod and spacer are primarily due to bowing induced by temperature gradients and irradiation-induced swelling. Rubbing friction and wear occur during relative axial motion of the rod and spacer resulting from reactor operational transients. These tests will provide a data base for standards of acceptable friction and wear.

Initially, combinations of pressed spacers with convex contact surfaces and smooth or ribbed rods were tested. Spacers and rods were made of type 316 stainless steel. Adhesion was observed in tests on smooth rods in an environment containing 900/90 μatm of H_2/H_2O in helium. No adhesion was observed when the H_2/H_2O ratio was increased to 100 at the same absolute level of H_2O. Adhesion has not been observed with Inconel 718, Inconel 625, or Hastelloy spacers against 316 stainless steel smooth rods.

The current GCFR reference design includes spacers fabricated by electrodischarge machining (EDM). Tests to determine the effect of environment (various H_2/H_2O ratios and surface roughness) have been completed on EDM spacers. No adhesion has ever been observed on the EDM spacers. In addition, the effect of contact surface geometry was investigated, and a flat surface was selected as an optimum geometry. Reproducibility tests were then conducted to increase confidence in the test results. Finally, the effect of long dwell times between strokes was investigated.

During this quarter, reproducibility tests at 750°C on ribbed rods were completed. The test results are given in Table 2-2. The tests consisted of two long-stroke and two short-stroke tests. The ribbed rods were fabricated by mechanical grinding at Kraftwerk Union (KWU) using 20% cold-worked 316 stainless steel tubing supplied by GA. The simulated spacers were fabricated by EDM by a U.S. vendor from 20% cold-worked 316 stainless steel plate and had flat contact surfaces with a surface finish of 2 to 4 μm rms for bearing against the ribbed tube surface. The results given in Table 2-2 show that the coefficient of friction was in the normal range of 1.0 or less, but wear was usually greater than the normal amount of 20 to 40 μm. However, in these tests, an additional effect was a peculiar oxidation of the mechanically ground ribbed tubing. Studies on this effect were initiated under the cladding technology program after discussions with KWU, where the grinding was done.

During this quarter, two long dwell time tests which included the effect of environment on the rod spacer were completed. Smooth rods and EDM spacers were used at a test temperature of 550°C. The H_2/H_2O ratio conditions for the two tests were 90/90 and 3000/30 μatm (Table 2-3). The tests were conducted by using twenty-five 1-hr dwell times between strokes followed by six 100-hr dwell times between strokes, followed by seventy 1-hr dwell times between strokes. Nothing unusual was observed during these tests except a somewhat higher coefficient of friction.

In addition, two other tests were performed; the results are shown in Table 2-3. These tests were conducted to investigate the effect of combined long and short strokes. During the interaction and wear, material from a wear groove is deposited at the end of a groove. A long stroke

TABLE 2-2
FUEL ROD/SPACER INTERACTION REPRODUCIBILITY TESTS(a)

Temperature (°C)	Stroke Length (mm)	H_2 (μatm)	H_2O (μatm)	Coefficient of Friction	Wear Depth (μm)
750	3.8	3000	850	0.7	100
750	3.8	3000	850	1.0	50
750	0.76	3000	850	0.9	20
750	0.76	3000	850	0.52	50

(a) Rods had mechanically ground ribbing from KWU, spacers were made by a U.S. vendor using EDM, and rod and spacer material was 20% cold-worked 316 stainless steel.

TABLE 2-3
ROD/SPACER INTERACTION LONG DWELL TESTS [(a)]

Temperature (°C)	Stroke Length (mm)	H_2 (μatm)	H_2O (μatm)	Coefficient of Friction	Wear Depth (mm)	Remarks
550	3.8	90	90	0.87	Negligible	Long dwell
550	3.8	3000	30		30	Long dwell
550	3.8	90	90	0.7	30	Combination long and short strokes
550	0.76	90	90	0.7	25	

(a)Rods were 20% cold-worked 316 stainless steel and had a smooth surface; spacers were made by EDM and were 20% cold-worked 316 stainless steel.

occurring after many short strokes will encounter this material buildup, possibly causing higher friction or adhesion. In the tests, 2000 short strokes were followed by 6 long strokes. During the long strokes, the axial forces generated were at the same level as those generated during the short strokes. This indicates that this combination of cycling and interaction in a reactor would not pose any additional friction or wear problems.

Preparations are being made to test the current GCFR spacer design configuration, i.e., the modified hexagonal spacer cell. An AGATHE spacer is being procured and will be cut for sample test cells. A test cell holder will be fabricated by GCFR laboratory personnel.

2.3.2. Transient Interaction Tests

Planning continued for initiating the transient temperature rise testing of the fuel cladding and spacer to simulate reactor transient operation. Inquiries have been made of heater manufacturers for heaters that could be used in the current test furnaces to ramp the temperature from 750° to 850°C in a few seconds. It is planned to procure single heaters for preliminary heating tests in the present furnaces. An alternate design using induction heating is being considered.

2.4. CORE TEMPERATURE MONITORING

The core temperature monitoring design requirements of the core elements were reviewed to determine how they might be affected by

1. Alternate core temperature monitoring techniques to replace the thermocouple system of the reference design.

2. Changes proposed in the core element locking system for eliminating the array of locking mechanism tubes for each element to

reduce the mechanical complexity and upper plenum/pressure drop. These straight tubes were to be used for replacement of the thermocouple and lead assemblies as required by the criteria.

The design requirements and criteria for the core temperature monitoring requirements must be based on reactor system requirements and thus must be independent of other hardware functions. It appears that most of the promising temperature sensor concepts can fit into the envelope diameter requirements of a thermocouple (∿3-mm-diameter), and the lead assembly can be replaced through a tube which is not straight. Thus, the design criteria for the core element function of temperature monitoring will remain the same as that given in Ref. 2-14.

2.5. HEAT TRANSFER AND FLUID FLOW TESTING

The parts for the fuel element nozzle flow test have been completed and are shown in Fig. 2-7. A subassembly of the grid plate shield and annular fission product trap is shown in Fig. 2-8. Minor alterations are being made for final assembly, and the model was delivered to Experimental Engineering in July for instrumentation prior to initiation of testing in the transition quarter.

Because of design changes in the shielding, the current model test will be for correlation of analytical predictions of pressure drop. However, the internal shape of the model components can be changed. A new shield and trap design for improved shielding performance is in progress, and design and fabrication of plastic parts for the new design is planned in the FY 76 transition quarter if funds become available.

REFERENCES

2-1. "Gas-Cooled Fast Breeder Reactor Quarterly Progress Report for the Period February 1, 1976 Through April 30, 1976," ERDA Report GA-A13868, General Atomic, May 31, 1976.

76G1416

Fig. 2-7. Fuel element nozzle flow test parts

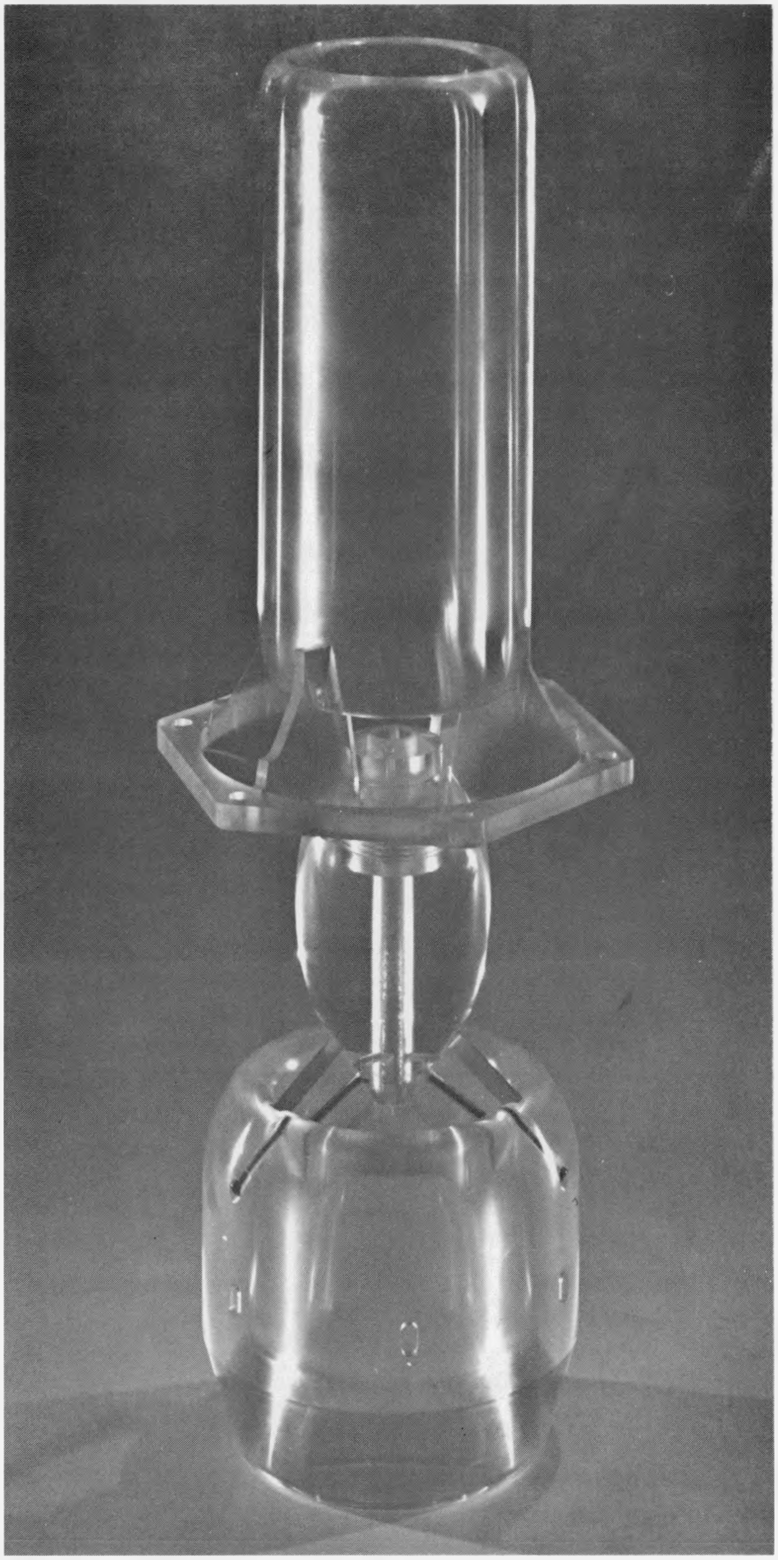

76G1423

Fig. 2-8. Flow test subassembly of grid plate shield and annular fission product trap

2-2. Le Tourneau, B. W., and R. E. Grimble, "Engineering Hot Channel Factors for Reactor Design," Nucl. Sci. Eng. 1, 359 (1956).

2-3. Rude, P. A., and A. C. Nelson, Jr., "Statistical Analysis of Hot Channel Factors," Nucl. Sci. Eng. 7, 156 (1960).

2-4. Abernathy, F. H., "The Statistical Aspects of Nuclear Reactor Fuel Element Temperature," Nucl. Sci. Eng. 11, 290 (1961).

2-5. "APDA Introduces Statistical Hot Spot Factors," Nucleonics 17, 92 (1960).

2-6. Antognetti, G., et al., "Statistical Methods for Hot Channel and Hot Spot Calculations," Euratom Report EUR 1703e, 1964.

2-7. Businardo, V. L., and G. P. Pozzi, "A New Approach on Engineering Hot Channels and Hot Spot Statistical Analysis," Swiss Federal Institute for Reactor Research Report EIR 1302e, 1964.

2-8. Nelson, A. C., and W. S. Minkler, "A General Method for Evaluating the Effects of Uncertainties in Design Variables on Core Thermal Performance," Nucl. Sci. Eng. 17, 101 (1963).

2-9. Judge, F. D., and L. S. Bohl, "Effective Hot Channel Factors for Flat Power Reactors," Trans. Am. Nucl. Soc. 7, 497 (1964).

2-10. Fenech, H., and H. M. Gueron, "The Synthesis Method of Uncertainty Analysis in Nuclear Reactor Thermal Design," Nucl. Sci. Eng. 31, 505 (1968).

2-11. Chelemer, H., and L. S. Tong, "Engineering Hot Channel Factors for Open-Lattice Cores," Nucleonics 20, 68 (1962).

2-12. "CRBRP Assemblies Hot Channel Factors Preliminary Analysis," Westinghouse Electric Report WARD-D0050, October 1974.

2-13. Arnsberger, P. L., "Some Aspects of Overall Statistical Hot Spot Factor Analysis for LMFBR Core," in Proceedings of the International Meeting on Fast Reactor Fuel and Fuel Elements, Karlsruhe, September 28-30, 1970, M. Dalle Donne, K. Kummerer, and K. Schroe (eds.), Gesellschaft für Kernforschung, Karlsruhe, 1970.

2-14. "Gas-Cooled Fast Breeder Quarterly Progress Report for the Period August 1, 1975 Through October 31, 1975," ERDA Report GA-A13766, General Atomic, January 5, 1976.

3. PRESSURE EQUALIZATION SYSTEM FOR FUEL (189a No. SU006)

3.1. FUEL ELEMENT AND VENT CONNECTION SEALS

In the GCFR, the core elements (fuel, control, and blanket) are clamped at the conical surfaces of the elements to the matching surfaces in the grid plate with a force sufficient to support the elements, which are cantilevered downward. The elements must also be sealed to the grid plate to limit the coolant flow that can bypass the elements, and their vents must be connected and sealed to matching gas passages in the grid plate. The element seals must function at the coolant pressure difference between the reactor core inlet and exit plenums. The effectiveness of the seals over the life of the core is uncertain, not only because each element may be rotated several times over its useful life, but also because the seals must be effective in a high-purity, high-temperature helium environment while subject to mechanical, vibrational, and thermal effects. Most of the uncertainties are expected to be resolved in a two-part program: (1) a materials screening test program for the study of static adhesion of simulated fuel element and grid plate parts clamped together and (2) leakage tests of fuel element and vent connection seals to the grid plate. Current progress in these activities is described below.

3.1.1. Static Adhesion Tests

Evaluation of alternate materials exposed in a 3000-hr static adhesion test was completed, and the results are given in Table 3-1 and Figs. 3-1 through 3-4. The results in Table 3-1 are for only the 9 couples which adhered during the test out of the total 36 couples. First of all, it is noted that the only couples which adhered were those with 30-deg cone angles. The second unexpected result was that of the 9 couples which adhered, 8 were made of Inconel 718 (6 with 316 and 2 with 304 stainless

TABLE 3-1
STATIC ADHESION TEST RESULTS(a)

Couple No.	Material		Nominal Clamping Load (N)	Pull-Apart Load (N)
	Element	Grid Plate		
3	Inconel 718	304 stainless steel	900	1000
4	Inconel 718	304 stainless steel	900	300
7	Inconel 718	316 stainless steel	900	470
8	Inconel 718	316 stainless steel	900	600
15	Inconel 718	316 stainless steel	1350	920
16	Inconel 718	316 stainless steel	1350	680
19	Inconel 718	304 stainless steel	1800	300
24	Inconel 718	316 stainless steel	1800	850
32	316 stainless steel	304 stainless steel	1350	555

(a)Test conditions: helium at 350°C with 9000 μatm H_2 and 90 μatm H_2O. Half-cone angle of mated couples = 30 deg.

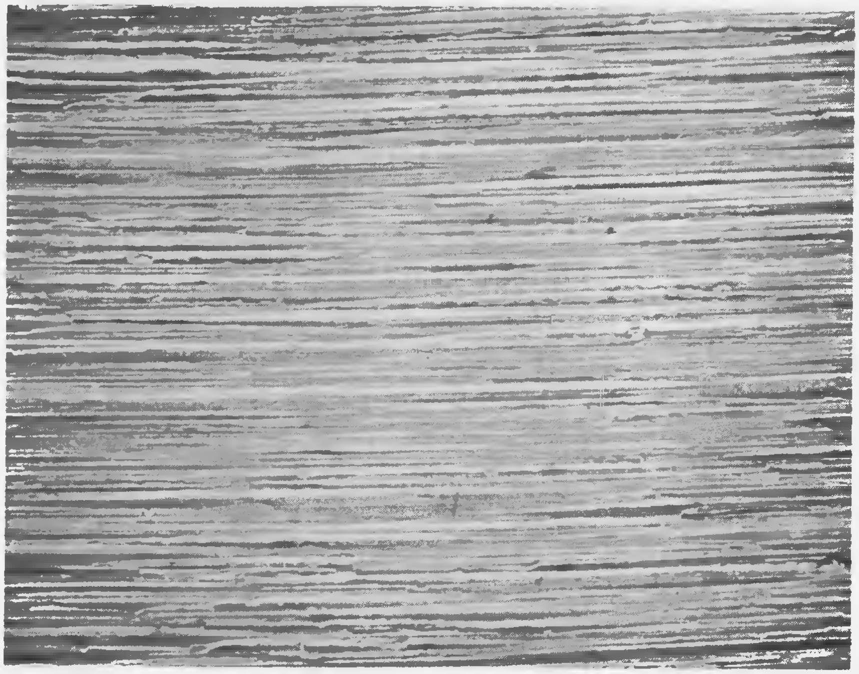

(a) 250X

(b) 250X

Fig. 3-1. Inconel 718 couple No. 8: (a) before test, (b) after test

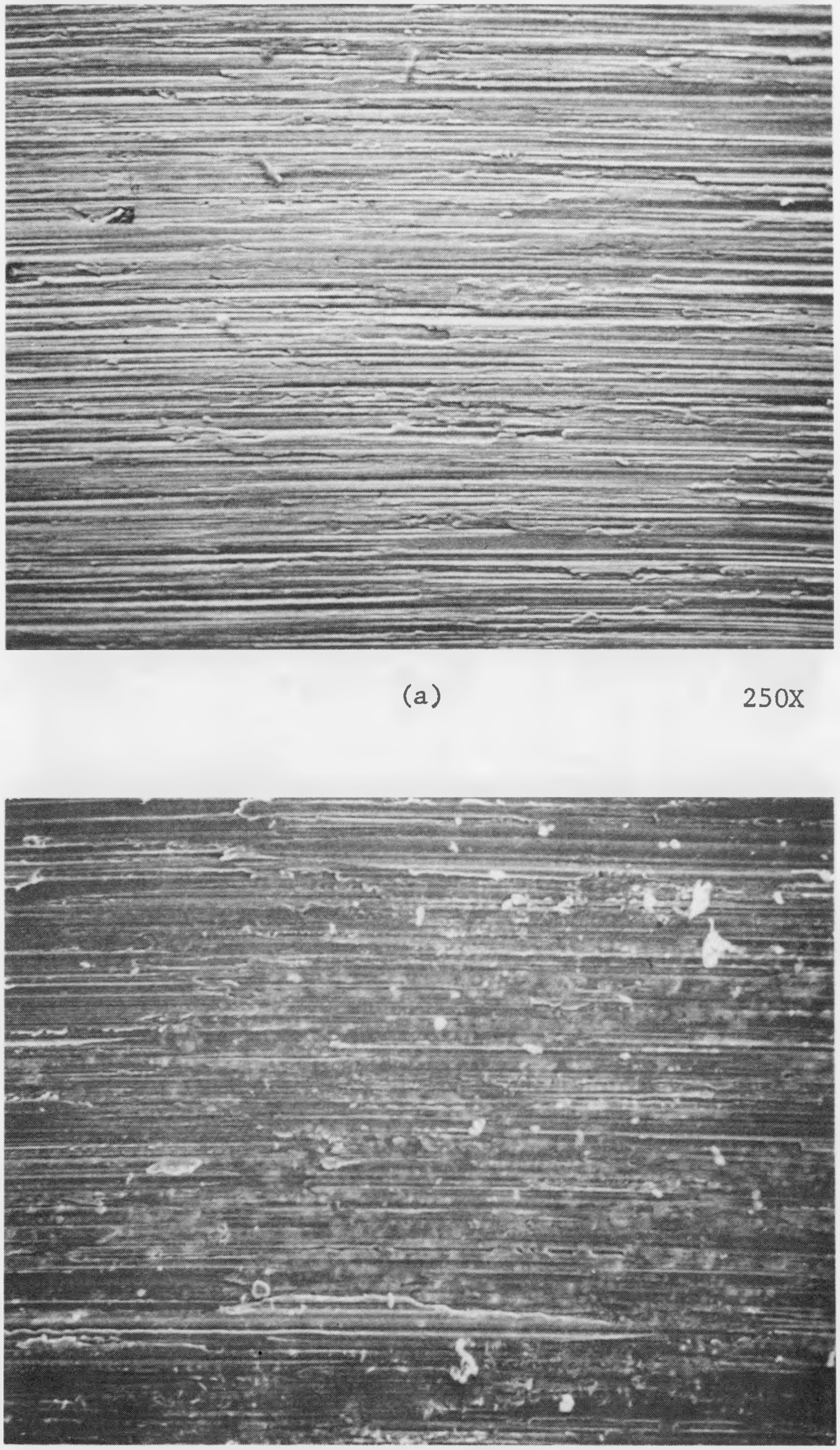

(a) 250X

(b) 250X

Fig. 3-2. Type 316 stainless steel couple No. 8: (a) before test, (b) after test (adhesion to Inconel 718)

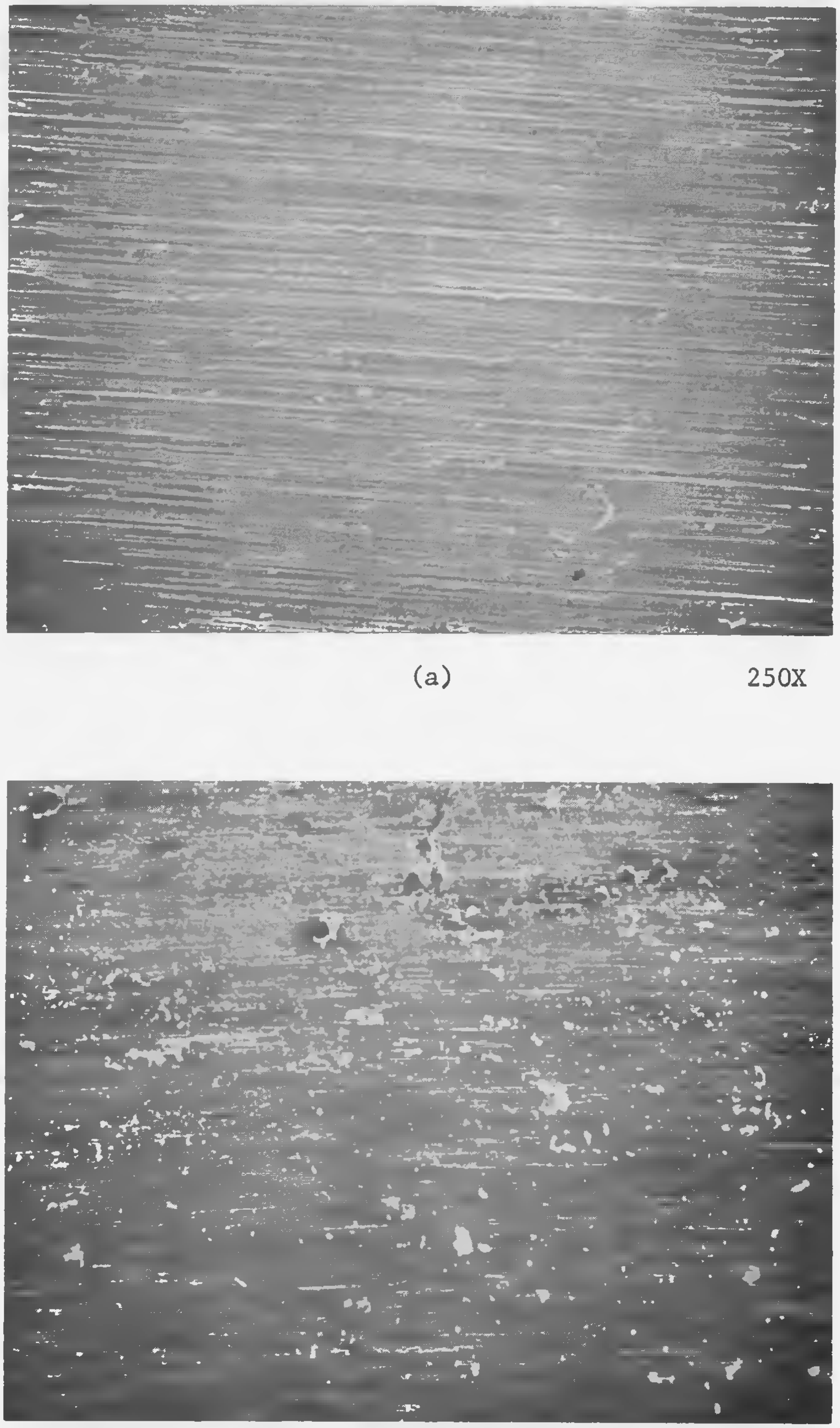

(a) 250X

(b) 250X

Fig. 3-3. Type 304 stainless steel couple No. 32: (a) before test, (b) after test (adhesion to 316 stainless steel)

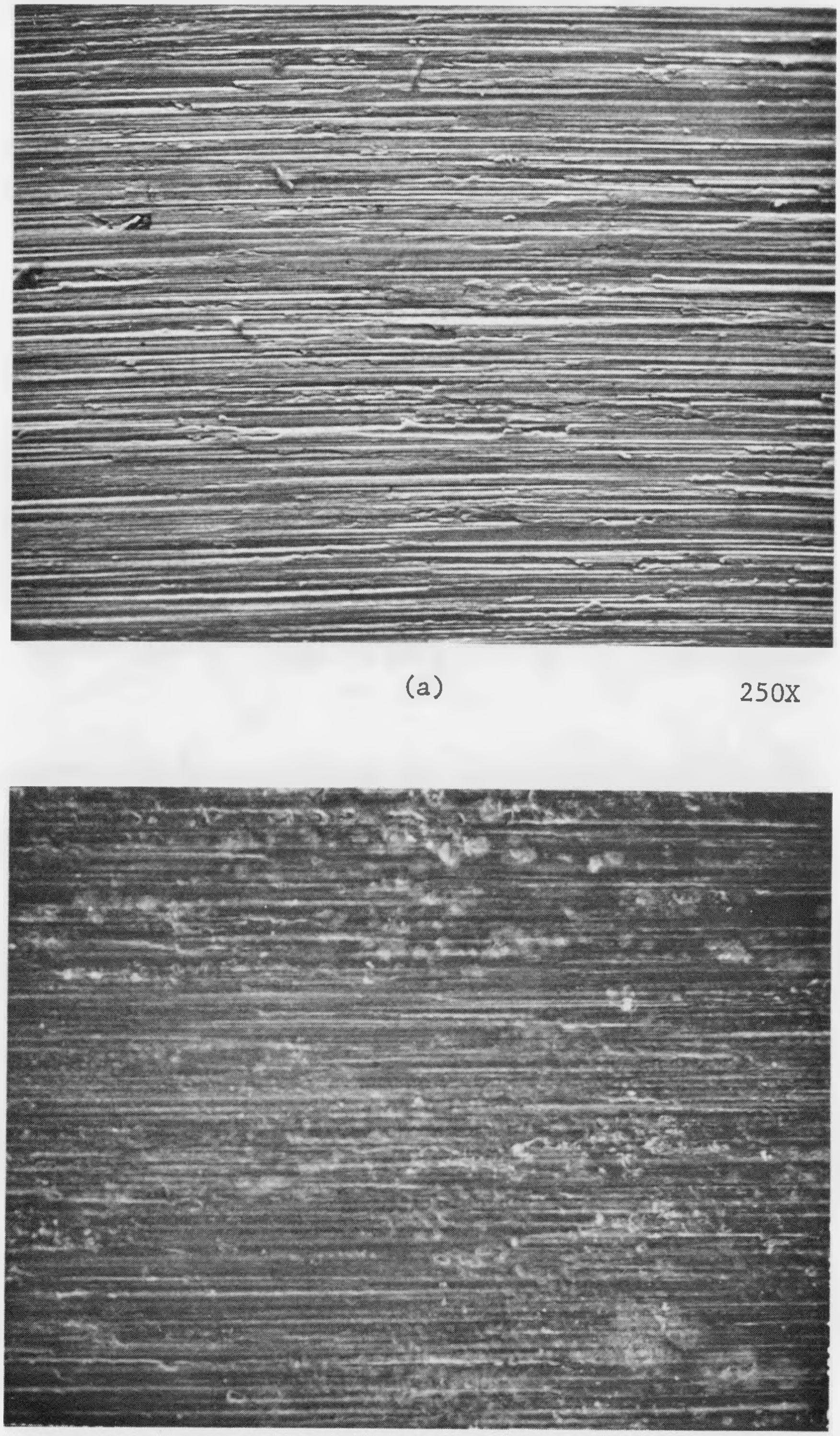

(a) 250X

(b) 250X

Fig. 3-4. Type 316 stainless steel couple No. 32 (adhesion to 304 stainless steel): (a) before test, (b) after test steel), and only one was made of 316 and 304 stainless steel. The pull-apart load required to separate the adhered couples was independent of the initial clamping loads.

The effects of adherence on the surfaces are shown in Figs. 3-1 through 3-4. Although the Inconel - stainless steel couples seemed to adhere together readily, there was no evidence of any material transfer (Figs. 3-1 through 3-2), as evidenced in the previous tests of 316 versus 304 stainless steel (Ref. 3-1). In addition, the single couple (No. 32) of 304 versus 316 stainless steel which did adhere showed material transfer [see Figs. 3-1 and 3-4(a,c)].

One conclusion of the above results is that an Inconel fuel element and stainless steel grid plate with 30-deg cones might require some force to pull them apart after being clamped together. However, adherence will probably not result in damage to the stainless steel grid plate by material transfer, and the force required to pull them apart will be of the order of the weight of a core element. However, longer-term tests of full-size cones will be necessary to fully establish the pull-apart force to be used in core element designs.

3.1.2. Fuel Element Ring Seal Leakage Tests

An alternative to the conical metal-to-metal core element seal design in which piston rings are used as sealing members is being developed. Piston ring seal tests are in preparation and are based on the design incorporated into the joint KWU-GA model core element being built by KWU in Germany. Test equipment and test grid plate and fuel elements parts used for metal-to-metal conical seal testing will be modified to test the piston ring seals. The test plan includes testing of the basic German piston ring design and the piston ring designs of two U.S. vendors, including three different ring materials.

The piston rings from the two U.S. vendors were received and inspected. All rings and parts met the vendors specifications. Adapters were designed to mate these ring types to the simulated element nozzle (piston) and grid plate (cylinder). The adapter design is shown in Fig. 3-5. The design includes five sizes of the cutout (B dimension in Fig. 3-5) to test the ring sets. The comparative test results will be evaluated to determine the sealing effectiveness of the various ring assemblies.

Two sets of the piston rings to be tested are shown in Fig. 3-6. In the lower left part of Fig. 3-6 is a single-piece stainless seal ring made of type 410 stainless steel. In the lower right part of Fig. 3-6 are two inner rings of the five-piece Dover seal assembly, and at the top of Fig. 3-6 is another inner ring, the radial (marcel) spring and the axial (wave) spring. The outer ring materials of the Dover assemblies are S-Monel, Inconel 718, and type 410 stainless steel. The inner rings are 17-4 PH stainless steel, the axial springs are 17-7 PH stainless steel, and the radial springs are Inconel X750.

The parts for the piston ring test facilities have been machined, and one assembly has been welded together, with final alignment machining accomplished. One completed set of assemblies and parts is shown in Fig. 3-7. In the left part of Fig. 3-7 are the simulated grid plate test parts and at the right are the simulated core element parts. In the left foreground of Fig. 3-7 are the piston ring seal parts and a flange for suspending the assembly in the test autoclave. The tall cylindrical tube at the right is the mounting cylinder for the band heaters for temperature control of the test.

3.1.3. Vent Assembly Seals

A vent assembly is being developed for connecting the GCFR fuel element vents to the passages in the grid plate and for sealing the core element vents when the elements are removed from the grid plate for handling, storage, and transport. The design for testing the vent assembly in the element seal test autoclave depends on the installation of the vent assembly in the conical surface of the element. Two installation designs have evolved. In one installation, the vent assembly is radially oriented and

GA 1279 B 9-2-75

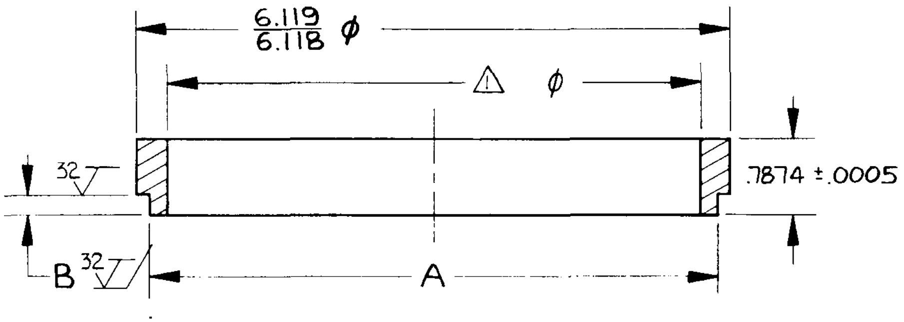

NOTES

⚠ MACHINE FOR SLIP FIT ON PART NO. 3228022109-1. USE DIM ON DWG NO. 3228022103 FOR REF.

DASH NO.	DIM. A	DIM B	
-5	5.680 / 5.670 ϕ	.159 / .158	DOVER, NO SPRINGS
-4	5.710 / 5.700 ϕ	.159 / .158	DOVER + MARCEL SPRING
-3	5.680 / 5.670 ϕ	.180 / .179	DOVER + WAVE SPRING
-2	5.710 / 5.700 ϕ	180 / .179	DOVER + MARCEL + WAVE SPRINGS
-1	5.665 / 5.660 ϕ	.2025 / .2015	STEIN

PARTS LIST

REQD/ASSEMBLY	ITEM	PART NO.	DESCRIPTION	MATL/MATL SPEC
		-5	RING	316 SS
		-4	↕	↕
		-3	↕	↕
		-2	↕	↕
		-1	RING	316 SS

DIST.

GENERAL ATOMIC COMPANY
SAN DIEGO, CALIFORNIA

LTR	DATE	ISSUE DESCRIPTION	DR	CHK.	DES	APPD	APPD.
A		FOR CONSTRUCTION					

UNLESS OTHERWISE SPECIFIED
DIMENSIONS ARE IN INCHES
NO BURRS OR SHARP EDGES
DIMENSIONS PER ANSI-Y-14.5
TOLERANCE:
DECIMAL FRACTION ANGLE
XXX = ± ± ±
.XX = ±
63 √
ALL MACHINED SURFACES
DO NOT SCALE PRINT

PROPRIETARY INFORMATION

THIS DOCUMENT IS THE PROPERTY OF GENERAL ATOMIC CO AND WILL BE RETURNED UPON REQUEST OR WHEN NO LONGER NEEDED BY THE RECIPIENT. INFORMATION CONTAINED HEREIN MAY NOT BE COMMUNICATED TO OTHERS NOR MAY THE DOCUMENT BE COPIED IN WHOLE OR IN PART WITHOUT THE EXPRESS CONSENT OF GENERAL ATOMIC CO

TITLE
RING,
PISTON RING TEST APPARATUS

SIZE	CODE IDENT NO.	DWG. NO.	ISSUE
B	32334	3228022125	A

SCALE 1/1 QAL SHEET 1 OF 1

N20857

Fig. 3-5. Piston ring test apparatus

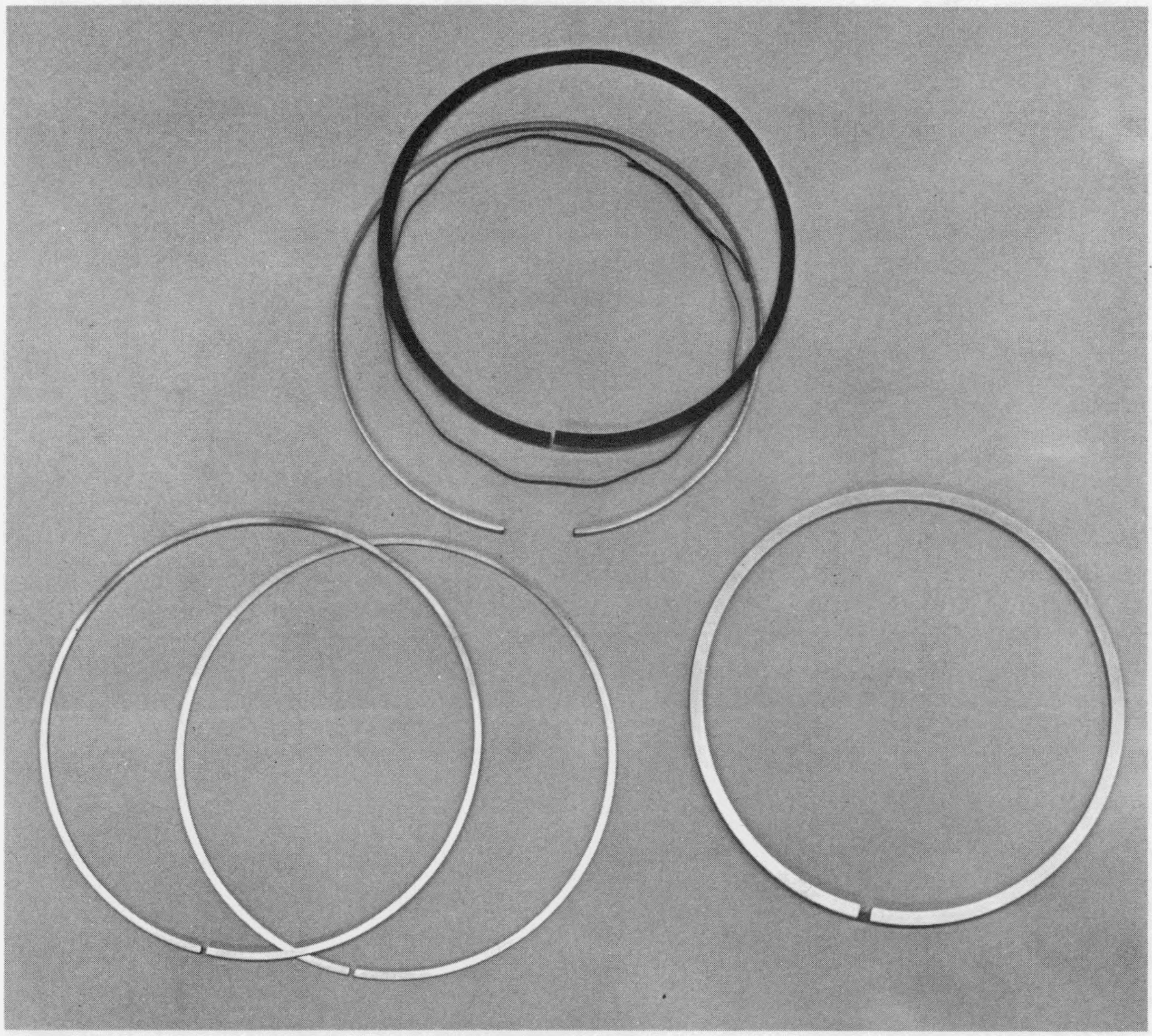

76G1434

Fig. 3-6. Piston ring parts for element seal test

76G1435

Fig. 3-7. Test facility parts for fuel element ring seal test normal to the cone surface. In the second installation, the vent assembly is vertically oriented in the element conical surface. The first installation design is shown schematically in Fig. 3-8. This installation will require machining of a flat (spot face) on the conical surfaces of the fuel element and the grid plate. The second installation is still being designed and requires projection of flat surfaces on either the fuel element conical surface or the grid plate conical surface with a mating recess on the grid conical surface or element conical surface.

The reason for using the Belleville washer springs is to obtain a high load for a small deflection for compactness of the assembly. However, the springs are highly stressed and relaxation can occur at the operating temperature of ∿350°C. Thus, materials with high thermal creep strength are being considered. Belleville springs made of 17-7 PH material were procured and tested. The spring-load deflection curves from a test (room temperature) of washer stacks of 7 series X 2 parallel are given in Fig. 3-9. The maximum and minimum values for six tests of randomly selected washer stacks (no washers repeated in any test) are given. The statistical variation was such that twice the standard deviation was about 4%. The manufacturer's (Associated Spring Corporation) recommended design tolerance is ±15% from nominal. These tests show that the springs probably can be designed to ±10% without highly restrictive controls on production. The same manufacturer's recommended design range for coil springs is ±10%, however coil springs cannot provide the compact design needed for this vent seal application.

3.2. ANALYSIS, MODELS, AND CODE DEVELOPMENT

The GCFR is designed with pressure-equalized and vented fuel and blanket assemblies or elements. A pressure equalization system (PES) is provided to perform these functions and contains one unit of the helium purification system (HPS). The PES shown schematically in Fig. 3-10 is a complex flow network consisting of the manifolded fuel rods, fuel and blanket elements, monitor lines through which the vented fission gases are swept by inflowing coolant, the HPS unit, and the check valves leading to

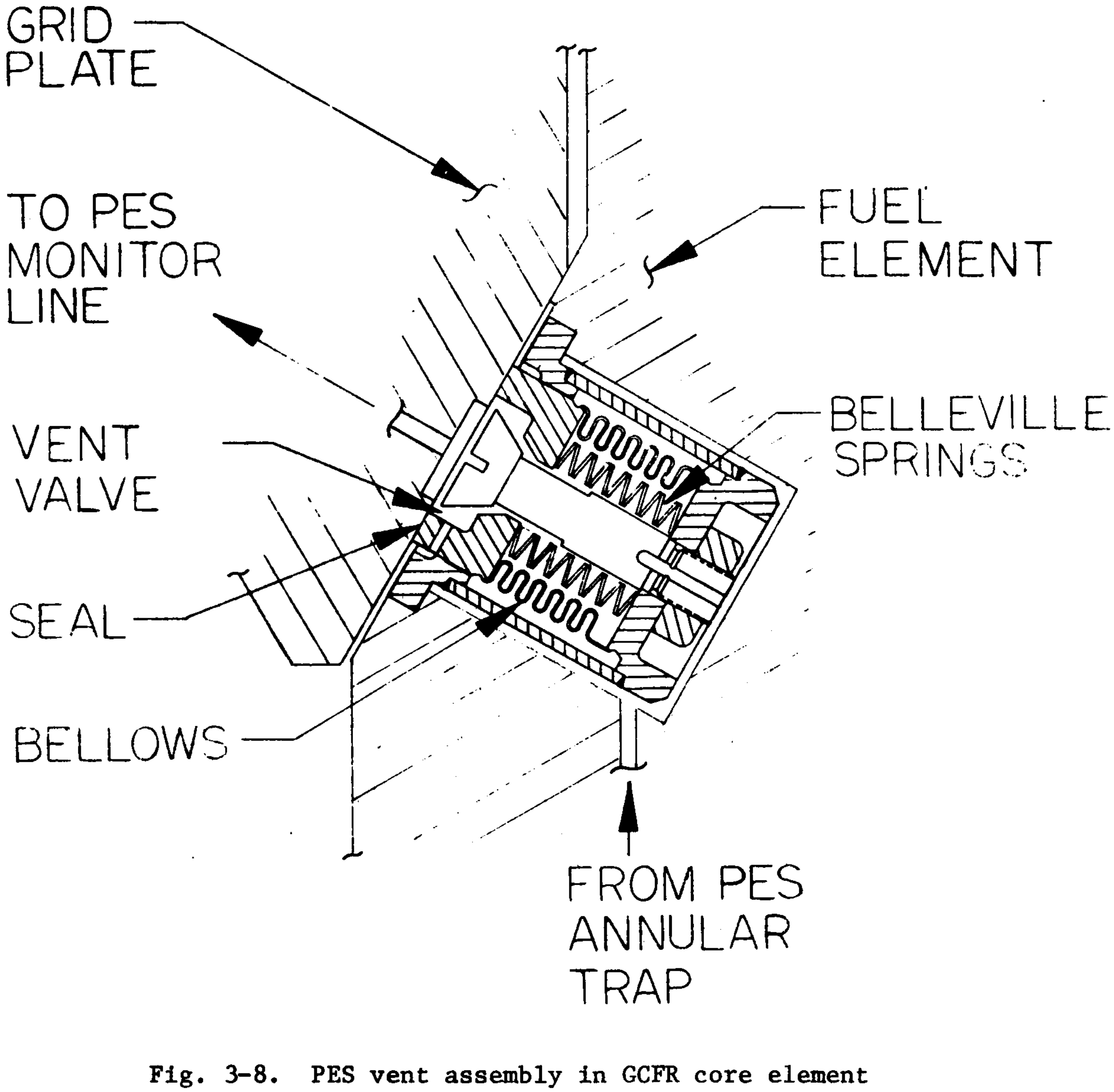

Fig. 3-8. PES vent assembly in GCFR core element

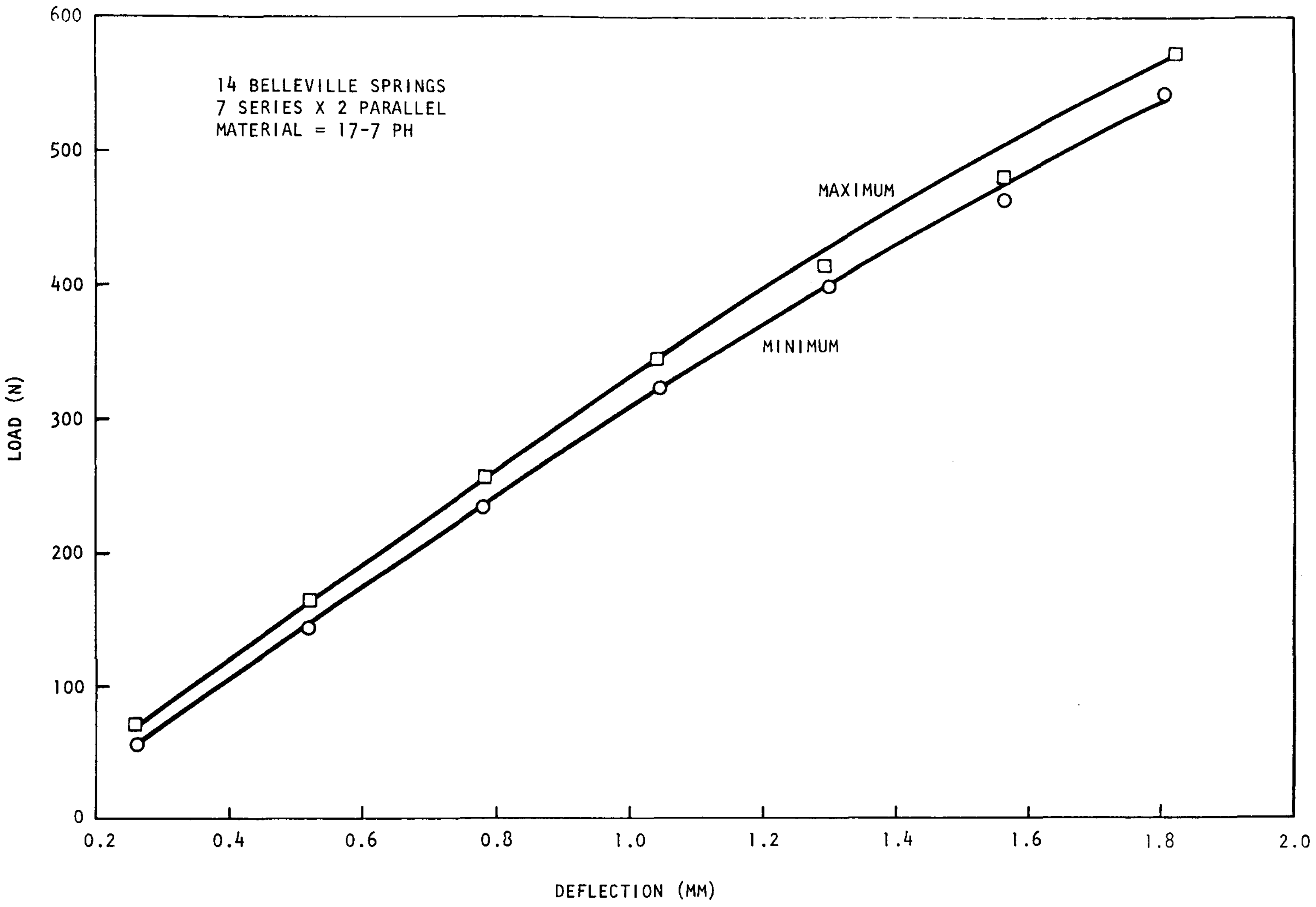

Fig. 3-9. Load deflection

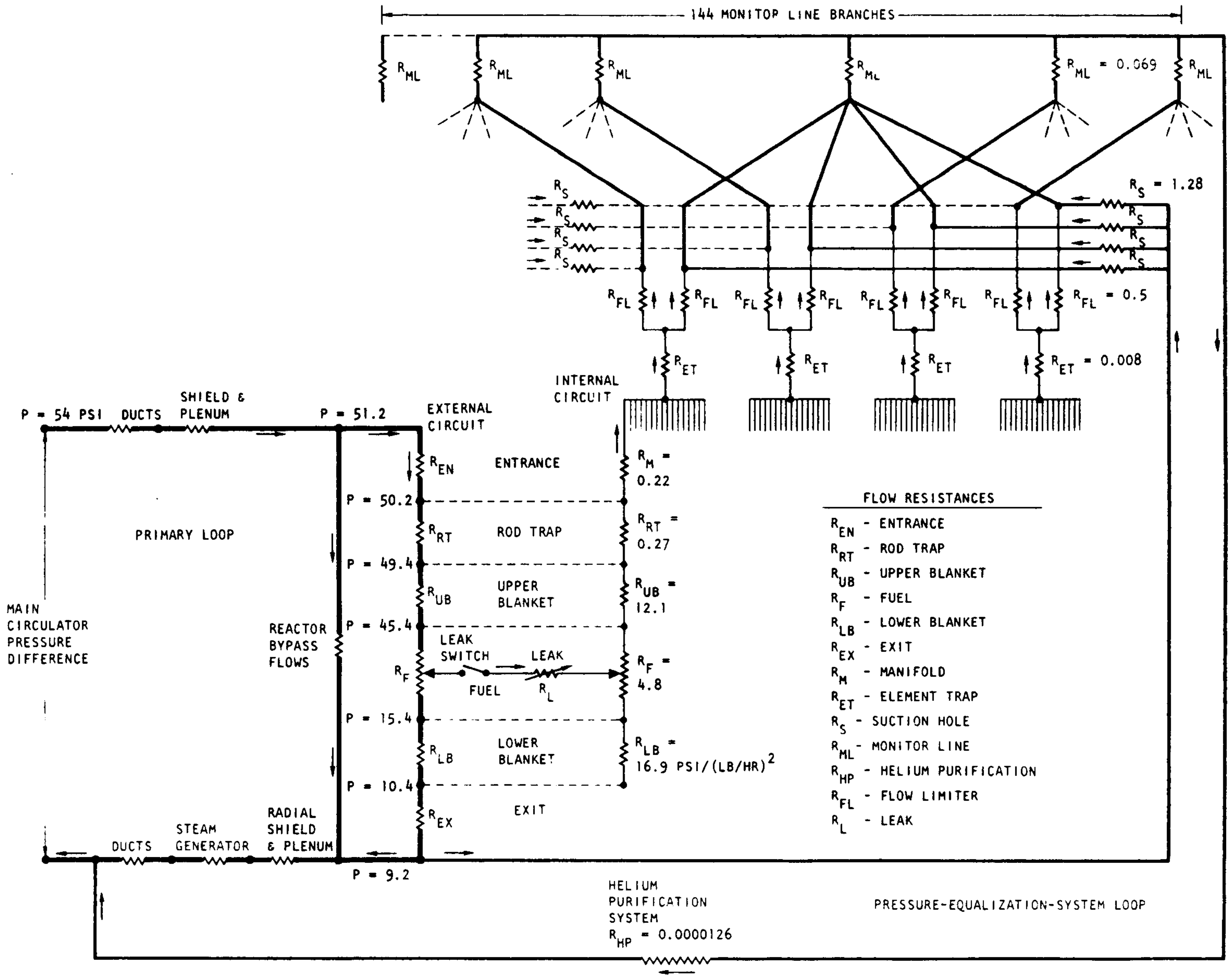

Fig. 3-10. Pressure equalization system flow network and its relationship to the primary coolant circuits

the suctions of the main and auxiliary circulators which power the system. The HPS unit contains two parallel trains of filters, heaters, and coolers. Only one train, shown schematically in Fig. 3-11, is in service at any time. During this quarter, development continued on modeling and computer code development for design and transient analysis of the PES flow network.

Steady-state flow analyses of the PES/HPS network have been done (Ref. 3-2) using the FLAC code (Ref. 3-3). The results of those studies indicate satisfactory performance of the PES/HPS during steady-state operation. Of considerable importance to the GCFR is the analysis of the behavior of the PES/HPS during transients. An earlier literature survey (Ref. 3-4) indicated that no computer codes were commercially available for this purpose. Two in-house transient flow network codes, FAT (Ref. 3-5) and RATSAM (Ref. 3-6), were reviewed to determine their applicability to the PES/HPS analysis. It was found that neither code could be directly applied to the PES/HPS analysis, although it did appear that modifications might be made to either code, which might enable the codes to be used for this task. Because of the lack of certainty as to whether these code modifications could be successfully completed within a reasonable time span, it was decided that a new code designed specifically for the PES/HPS transient flow analysis should be developed. The SYSL (Ref. 3-7) system simulation language was selected as the basis of the PES/HPS code (although the formulation that has been developed is amenable to FORTRAN V coding as well).

In order to solve the transient flow network problem, the network is idealized as a system of volume nodes connected together by flow lines. The equations of continuity and energy are solved for each node, and the momentum equation is solved for each flow line. Heat may be added to or removed from any node, but the flow through a flow line is assumed to be adiabatic and isothermal. The flow is also assumed to be subsonic. Thus, at each node there are

$$\text{continuity,} \qquad \frac{dm}{dt} = \sum_i w_i \quad , \tag{3-1}$$

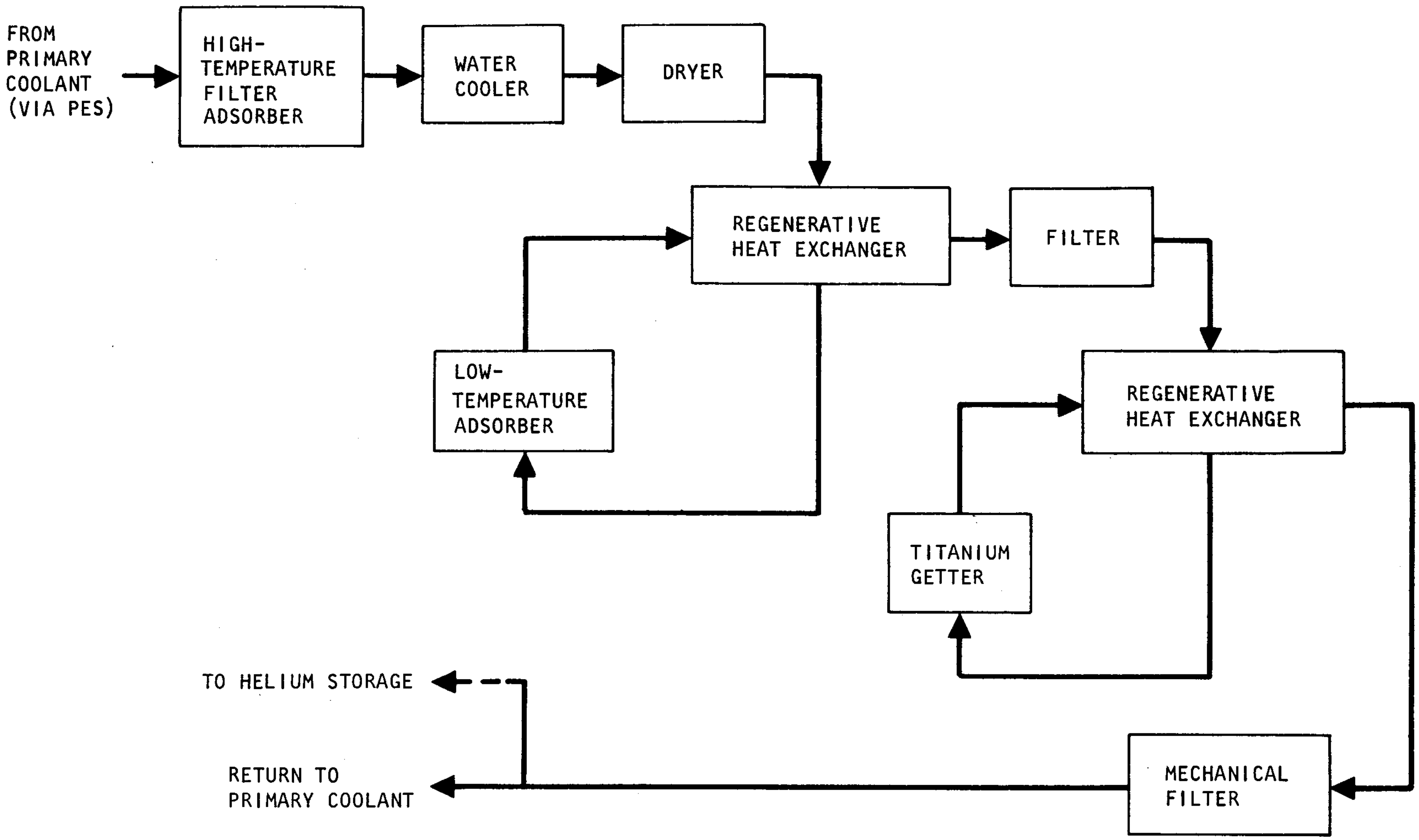

Fig. 3-11. Schematic of GCFR HPS unit 2

energy, $$\frac{dP}{dt} = \frac{\gamma R}{V} * \sum w_i T_i + Q * \frac{R}{Vc_v} \quad , \tag{3-2}$$

where m = mass of gas in the node,

w = mass flow rate into the node,

P = gas pressure in the node,

γ = ratio of specific heats for helium,

R = helium gas constant,

V = node volume,

T = temperature of the gas entering ($w_i > 0$) or leaving ($w_i < 0$) the node,

Q = heat generated in the node,

c_v = specific heat at constant volume for helium.

For each flow line there is

momentum, $$\frac{dw}{dt} = \frac{A}{L}\left(P_{in} - P_{out} - \frac{KRT}{A^2} * \frac{w|w|}{P_{in} + P_{out}}\right) \quad , \tag{3-3}$$

where w = mass flow in the line,

A = line cross-sectional area,

L = line length,

P_{in} = pressure at the line inlet,

P_{out} = pressure at the line outlet,

K = loss coefficient for the line,

R = helium gas constant,

T = gas temperature in the line.

The momentum equation in this form explicitly includes the effect of the inertia of the gas in the line. Gravitational effects on the flow are excluded in the present analysis, although they may be important for very low flow conditions. These effects can easily be included at a later date if necessary.

If the flow is assumed to be quasi-steady, i.e., if the flow is always

If the flow is assumed to be quasi-steady, i.e., if the flow is always in equilibrium with the pressure drop across the pipe, then Eq. 3-3 reduces to the familiar form

$$\Delta P = K * 1/2\ \rho v|v| \quad . \tag{3-4}$$

Equations 3-1 and 3-2 and 3-3 or 3-4 are the basic equations from which the PES/HPS codes have been developed. The code development has gone through three distinct phases. The initial phase consisted of solving Eqs. 3-1 through 3-3 for a simple model of the HPS. The second phase consisted of examining the effects of replacing Eq. 3-3 with Eq. 3-4. The third and final phase involved returning to the use of Eq. 3-3 and recoding the code into its present form. A chronology of the PES/HPS code development is given below.

1. HPS1. HPS1 was the first code developed for HPS/PES transient flow analysis. It solved the full set of describing equations, Eqs. 3-1 through 3-3, for the simple linear HPS model shown in Fig. 3-12. The code worked satisfactorily and was used to study the effects of various pipe sizes and check valves on an idealized HPS model.

2. HPS/PES1. This was an extension of the HPS1 model to include a simplified PES network. This code failed to work properly, and considerable investigation was unable to ascertain whether coding errors or numerical difficulties were at fault. It was felt that a possible source of trouble in the formulation was the use of Eq. 3-1 rather than Eq. 3-4, for the momentum equation.

3. HPS2. HPS2 was a completely new code for analyzing the simple HPS model. This code used the momentum equation (Eq. 3-4). The code worked and gave results which were very similar to the results obtained with HPS1, although there were some differences.

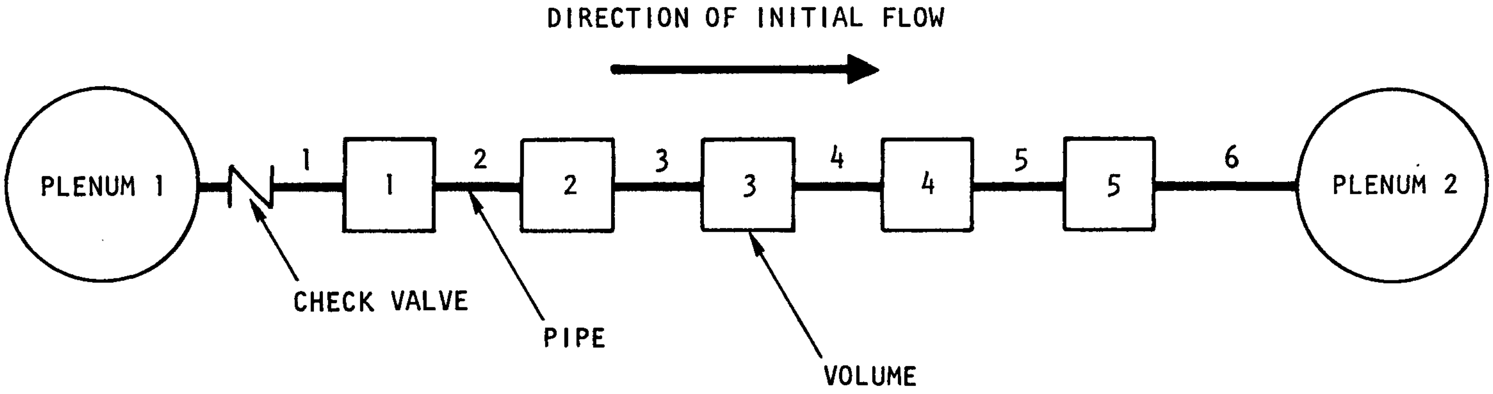

Fig. 3-12. Simplified HPS test model

4. HPS/PES2. This was a modification of the HPS2 model to simulate the simplified PES/HPS flow network shown in Fig. 3-13. Again, the simpler momentum equation, Eq. 3-4, was used. This model ran successfully for hypothetical geometry data and actual approximate GCFR data.

The similarity between the results of HPS1 and HPS2 was sufficient to justify the use of the simplified method for the PES/HPS analysis. However, there were also some problems with this method. In particular, because certain equations in the model were linearly dependent, the code would only converge to a consistent initial steady-state if exact estimates on the initial state of certain variables were made. Although this was not a serious problem, it was a definite drawback to the simplified method and did not occur if the full momentum equation was used. Also, a reexamination of the coding of HPS/PES2 led to the conclusion that the full momentum equation could be incorporated into the code. This led to the third generation of PES/HPS codes:

1. HPS3. HPS3 again modeled the simple HPS model using the complete set of equations used by HPS1, but it used the coding methods of HPS2. Nearly exact agreement was found between the results of HPS2 and HPS3.

2. PES3. The equation and methods of HPS3 were applied to the analysis of the simplified PES/HPS model using actual approximate GCFR data. The code achieved a consistent initial steady state and ran successfully in the transient mode, simulating a very severe depressurization accident. Results for this transient are shown in Figs. 3-14 through 3-16. These results should be regarded as very tentative and are presented only to illustrate the operation of the code.

Up to this point, none of the models tested had any closed-loop flow paths, i.e., flow paths which formed a closed loop between three or more

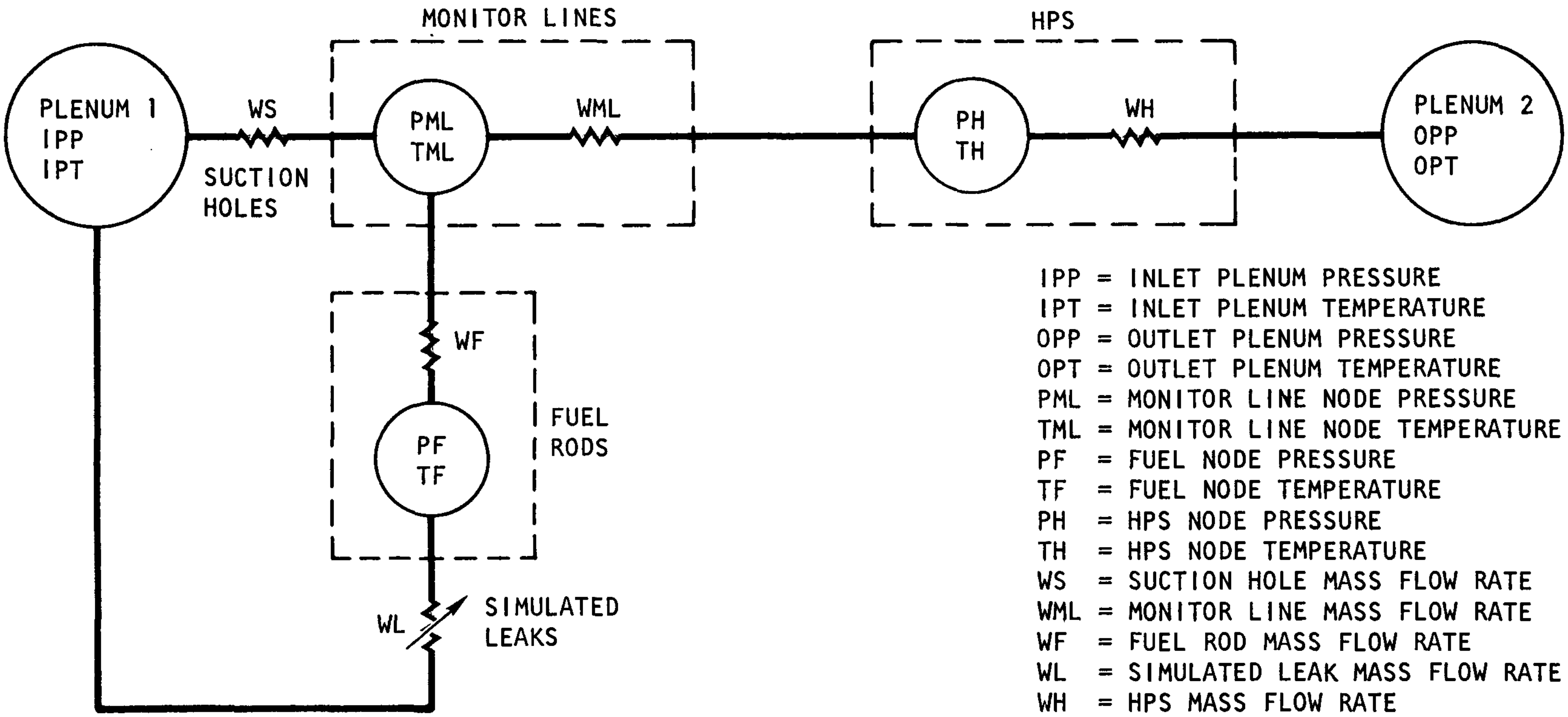

Fig. 3-13. Simplified PES/HPS transient flow network model

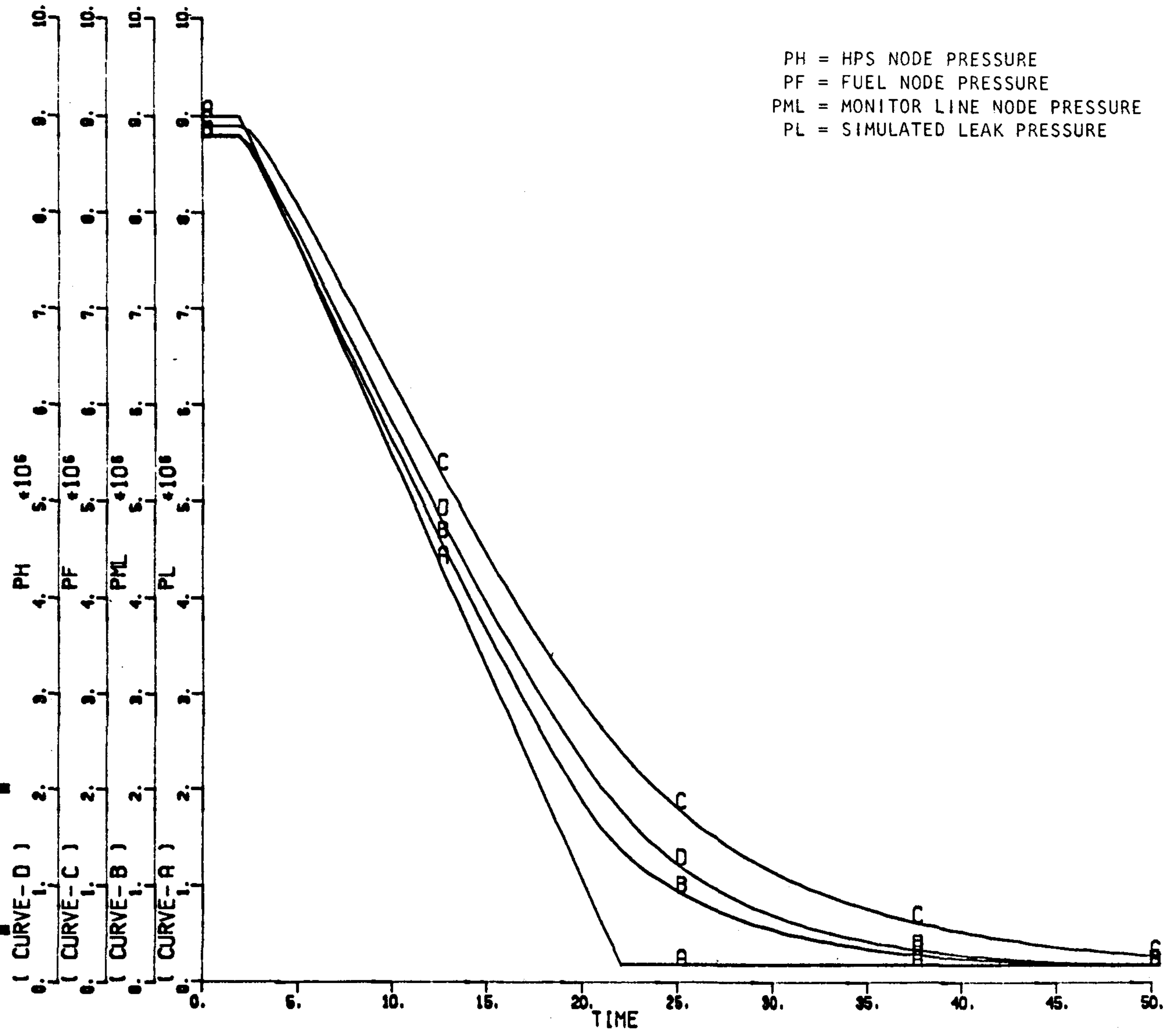

Fig. 3-14. Simplified PES/HPS network during rapid depressurization: pressure vs time

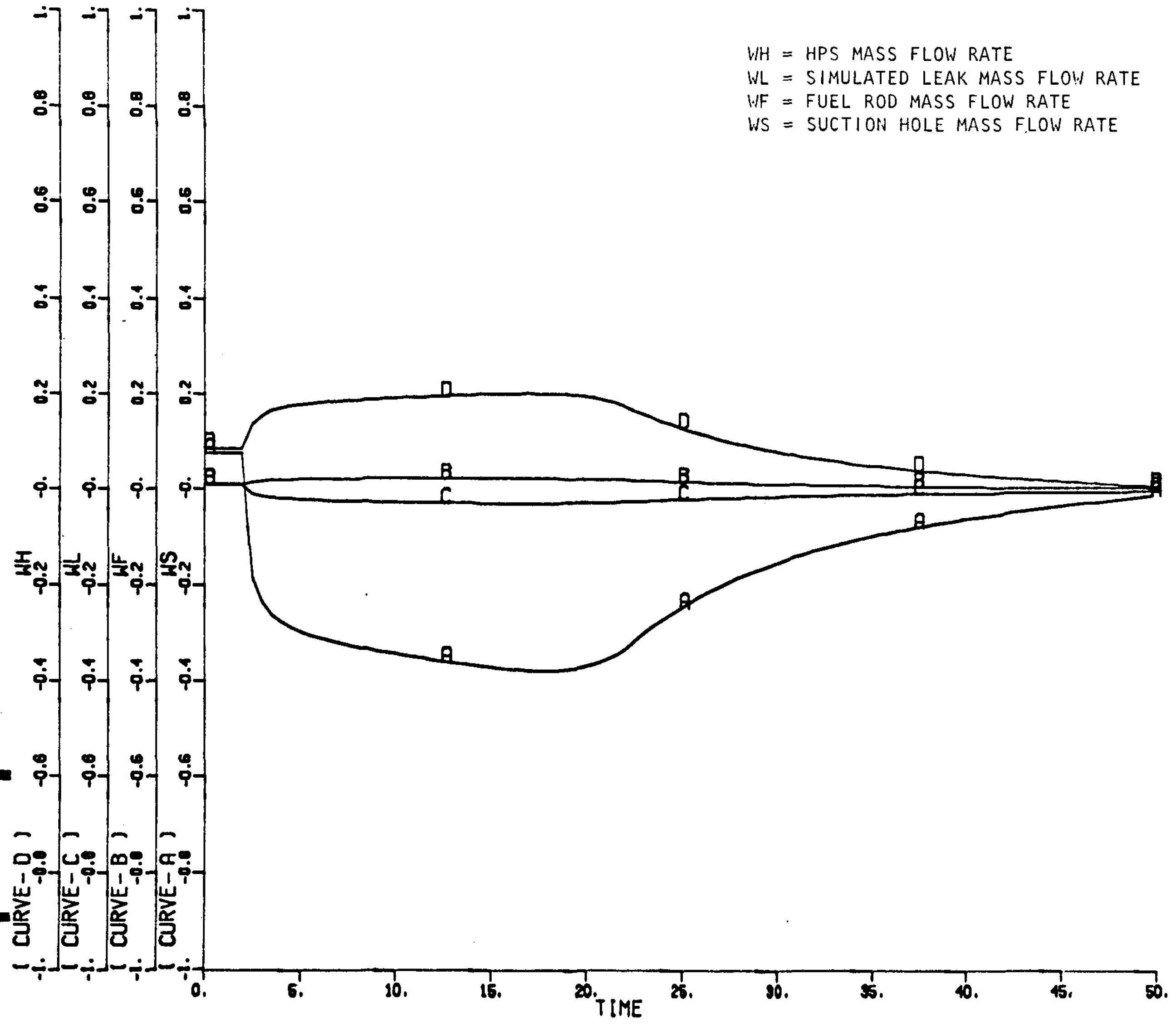

Fig. 3-15. Simplified PES/HPS network during rapid depressurization: flow rate vs time

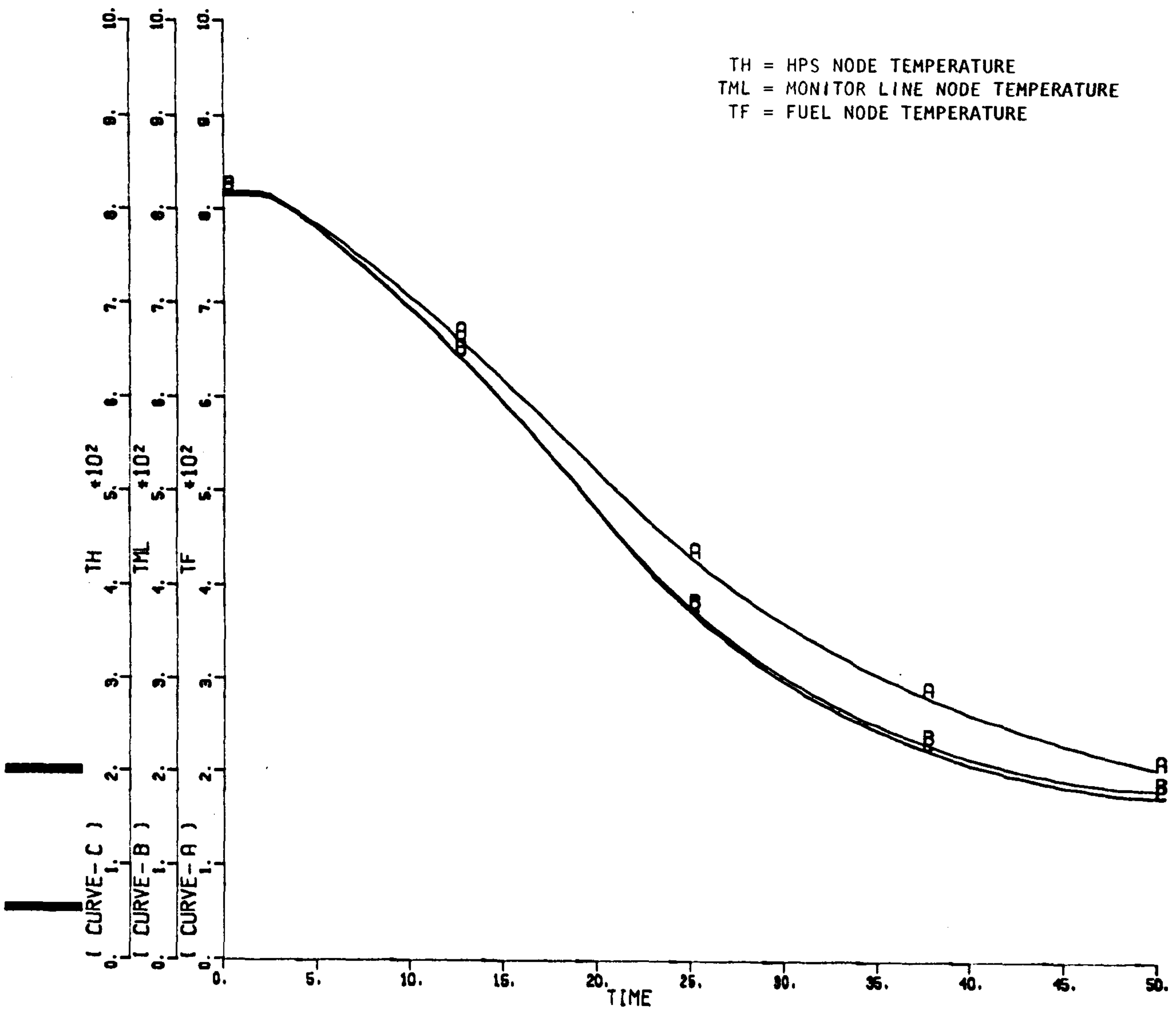

Fig. 3-16. Simplified PES/HPS network during rapid depressurization: temperature vs time

nodes. To check that the code would function properly in such a situation, the model shown in Fig. 3-13 was modified to include a fictitious flow line running from the fuel rod volume to the HPS volume. This test case was successfully handled by the code.

The development work described above has led to a code which can be used to analyze a model of the PES/HPS suitable for obtaining actual design information. Such a model is currently under development. The model being developed will be a modified version of the model which was used for the earlier steady-state flow network analysis (Fig. 3-17).

3.3. PLATEOUT AND PLUGGING

3.3.1. Oxygen Potential Analyzers

A comprehensive evaluation was made of the performance of two oxygen potential analyzer/EMF cells in anticipation of their use in monitoring the oxygen potential of the gaseous environment in the plateout-and-plugging test loop. One cell has a ZrO_2 (calcia stabilized) electrolyte and the other has a ThO_2 (yttria doped) electrolyte. Both cells are equipped with reference gas sleeves. The reference gas used in these tests was ∿1% H_2 in helium saturated with water vapor at ambient temperature, 296 ± 2 K and supplied to the oxygen analyzer through heated lines.

Three concentrations of H_2 in helium were used as sample gases: 1023, 573, and 28 ppm [1 atm (101 kPa) total pressure]. Hydrogen analyses were performed with a helium ionization chromatograph. Controlled concentrations of water vapor were produced in each sample gas by passing the gas through the GA high-pressure water vapor saturator. Previously determined characteristics of saturator temperature versus water vapor content (frost point measurements) were used. Water concentrations of ∿2 to ∿1200 ppm [1 atm (101 kPa) total pressure], were used, corresponding to a saturator temperature of ∿203 to ∿253 K. Oxygen removal from the sample gas was effected by passing it through a small (0.16-g) charcoal trap cooled to 77 K. The trap was located just upstream of the saturator.

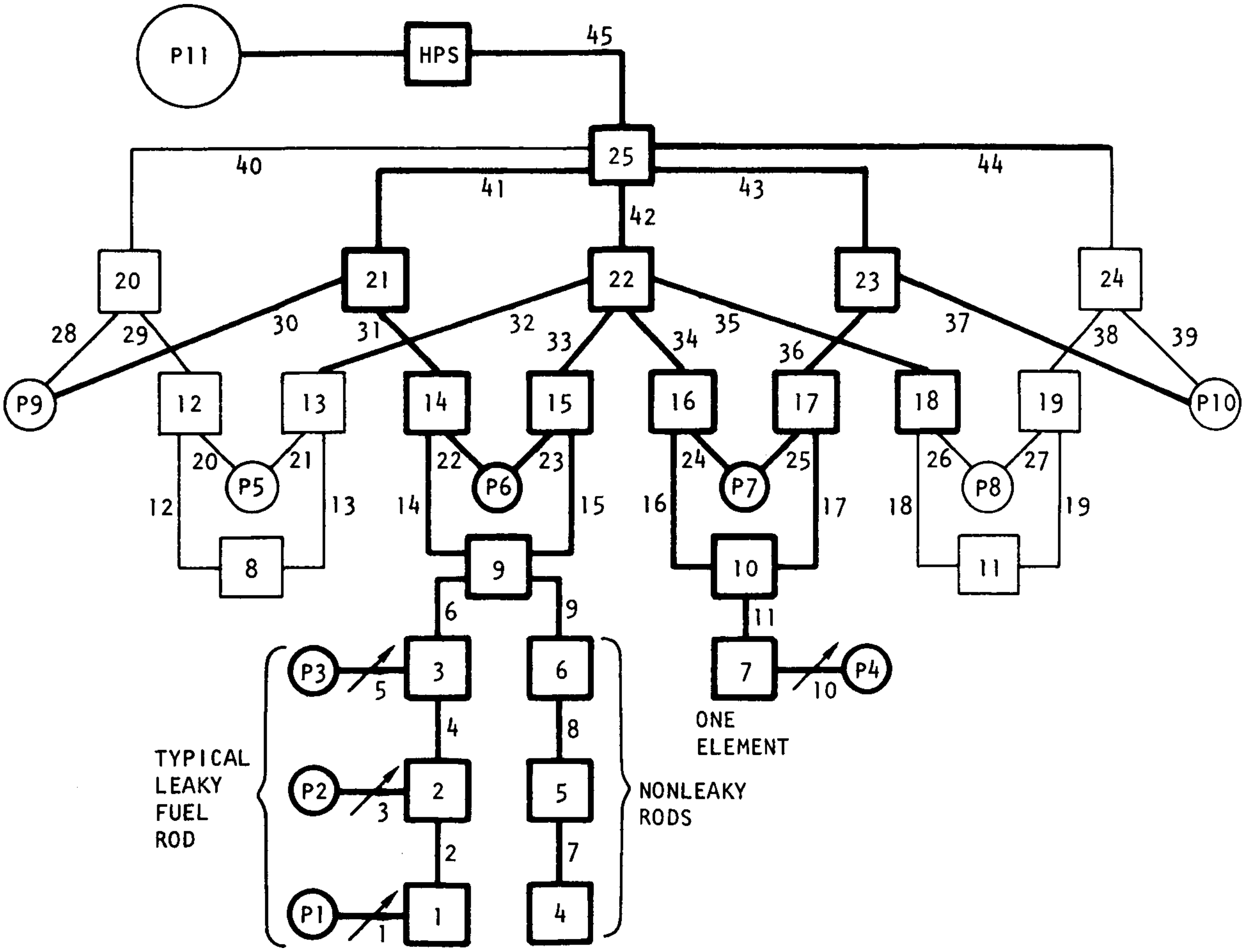

Fig. 3-17. HPS/PES transient flow network model

Since the only oxidizable/reducible gases present in the sample are H_2 and H_2O, the oxygen potential will be governed by their partial pressure ratio. Figures 3-18 and 3-19 show plots of the $\log(H_2/H_2O)$ versus EMF for the ThO_2 and ZrO_2 cells, respectively. At saturator temperatures greater than 223 K, corresponding to water vapor concentrations of >39 ppm, the relationship of $\log(H_2/H_2O)$ versus EMF is quite linear. At temperatures less than 223 K, the deviation from linearity indicates a higher moisture content in the sample gas than would be predicted from the saturator behavior. Preliminary results indicate that this deviation is due to an inherent "leak" in the oxygen analyzer, and when an appropriate correction is made, the data can be linearized over the entire range of H_2/H_2O ratios anticipated. However, this hypothesis must be experimentally proved.

3.3.2. Plateout and Plugging Test Loop Construction

3.3.2.1. Helium Circulators. After repeated pressurization-depressurization cycles ($0.1 \leq P_T \leq 8.6$ MPa), one of the helium circulators failed. Visual inspection indicated that a crack in the ceramic magnet had developed. This could have been due to helium entering a pocket (either in the ceramic or in a glue line on the ceramic) at high pressure and then expanding in the confined space during depressurization. New circulators were obtained, and the original pump was repaired and is being kept as a spare. The new circulator assembly successfully passed a 100-hr test at 8.6 MPa in helium.

3.3.2.2. Circulator Drive Assembly. A square-wave driver (amplifier) was built for use with the test loop circulator. Since it is directly coupled, as compared with the transformer-coupled audio amplifier previously used, it should be easily adapted for servoregulation of flow rate if that provision is required. The circuit diagram is given in Fig. 3-20. Testing on the driver has been successfully completed.

3.3.3. Cesium Source Development

Elemental cesium will be used as the source of cesium in the plateout and plugging loop experiments. To this end a distillation apparatus has

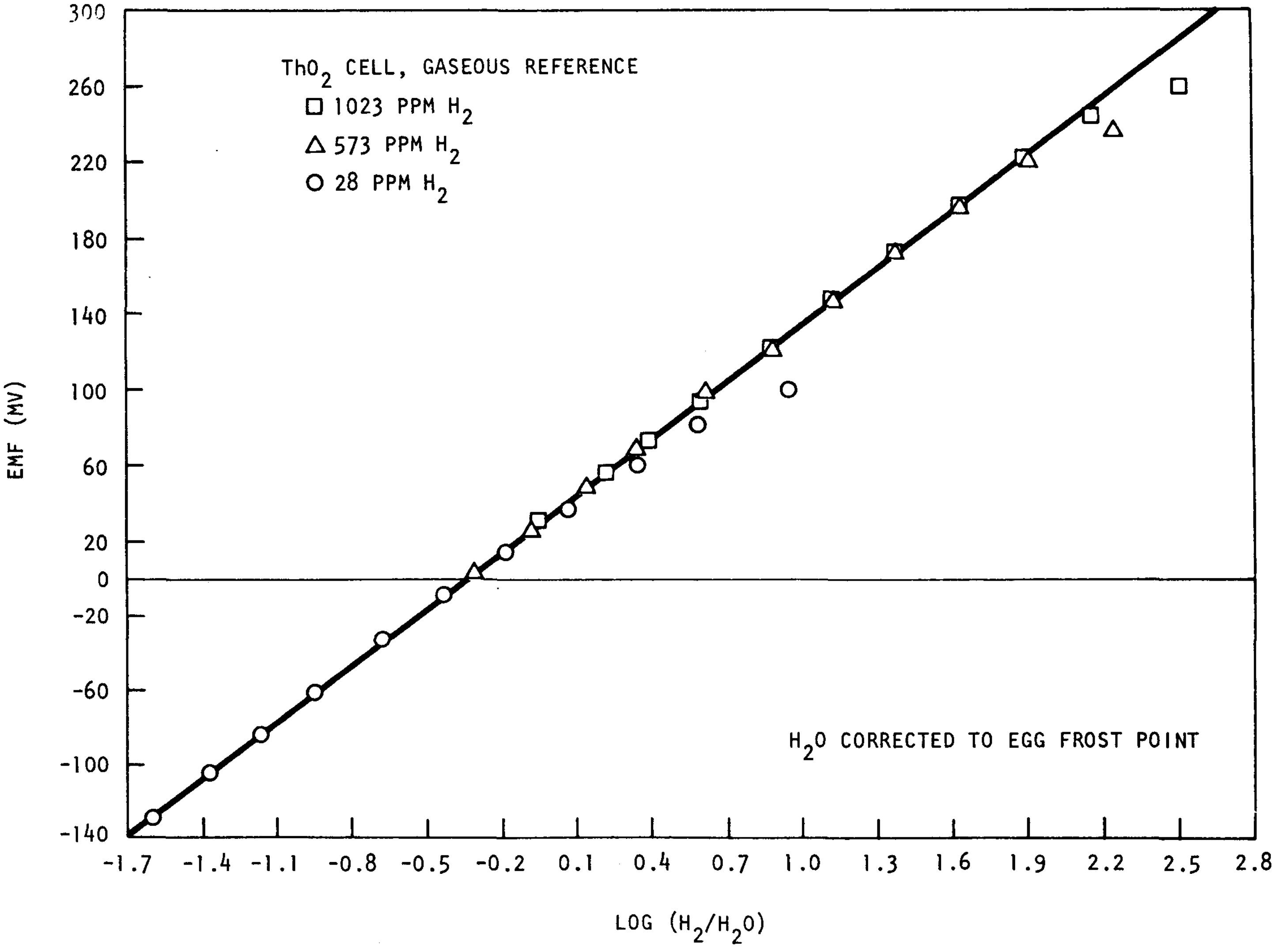

Fig. 3-18. ThO$_2$ cell response

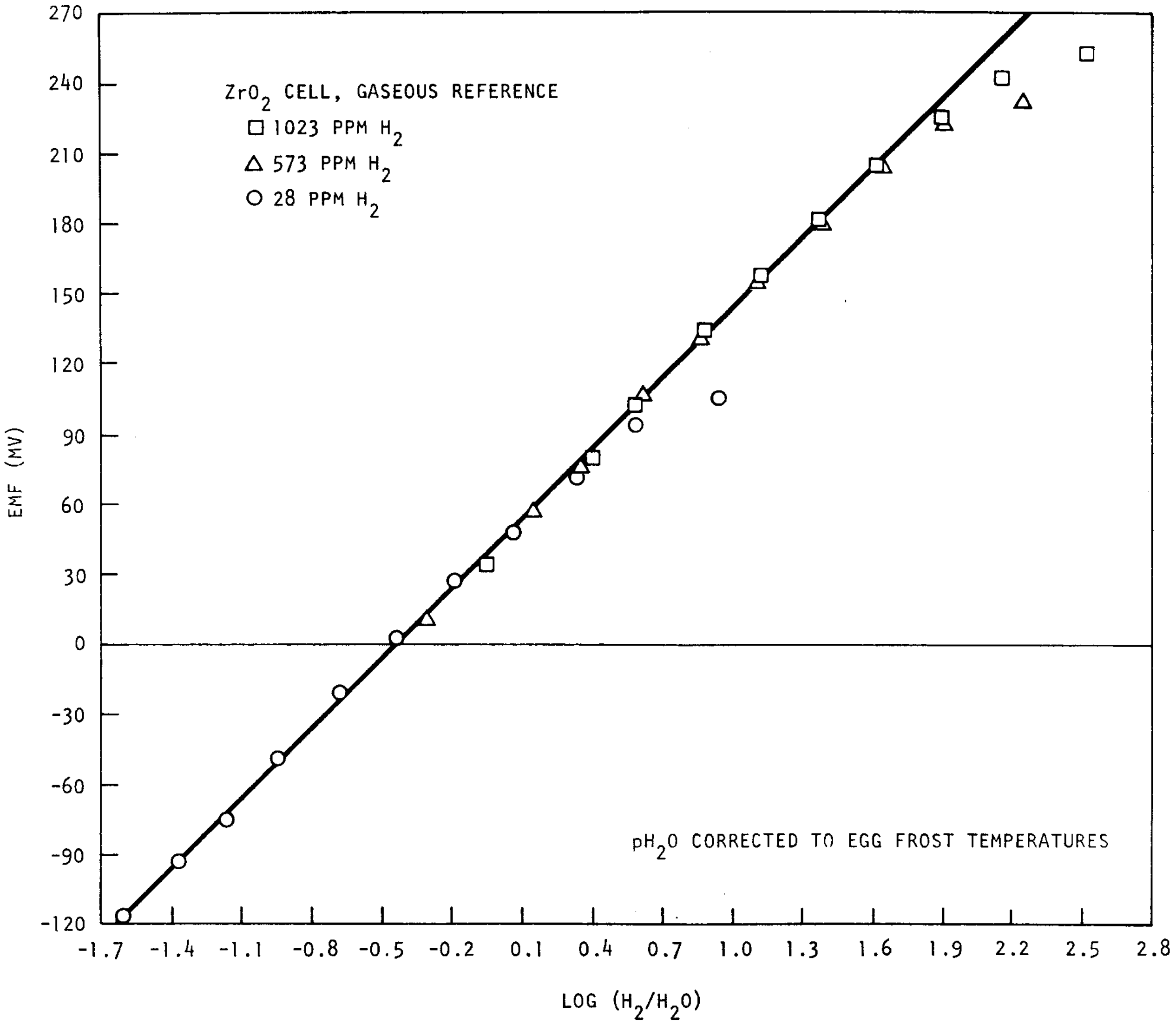

Fig. 3-19. ZrO_2 cell response

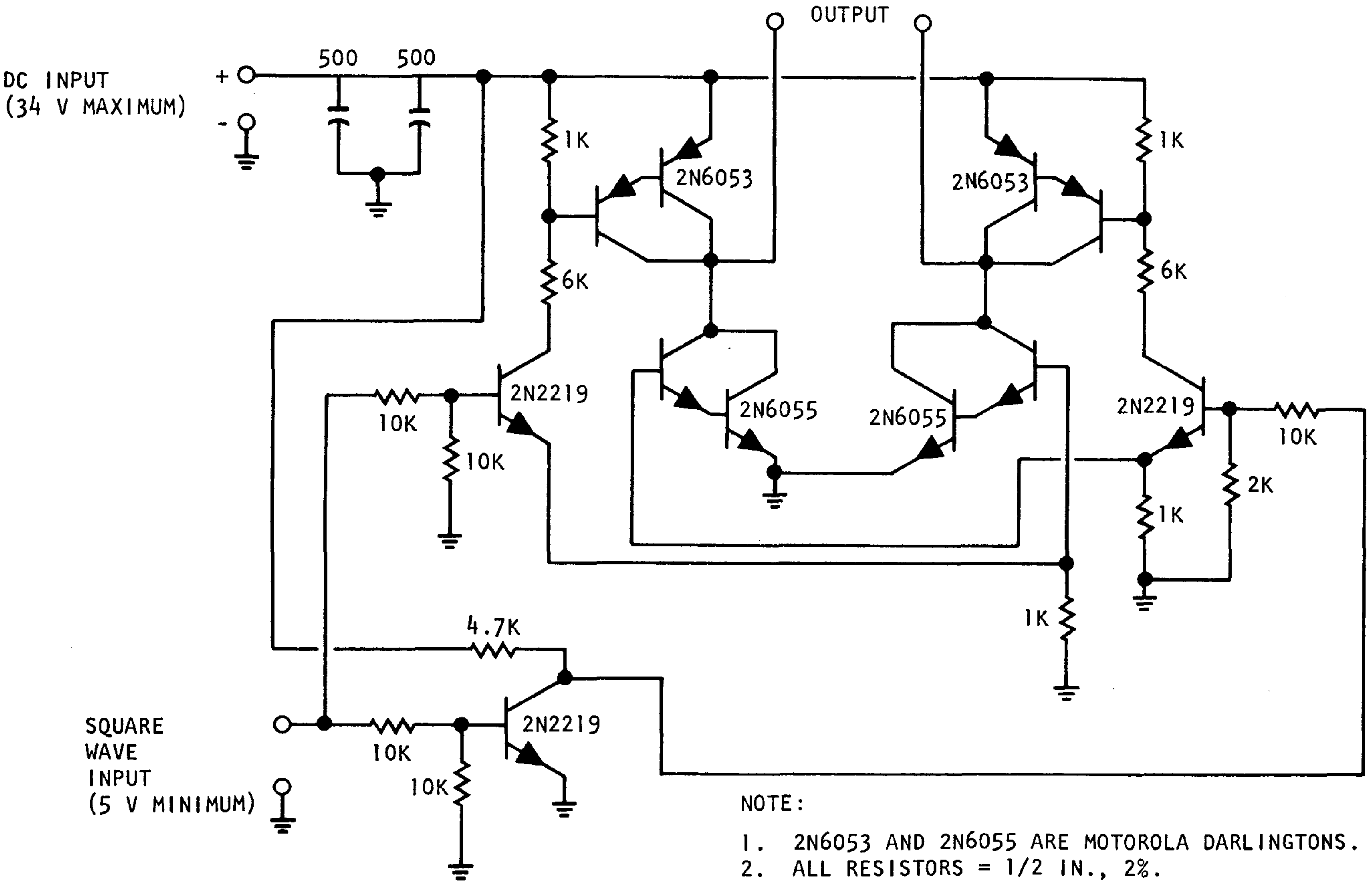

NOTE:

1. 2N6053 AND 2N6055 ARE MOTOROLA DARLINGTONS.
2. ALL RESISTORS = 1/2 IN., 2%.
3. CAPACITANCES ARE IN μF.

Fig. 3-20. Circulator driver circuit

been designed and constructed which will permit loading and sealing of cesium in a tube and valve assembly. The cesium can then be transferred to the high-pressure loop. A sketch of the apparatus is given in Fig. 3-21. Calcium metal shot and CsCl powder are used as the starting materials and are reacted in an evacuated quartz vessel. The cesium thus produced is thermally "chased" into the collection tube by maintaining a temperature of ∿527 K on the walls of the apparatus up to, but not including, the collection tube. Cesium yields of ∿25% have been measured (based on the CsCl starting material). Analysis for chlorine of the cesium produced in this manner yields values in the low (1 to 3 ppm) range.

3.4. PES MANIFOLD FABRICATION

Manifold fabrication development during this quarter consisted of measuring the microstructure and composition of the full-size manifold castings shown in Fig. 3-22 and reviewing the status of the manifold fabrication work at KWU.

Metallographic and microprobe examinations of sections cut from a full-size 316 stainless steel vacuum-investment-cast manifold have been completed. Metallography showed that although pores and inclusions were present, no interconnected porosity was evident. The grain size was large, and a different structure was exhibited at the triple points where grain boundaries meet as compared with the main portion of the grains. Microprobe analysis showed some segregation of the main alloying constituents in the grain boundaries, i.e., the chromium content was higher and the iron and nickel content was lower in the boundaries as compared with their content within the grains. The pore inclusions showed a variable composition; i.e., some were high in manganese and silicon and some showed sulfur to be present, although others did not.

The work on the GCFR manifold fabrication at KWU currently consists of fabrication of a fission product manifold for a full-size GCFR core element model. The design of the manifold has been changed in that some risers and a flange have been added to the structure (see Fig. 3-23). The fabrication

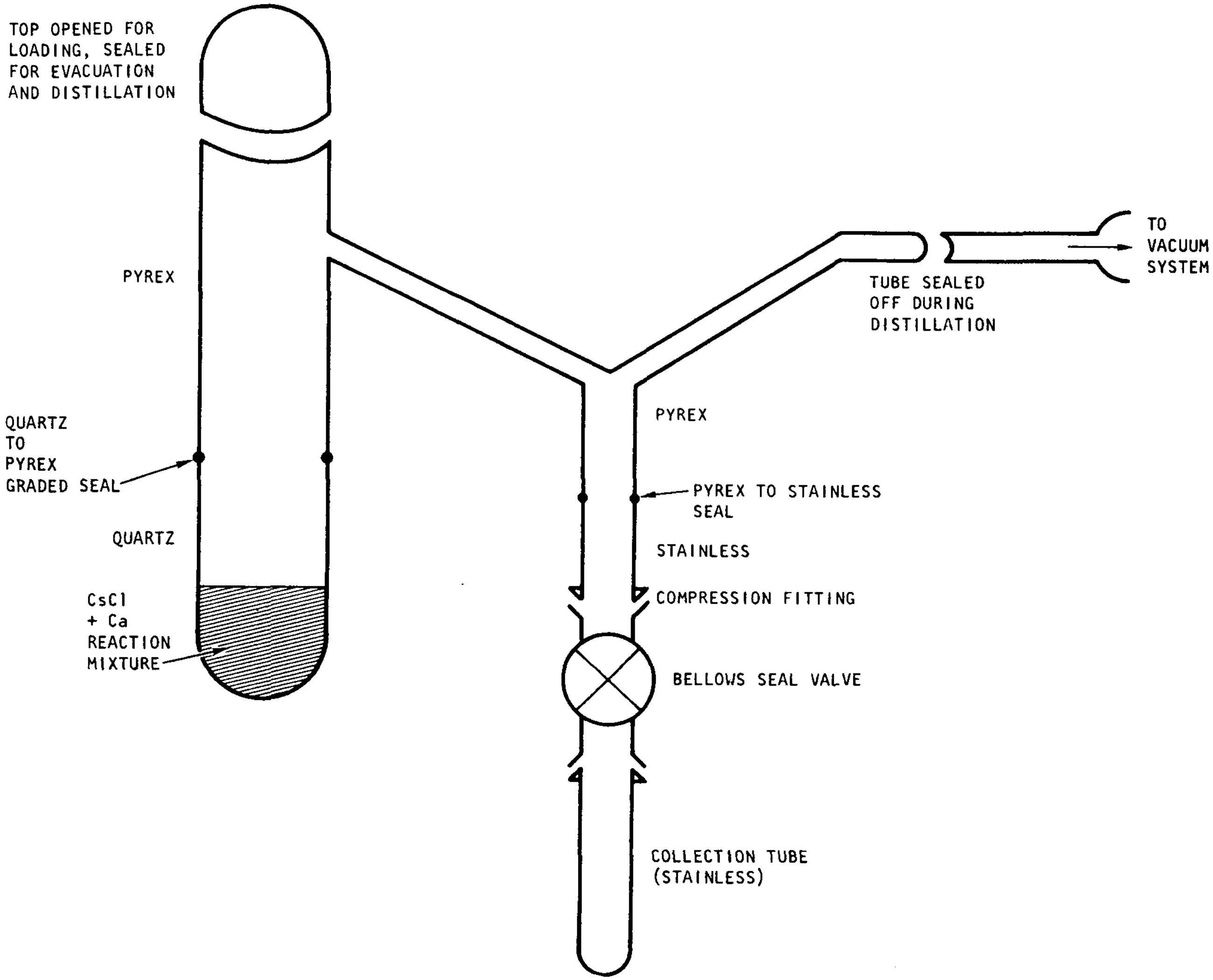

Fig. 3-21. Cesium distillation apparatus

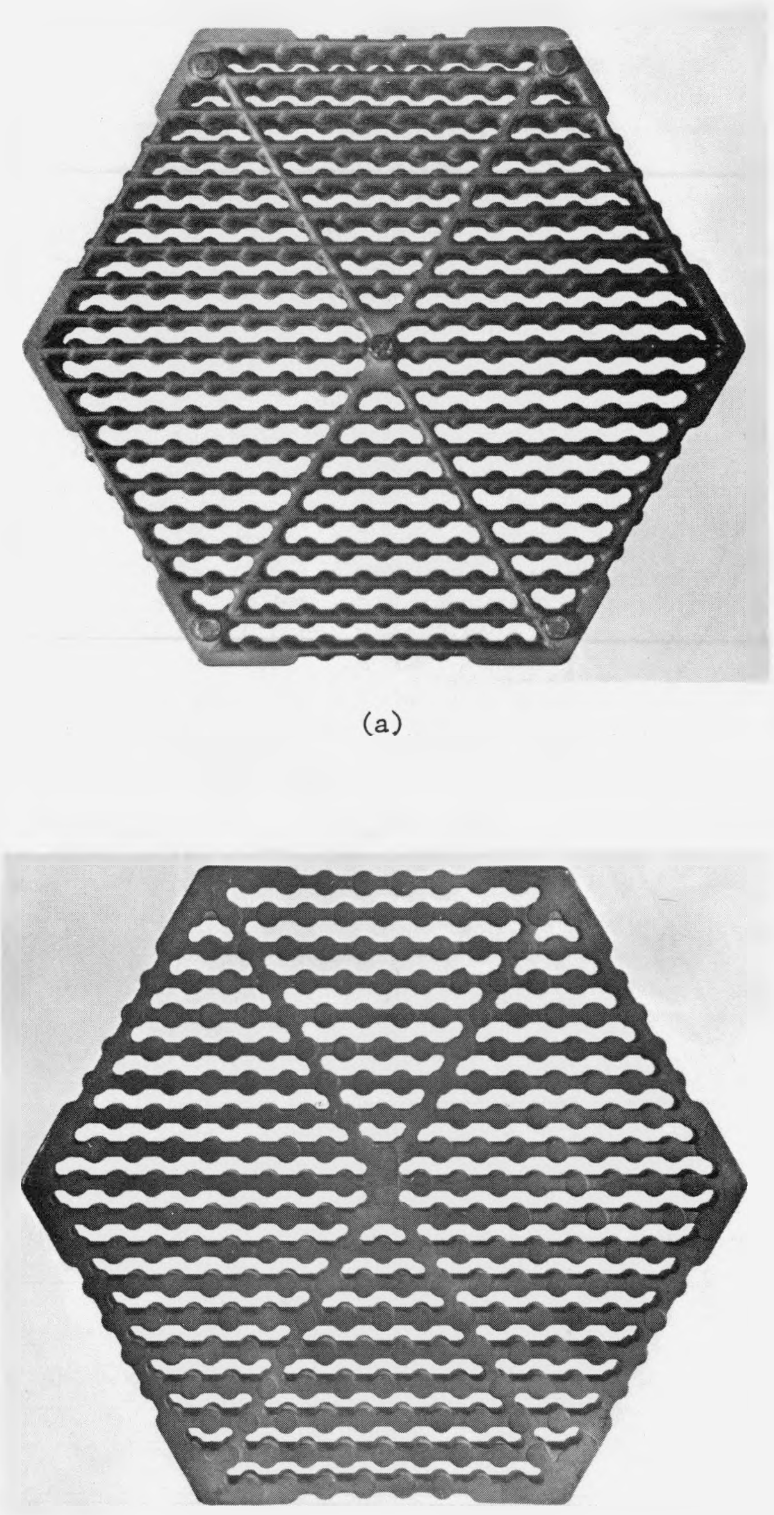

(a)

(b)

Fig. 3-22. Investment cast manifold: (a) top view, (b) bottom view

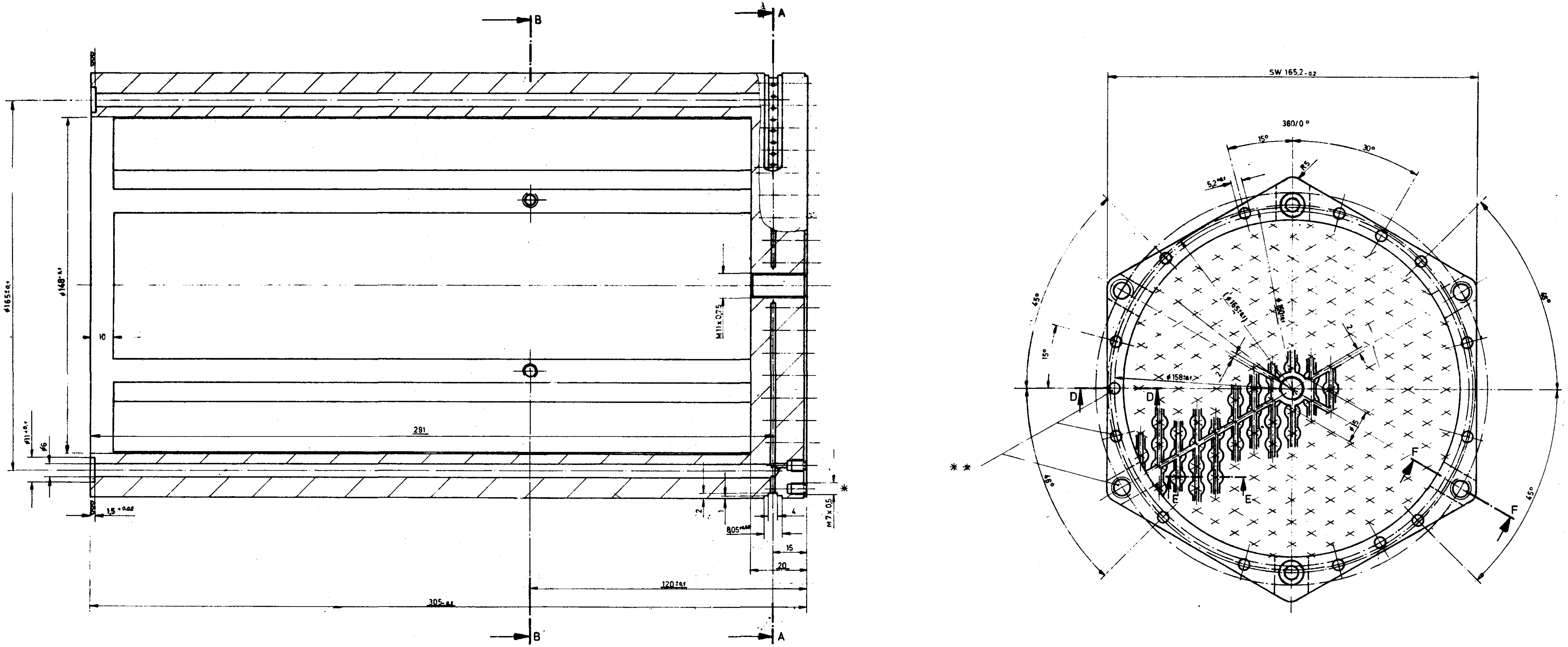

Fig. 3-23. Fission product manifold for GCFR fuel element model fabricated by KWU (Sheet 1 of 2)

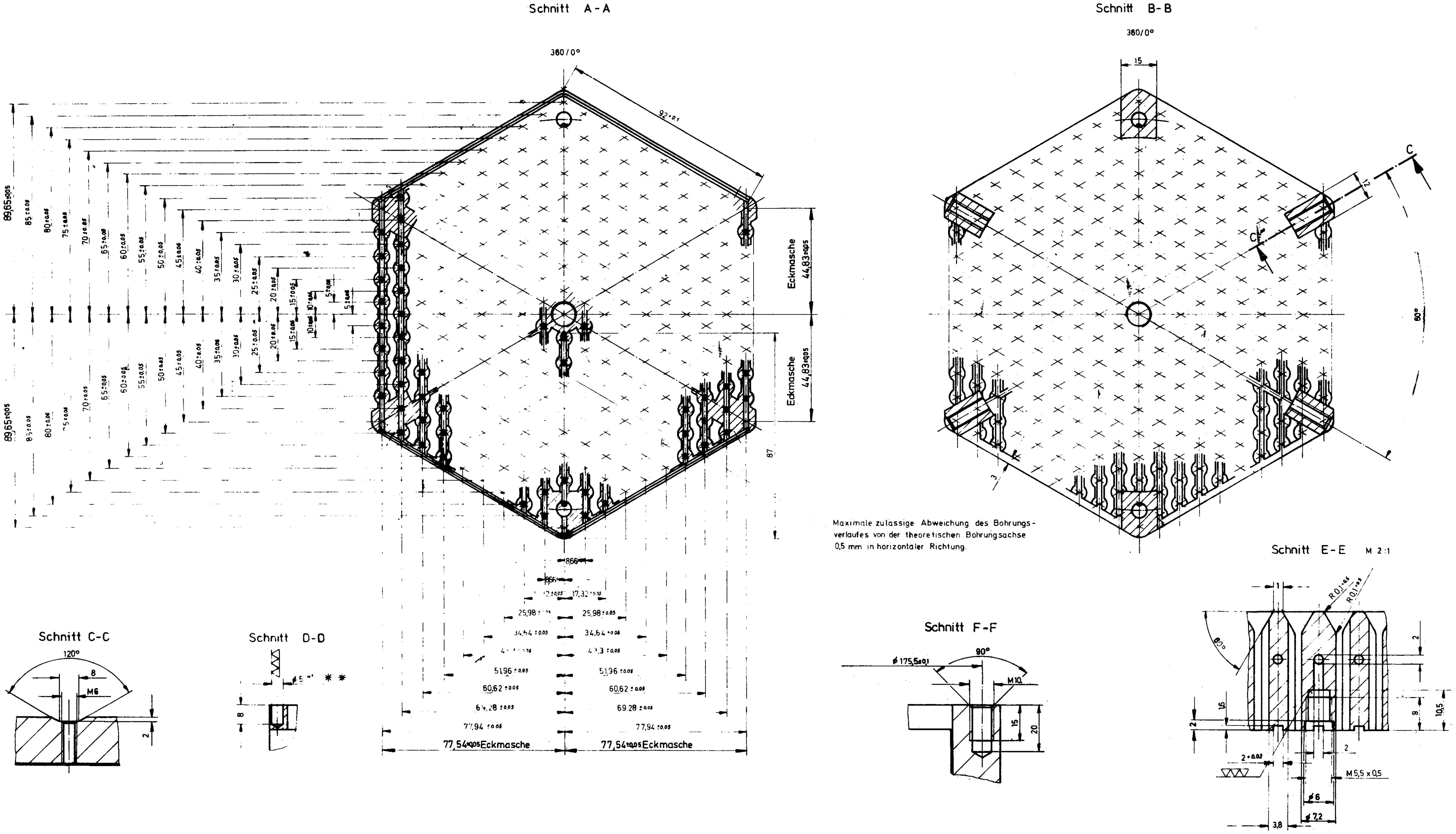
Schnitt A-A

Schnitt B-B

Schnitt C-C

Schnitt D-D

Schnitt E-E M 2:1

Schnitt F-F

Maximale zulassige Abweichung des Bohrungsverlaufes von der theoretischen Bohrungsachse 0,5 mm in horizontaler Richtung.

Fig. 3-23. Fission product manifold for GCFR fuel element model fabricated by KWU (Sheet 2 of 2)

method chosen by KWU is fabrication by conventional machining and EDM of the manifold from a solid bar, followed by deep-hole gun drilling of the fission gas passages. The status of the fabrication of the manifold as of May 1976 is illustrated in Fig. 3-24. Note that the portion of the manifold which contains the horizontal fission gas passages has been left square to accommodate deep-hole drilling of the passages. After completion of passage drilling, the manifold will be finish machined to the required hexagonal shape.

REFERENCES

3-1. "Gas-Cooled Fast Breeder Reactor Quarterly Progress Report for the Period February 1, 1976 Through April 30, 1976, ERDA Report GA-A13868, General Atomic, May 31, 1976.

3-2. O'Hanlon, T. W., "PES Flow Network Analysis," General Atomic, unpublished data.

3-3. Lund, K. O., "1972 Status of FLAC-A Flow Network Analysis Code," Gulf General Atomic, unpublished data.

3-4. "Gas-Cooled Fast Breeder Reactor Quarterly Progress Report for the Period August 1, 1974 Through October 31, 1974," USAEC Report GA-A13238, December 12, 1974, pp. 102-105.

3-5. "FAT, A Computer Program for the Analysis of Transients in Gas Flow Systems," General Atomic, unpublished data.

3-6. Deremer, R. K., "Description of the RATSAM Program," General Atomic, unpublished data.

3-7. Estrin, E. A., "Users Manual for the System Simulation Language (SYSL) Code," General Atomic, to be published.

Fig. 3-24. GCFR manifold

4. CORE FLOW TEST LOOP PROGRAM (189a No. SU006)

A series of out-of-pile simulation tests will be performed (1) to demonstrate the ability of the GCFR fuel, control, and blanket assembly designs to meet design goals and (2) to verify predictions of analytical models that describe design operation and accident behavior. The test emphasis will be on obtaining thermal-structural data for steady-state, transient, and margin conditions using electrically heated rod bundles in a dynamic helium loop. The requirements include testing in the range of cladding melting and the consequences of local initiation of melting. The core flow test loop (CFTL) program plan (Ref. 4-1) contains the requirements for the test program to be conducted in the CFTL, which will be constructed and operated by Oak Ridge National Laboratory (ORNL). The principal work accomplished during this quarter is as follows:

1. The draft of the CFTL Program Plan, Revision I, was issued for review.
2. The performance of a test bundle was calculated using the parameters for the low-pressure-drop core.
3. Preliminary test specifications were issued for the CFTL.
4. The draft program plan for the prototype test was issued in outline form.

4.1. PROGRAM PLANNING

4.1.1. Program Plan

The draft of the first revision to the CFTL Program Plan (Ref. 4-1) was completed and sent to the Nuclear Research and Applications Division

(NRA) of ERDA for review and approval. The following noteworthy changes were made: a detailed Section 7, "Test Analysis and Prediction Requirements," was included; the "Test Measurement Information Sheets" were deleted from the appendix since experience has indicated that this depth of detail is more appropriate for the test specifications; the GCFR core assembly designs were updated to include data on the low-pressure core and the definition of an alternate priority one-test program that considered the replacement of six fueled rods by six tie rods to support the grid spacers; and references to out-of-pile testing in support of the in-pile test program were rewritten to reflect the recent evaluation of the in-pile safety test program.

4.1.2. GCFR and CFTL Schedule

A review of fuel element development in connection with updating the GCFR schedule has confirmed that CFTL construction and testing are on the critical path for development. Figure 4-1 illustrates the critical path for fuel element development.

4.2. TEST ANALYSIS AND PREDICTION

4.2.1. Bundle Performance

The special-purpose computer code TSPEC was used to predict the simulated scram performance of a 37-rod fuel assembly model of the low-ΔP GCFR core. The results of the calculations are given in tabular form as follows: Table 4-1 gives input parameters and geometric data; Table 4-2 provides transient and general flow thermal data; Table 4-3 presents axial flow thermal data; Table 4-4 lists initial and final transient parameters; and Table 4-5 gives transient temperatures. The predictions are similar to the previously reported (Ref. 4-2) higher-pressure-drop model except that the cladding temperature distribution has shifted. The higher inlet temperature and low heat transfer coefficient have caused the maximum cladding temperature to occur just before the start of roughening; this value

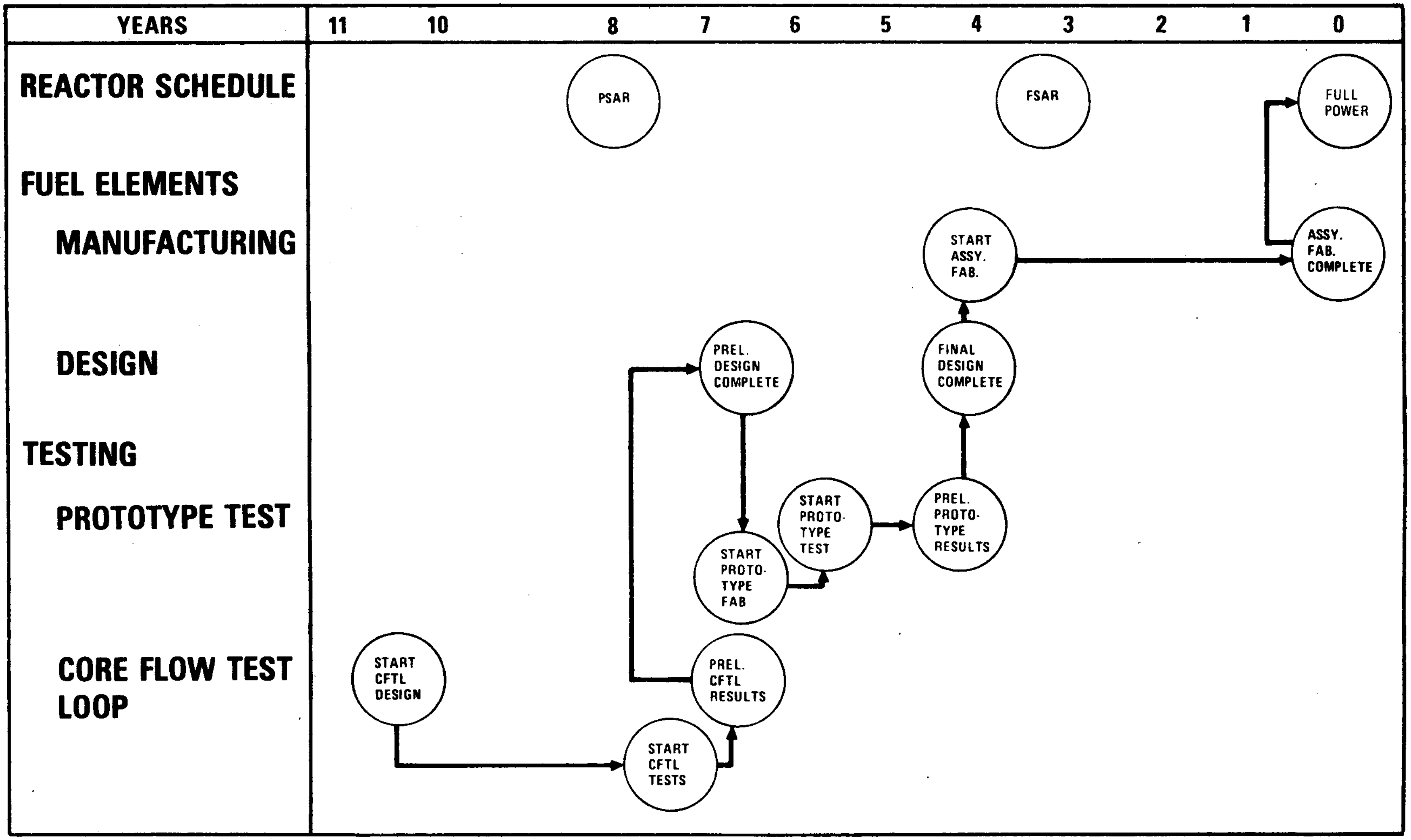

Fig. 4-1. Fuel element critical path

TABLE 4-1
INPUT PARAMETERS AND GEOMETRIC DATA

```
                    CFTL TEST SPECIFICATION FOR TEST - LOW DP CORE SAMPLE BUNDLE -      A

BUNDLE DESIGN
     BUNDLE TYPE - FUEL
     BUNDLE IDENTIFICATION -     A

   BUNDLE DATA
     RODS PER BUNDLE =  37.     HEATED =  31.     UNHEATED =   6.
     BUNDLE OD =   83.4 MM
     DUCT WALL THICHNESS =  2.500 MM
     BUNDLE FLOW AREA =   2393. MM**2
     DUCT PERIMETER =  235.20 MM
     AVG BUNDLE HYDRAULIC DIAMETER =   8.67 MM

   ROD DATA
     ROD DIAMETER =  7.48 MM
     ROD PITCH = 11.20 MM
     HEIGHT OF ROUGHENING = 1.400 MM
     PITCH OF ROUGHENING =    1.68 MM
     FLOW AREA PER ROD =  64.69 MM**2
     H T PERIMETER PER ROD =  23.50 MM
     LOCAL HYDRAULIC DIAMETER =  11.01 MM
     UPPER BLANKET LENGTH =  650.5 MM
     HEATED LENGTH = 1140.0 MM
     LOWER BLANKET LENGTH =  450.0 MM
     TOTAL LENGTH = 2240.5 MM

   ROUGHENING DATA
     ROUGHENED FRACTION OF HEATED LENGTH =  .750
     ROUGHENED LENGTH =  855.0 MM
     FRICTION FACTOR MULTIPLIER = 4.40
     HEAT TRANSFER MULTIPLIER = 2.30
     REFERENCE REYNOLDS NO = 100000.

   SPACER AND FLOW COEFFICIENT DATA
     NUMBER OF SPACER = 10.
     SPACER COEFFICIENT =  .600
     SPACER SOLIDITY =  .145
     INLET COEFFICIENT =  .100
     OUTLET COEFFICIENT =  .500

   HEATER AXIAL POWER PROFILE
     AXIAL QMAX/QAVG =  1.210
     QX/QMAX = COS( 1.049*(2*X/L - 1))
         X/L     QX/QMAX
         .000     .4984
         .100     .6681
         .200     .8084
         .300     .9133
         .400     .9781
         .500    1.0000
         .600     .9781
         .700     .9133
         .800     .8084
         .900     .6681
        1.000     .4984
```

TABLE 4-1 (Continued)

```
                              CFTL TEST SPECIFICATION FOR TEST - LOW DP CORE SAMPLE BUNDLE -      A
TRANSIENT TEST SERIES          RUN NO. -   1
    LINEAR POWER AND FLOW RAMP
                  FRACTION        START TIME (S)  DECAY TIME (S)
              (1)      (2)     (3)                    (2)-(1)    (3)-(2)
       POWER    1.000   .400    .100          .2          .7        2.2
       FLOW     1.000   .290    .100         2.2         3.8       39.0

                                                              INITIAL CONDITIONS                      FINAL CONDITIONS
INPUT PARAMETERS
  TOTAL BUNDLE HEAT INPUT, KW                                       734.700                               73.470
  AVG POWER PER ROD, KW                                              23.700                                2.370
  MAX POWER PER ROD, KW                                              25.300                                2.530
  MIN POWER PER ROD, KW                                              22.200                                2.220
  FLOW PER BUNDLE =, KG/SEC                                            .815                                 .081
  HELIUM INLET TEMPERATURE, C                                          351.0                                351.0
  HELIUM INLET PRESSURE, MPA                                          8.800                                8.800

THERMAL OUTPUT PARAMETERS
  AVERAGE BUNDLE OUTLET TEMPERATURE, C                               524.7                                524.7
  AVERAGE BUNDLE TEMPERATURE RISE, C                                 173.7                                173.7
  OUTLET TEMPERATURE - AVG POWER ROD, C                              558.3                                558.3
  TEMPERATURE RISE - AVG POWER ROD, C                                207.3                                207.3
  OUTLET TEMPERATURE - MAX POWER ROD, C                              572.3                                572.3
  TEMPERATURE RISE - MAX POWER ROD, C                                221.3                                221.3
  OUTLET TEMPERATURE - MIN POWER ROD, C                              545.1                                545.1
  TEMPERATURE RISE - MIN POWER ROD, C                                194.1                                194.1
  MAX SURFACE TEMPERATURE, C (AT X/L = )                      659.2 ( .750)                        617.3 ( .950)
  FILM DROP AT MAX SURFACE, C                                        132.1                                 52.3
  MAX POWER DENSITY, W/CM                                            268.5                                 26.9
  SMOOTH H. T. COEF,  W/M*M/C                                         4778.                                 836.
  ROUGTH H. T. COEF,  W/M*M/C                                        11967.                                2047.

FLOW OUTPUT PARAMETERS
  BUNDLE AVG. RE                                                     83128.                                8313.
  LOCAL RE                                                           95010.                                9501.
  TOTAL BUNDLE PRESSURE DROP, KPA                                  136.314                                1.534
    INLET, KPA                                                        .909                                 .009
    UPPER BLANKET, KPA                                              12.796                                 .203
    SMOOTH CORE LENGTH, KPA                                          6.550                                 .103
    ROUGHENED CORE LENGTH, KPA                                      83.319                                 .827
    LOWER BLANKET, KPA                                              11.879                                 .185
    ACCELERATION LOSS, KPA                                           2.548                                 .025
    SPACERS LOSS, KPA                                               12.415                                 .123
    OUTLET LOSS, KPA                                                 5.899                                 .058

THERMAL EXPANSION PARAMETERS
  THERMAL INPUT   AS FABRICATED                             TEST TEMPERATURE                     TEST TEMPERATURE
                                                         DUCT      ROD      DIF               DUCT      ROD      DIF
    AVERAGE, MM           2240.5                        2257.5    2259.0    1.5              2257.5    2258.3     .9
    HOTTEST, MM           2240.5                        2257.7    2259.3    1.6              2257.7    2258.7     .9
    COLDEST, MM           2240.5                        2257.2    2258.6    1.4              2257.2    2258.0     .8
  MAX BOW DISPLACEMENT, MM                                          5.5                                  5.5
```

TABLE 4-2
TRANSIENT AND GENERAL FLOW THERMAL DATA

CFTL TEST SPECIFICATION FOR TEST - LOW DP CORE SAMPLE BUNDLE - A

INITIAL AXIAL PRESSURE, POWER, AND TEMPERATURE VALUES

LOCATION	X MM	X/L	DP KPA	AVERAGE POWER W/CM	AVERAGE HELIUM C	AVERAGE CLAD C	MAXIMUM POWER W/CM	MAXIMUM HELIUM C	MAXIMUM CLAD C	MINIMUM POWER W/CM	MINIMUM HELIUM C	MINIMUM CLAD C
INLET	.0		.909	.0	351.0	351.0	.0	351.0	351.0	.0	351.0	351.0
CORE INLET	650.5	.000	17.309	125.4	351.0	519.7	133.8	351.0	532.0	117.4	351.0	508.2
SMOOTH	793.0	.125	21.387	177.6	370.0	616.1	189.6	371.3	635.[illegible]	166.4	368.8	597.8
SMOOTH	934.4	.249	25.432	217.5	394.5	701.7	232.2	397.5	727.9	203.7	391.8	677.3
ROUGH	936.6	.251	25.432	218.0	395.0	519.6	232.7	397.9	531.5	204.2	392.2	508.6
ROUGH	1220.5	.500	54.703	251.6	454.6	598.9	268.5	461.6	616.2	235.6	448.1	582.8
ROUGH	1334.5	.600	66.459	246.0	479.5	620.2	262.6	488.2	638.8	230.5	471.4	602.8
ROUGH	1448.5	.700	78.215	229.7	503.3	634.0	245.2	513.6	653.5	215.2	493.7	615.8
ROUGH	1562.5	.800	89.970	203.4	525.0	639.8	217.1	536.7	659.6	190.5	514.0	621.3
ROUGH	1676.5	.900	101.726	168.1	543.6	637.7	179.4	556.6	657.2	157.4	531.4	619.4
ROUGH	1733.5	.950	107.604	147.5	551.4	633.7	157.5	565.0	652.9	138.2	538.7	615.7
CORE OUTLET	1790.5	1.000	113.482	125.4	558.2	627.8	133.8	572.2	646.6	117.4	545.1	610.2
OUTLET	2240.5		136.314	.0	558.2	558.2	.0	572.2	572.2	.0	545.1	545.1

FINAL AXIAL PRESSURE, POWER, AND TEMPERATURE VALUES

LOCATION	X MM	X/L	DP KPA	AVERAGE POWER W/CM	AVERAGE HELIUM C	AVERAGE CLAD C	MAXIMUM POWER W/CM	MAXIMUM HELIUM C	MAXIMUM CLAD C	MINIMUM POWER W/CM	MINIMUM HELIUM C	MINIMUM CLAD C
INLET	.0		.009	.0	351.0	351.0	.0	351.0	351.0	.0	351.0	351.0
CORE INLET	650.5	.000	.248	12.5	351.0	449.6	13.4	351.0	456.5	11.7	351.0	443.0
SMOOTH	793.0	.125	.307	17.8	370.0	512.1	19.0	371.3	523.6	16.6	368.8	501.4
SMOOTH	934.4	.249	.366	21.7	394.5	570.6	23.2	397.5	586.3	20.4	391.8	555.9
ROUGH	936.6	.251	.366	21.8	395.0	468.5	23.3	397.9	476.6	20.4	392.2	460.9
ROUGH	1220.5	.500	.657	25.2	454.6	539.6	26.9	461.6	552.5	23.6	448.1	527.5
ROUGH	1334.5	.600	.773	24.6	479.5	562.4	26.3	488.2	576.9	23.0	471.4	548.9
ROUGH	1448.5	.700	.890	23.0	503.3	580.5	24.5	513.6	596.1	21.5	493.7	565.9
ROUGH	1562.5	.800	1.007	20.3	525.0	593.0	21.7	536.7	609.5	19.0	514.0	577.6
ROUGH	1676.5	.900	1.123	16.8	543.6	599.5	17.9	556.6	616.4	15.7	531.4	583.7
ROUGH	1733.5	.950	1.182	14.8	551.4	600.4	15.7	565.0	617.3	13.8	538.7	584.6
CORE OUTLET	1790.5	1.000	1.240	12.5	558.2	599.8	13.4	572.2	616.6	11.7	545.1	584.0
OUTLET	2240.5		1.534	.0	558.2	558.2	.0	572.2	572.2	.0	545.1	545.1

TABLE 4-3
AXIAL FLOW THERMAL DATA

```
                          CFTL TEST SPECIFICATION FOR TEST - LOW DP CORE SAMPLE BUNDLE -     A
TRANSIENT TEST SERIES      RUN NO. -   1

                                       INITIAL AXIAL VALUE FOR AVERAGE ROD
              AVG POWER PER ROD = 23.700 KW
              STORED ENERGY BASE TEMPERATURE = 351.0 C
              AVG STORED ENERGY PER ROD =  89.568 KW-S
              STORED ENERGY/POWER FOR AVG ROD =   3.8 S

LOCATION        X      X/L      POWER   STORED ENERGY  ENERGY/POWER  HELIUM   CLAD   WALL DT  HT*A/L  TEMP/TIME   ROD CENTER
               MM               W/CM      W*S/CM            S          C        C       C     W/CM/C    C/S           C

 INLET          .0                 .0          .0           .0      351.0   351.0      .0     .80       .0        351.0
 CORE INLET  650.5    .000      125.4       397.7          3.2      351.0   519.7   168.7     .74     71.2        672.8
 SMOOTH      793.0    .125      177.6       609.4          3.4      370.0   616.1   246.1     .72    100.9        833.0
 SMOOTH      934.4    .249      217.5       792.1          3.6      394.5   701.7   307.1     .71    123.6        967.3
 ROUGH       936.6    .251      218.0       471.7          2.2      395.0   519.6   124.6    1.75    123.9        785.9
 ROUGH      1220.5    .500      251.6       638.3          2.5      454.6   598.9   144.3    1.74    142.9        906.1
 ROUGH      1334.5    .600      246.0       671.4          2.7      479.5   620.2   140.7    1.75    139.8        920.7
 ROUGH      1448.5    .700      229.7       682.7          3.0      503.3   634.0   130.7    1.76    130.5        914.6
 ROUGH      1562.5    .800      203.4       671.9          3.3      525.0   639.8   114.9    1.77    115.5        888.2
 ROUGH      1676.5    .900      168.1       639.9          3.8      543.6   637.7    94.1    1.79     95.5        843.0
 ROUGH      1733.5    .950      147.5       616.4          4.2      551.4   633.7    82.3    1.79     83.8        813.9
 CORE OUTLET 1790.5  1.000      125.4       588.3          4.7      558.2   627.8    69.6    1.80     71.2        781.0
 OUTLET     2240.5                 .0       426.5           .0      558.2   558.2      .0     .80       .0        558.2

                                       FINAL AXIAL VALUES FOR AVERAGE ROD
              AVG POWER PER ROD =  2.370 KW
              STORED ENERGY BASE TEMPERATURE = 351.0 C
              AVG STORED ENERGY PER ROD =  59.919 KW-S
              STORED ENERGY/POWER FOR AVG ROD =  25.3 S

LOCATION        X      X/L      POWER   STORED ENERGY  ENERGY/POWER  HELIUM   CLAD   WALL DT  HT*A/L  TEMP/TIME   ROD CENTER
               MM               W/CM      W*S/CM            S          C        C       C     W/CM/C    C/S           C

 INLET          .0                 .0          .0           .0      351.0   351.0      .0     .13       .0        351.0
 CORE INLET  650.5    .000       12.5       183.8         14.7      351.0   449.6    98.6     .13      7.1        464.9
 SMOOTH      793.0    .125       17.8       298.2         16.6      370.0   512.1   142.1     .12     10.1        533.8
 SMOOTH      934.4    .249       21.7       404.4         18.6      394.5   570.6   176.0     .12     12.4        597.1
 ROUGH       936.6    .251       21.8       224.5         10.3      395.0   468.5    73.5     .30     12.4        495.1
 ROUGH      1220.5    .500       25.2       352.5         14.0      454.6   539.6    85.0     .30     14.3        570.3
 ROUGH      1334.5    .600       24.6       392.4         15.9      479.5   562.4    82.9     .30     14.0        592.5
 ROUGH      1448.5    .700       23.0       422.9         18.4      503.3   580.5    77.2     .30     13.1        608.6
 ROUGH      1562.5    .800       20.3       442.9         21.8      525.0   593.0    68.0     .30     11.6        617.9
 ROUGH      1676.5    .900       16.8       451.5         26.9      543.6   599.5    56.0     .30      9.5        620.0
 ROUGH      1733.5    .950       14.8       451.5         30.6      551.4   600.4    49.0     .30      8.4        618.4
 CORE OUTLET 1790.5  1.000       12.5       448.5         35.8      558.2   599.8    41.5     .30      7.1        615.1
 OUTLET     2240.5                 .0       426.5           .0      558.2   558.2      .0     .13       .0        558.2
```

TABLE 4-4
INITIAL AND TRANSIENT PARAMETERS

CFTL TEST SPECIFICATION FOR TEST - LOW DP CORE SAMPLE BUNDLE - A

TRANSIENT TEST SERIES RUN NO. - 1

LINEAR POWER AND FLOW RAMP

	FRACTION (1)	(2)	(3)	START TIME (S)	DECAY TIME (S) (2)-(1)	(3)-(2)
POWER	1.000	.400	.100	.2	.7	2.2
FLOW	1.000	.290	.100	2.2	3.6	39.0

APPROXIMATE TRANSIENT HISTORY

TIME S	AVG POWER PER ROD KW	FLOW KG/S	EQ. STORED Q PER ROD KW-S	EQ. STORED Q CHANGE/T KW	TIME CONSTANT S	OUTLET TEMPERATURE EQ. C	OUTLET TEMPERATURE ACT. C	CLAD TEMPERATURE, AVG EQ. AVG. C	ACT. AVG. C	ACT. MAX. C
.0	23.700	.815	89.570	.000	3.8	558.	556.	523.	523.	628.
1.9	6.282	.815	23.562	-35.194	3.8	406.	498.	396.	473.	548.
3.8	2.370	.577	11.461	-5.005	4.8	380.	452.	374.	434.	486.
6.2	2.370	.236	23.631	2.441	10.0	423.	440.	404.	422.	468.
11.2	2.370	.216	25.461	.341	10.7	429.	436.	408.	417.	461.
16.5	2.370	.195	27.834	.404	11.7	438.	437.	414.	416.	460.
22.4	2.370	.171	31.078	.495	13.1	450.	442.	422.	418.	465.
29.0	2.370	.145	35.883	.635	15.1	467.	452.	433.	424.	477.
36.5	2.370	.115	44.026	.877	18.6	498.	470.	453.	435.	498.
45.8	2.370	.081	59.921	1.257	25.3	558.	505.	491.	457.	538.
58.5	2.370	.081	59.921	.000	25.3	558.	526.	491.	470.	562.
71.1	2.370	.081	59.921	.000	25.3	558.	539.	491.	479.	577.
83.8	2.370	.081	59.921	.000	25.3	558.	546.	491.	483.	586.
96.4	2.370	.081	59.921	.000	25.3	558.	551.	491.	486.	591.
109.0	2.370	.081	59.921	.000	25.3	558.	554.	491.	488.	595.
121.7	2.370	.081	59.921	.000	25.3	558.	556.	491.	489.	597.
134.3	2.370	.081	59.921	.000	25.3	558.	557.	491.	490.	598.
147.0	2.370	.081	59.921	.000	25.3	558.	557.	491.	490.	599.
159.6	2.370	.081	59.921	.000	25.3	558.	556.	491.	491.	599.
172.2	2.370	.081	59.921	.000	25.3	558.	556.	491.	491.	599.

TABLE 4-5
TRANSIENT TEMPERATURES

Time (s)	Fig. 4-2(a) Helium Outlet Temperature (°C)		Fig. 4-2(b) Maximum Cladding Temperature (°C)	
	TSPEC	ROD*SIM	TSPEC	ROD*SIM
0	521	521	562	562
1.4	468	468	499	482
2.9	423	430	444	436
4.5	398	422	413	432
6.6	396	426	410	452
10.5	397	429	410	440
14.5	400	412	413	423
18.9	404	398	418	413
23.6	411	398	426	414
28.9	420	403	437	422

exceeds the design limit of 700°C. Since the test conditions are a compromise between operating at GCFR conditions and compensating for the relatively small test bundle size, i.e., relatively more nonheated area in the test bundle than in a GCFR fuel assembly, the tendency is to operate the heater rods at a higher surface temperature than the corresponding GCFR operating condition. In addition, TSPEC neglects lateral gas mixing for the sake of simplicity, which causes the surface temperatures to be overestimated. Further study of the operating conditions and the design is planned to aid in developing the simulation strategy. Another property of the low-pressure design is that the stored energy is about 25% higher and the time constant for the cooling rate is about 25% longer. This should result in slower rod/spacer relative movement during rapid transients.

4.2.2. Comparison of Transient Predictions

The dynamic simulation calculations of the GCFR fuel rods and the CFTL heater rods have been performed with the ROD*SIM computer code, as reported in Ref. 4-3. The power and flow transient functions were studied to determine the approximation transient parameters that would compensate for the thermal response difference between fuel rods and heater rods. The resultant time functions of power and flow were applied to the approximate transient computer code TSPEC. As a verification of TSPEC, the transient helium outlet temperature, Fig. 4-2(a), and maximum cladding temperature, Fig. 4-2(b), are compared with the ROD*SIM predictions. To facilitate this comparison, the initial steady-state temperatures prediced by ROD*SIM were adjusted to equal the TSPEC values, and this temperature correction was applied to all ROD*SIM temperatures. The initial slopes of the temperature declines are in good agreement, and the temperature minimums agree, but the temperature minimums do not occur at the same time. ROD*SIM predicts an intermediate temperature peak of about 20°C which does not appear in the TSPEC results. It is concluded that the approximation in TSPEC is satisfactory for general prediction of transient behavior, but to provide detailed information, the more sophisticated algorithms in ROD*SIM are needed.

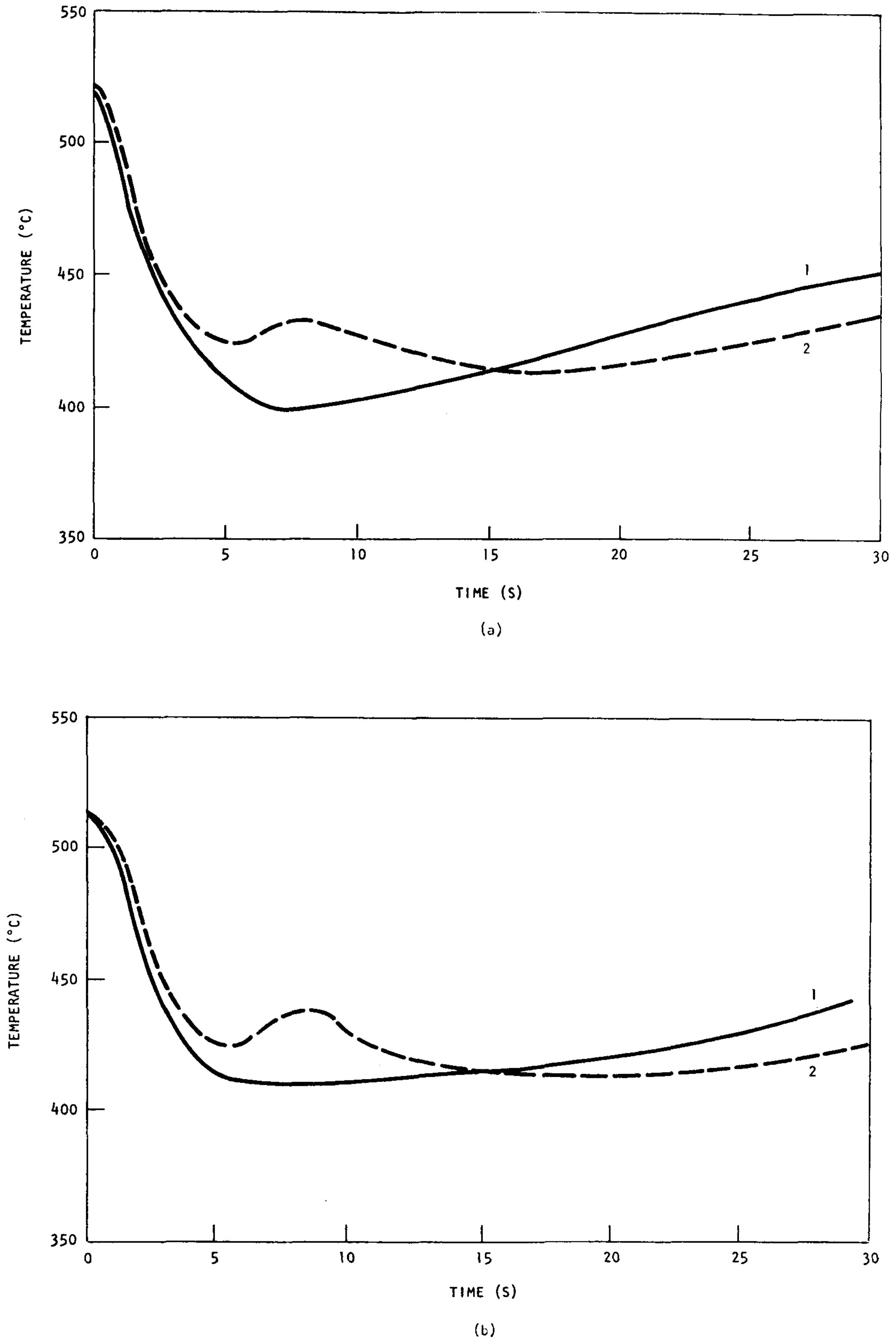

Fig. 4-2. Comparison of (a) helium outlet temperature and (b) maximum cladding temperature as predicted by TSPEC (1) and ROD*SIM (2)

4.3. TEST SPECIFICATION

A test specification draft for the preliminary series of tests on models of fuel assemblies with unheated and heated fuel pin simulators (heater rods), was submitted to ORNL and NRA. Tests will be conducted on three 37-rod bundles. Each bundle in the preliminary series P-1 (unheated) and P-2 (heated) will have 31 fuel pin simulators. The specification draft contains tables which denote test conditions which update information that was presented in Ref. 4-4. Table 4-6 lists the test groups and subgroups and their respective titles (general test parameters) for the preliminary test series as denoted in the specification draft. The outline specification (Ref. 4-4) was used to solicit comments on the content and format of the test specification. It has served its purpose and will no longer be used as a working document for the test program.

4.4. TEST BUNDLE DESIGN AND FABRICATION

Figure 4-3 shows a cross section of a blanket assembly model for a proposed GCFR low-ΔP core design. As noted in the last quarterly report (Ref. 4-2), a design change has been made: the 127-rod bundle has been replaced by a 61-rod bundle.

Agreement on the division of design and fabrication responsibilities between ORNL and GA has been attained for the simulated fuel assembly models. A summary of the major activities and responsibilities is listed in Table 4-7; this table includes additions and changes in terminology. Although not shown in Table 4-7, a review of the design (proposed by ORNL) by the organization which does not have the major responsibility for a particular activity.

4.5. LIAISON WITH ORNL

Blanket rod and assembly power requirements for the 61-rod bundle (Table 4-8) were sent to ORNL. The values listed in Table 4-8 are for a thorium oxide radial blanket assembly. ORNL was also provided with a

TABLE 4-6
GENERAL TEST CONDITIONS OF CFTL TEST GROUPS,
PRELIMINARY TEST SERIES

P-1.1	Steady-state flow, zero power
P-1.2	Subgroup 1.2.1, normal transients, unheated
P-1.2	Subgroup 1.2.2, upset transients, unheated
P-1.2	Subgroup 1.2.3, emergency transients, unheated
P-1.3	Depressurization transients, unheated
P-2.1	Steady-state flow, uniform power
P-2.2	Steady-state flow, skewed power
P-2.3	Thermal mixing tests, steady-state flow, single heated rod
P-2.4	Subgroup 2.4.1, normal transients, uniform power
P-2.4	Subgroup 2.4.2, normal transients, skewed power
P-2.5	Subgroup 2.5.1, upset transients, uniform power
P-2.5	Subgroup 2.5.2, upset transients, skewed power
P-2.5	Subgroup 2.5.3, emergency transients, uniform power
P-2.6	Depressurization transients, uniform power
P-2.7	Steady-state flow, margin undercooling
P-2.8	Undercooling transient design limits

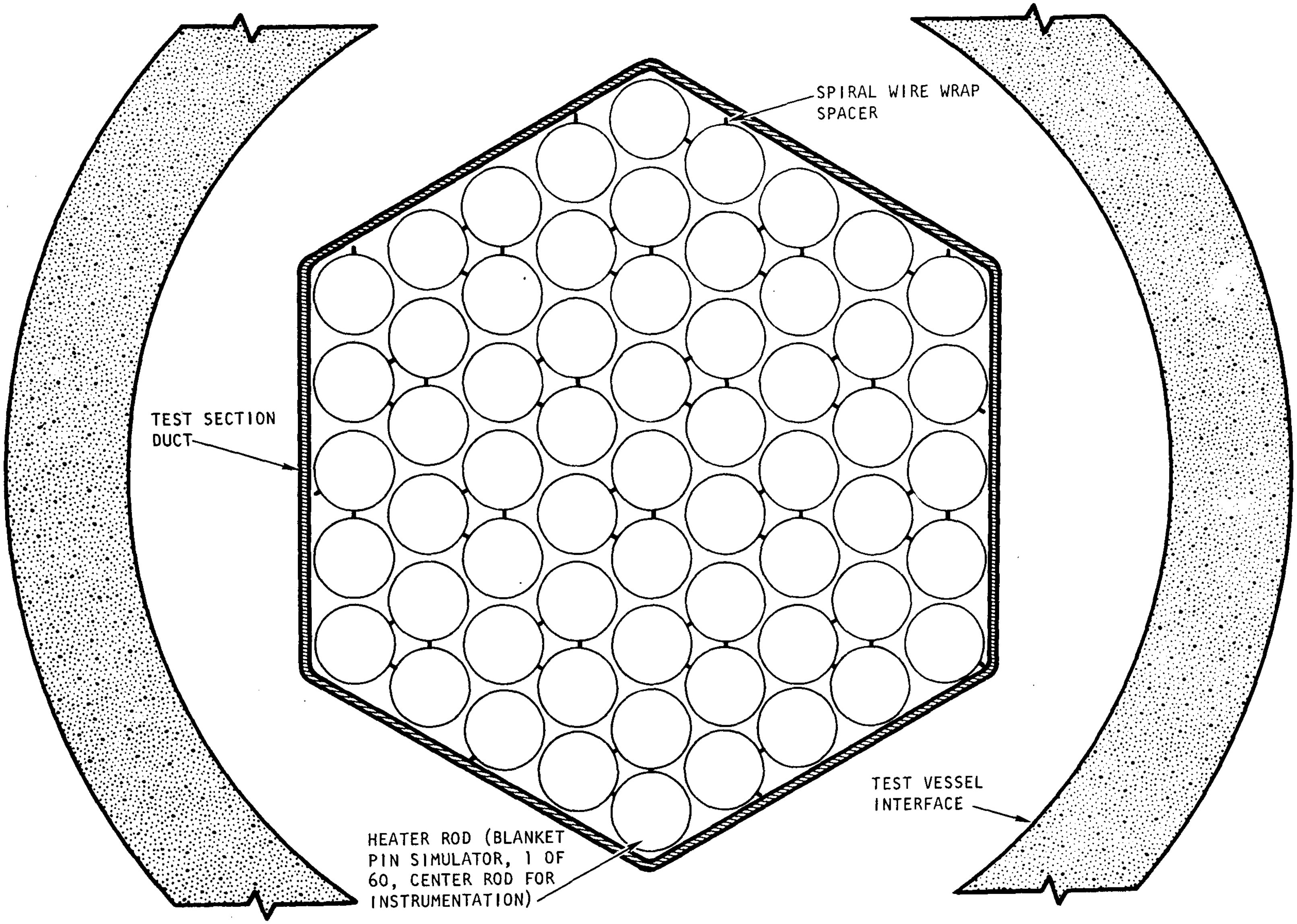

Fig. 4-3. Cross section of 61-rod blanket assembly model

TABLE 4-7
SUMMARY OF MAJOR DESIGN AND FABRICATION ACTIVITIES

Major Responsibility	Activity
GA	Reference GCFR fuel assembly design
GA	CFTL fuel test section design
ORNL	Test bundle design (integrates test section into loop)
ORNL	Instrumentation design and test integration
ORNL	Component design, procurement, and quality assurance
	Fuel pin simulator (all activities except heater roughening, which would be responsibility of GA)
GA	Intermediate spacer grids
GA	Inlet spacer grid
GA	Spacer tie bars (support rods)
GA	Test section duct
GA	Test section outlet
GA	Test section duct flange
ORNL	Test section flange to test vessel adapter
ORNL	Test bundle pressure closure
ORNL	Test section instrumentation (except prototypical GCFR temperature instrumentation at test section outlet); GA to specify test section instrumentation type and location
ORNL	Test bundle instrumentation (routing of leads and all other bundle instrumentation not identified as test section instrumentation)
ORNL	Test bundle assembly
	Assembly and inspection procedures
	Assembly and inspection

TABLE 4-7 (Continued)

Major Responsibility	Activity
ORNL	As-built report
ORNL	Test vessel components (pressure boundary and closures, inlet plenum, outlet plenum and mixing section, attemperation annulus)
	Design
	Specifications
	Procurement
	Inspection

TABLE 4-8
BLANKET ROD AND ASSEMBLY POWER FOR THE CFTL

	ThO_2 Blanket(a)	
	Current High-ΔP Core (290 KPa)	Proposed Low-ΔP Core (155 KPa)
Peak rod power with overpower factor (kW)(b)	27.1	32.6
Average rod power with overpower factor (kW)	17.1	20.5
Total power in peak power assembly (kW)(c)	1024	1230

(a) Values for a UO_2 blanket assembly are ∿150% of the values listed.

(b) Overpower factor = 1.1.

(c) 61-rod assembly with unpowered center instrument rod.

revision to the steady-state operating requirements for the CFTL. The requirements are under review and will be updated in revision 1 to the CFTL Program Plan (Ref. 4-1).

Also under review are the circulator performance parameters listed in Ref. 4-5. The effect on circulator requirements of low-flow test conditions, such as would occur for a simulated depressurization accident, is being studied.

4.6. GCFR PROTOTYPE CORE ASSEMBLY TEST PLANNING

Program planning for testing of the full-size prototype core assemblies is continuing. The outline plan for the GCFR Prototype Core Element Test Program was completed and issued to ERDA for review.

The prototype core assembly tests will be conducted on full-size core assemblies to provide assurance that the core assemblies meet design qualification requirements prior to the fabrication of the GCFR demonstration plant initial core. With the exception that the mixed PuO_2-UO_2 fuel in the rods will be simulated by depleted UO_2, the prototype assemblies will duplicate the GCFR demonstration plant core assemblies. As shown in Fig. 4-1, this test is also on the critical path for core element development.

The objective of the prototype test program is to evaluate the preliminary design of the full-size assemblies by subjecting the assemblies to maximum GCFR helium flow conditions under a close simulation of the reactor core environment, but without radiation. One assembly of each type (fuel, control, and blanket) will be subjected to the equivalent of approximately one year of reactor operation in a hot helium test loop. The helium test loop temperature will be maintained external to the test section since fuel rod heating will not be simulated in these tests.

Review of the test loop facility options for the prototype tests has been initiated. The evaluation will compare existing helium test loop facilities with each other and with a new facility especially designed for prototype testing. The first loop to be considered is the HHV loop in Jülich, Federal Republic of Germany. Prototype test loop requirements versus HHV capabilities are shown in Table 4-9. As shown in Table 4-9, the HHV has a much higher flow capability than necessary and can therefore test all three types of core assemblies (fuel, control, and blanket) at the same time and in parallel. However, since the loop pressure is lower than the normal GCFR operating pressure (5.1 versus 9.0 MPa), the pertinent modeling factors cannot be simultaneously simulated for parallel flow and cross-flow vibration effects. For the long-duration test, the induced vibration caused by parallel flow would be simulated in this loop by operating the assemblies at a flow which is higher than reactor flow by a factor of 1.75 in order to obtain Reynolds number similitude. In addition, a short-duration test would be required to determine the effects of cross-flow-induced vibration. This test would require Strouhal similarity in which test velocity equals reactor velocity. To summarize, the low total pressure capability of the HHV as compared with the operating pressure of the GCFR introduces Reynolds and Strouhal number mismatches. An engineering evaluation will be undertaken to determine the effect of these mismatches, possible operating compromises, and the feasibility of increasing the HHV pressure capability.

REFERENCES

4-1. Hopkins, H. C., Jr., "Program Plan for GCFR Core Flow Test Loop," USAEC Report GA-A13080, General Atomic, August 9, 1974.

4-2. "Gas-Cooled Fast Breeder Reactor Quarterly Progress Report for the Period February 1, 1976 Through April 30, 1976," ERDA Report GA-A13868, General Atomic, May 31, 1976.

4-3. "Gas-Cooled Fast Breeder Reactor Quarterly Progress Report for the Period November 1, 1975 Through January 31, 1976," ERDA Report GA-A13815, General Atomic, March 22, 1976.

TABLE 4-9
PROTOTYPE TEST LOOP REQUIREMENTS VERSUS HHV CAPABILITIES

Parameter	Prototype	HHV
Flow (kg/s)	0 to 8	200(a)
Test section inlet pressure (MPa)	9.0	5.1(b)
ΔP(KPa)	155	200(c)
Temperature (°C)	350 to 550	1000(c)

(a)Facility capable of much higher (approximately 20 times more) flow than required.

(b)HHV capable of approximately five-ninths of required pressure.

(c)HHV capable of higher temperature and ΔP than required for normal GCFR operating conditions.

4-4. "Outline Test Specification for GCFR-CFTL Priority One Tests," General Atomic, unpublished data.

4-5. "CFTL Helium Circulator Design Study Report," Mechanical Technology, Incorporated, Latham, New York.

5. FUELS AND MATERIAL ENGINEERING (189a No. SU007)

5.1. OXIDE FUEL, BLANKET, AND GRID PLATE SHIELDING MATERIALS TECHNOLOGY

It is the responsibility of this subtask to maintain liaison with and surveillance of other ERDA and non-ERDA programs, especially the liquid metal fast breeder reactor (LMFBR) program, to ensure the availability of all relevant information for the GCFR design. The areas included in this subtask are

1. Oxide fuel technology.
2. UO_2 (axial) blanket technology.
3. ThO_2 (radial) blanket technology.
4. Grid plate shielding technology.

During this quarter, the irradiation test matrices were updated to indicate that irradiation experiments F-1 (X094) and F-3 (X206) had been terminated.

5.2. CLADDING TECHNOLOGY

5.2.1. Mechanical Testing Program at Argonne National Laboratory

The purpose of this program is to determine the effects of the following factors on the behavior and mechanical properties of GCFR cladding:

1. Ribs, rib geometry, and fabrication technique.
2. Helium impurity levels typical of the GCFR environment.

The effects of end cap design and specimen length were determined in early tests. All tests at ANL are being performed in a quasi-static helium environment.

During this quarter, testing of the second test matrix has been completed. This test matrix included smooth and ribbed test specimens fabricated by electrochemical etching and mechanical grinding. The tests were performed at 650°C at a hoop stress of 238 MPa in a purified helium atmosphere. The helium was purified by passing it through activated charcoal at liquid nitrogen temperature. The tests were completed in early May 1976. On the basis of information received from ANL, the following qualitative observations can be made:

1. The ribs improve the mechanical behavior of the cladding irrespective of the method of fabrication.

2. Based on creep rupture performance, the mechanical grinding process appears to be better than etching.

5.2.2. Helium Loop Test Program at Pacific Northwest Laboratory

The primary objective of this program is to permit comparison of the mechanical properties determined in recirculating helium at Pacific Northwest Laboratory (PNL) with those determined in quasi-static helium in the test program at ANL. The scope of work has been agreed upon, and the evaluation of techniques for detection of pinhole leaks and ruptures has been completed. In preparation for the test program, the loop has been modified for unattended operation. The impurity monitoring system has been installed, and the loop has been satisfactorily operated with desired impurities.

During this quarter, the welding of end caps to the specimens was completed at ANL. These specimens were welded to the test train and installed in the loop. After the welds were checked for leaks, the loop was operated for a short period of time before being shut down for instrument (recorder) repair. The loop will be restarted at the beginning of the transition quarter when additional funding becomes available.

5.3. F-1 FAST FLUX IRRADIATION EXPERIMENT

Postirradiation examination of the encapsulated seven-fuel-rod F-1 (X094B) experiment, which achieved a maximum burnup exposure of 121 MW/kg, has been initiated. The operating conditions for the most recently removed seven capsules which were in the X094B segment of the irradiation and for the highest powered run for X094B (run 70B) have been recalculated using detailed fission rate and subassembly flow information received from the EBR-II project. The conditions for the fuel rod capsules and the exposures observed are given in Table 5-1.

Neutron radiography has been performed on six (G-4, G-8, G-9, G-10, G-11, and G-13) of the seven capsules, and the radiographs show that the rods exhibit no anomalies, confirming Xe-133 gamma scanning results which indicated that all the rods were intact. The remaining capsule, G-12, will be neutron radiographed during the next available window at TREAT, when other B-7 capsules are scheduled for radiography.

Silicon carbide rods were placed in the thermal barriers of the F-1 fuel rod capsules for the purpose of determining capsule operating temperatures. By measuring changes in the lengths of the rods following isochronal anneals, an estimate of the temperature during the last cycle of irradiation can be made. The anneals for samples from capsules G-1 and G-6 removed at an exposure of 50 MWd/kg have been completed, and a decrease in length of all the samples has been measured as a function of temperature. The results remain to be analyzed for temperature determination and comparison with calculated capsule temperatures.

TABLE 5-1
IRRADIATION CAPSULE LOADINGS AND CONDITIONS FOR F-1 SUBASSEMBLY

Capsule	Test Condition		Type of Pellet[a]	Fuel O/M	Burnup [MWd/kg (at. %)]					Type of Trap[b]	Peak Total Fluence[c] ($n/cm^2 \times 10^{22}$)	Purpose (Status)
	Maximum Cladding Midwall Temperature (°C)	Peak Linear Heat Generation Rating (kW/m)			25 (2.7)	50 (5.4)	73 (7.7)	97. (10.4)	121 (13.0)			
G-1	740	45.6	A	1.992	—	→				S	3.4 (2.8)	Temperature effect, post-irradiation examination completed
G-2	705	43.9	A	1.971	—	→				S	3.4 (2.8)	Temperature effect, PIE completed
G-3	675	43.9	A	1.987	→					S	1.7 (1.4)	Temperature calibration, PIE completed
G-4(d)	700	44.3	A	1.983	—	—	—	—	→	A	8.2 (6.7)	Burnup effect
G-5	620	40.5	A	1.990	—	→				S	3.4 (2.8)	Temperature effect, PIE completed
G-6	665	40.8	A	1.972	—	→				A	3.4 (2.8)	Reference/fast flux - thermal flux comparison, PIE completed
G-7	570	39.0	A	1.984	—	→				A	3.4 (2.8)	Overlap with LMFBR/temperature effect, PIE partially completed
G-8(d)	698	45.8	A	1.985	—	—	—	→		S	6.8 (5.6)	Burnup effect
G-9(d)	714	45.4	A	1.968	—	—	→			A	5.1 (4.2)	Surface roughening effect
G-10(d)	730	47.8	A	1.968	—	—	→			A	5.1 (4.2)	Surface roughening effect, reproducibility
G-11(d)	732	50.3	A	1.947	—	—	→			A	5.1 (4.2)	Low fuel oxygen-to-metal effect
G-12(d)	722	45.3	S	1.976	—	—	→			A	5.1 (4.2)	Solid pellet effect at reference cladding temperature
G-13(d)	758	50.4	S	1.973	—	—	→			A	5.1 (4.2)	Solid pellet effect at high cladding temperature

(a) A = annular, S = solid.

(b) A = active, S = sealed.

(c) Numbers in parentheses indicate fast > 0.1 MeV.

(d) Rods most recently in the experiment, removed for final PIE during April 1976.

A series of coated fuel particles containing U-238, U-235, and Th-232 isotopes which were contained in the dosimetry of the F-1 fuel rod capsules was examined for tritium content, and results have been reported (Ref. 5-1). However, because of uncertainties in the identity of some of the fuel particles examined, the results were considered tentative. Analysis of these fuel particles for material characterization was initiated during this quarter. The characterization of the particle thus far has confirmed the enhanced tritium yields for U-238 and Th-232. The preliminary reported value is 2.8×10^{-3} tritons per fission, an increase of 10 to 20 above the reported U-238 yield value (Ref. 5-2). Additional samples have been processed for tritium content analysis and need to be characterized to complete this study.

The fuel particles examined thus far were irradiated in the F-1 experiment (EBR-II, row 7). Additional fuel particles are expected from the F-3 capsules which were in an in-core position (EBR-II, row 4) and are thus more nearly typical of the GCFR neutron spectrum. The row 4 position represents a substantially more energetic neutron spectrum than the row 7 position and may influence the ternary fast fission yield of U-238. These measurements are quite important to the basic technology of the fast breeder reactor program. The tritium production rate in the GCFR demonstration plant based on the enchanced tritium yields is increased by a factor of 2.7 more than the value used in the Preliminary Environmental Report (8500 Ci). A similar increase may be expected to impact the LMFBR program.

In view of the potential impact on reactor safety considerations, a comprehensive effort to examine all fissile and fertile species in the GCFR program was initiated. An overview of the work plan and time schedule for performing ternary fast fission yields has been issued. The termination of the F-3 experiment interrupted prospective measurements on a variety of isotopes to be irradiated in the EBR-II core. An alternate irradiation plan for the ternary yields of U-233 and Pu-239 is under consideration and is incorporated in the FY 77 work scope.

5.4. F-3 FAST FLUX IRRADIATION EXPERIMENT

The F-3 experiment was irradiated in location 4B3 in EBR-II to an exposure of 46 MWd/kg; the burnup goal was 100 MWd/kg. These capsules shared a type J19A subassembly (X206) with the ANL group-08 high-temperature chemistry experiment, as reported in Ref. 5-3. The experiment reached an exposure of 46 MWd/kg on February 11, 1976, at which time it was removed from the core for a planned interim examination. The conditions for the F-3 fuel rod capsules are given in Table 5-2.

Neutron radiography of the capsules has confirmed Xe-133 gamma scanning, which indicated that nine out of the ten fuel rods had failed. The neutron radiography results are summarized in Table 5-3. Four of the fuel rods, G-14, G-18, G-19, and G-20, are at the Material Science Division of ANL (ANL-MSD) for posirradiation examination. Emphasis is on the examination of intact rod G-18.

Argonne National Laboratory East (ANL-E) reports that postirradiation examination of the unfailed rod containing capsule G-18 is under way. A detailed postirradiation examination (PIE) plan has been prepared, and capsule profilometry and puncturing have been completed. The profilometry shows a nonuniform increase in the outer diameter of the 304 stainless steel capsule; this increase may be due to neutron-induced swelling. The maximum increase in diameter is 0.2 mm. None of the peaks in diameter increase appear to be directly identifiable as being located near the region where a "bump" was found on the fuel rod outer surface in the neutron radiograph of the capsule. ANL-E personnel have postulated that this increase may at least be partially due to fuel rod - capsule mechanical interaction. However, the F-1 capsules had similar nonuniform diameter increases, and rod - capsule mechanical interaction is not possible in them because a thermal barrier is present between the fuel rod and the capsule. Puncturing of the G-18 capsule plenum showed that no fission gases were present, substantiating the gamma scanning (for Xe-133) results which showed the fuel rod to be intact.

TABLE 5-2
F-3 FUEL ROD CAPSULE CONDITIONS[(a)]

	Peak Linear Heat Generation Rate (kW/m)	Type of Pellet[(b)]	Fuel O/M	Burnup (MWd/kg)	Type of Trap[(c)]	Trap Location[(d)] (mm)	Remarks[(e)]
INTACT							
G-18	40.5	S	1.98	39	S	251	G,E
FAILED							
G-14	41.2	S	1.94	39	A	251	M,E
G-15	40.7	S	1.94	39	A	192	E
G-16	41.5	S	1.94	39	S	192	G,E
G-17	41.0	S	1.98	39	A	192	E
G-19	50.4	A	1.94	46	A	251	A
G-20	49.9	A	1.98	46	A	251	E
G-21	49.3	A	1.94	46	A	251	E
G-22	47.9	S	1.94	46	A	192	E
G-23	47.3	S	1.98	45	A	251	E

(a) Cladding midwall temperatures are being recalculated (using TAC2D) for maximum-powered run 76, based on fission rate and subassembly coolant flow information received from the EBR-II project. These temperatures will be published in the next quarterly report.

(b) A = annular, S = solid.

(c) A = active, S = sealed.

(d) Distance from core midplane to trap midplane.

(e) G = contains solid graphite shield material sample; M = contains ZrH_2, Be, and BeO shield material samples; A = cladding ribs formed by alpha cutting; E = cladding ribs formed by GA electroetching.

TABLE 5-3
NEUTRON RADIOGRAPHY RESULTS, F-3 FUEL ROD CAPSULES

Region	G-14[(a)]	G-18[(b)]	G-19[(a)]	G-20[(a)]
Upper blanket	No change visible	No change visible	No change visible	No change visible
Upper fuel - blanket interface	Swollen for 1-mm length	No change visible	No change visible	Swollen over 2-mm length
Fuel column growth (includes gaps if present)	3%	0%	2%	3%
Fueled region				
Upper	3 pellet separations; 4-mm gap; partly filled with fuel chunks; fuel melting indicated	No change visible	1 pellet-to-pellet separation; central part filled with fuel at separation; fuel melting indicated	4 gaps between pellets; central part filled with fuel except in 1 gap
Lower	OK; some transverse pellet cracking; irregular diametral swelling of 0.5 mm	1 pellet separation; central portion filled with fuel	Some fuel melting indicated	1 gap between pellets; fuel melting indicated
Overall	Fission product ingots in central portion of fuel; failure and fuel melting in upper region of fuel column	Original pellet interfaces visible; central void normal and exists to within 2 to 3 mm of fuel - blanket interface	Fission product ingots in central void, which is discontinuous and irregular to within 2 mm of fuel - blanket interface; transverse cracking; fuel melting from about the midplane to the upper end of column	Central void very irregular and discontinuous (worst case); extends to 1 to 3 mm of fuel - blanket interface and contains fission product ingots; fuel melting indicated over most of fueled length
Lower fuel - blanket interface	No change visible	No change visible	No change visible	No change visible
Lower blanket	Slight possible swelling of pellet nearest fuel - blanket interface, may be due to Na reaction with UO_2	No change visible	Gap 5 to 6 mm below fuel - blanket interface; pellet swollen out to capsule, may be due to Na reaction with UO_2	Pellet nearest fuel - blanket interface swollen on one side, may be due to NA reaction with UO_2
Shield materials	No change visible	None placed in fuel rod	No change visible	No change visible
Trap	Charcoal shrinkage to 44% of original; uneven packing; possible Na intrusion	Charcoal shrinkage to 37%; even packing; graphite sample intact	Charcoal shrinkage to 42%; uneven packing; possible Na intrusion	Charcoal shrinkage to 48%; uneven packing; possible Na intrusion
Cladding	Seems intact over lower half of fuel column; several breaches in upper half	Intact; bulge present (2 mm long, 40 mm above midplane of fueled region)	Not clearly visible, but appears breached over most of the upper half of the fueled region	Not visible; material near capsule i.d. wall appears to be mixture of fuel and cladding; cladding appears to be breached over most of fueled length

TABLE 5-3 (Continued)

Region	G-15(a)	G-16(a)	G-17(a)	G-21(a)
Upper blanket	Top pellet separated by 1 mm from column; several pellets swollen	Some pellet separation at 65 mm; stack appears buckled; many cracks in pellets	Axial crack in first pellet; small amount of fuel in interface between first and second pellet; axial crack in pellet at middle of stack	Several transverse cracks or pellet separations in lower part; axial crack in middle of stack; stack appears buckled; opaque spot in first pellet
Upper fuel - blanket interface	1.5-mm gap containing fuel, or fuel has intruded into first blanket pellet	Some fuel intrusion into center of first blanket pellet	No change visible	No change visible
Fuel column growth	2%	2%	3%	4%
Fueled region				
Upper	Fission product ingots	Fission product ingots	Variable-diameter bulge near upper end; small gap	Gap partially filled with fuel; melting indicated; fission product ingots
Lower	--	--	Several gaps	--
Overall	Gaps; central void discontinuous and irregular	Gaps; central void discontinuous and irregular; o.d. also irregular	Central void discontinuous and irregular	Central void discontinuous and irregular
Lower fuel - blanket interface	--	--	--	--
Lower blanket	No change in pellets; cladding near pellet interface swollen out to capsule	gap between pellets; half of each pellet swollen near gap	First pellet swollen; fuel in interface between the two pellets (seen also in preirradiation radiograph)	Possible swelling of lower pellet
Shield materials	None	None	None	None
Trap (percent shrinkage is fraction of height in preirradiation radiograph, gaps included where present)	Charcoal shrinkage to 52%; gaps in packed column; Na level = 83 mm	Charcoal shrinkage to 68%; gaps in packed column;(c) graphite cylinder appears intact but has moved up and some material is in the space between the graphite and the washer originally on the top of the cylinder	Shrinkage to 50%; irregular packing	Shrinkage to 52%; irregular packing
Cladding	Appears intact in some areas since ribs are visible	Appears intact in some areas	Not visible in fueled region	Ribs visible in some areas
Other observations			Small amount of fuel in lower end of fuel rod present prior to irradiation	

TABLE 5-3 (Continued)

Region	G-22(a)	G-23(a)
Upper blanket	Some low-density spots in lower part; opaque spot near top; stack appears buckled	Fuel in interface between first and second pellet; significant fuel intrustion into first pellet
Upper fuel - blanket interface	No change visible	No change visible
Fuel column growth	5%	5%
Fueled region		
Upper	Gaps with some fuel intrusion; melting indicated; fission product ingots	Large gap
Lower	Gaps; fission product ingots	Several small gaps
Overall	Central void discontinuous and irregular	Central void discontinuous and irregular
Lower fuel - blanket interface	No change visible	No change visible
Lower blanket	First pellet swollen	First pellet swollen
Shield materials	None	None
Trap (percent shrinkage is fraction of height in preirradiation radiograph, gaps included where present)	Shrinkage to 47%; irregular packing	Shrinkage to 61%; irregular packing; dosimeter tube bent or buckled in centerline of trap
Cladding	Not visible	Not visible

(a) Failed.

(b) Intact.

(c) This rod contains a trap which was originally sealed, however the appearance of the charcoal is the same as in the open (active) traps, and some reaction products appear adjacent to the graphite cylinder in the trap. The top end of the trap has an unusual appearance in the preirradiation radiographs, as if some fuel is present at the upper end of the trap.

Eddy current measurements performed on the G-18 fuel rod capsule from the F-3 experiment in which the fuel was intact (but which was shown by neutron radiography to have a very localized bump) showed what was interpreted to be "sponginess" in the capsule sodium bond. The sponginess was found over two-thirds of the capsule circumference for a length of ∿30 mm in the region where the bump in the fuel rod was located. This result is an indication that the F-3 fuel rod capsule failures occurred because of inadequate sodium bonds in the capsules. Preparations are under way to transfer the remaining F-3 rods from EBR-II to ANL-E.

5.5. F-5 PROTOTYPE IRRADIATION EXPERIMENT

Design work continued on the F-5 prototype design fuel rod experiment to be carried out for experimental study of the performance of fuel rods irradiated under simulated GCFR conditions to high burnups for the purposes of (1) determining the reliability of the GCFR fuel rod design, (2) discovering what failure modes may exist, and (3) studying the effect of a step power increase which simulates the 180-deg rotation of a subassembly at the core blanket interface in the proposed GCFR demonstration plant. Decisions were made on the design and location of fission product traps and dosimeters for this experiment and have been forwarded to ANL-MSD for incorporation in the design. A review and check of the physics and thermal design calculations for the F-5 fuel rods was completed at GA, and the results were in good agreement with those obtained by ANL-MSD.

5.6. GB-10 VENTED FUEL ROD EXPERIMENT

Fission product release and transport in GCFR fuel are being measured and studied in capsule GB-10, which is being irradiated in the Oak Ridge Reactor (ORR). The burnup of the pressure-equalized and vented fuel rod in capsule GB-10 has reached approximately 100 MWd/kg, which is the exposure goal. The first 27 MWd/kg were accumulated at a heat generation rate of

39.4 kW/m and a cladding outside surface temperature of 565°C; from 27 to 75 MWd/kg have been accumulated at 44.3 kW/m at a cladding outside surface temperature of 630°C, and from 75 MWd/kg to the current burnup have been accumulated at 48 kW/m and a cladding outside temperature of 685°C.

Loss of flow conductance through the fuel region of the fuel rod in irradiation capsule GB-10 continued with increasing burnup as the capsule approached 100 MWd/kg and its termination on August 1, 1976. At operating levels of 39 to 49 kW/m, an imposed ΔP of 1.7 MPa did not result in measurable convective flow through the fuel region of the rod. In addition, it was not possible to measure the flow by pressure decay over periods as long as two days. The venting fraction of radioactive gases vented from the fuel rod has been measured to determine the venting capability of the rod. Although significant levels of radioactive gas activity have been measured, the data have not been reduced to a form which allows comparison with previous measurements as an indicator of any reduction in the venting capability of the rod. Testing with special, rapidly responding instrumentation, however, has indicated pressure release beginning within 2.5 s after shutdown of the ORR or retraction of the irradiation capsule from the neutron flux. Thus, the constriction that has developed, if it were to occur in an operating GCFR fuel rod, would not affect the capability of the fuel to follow the coolant pressure during a design basis depressurization accident or to pressure-equalize the rod during normal power transients of cycling during normal GCFR operations. Significant buildup of internal gas pressure from fission gas release between significant power cycles of the GCFR is very unlikely.

Part of the simulated leak flow rate test was performed. The first half of the test in the TT-TT (no leak) flow mode was completed according to prepared procedures. However, when the BF-TT (leaking rod) flow test was attempted, flow through the fuel rod was too low and the flow range too narrow to constitute a good test. Nevertheless, some data were acquired at 31 kW/m and 20 and 50 ml STP/min; flows up to 800 ml STP/min were desired. These data have not yet been reduced and transmitted to GA for analysis.

Several small charcoal traps have been tested for possible use in predicting the potential for plugging of the charcoal traps in the tritium monitoring instrumentation in the capsule. Plugging of the traps by ice formation was found at the high and low moisture levels needed for the tritium tests after about 2 hr of operation. The MgO converter, which is one of the components in the tritium instrumentation system and has a capacity of about 4 hr at the maximum moisture level planned, was inadequate. Thus, the addition of moisture to the hydrogen impurity in the helium was cancelled. Furthermore, because of the need to preserve the nature and formation of the constriction for PIE, the tritium testing to be done during the transition quarter was limited to the addition of 1% hydrogen in helium (no moisture addition) flow through the charcoal trap and the sweep gas lines across the top of the charcoal trap.

Preparations and decisions required for the PIE of the fuel rod being irradiated in capsule GB-10 are in progress. Thermocouple data received recently from ORNL indicate uncertainties in the temperatures in the fuel rod during the irradiation of up to 100°C as a result of (1) changes in the power and temperature distributions in the fuel rod as a function of burnup, (2) corrections to the thermocouple readings to indicate the actual cladding outside surface temperatures, and (3) bowing of the fuel rod within the capsule. Consideration has been given to postirradiation calibration of the thermocouples, postirradiation measurement of the isotropic fission atom distribution, and measurement of precipitate formation in the cladding. After some study at ORNL, ANL, and GA, it was determined that decalibration of the Chromel-Alumel thermocouples in the capsule as a result of temperature and neutron flux and gradients was unlikely. Thus, postirradiation calibration will not be performed unless other circumstances develop which indicate its requirement. The distribution of fissile atoms (U-235 and Pu-239) in the fuel will be determined by a combination of electron and ion microprobe analyses. The fissile distribution will subsequently be used in neutronic and thermal calculations to establish the corrections to be applied to the thermocouple readings at the end of life in order to reduce the uncertainties in the operating temperatures.

5.7. HEDL CLADDING IRRADIATIONS

A letter has been sent to Hanford Engineering Development Laboratory (HEDL) requesting shipment of the 15 GCFR cladding samples irradiated in HEDL capsules and all unirradiated cladding samples (and the associated characterization documentation and history) to ANL-MSD for testing. A letter was sent to ANL describing the test conditions desired for the above specimens along with a suggested test matrix for future cladding irradiations.

REFERENCES

5-1. "Gas-Cooled Fast Breeder Reactor Quarterly Progress Report for the Period November 1, 1975 Through January 31, 1976," ERDA Report GA-A13815, General Atomic, March 22, 1976.

5-2. Larsen, R. P., et al., "Chemical Engineering Division Burnup, Cross Sections and Dosimetry Semi-annual Report, January-July 1972," Argonne National Laboratory Report ANL-7924, 1972, pp. 18-21.

5-3. "Gas-Cooled Fast Breeder Reactor Quarterly Progress Report for the Period February 1, 1976 Through April 30, 1976," ERDA Report GA-A13868, General Atomic, May 31, 1976.

6. FUEL ROD ENGINEERING (189a No. SU007)

The objective of this task is to evaluate the steady-state and transient performances of the fuel, blanket, and control rods for the determination of performance characteristics, operating limits, and design criteria. To this end, analytical tools (such as the LIFE-III code) are being adapted and/or developed and applied to the analysis of the GCFR prototypical rods and experimental rods. In addition, continuous surveillance of the LMFBR fuels and materials development programs and technology is maintained to maximize the use of developing technology and material properties. Support is also given for the planning and designing of irradiation experiments.

6.1. FUEL, BLANKET, AND CONTROL ROD ANALYTICAL METHODS

6.1.1. LIFE Code Development Activities

A meeting of the LIFE Working Group was held at the ERDA Reactor Research and Development Division (RRD) from April 1-2, 1976. The objectives of this meeting were (1) to review the LIFE-IIIA updates and calibrations and (2) to discuss the work plan for the LIFE-IV and LIFE-IVT (transient) code development activities. The following major items were achieved at this meeting: (1) The LIFE-IIIA updates were completed and the code was approved by the Working Group and should be released to the Clinch River breeder reactor for use in upcoming preliminary fuel rod design analyses; (2) ANL will prepare and issue the LIFE-IIIA users manual to the Working Group in the near future; (3) lifetime models will be added to LIFE-IIIA; (4) a National Experiment Evaluation Program (NEEP) on the EBR-II run-to-breach program will be established, and each Working Group member will be responsible for issuing the experimental data from his organization to NEEP for analysis; and (5) the development of LIFE-IV and

LIFE-IVT will be completed in September 1978. Moreover, lead and support organizations were designated for each activity required for the development of these two codes. GA will play the role of support organization in the areas of mechanical analysis, thermal analysis, fuel properties utilization, cladding properties utilization, and irradiation test data compilation.

6.1.2. Control Rod Analytical Methods

An evaluation of control rod analytical methods has been conducted. First, the CONROD code (Ref. 6-1) developed at HEDL was reviewed. This code was developed for FFTF control element design analysis and has been applied to other LMFBR designs by making appropriate changes in data statements and geometrical correlations of the program. The code performs calculations for thermal performance, boron carbide gas release, swelling, cladding stress and strain, coolant flow split, pressure drop, and reactivity depletion as a function of operating time. Moving and fixed control elements can be analyzed, however the CONROD code is programmed to treat control elements of hexagonal geometry. In view of the different geometry of the GCFR control element design, it requires a great deal of effort to modify CONROD for the use of a single GCFR control rod design analysis.

Another effort was made to evaluate the ABSORB code developed at ORNL (Ref. 6-2). This code evolved from FMODEL, an LMFBR fuel rod thermomechanical analysis code (Ref. 6-3), and as a result, it possesses the important features of the fuel rod thermal and mechanical models. Moreover, because ABSORB is programmed to treat a single control rod analysis, it is more applicable for performance of the GCFR design analysis.

6.1.3. LIMDA Code Modifications and Verification

The LIMDA code has been used in the preparation of experimental fuel rods for the EBR-II irradiation test to determine the relationship among enrichment, linear power rating, and fission rate. However, the code has frequently produced inconsistent results, and therefore an effort was made to verify the code. Accordingly, the theoretical formulation and the programming structure of LIMDA were examined.

6.2. ANALYSIS OF IRRADIATION TESTS

6.2.1. Cladding Hot Spot Temperature of F-3 Rods

Because of the failure of the F-3 series irradiation test rod in EBR-II, an effort was directed toward evaluating the cladding hot spot temperature which, if caused by sodium debonding, could be high enough to result in cladding melting. Assuming that a small section of sodium between the test capsule and the rod is displaced by helium and heat flow is confined to only the radial direction, the cladding outside diameter temperature was found to be 2538°C, which is much higher than the cladding melting temperature (∿1371°C). This result is high because heat transfer in the tangential and axial directions was neglected. However, it indicates that sodium debonding could cause cladding temperatures high enough to cause melting.

6.2.2. Verification of F-1 Rod Cladding Temperatures

Because questions were raised in regard to the cladding temperatures of the F-1 experimental rods in EBR-II, an effort was made to verify their accuracy. The cladding temperatures of these experimental rods were previously obtained from analyses using a combination of the computer codes LIMDA and TAC2D. If the fission rate of the rod in EBR-II is known, LIMDA is able to determine the linear power which is used as an input to TAC2D to obtain the cladding temperature. In the process of verification, the LIMDA code was carefully reexamined (Section 6.1.3) and the input to TAC2D was scrutinized. The cladding temperatures of rods G-1 and G-13 were hand calculated by assuming one-dimensional heat flow in the radial direction. The results are in good agreement with the corrected TAC2D results.

6.3. DESIGN CRITERIA

Work is continuing on publication of a draft version of the GCFR fuel, blanket, and control component structural criteria. During this quarter, the draft version was reviewed and numerous editorial changes made. In particular, the introduction was modified to emphasize design requirements for assured structural integrity as the basis for establishing the design limits. This resulted from the changes made during the previous quarter in the design limits and the methods recommended for classifying components according to the degree of reliability required in relation to the total system during specific events.

A method to extrapolate from a nominal data base to the required minimum values of material properties has been incorporated into the criteria. This minimum value will be obtained by subtracting 1.65 multiplied by the standard error of the estimate from the nominal value of the correlation. This will require that the standard error be included in the material properties data base and is being worked on by the Nuclear Systems Materials Handbook (NSMH) Advisory Group.

The final modification concerned welds. Non-full-penetration welds will be permitted provided adequate justification by appropriate tests or detailed analysis of the weld region is included in the design documents.

6.4. FUEL ROD ANALYSIS AND PERFORMANCE

The functioning of the PES is of critical importance to the success of the GCFR fuel rod. By controlling the internal pressure of the rod so that it is in equilibrium with the environment, two major failure mechanisms, cladding creep collapse and creep rupture, are eliminated. However, the inadvertant blockage of the PES is a postulated accident condition, and its effects on the fuel rod cladding must be considered. This blockage could occur under two conditions: (1) prior to reactor start-up (i.e., during rod manufacture, core assembly, etc.) or (2) during the operating lifetime. It is the second condition to which this study addressed itself, in particular, the effects of PES blockage concurrent with a worst-possible ($429-cm^2$ leak) design basis depressurization accident (DBDA).

The LIFE-III code was used to predict preaccident gas temperatures, volumes, and pressures assuming beginning-of-life conditions based on maximum power operation (41.04 kW/m). Using these results as a starting point, the GAFTRAN code calculated gas, fuel, and cladding temperatures and internal and external pressures as functions of time after depressurization. From these results, the cladding temperature and subsequent internal pressure were obtained. Maximum values were reached 111 s after depressurization, at which time the external pressure was 0.1655 MPa, the cladding temperature 755°C (818°C with hot spot factor), and the internal pressure 5.654 MPa (5.964 MPa with hot spot factor.

Stresses were calculated for the hoop and axial directions using the maximum internal pressure and an estimated 14°C temperature gradient through the wall. The maximum pressure stresses were 49.02 MPa and 24.51 MPa in the hoop and axial directions, respectively. The thermal stresses were 24.99 MPa in both directions. The total stresses were combined into an equivalent stress of 92.36 MPa. Two material properties were required to assess the failure potential of such a stress state: the unirradiated instantaneous burst pressure and the time to rupture of 20% cold-worked 316 stainless steel. The following table presents the pertinent comparison quantities.

Temperature (°C)	Burst Hoop Stress (MPa)		Time to Rupture (hr)	
	Minimum	Nominal	Minimum	Nominal
755	482	567	85.9	359.2
818	384	436	4.7	18.1

It can be concluded that it is not likely that the cladding will fail during such a combination of events whether the materials are brittle or ductile. However, a return to the operating conditions in the hot spot rod should be studied further since this type of accident may have exhausted a considerable portion of the cladding creep rupture "life."

6.4.1. Fuel Rod Thermal Distortion

Work continued on the evaluation of the elastic-thermal-induced and irradiation-induced swelling distrotion of a full-power edge fuel rod. An analytic closed-form solution was developed for the thermal bowing of a fixed end beam subjected to thermal gradients which are linear in the radial direction and arbitrary in the axial direction. This was accomplished by constructing a least-squares polynomial fit to the temperature and flux data and then integrating the thermal bending moment twice to yield the displacement. The swelling is accounted for by differentiating the current swelling equation of Ref. 6-4 with respect to temperature and adding this to the coefficient of thermal expansion before the integrations. This method is capable of providing distorted profiles at any time for the given temperature and fluence distribution with a single set of integrations. Using the free thermal distortion, constraints are added to provide the spacer reaction loads and the final distorted shape. Because of the short computation time involved, this approach has the potential to be used in a complete bundle interaction study. This method provides preliminary, worst-case (full power, edge rod) rod distortion information and was compared to CRASIB results to verify the accuracy of the code. The results agreed remarkably well, deviating somewhat (<10%) at times near end of life.

6.4.2. Gas Temperature in Rod Fuel Region

The gas temperature in the fuel region was obtained for a typical GCFR fuel rod with a maximum linear power of 410 W/cm. The calculation was based on the LIFE-III analysis of a fuel rod having its vent passage plugged. The gas temperature was obtained for use as an initial condition for the calculation of temperature and pressure histories of the rod internal gas in the event of a DBDA. In addition, gas pressure, fission gas release and composition, gas volume distribution in the rod, and plenum gas temperature were also obtained. The results are summarized in Table 6-1.

6.4.3. Fuel Rod Parametric Study

A preliminary parametric study was conducted to evaluate the effects of variation of design parameters on fuel rod thermomechanical performance. Two important parameters, namely cladding thickness and fuel pellet geometry, were chosen for the study of the cladding structural integrity and the fuel centerline temperature, respectively. The analysis was performed using the LIFE-III code on the Berkeley CDC-7600 computer. The rod fuel region was divided into three equal axial sections in accordance with the LIFE-III model. An additional, arbitrarily large plenum section was connected to the rod to simulate the pressure equalization of the GCFR vented rod.

To study the cladding structural behavior, analyses were made for cladding thicknesses of 0.51, 0.46, 0.38, 0.30, and 0.25 mm. In order to compare the results from the different cladding thicknesses, the rod diameter and fuel-cladding gap were kept constant so that the fuel pellet outside diameter was increased accordingly for the lower values of cladding thickness. However, to compensate for the increased fuel diameter, the enrichment was proportionally decreased rather than decreasing the fuel density.

The effect of the pellet geometry on the fuel centerline temperature was investigated by analyses using the reference design annular pellet and a solid pellet geometry. The absence of the central void was compensated for by decreasing the fuel density (thus maintaining a constant fuel smear density).

TABLE 6-1
RESULTS OF LIFE-III ANALYSIS

	Time (hr)			
	1020	1663	2020	4020
Gas pressure (MPa)	1.985	3.337	3.778	7.397
Fission gas release (moles)	0.00124	0.00231	0.00294	0.00616
Fission gas composition (%)	84.88	91.29	93.03	96.55
Central void volume (cm^3)	1.5534	1.7485	1.9058	2.2598
Fuel-cladding gap volume (cm^3)	0.0	0.0262	0.1229	0.6194
Plenum volume (cm^3)	5.4602	5.4651	5.4618	5.4700
Plenum gas temperature (°C)	550	549	548	547
Fuel gas temperature (°C)	1919	2006	2053	1946

As shown in Fig. 6-1, the reactor power history was taken to be at the full power of 300 MW for 750 days. In addition, three 15% overpowers were arbitrarily superimposed on the reactor power history. The normalized axial power profile of the fuel rod is given in Fig. 6-2; the maximum linear power corresponds to 377 W/cm.

The accumulated cladding circumferential thermal creep stains for annular-pelleted rod designs is plotted in Fig. 6-3. The three steep slopes in the curves were caused by the overpower condition. It is seen that for cladding thicknesses of 0.30 and 0.25 mm, the circumferential thermal creep strain exceeds 1%. The thermal creep strain results from the stress induced by fuel-cladding interaction (fuel-cladding gap closed all the time after full power).

The fuel centerline temperature for the annular and solid pellets is shown in Fig. 6-4. Again, the "humps" in the curves were caused by the overpower situation. It is seen that the fuel centerline temperature of the solid pellet is approximately 110°C higher than that of the annular pellets. Also, it is of interest to note that the fuel centerline temperature decreases with time. This tendency was caused by (1) the increase of the fuel-cladding gap conductance which results from fuel-cladding gap closure and (2) the negligible helium dilution by fission gas due to the vented GCFR rod.

REFERENCES

6-1. Birney, K. R., and A. L. Pitner, "User's Manual for CONROD - A Computer Program for the Design Analysis of LMFBR Control Elements," ERDA Report HEDL-TME 75-131, Hanford Engineering Development Laboratory, December 1975.

6-2. Homan, F. J., "Performance Modeling of Neutron Absorbers," Nucl. Technol. 16, 216-225 (1972).

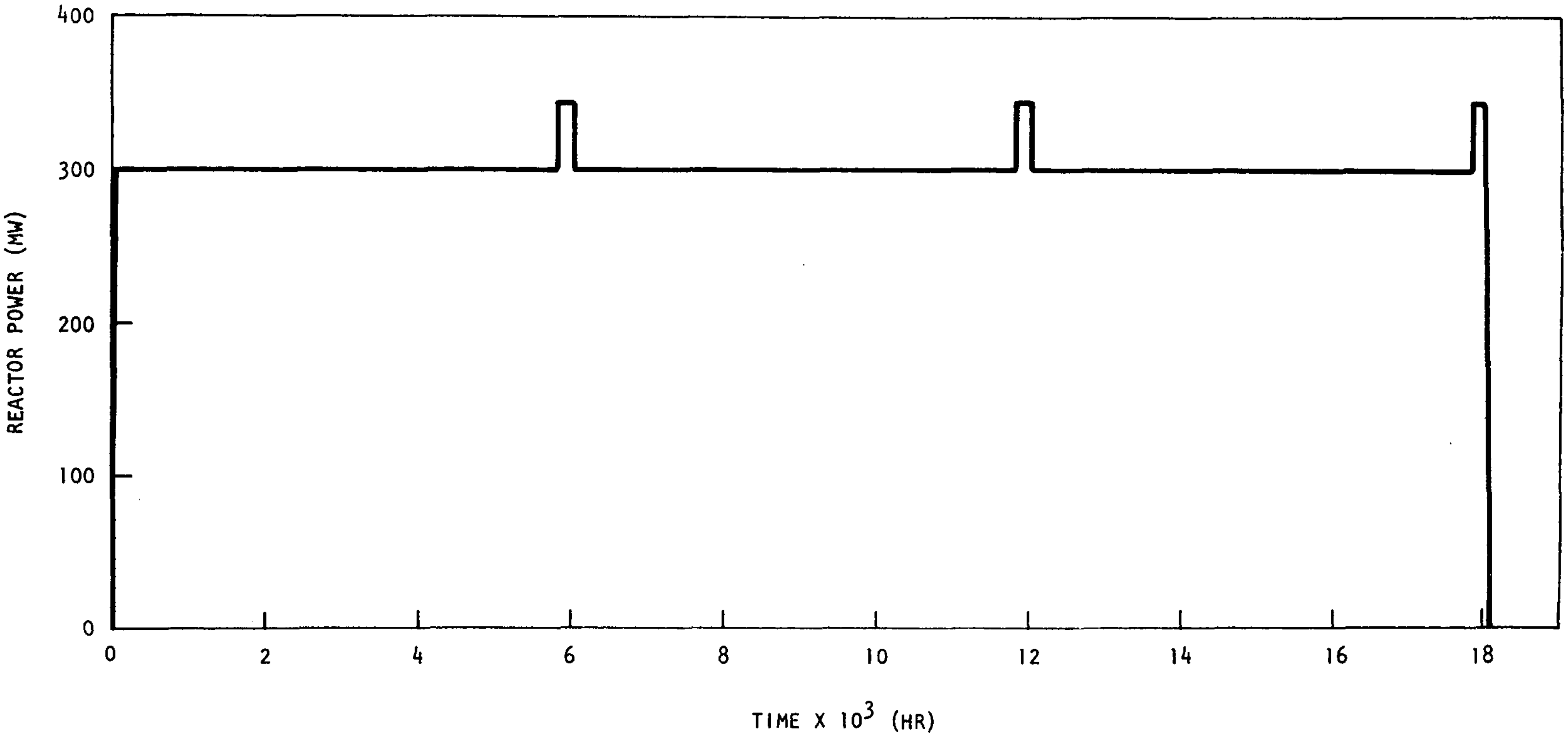

Fig. 6-1. Reactor power history

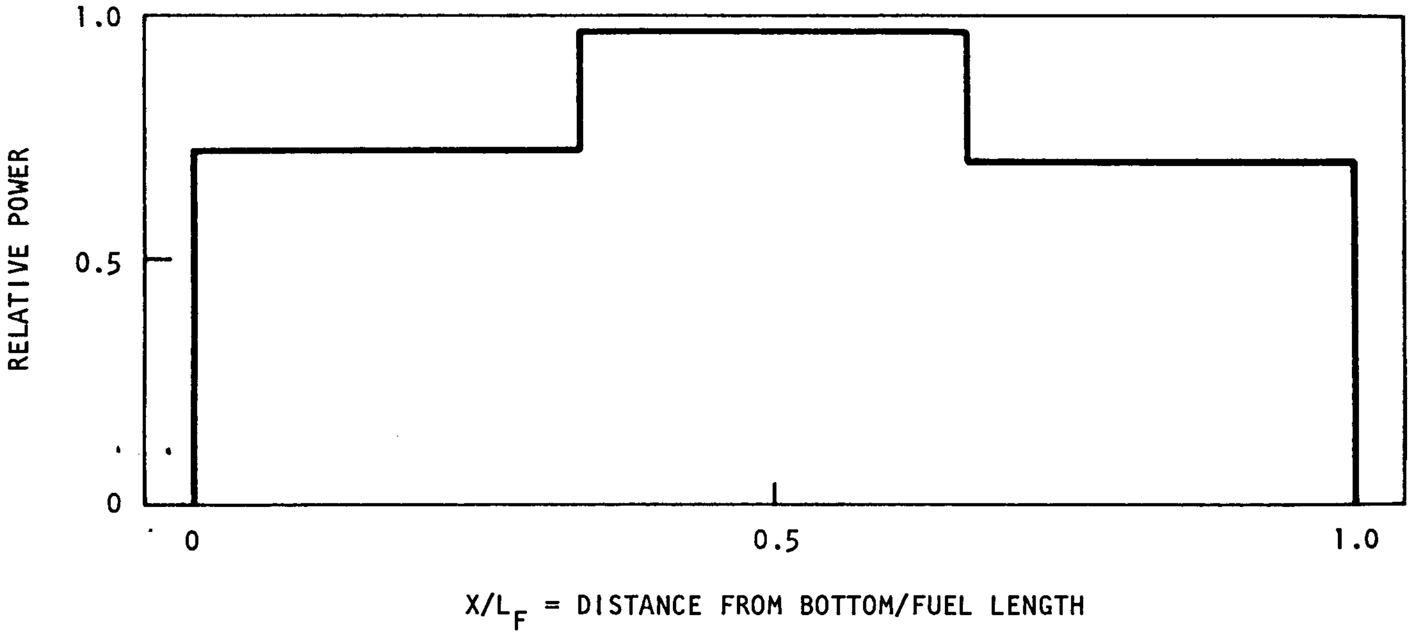

Fig. 6-2. Rod axial power profile

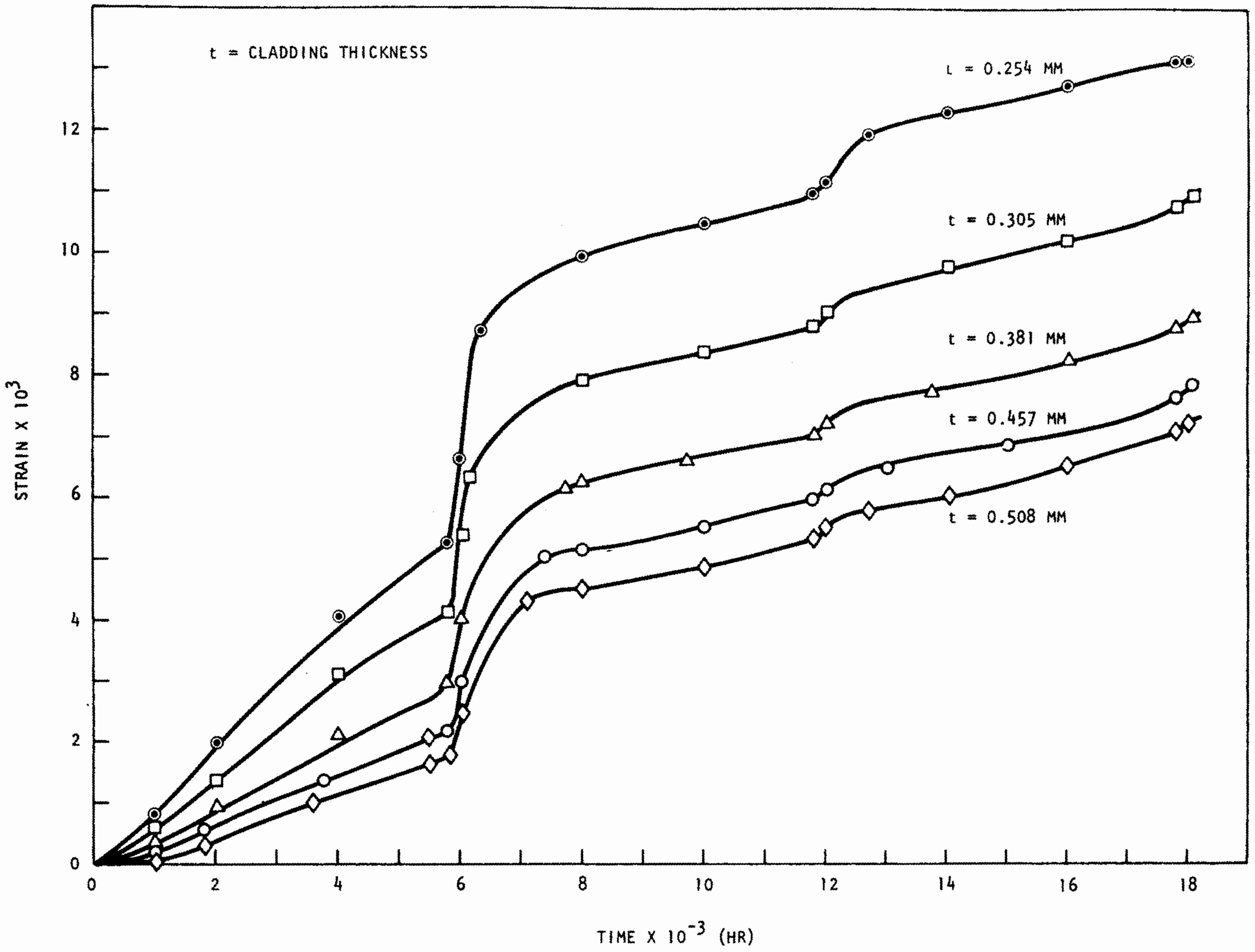

Fig. 6-3. Accumulated cladding circumferential thermal creep strain for annular pelleted rod

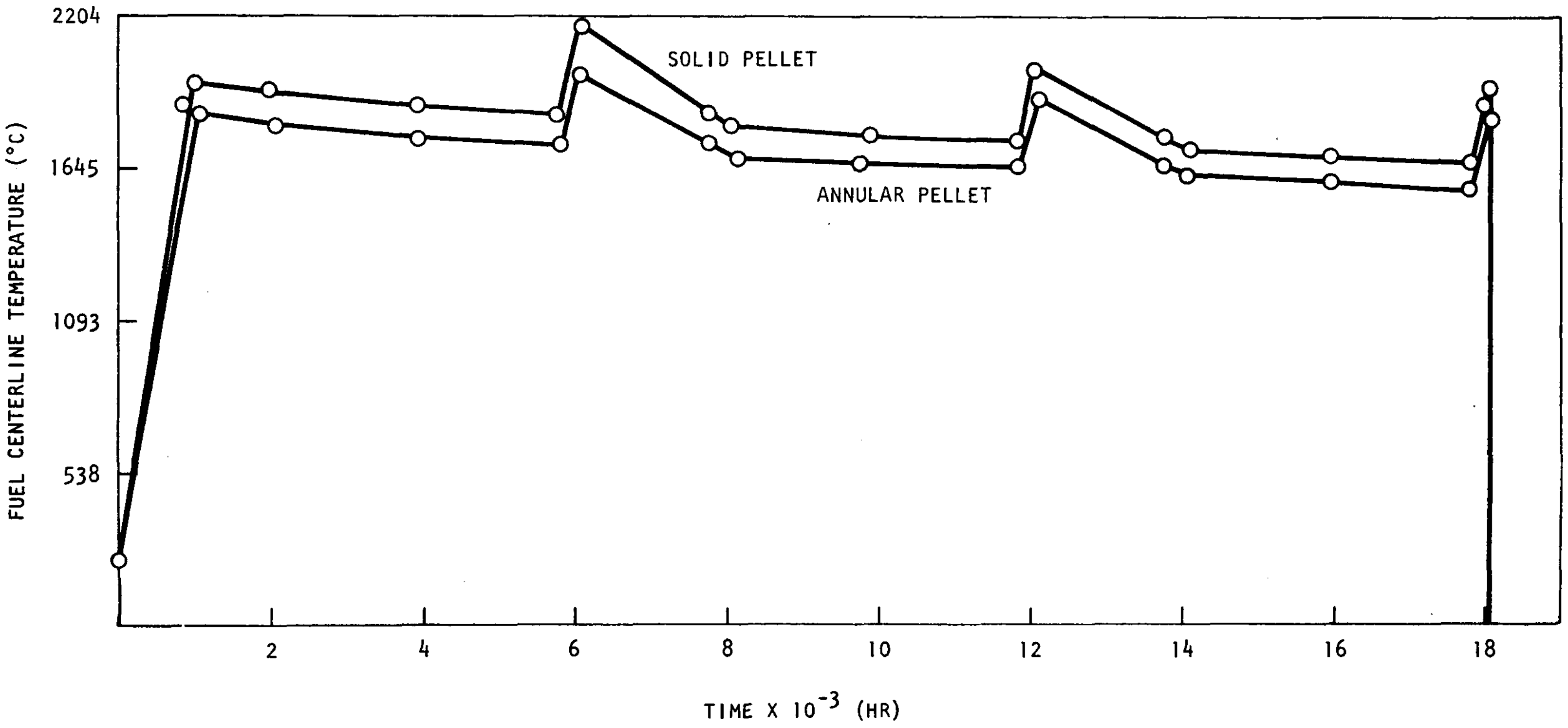

Fig. 6-4. Fuel centerline temperature

6-3. Homan, F. J., W. J. Lackey, and C. M. Cox, "FMODEL - A Fortran IV Computer Code to Predict In-Reactor Behavior of LMFBR Fuel Pins," USAEC Report ORNL-4825, Oak Ridge National Laboratory, January 1973.

6-4. Nuclear Systems Materials Handbook, Hanford Engineering Development Laboratory (TID-26666).

7. NUCLEAR ANALYSIS AND REACTOR PHYSICS (189a No. SU008)

The scope of activities planned under this subtask encompasses the validation and verification of the nuclear design methods that will be applied to the GCFR core design. This will primarily be done by direct evaluation of the methods with a critical assembly experimental program specifically directed toward GCFR development. Program planning and coordination activities, critical assembly design and analysis, and the necessary methods development will be carried out during the course of this program.

During the previous quarter, preanalysis was completed for the design of the Phase III assembly with three core enrichment zones. Postanalyses for the Phase I assembly included an evaluation of the effects of the methods on the calculations of central zone steam worths. Analysis was begun on the full-assembly steam flooding in Phase II. The 2DB diffusion code and the associated perturbation code PERT were implemented as production codes. Development of the PINDF3 code, which correctly computes bidirectional diffusion coefficients in pin geometry, was completed.

The major effort during this quarter was directed toward postanalysis of the as-built configurations of the Phase II GCFR critical assembly, including the effect of a steel reflector added around the blankets. The effects of the ZPR-9 steel structure surrounding the Phase I configuration were also studied. The Phase II work included studies of neutron balance and the core-center conversion ratio. Analyses of steam worths in Phase I and Phase II continued. Cross-section preparation was completed for the pending postanalysis of Phase III, which went critical on June 25, 1976. The prime accomplishment in methods development, was a revision to the GFE4 code to enable self-shielding of resonance cross sections for the structural materials.

7.1. PHASE I CGFR CRITICAL ASSEMBLY

7.1.1. Effects of ZPR-9 Structure Exterior to Blankets

Mappings of foil activations in the Phase I assembly indicated a considerable perturbation of blanket flux profiles due to reflection from the massive steel platform under the matrix and the "knees" forming the side support. As a preliminary step to evaluation of the reactivity effect of this structure, regions of steel were added around the blankets in the 2DB calculational model to approximately reproduce (in cylindrical representation) the empty matrix tubes plus the platform and knees surrounding the as-built configuration. The structural worth was found to be +0.50% $\Delta k/k$ using ten-group R-Z calculations. Further analysis is under way to determine the influence, if any, of this exterior structure on calculated core-center indices and steam zone worths. In addition, more exact x-y models will be calculated to match the machine geometry and to effect the different vertical and horizontal streaming characteristics for the plate loadings.

7.1.2. Steam Worth Calculations

In the previously reported postanalysis for the simulated steam flooding of the central zone in Phase II, the calculations included the effects of spectral degradation on the group-average cross sections of the zone for each of the three CH_2 flooding densities. Additional ten-group calculations were run with 2DB, wherein the CH_2 additions were modeled, but the medium cross sections were not reaveraged. The results of this less refined approach are compared in Fig. 7-1 with previous calculations and the experiments. As shown, the refined method, with cross-section reaveraging, gives good agreement with the positive measurements. The simpler approach, in which spectral effects are ignored, produces a grossly inaccurate curve which is negative until the hydrogen density approaches the steam equivalent of about 0.035 g/cm^3 in the coolant channels. The comparison thus illustrates the necessity of the refined approach as used for

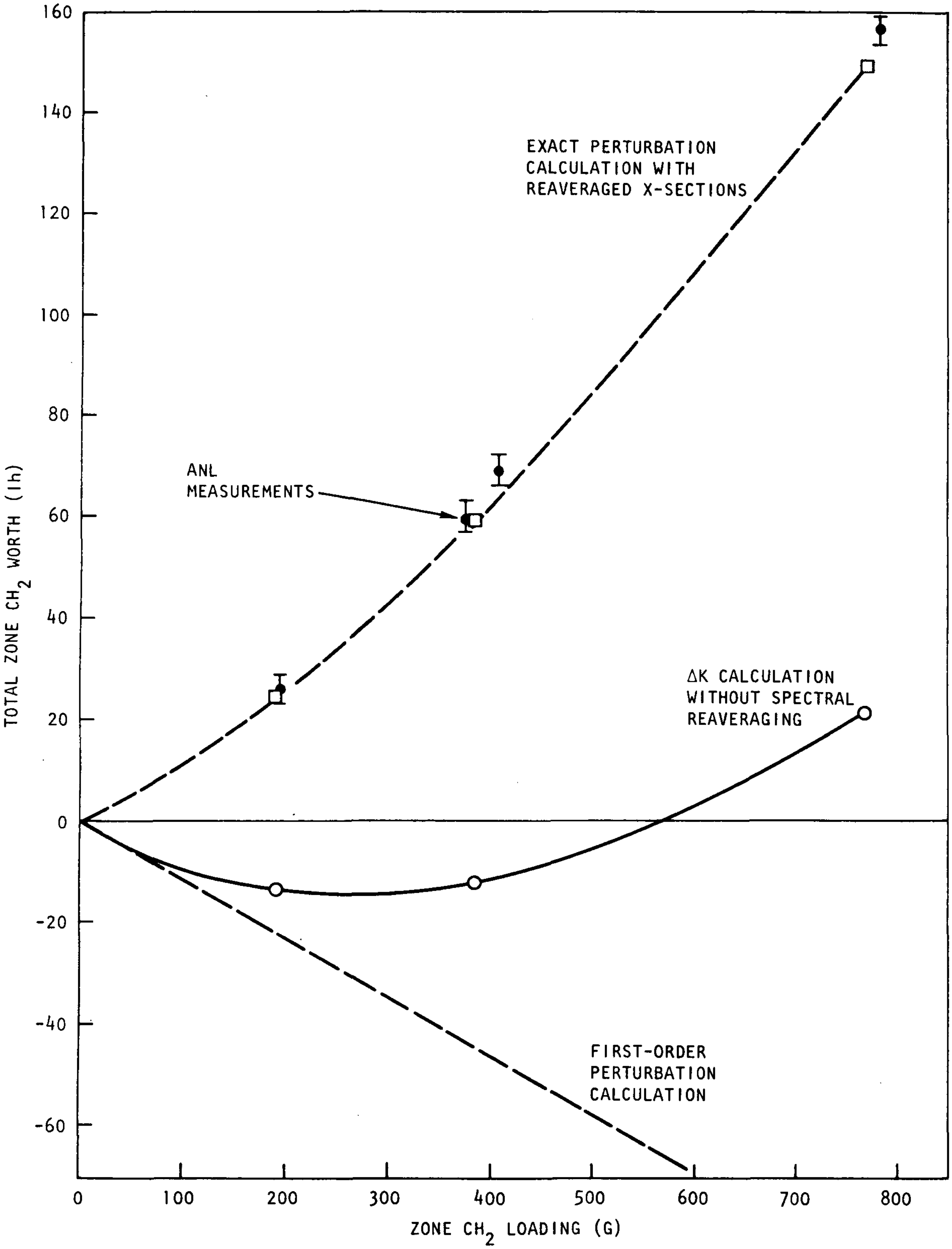

Fig. 7-1. Measured and calculated worths of steam flooding in central zone of Phase I GCFR critical assembly

analyses of these GCFR critical assembly studies as well as for past and present safety analyses carried out for GCFR designs. An interesting point of the Fig. 7-1 data is that the worth curve obtained by not reaveraging converges at zero density to the same slope (-115 Ih/kg) as that given by first-order perturbation theory using the same "dry-case" cross sections.

7.2. PHASE II GCFR CRITICAL ASSEMBLY POSTANALYSIS

7.2.1. Calculations for As-Built Phase II Configurations With and Without Reflector

Postanalysis of the Phase II assembly continued with the receipt of experimental results and configuration descriptions from ANL. A recent report (Ref. 7-1) gave the specifications for the two as-built critical configurations of Phase II, i.e., the cores with and without a steel reflector. Figure 7-2 illustrates the loading pattern for the unreflected case; the reflected version had steel blocks axially loaded for 15.24 cm beyond the axial blankets and for two rows of matrix tubes surrounding the radial blanket. Table 7-1 summarizes the experimental parameters and gives the results of 2DB k-calculations using ten-group, ENDF/B-4 cross sections. The calculational models included the steel of the empty matrix and of the ZPR-9 structure beyond the blankets or reflector loadings.

Comparison of the calculated and measured eigenvalues for the as-built configurations shows discrepancies of -0.32% and -0.30% $\Delta\rho$ for the unreflected and reflected cases, respectively. The reflector has little influence on the effective delayed-neutron parameters, but substantially affects the critical mass and global conversion ratio. These results show the consequence of a relatively high-leakage blanket and clearly demonstrate the importance of the blanket/reflector design for the GCFR demonstration plant. The close agreement between the calculated eigenvalues with and without the reflector indicates an adequate assessment of the reflector reactivity effect. An experimental evaluation of the reflector worth, derived during reflector construction and core size reduction, gave 1019 + 25 Ih. The preanalysis prediction was +1.04% $\Delta k/k$, or about 973 Ih.

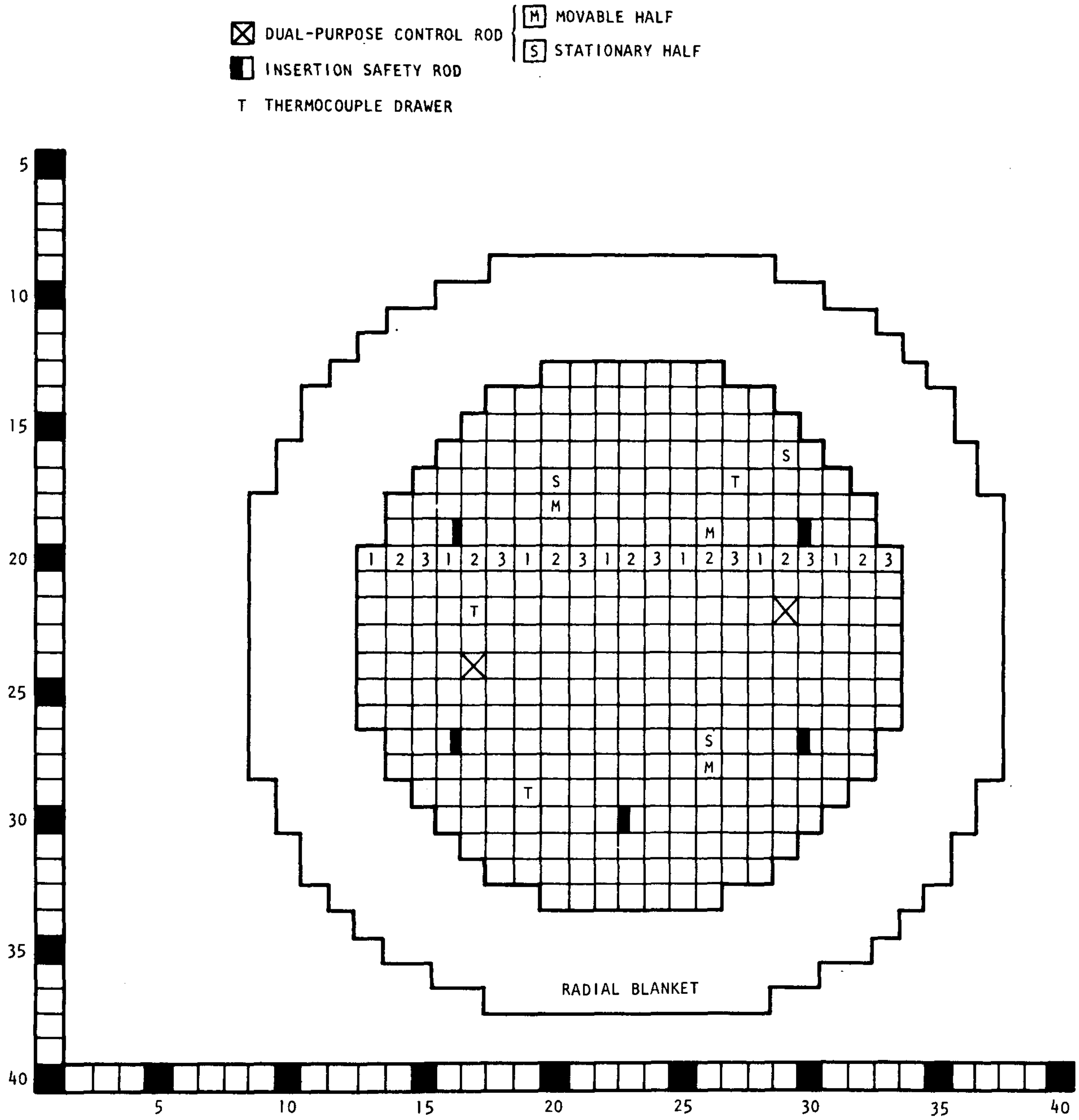

Fig. 7-2. Reference configuration for unreflected Phase II GCFR assembly on ZPR-9

TABLE 7-1
POSTANALYSIS OF PHASE II CRITICAL EXPERIMENT USING ANL AS-BUILT SPECIFICATIONS

Parameter	Unreflected Model	Reflected Model
Experimental results		
Fissile mass (kg Pu-239 + Pu-241)	622.74	∿594
Core volume (ℓ)	1300.26	1240.65
Average core radius (cm)	58.23	56.88
Average blanket Δr (cm)	24.53	25.88
Reflector thickness (cm)	--	13.46
As-built excess reactivity (Ih)	113 ± 1	66 ± 1
Experimental eigenvalue	1.012	1.0007
Calculated results		
Eigenvalue with streaming	0.99804	0.99767
Δρ for streaming	-0.01803	-0.01685
β-effective	0.003465	0.003464
Conversion factor (Ih/%)	934.14	935.54
Overall conversion ratio	1.043	1.190

7.2.2. Neutron Balance Calculation for the Reflected Assembly

The edit options of 2DB/PERT were used to prepare neutron balance tables, and the results from the calculation on the reflected Phase II configuration are presented in Table 7-2; similar computations have been made at ANL. Table 7-3 compares GA and ANL balance data and other calculated parameters for the reflected Phase II case.

The balance comparison reveals significantly higher captures in the GA calculations, predominantly because of softer spectra resulting from the GGC-5 generated cross sections. For the core, the difference is reflected in the lower k-infinity values calculated by GA methods. The long-standing discrepancy between ANL and GA calculations of leakage parameters is shown in Table 7-3. Thus, in the total balance, the absorption and leakage discrepancies are somewhat compensating, and the effective eigenvalues given by the different code systems are the same.

7.2.3. Point Conversion Ratio Calculation for the Unreflected Assembly

Calculations of the Phase II central point conversion ratio have been performed using the 2DB/PERT code. In addition, the U-238 capture/Pu-239 fission ratio has been calculated at several points throughout the reactor. Results of these calculations and comparison with ANL calculations and the experimental values (Ref. 7-2) are shown in Table 7-4 (recall that Phase II has a three-drawer unit cell, and therefore the measurement is a cell average over the three core drawers). These calculations were performed with the standard ten-group cross-section set and ENDF/B-IV data. The reactor was modeled without a reflector (to correspond to the actual measurement configuration), but with a matrix and matrix bed representation. Directional diffusion coefficients were used for all regions. Preliminary conclusions which can be drawn from this table are that the GA and ANL calculations are in very good agreement and both indicate that the 8% to 9% discrepancy in the breeding ratio calculation for the LMFBR critical assemblies apparently exists for the GCFR as well.

TABLE 7-2
NEUTRON BALANCE TABLE FOR AS-BUILT PHASE II ZPR-GCFR CRITICAL ASSEMBLY WITH REFLECTOR
(PERCENT OF TOTAL)

Region	Production	Fission	Absorption	Capture	Leakage
Core	95.36	32.55	61.39	28.84	33.97
Radial blanket	3.57	1.33	20.90	19.56	-17.32
Axial blanket	1.07	0.40	5.99	5.60	-4.93
Radial reflector	--	--	3.21	3.21	-3.21
Axial reflector	--	--	0.62	0.62	-0.62
Matrix	--	--	0.42	0.42	-0.42
Carriage	--	--	0.37	0.37	-0.37
Reactor total	100.00	34.28	92.90	58.62	7.10

TABLE 7-3
COMPARISON OF GA AND ANL CALCULATIONS FOR THE AS-BUILT PHASE II GCFR CRITICAL ASSEMBLY WITH REFLECTOR

	GA Calculation	ANL Calculation
Cross-section preparation codes	GGC-5/DTFX	MC^2-2/SDX
Number of broad groups	10	28
Assembly k_{eff} with streaming	0.9977	0.9994
$\Delta\rho$ due to streaming	-0.0169	-0.0151
Core center point k_∞	1.6027	1.6283
Core average k_∞	1.5533	1.5808
Neutron balance table (total production = 100)		
Core production	95.36	95.43
Fissions		
Core	32.55	32.53
Blankets	1.73	1.70
Captures		
Core	28.84	27.84
Blankets	25.16	23.98
Reflectors, structure	4.62	3.01
Leakage		
Core	33.97	35.06
Blankets	-22.25	-21.11
Reflectors, etc.	-4.62	-3.01
Reactor net	7.10	10.94

TABLE 7-4
POINT CONVERSION RATIO CALCULATIONS FOR UNREFLECTED PHASE II

	Location 1 Core Center	Location 2 Core Centerline	Location 3 Core - Blanket Interface
Drawers	S 22/22-24	S 22/22-24	S 33/22-24
Distance from axial midplane (cm)	0 to 5.08	55.88 to 60.96	0 to 5.08
c^{28}/f^{49}			
Measured	0.1196 ± 0.0008	0.1290 ± 0.0010	0.1355 ± 0.0015
ANL calculated	0.1301	0.1430	0.1446
ANL C/E	1.088	1.109	1.067
GA calculated	0.13277	0.14329	0.14621
GA C/E	1.110	1.111	1.079
Central point conversion ratio			
Measured	0.4712 ± 0.0139		
ANL calculated	0.5169		
ANL C/E	1.0970 ± 0.0324		
GA calculated	0.5216		
GA C/E	1.0990		

7.2.4. Analysis of Full-Assembly Steam Flooding

Results of the simulated steam flooding experiments in Phase II are compared with GA preanalysis predictions in Fig. 7-3. Postanalysis using as-built specifications was initiated, starting with cross-section generation for the flooded medium compositions involved in the final experimental program. Calculations with 2DB on the dry reference configuration for the flooding experiments accurately predicted the reactivity loss due to core size reduction (from the initial radius of 58.14 to 54.79 cm). However, a preliminary ten-group calculation for the 0.0175 g/cm^3 flooding case gave a worth of about \$3.12, which is 1.92 times the measured result [compared with a calculated/experimental (C/E) value of 1.62 by preanalysis for a larger radius]. Further investigation of methods is thus indicated, including the use of 28-group cross sections. In addition, improvements of resonance shielding treatments are under study; these calculations are continuing.

7.3. PHASE III GCFR CRITICAL ASSEMBLY

7.3.1. Preparations for Postanalysis

The generation of cross sections and adjustment factors for use in analyzing the Phase III experiments has been completed. Included in these preparations are numerous runs of GGC-5 for cross sections, DTFX transport theory slab calculations for cell spatial shielding factors, and PLADIF calculations for directional streaming modifiers. Distinct sets of data were obtained for each of the three core enrichment zones, the radial and axial blankets, and the core pin zone loading. Cross sections and factors were also obtained for a CH_2-flooded central zone with a plate and with pin loading cells.

7.3.2. Preliminary Critical Mass Value

The approach-to-critical was completed for Phase III, and the preliminary reports from ANL indicate a total core loading of 889 kg fissile plutonium. As requested by GA, core zones I and II contain 229 and 192

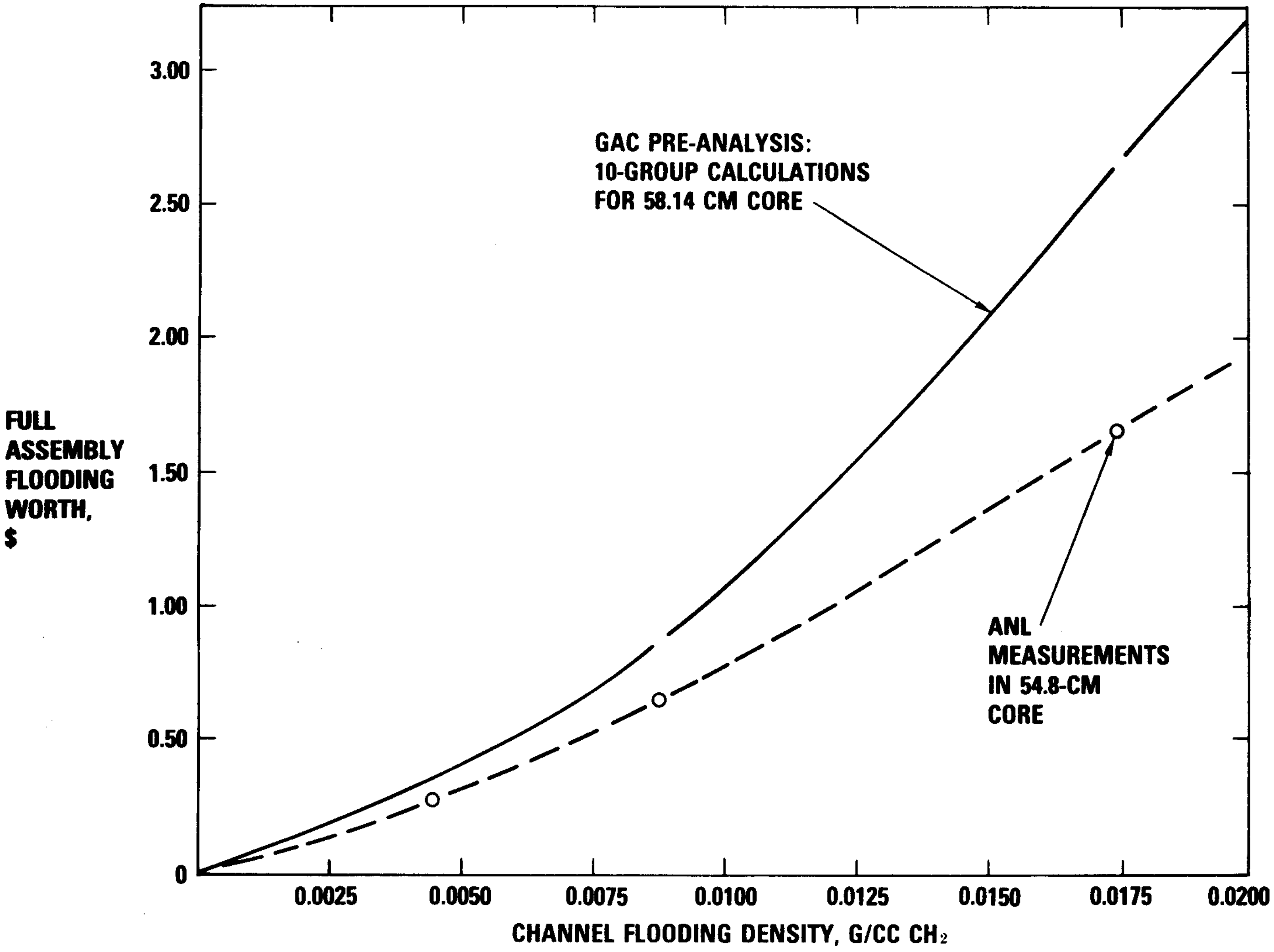

Fig. 7-3. Steam flooding experiments in reflected, unrodded Phase II GCFR critical assembly

drawers per half, respectively. For zone III, a criticality prediction of 100 drawers per half was provided by GA preanalysis (using Phase II based cross sections), whereas the initial as-built critical loading has 92 drawers per half in this zone.

7.4. METHODS DEVELOPMENT

7.4.1. Cross-Section Processing

The code GFE-4 is used to transcribe data on the ENDF/B-4 tapes to a library of 99-fine-group GAM-tape cross sections using specified within-group flux weightings. Development and testing was completed for a new GFE-4 weighting option using $[E(\sigma_t + \sigma_o)]^{-1}$ for the flux variation, which will provide self-shielding effects for resonances of important structural components. The high-speed GANDY subroutines which are needed when small σ_o values are to be used have been completed and checked out. Work on adding this weighting function to the resolved resonance region is under way, and a much more rigorous algorithm than was previously available in GFE-4 is being incorporated. When completed, this should remove most of the discrepancy between MC^2-2 and GGC-5 at the 25-keV iron scattering resonance.

The revised version of GFE-4 was used to prepare finite-dilution, 99-group cross sections for oxygen, chromium, iron, nickel, and U-238. Typical GCFR or critical assembly core compositions were used to specify the scatter-per-absorber atom (σ_t) employed in the weighting. Memos describing the new procedures and data sets were prepared.

7.4.2. GGC-5 Spectrum Code

The above-cited self-shielded data sets for oxygen, chromium, iron, nickel, and U-238 were tested in GGC-5 calculations for the homogeneous Phase I core composition, and the results were compared with past GGC-5 runs and ANL-supplied results of MC^2-2 calculations for this composition. The new finite-dilution data sets appreciably harden the neutron spectrum owing to the increased leakage caused by smaller, shielded-transport cross sections. These changes significantly reduce the differences between the GGC-5 and the MC^2-2 results. Running times for GGC-5 problems have been reduced by about 15% for the above cases by reworking the scratch file allocations and the input/output processes involved in preparing 99-group macroscopic transfer arrays.

A stand-alone version of the unresolved resonance cross section generation section of the MC^2-2 code was received from ANL. This code is similar to the GANDY section of GGC-5 except that it includes corrections for overlapping resonances. Comparative runs will be made to determine the importance of the "self-overlap" effects.

7.4.3. Diffusion Theory Codes (2DB)

Convergence acceleration in the 2DB/PERT code received attention with the addition of group rebalance schemes and Chebyshev extrapolation of fluxes rather than fission sources for certain classes of problems. The Chebyshev acceleration of fluxes for problems with up-scatter was significantly improved by assuming an eigenvalue range of $-\sigma$ to $+\sigma$ instead of 0 to σ for the outer problem (σ is the dominance ratio λ_1/λ_0).

A number of improved edit options were added to 2DB, in particular, the detailed printouts of the zone-wise production, capture, and leakage rates required for constructing neutron balance tables. Other edit possibilities are under investigation. Changes to allow multiple files for the input and output flux tapes were tested along with changes to include atom densities and masses on the flux output tape. Complete input instructions for 2DB/PERT were issued, and the code is in production use for critical assembly analysis.

REFERENCES

7-1. Robinson, W. R., and R. B. Pond, "Reactivity Worth of the Axial and Radial Reflector on the GCFR Phase II Assembly," Argonne National Laboratory Report ANL-RDP-50, April 1976.

7-2. Bohn, E. M., Argonne National Laboratory, private communication.

8. SHIELDING REQUIREMENTS (189a No. SU008)

The purpose of the shielding task is to verify the adequacy of the methods and data (physics and engineering) for the design of GCFR shields and to evaluate the effectiveness of various shield configurations. In addition, this task coordinates and provides liaison with the analytical and experimental GCFR shielding activities at ORNL.

During the last quarter, analyses were performed for the lower, wraparound, and grid plate shields. One-dimensional calculations for the lower and wraparound shields were carried out to determine a revised configuration which would enable the prestressed concrete reactor vessel (PCRV) liner fluence limit and the PCRV concrete heating limit to be met. The model for the revised configuration was provided to ORNL so that another iteration of detailed two-dimensional calculations could be performed. Calculations were performed for the fluence and the neutron-induced embrittlement in the grid plate using the current B_4C grid plate shield design. Recent damage function data from Ref. 8-1 were utilized to estimate the time required to reach specific residual ductility levels in the grid plate.

Grid plate shielding studies were continued during this quarter to obtain a revised design which satisfied the grid plate design criterion requiring a minimum residual ductility of 10% based on total elongation. Analysis of a revised upper axial shield was also initiated; the results of the grid plate shield calculations provided a source for bootstrapping two-dimensional transport calculations.

8.1. GRID PLATE SHIELD DESIGN

The last quarterly report (Ref. 8-2) presented the results of a detailed analysis of the current grid plate shield design. A two-dimensional S_N calculation for the maximum neutron-induced embrittlement of the grid plate was performed, and energy-dependent damage functions from Ref. 8-1 were used to compute fluence limits to attain specific levels of residual ductility in the grid plate. The results indicated that the grid plate design criterion of 10% residual total elongation (RTE) would be reached in 48 effective-power years (EPY = years at 0.8 load factor) and 12 EPY for the nominal and the conservative case, respectively. The nominal case is based on the nominal fluence limit with no margin on the fluence calculation. the conservative case is based on the lower-bound fluence limit (2σ confidence level), and a factor of two margin is placed on the calculated fluence.

During this quarter, efforts were directed toward determining an improved design which would assure a 30-EPY grid plate design life based on the conservative case. A number of two-dimensional S_N calculations were performed to determine the relative effectiveness of various grid plate shield configurations and to gain a better understanding of streaming effects. Successive perturbations of these configurations provided an understanding of the problem, enabling further optimization of subsequent configurations. The relative merits of B_4C and $ZrH_{1.6}$ or a combination of the two materials as shield materials were also examined. The control element shield requirement was also investigated. This is important because the control rod guide tube further reduces the available helium flow area and therefore the area available for shielding. During these studies, close communication was maintained with cognizant fuel element designers so that an improved design satisfying the conflicting requirements of shielding and helium flow could be determined.

8.1.1. Transport Calculations

The methods, computer programs, and data used to perform the neutron transport calculations are described in Ref. 8-2. The R-Z model is a cylindrical grid plate equivalent cell at the location of the central fuel element and extends from 30 cm above the core - axial blanket interface to the top of the grid plate. The two-dimensional boundary source at 30 cm above the core - blanket interface was obtained from a one-dimensional calculation. All calculations used a 10-group structure (9 fast, 1 thermal) and P_3 anisotropic scattering. Initial calculations used a forward-peaked, asymmetric quadrature set with 76 forward and 24 backward angles. Subsequent calculations used a symmetric S_8 quadrature set (48 angles) which was found to yield satisfactory results with a considerable reduction in computation time.

8.1.2. Neutron Damage Calculation

Energy-dependent damage functions from Ref. 8-1 were used to compute nominal and lower-bound fluence limits for 5% and 10% uniform elongation (UE) for annealed type 316 stainless steel irradiated at 385°C. An exception was the generation of the upper-bound damage functions for use with the $ZrH_{1.6}$ shield. The Ref. 8-1 upper-bound damage functions for 5% and 10% UE at 385°C are unrealistically high over the thermal energy range, apparently owing to a lack of thermal reactor data in the spectra used as input to the damage function unfolding procedure. This is of negligible consequence with the B_4C shield because the thermal flux is insignificant; however, since a large thermal flux can result with $ZrH_{1.6}$ shielding alone, the effect can be significant. Therefore, the Ref. 8-1 upper-bound damage functions at 496°C were used to estimate the thermal group damage response functions with $ZrH_{1.6}$. This yields a conservative fluence limit since neutron-induced embrittlement due to helium production increases with increasing temperature in the 385° to 496°C range.

Based on data from Figs. 70 and 72 of Ref. 8-3, the following equation was used to evaluate the fluence limit for 10% RTE ($\phi t_{10,TE}$) from the computed fluence limits for 5% residual uniform elongation (RUE) ($\phi t_{5,UE}$) and 10% RUE ($\phi t_{10,UE}$):

$$\phi t_{10,TE} = \phi t_{5,UE} + 1/3\ (\phi t_{5,UE} - \phi t_{10,UE}) \quad .$$

This assumes that

10% RTE = 6.67% RUE

and the ductility varies linearly with fluence between 10% RUE and 5% RUE.

Figure 8-1 is a plot of the GGC-5 (Ref. 8-4) generated spectrum in a B_4C grid plate shield region and the Ref. 8-1 upper-bound damage function solution for 5% UE for 316 stainless steel irradiated at 385°C. It is evident that moderate-energy neutrons (i.e., $1.0 \text{ KeV} < E < 0.1 \text{ MeV}$) can significantly contribute to the damage response. The computer program DMGFCN (Ref. 8-2) was used to collapse the fine-group damage functions with the GGC-5 generated spectra to obtain the desired broad-group damage functions.

8.1.3. Results

The analyses compared the relative effectiveness of various shield configurations and materials. Figure 8-2 shows R-Z models of the shield geometries studied, i.e., the reference shield and four modified configurations. Table 8-1 summarizes the dimension and material specifications for the shield sections which comprise the 12 major cases studied. The location of each shield section is indicated by number in Fig. 8-2. The following two types of homogenized shield material regions were assumed:

1. 90% C + B_4C by volume (20% natural boron by weight in C + B_4C); 10% 316 stainless steel by volume.

2. 90% $ZrH_{1.6}$ by volume; 10% 316 stainless steel by volume.

Table 8-2 summarizes the results of the grid plate damage calculations for the 12 cases.

The total flux energing from the axial blanket, which is the source for the grid plate shield region, is 5.0×10^{14} n/cm^2-sec, with 42% of the total having $E > 0.1$ MeV. The flux is highly forward peaked above 1.0 MeV,

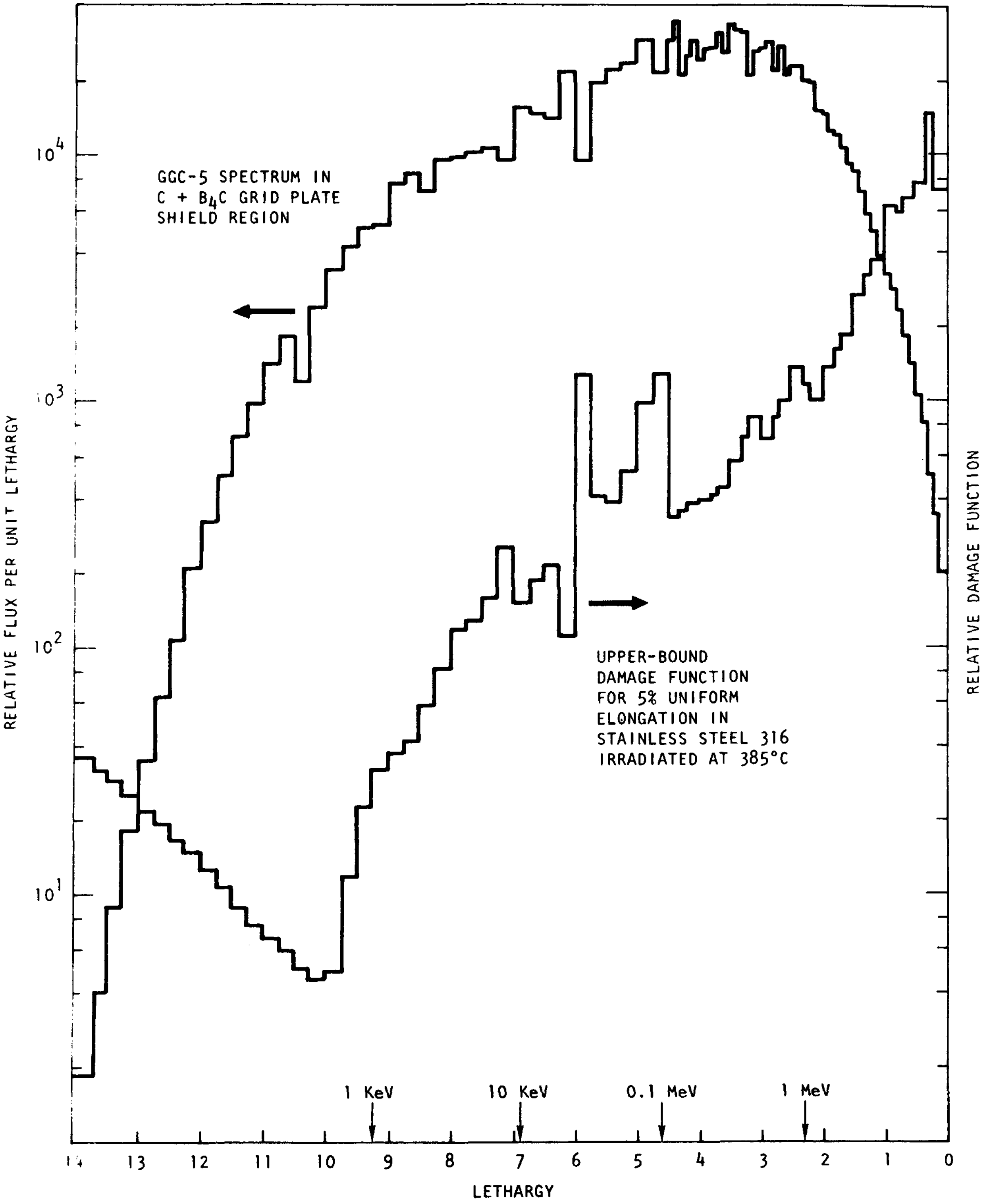

Fig. 8-1. Spectrum and damage function in C + B_4C grid plate shield region

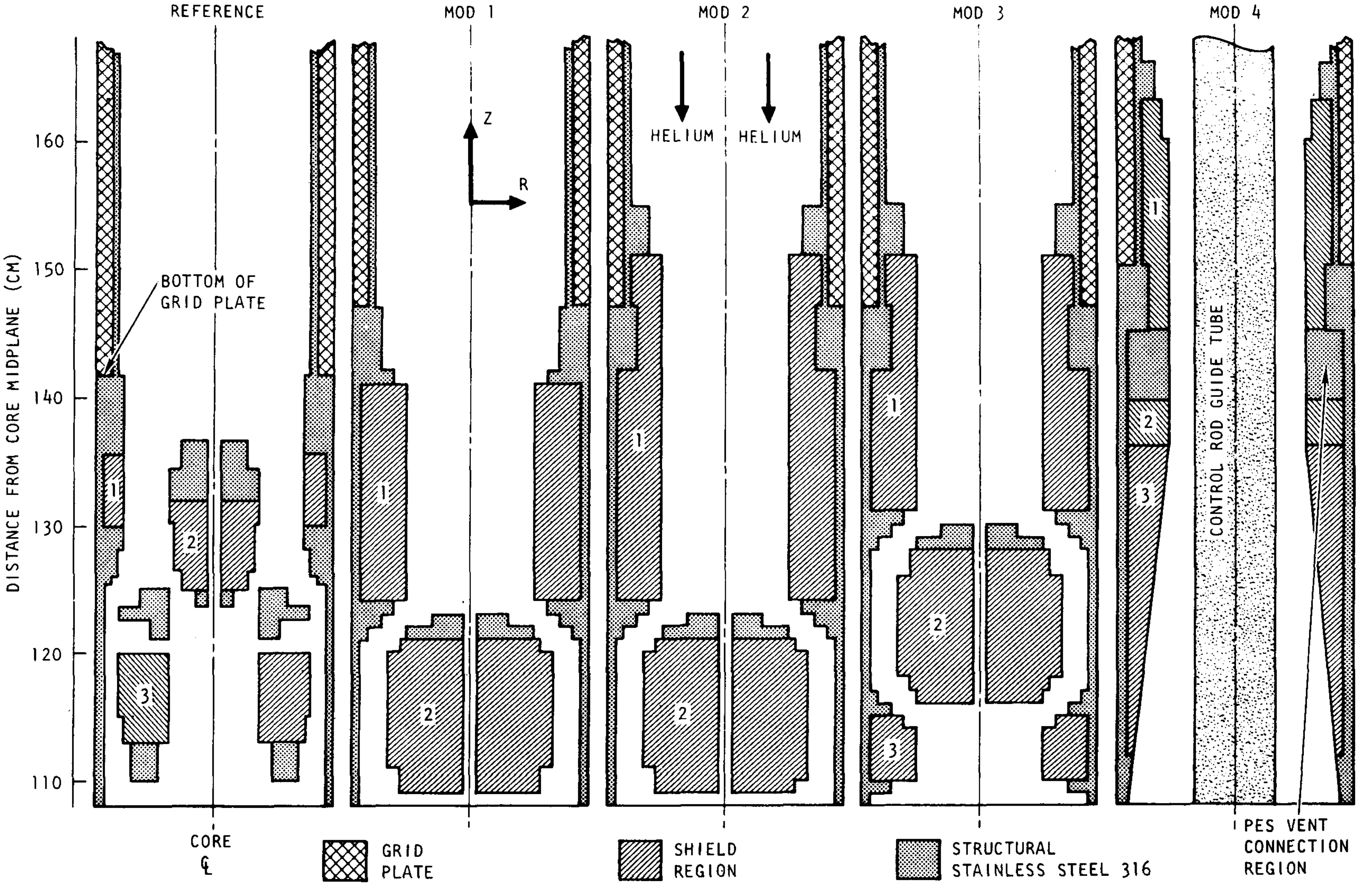

Fig. 8-2. R-Z models of grid plate shield configurations

TABLE 8-1
GRID PLATE SHIELDING SPECIFICATIONS FOR MAJOR CASES STUDIED

	Case											
	1	2	3	4	5	6	7	8	9	10	11	12
Configuration (see Fig. 8-2)	Ref	Ref	Ref	Ref	MOD 1	MOD 2	MOD 2	MOD 3	Ref	MOD 1	MOD 4	MOD 4
Core element length change(a) (cm)	0	0	0	0	5.4	5.4	0	5.4	25.4	25.4	18.4	8.4
Shield section 1												
Material	C + B_4C(b)	C + B_4C	$ZrH_{1.6}$	$ZrH_{1.6}$	C + B_4C	C + B_4C	C + B_4C	C + B_4C	C + B_4C	C + B_4C	C + B_4C	C + B_4C
Maximum o.d. (cm)	17.2	17.2	17.2	17.2	17.2	17.2	17.2	17.2	17.2	17.2	15.0	15.0
Minimum i.d. (cm)	14.2	14.2	14.2	14.2	10.0	10.0	10.0	10.0	14.0	11.0	11.0	11.0
Length (cm)	5.7	5.7	5.7	5.7	17.0	26.8	26.8	19.8	34.0	46.0	18.0	18.0
Shield section 2												
Material	C + B_4C	C + B_4C	$ZrH_{1.6}$	NA(c)	C + B_4C	C + B_4C	NA(c)	C + B_4C	NA(c)	NA(c)	C + B_4C	C + B_4C
Maximum o.d. (cm)	7.0	7.0	7.0	NA(c)	13.0	13.0	NA(c)	13.0	NA(c)	NA(c)	17.2	17.2
Minimum i.d. (cm)	1.0	1.0	1.0	NA(c)	1.0	1.0	NA(c)	1.0	NA(c)	NA(c)	11.0	11.0
Length (cm)	7.0	7.0	7.0	NA(c)	12.0	12.0	NA(c)	12.0	NA(c)	NA(c)	14.0	4.0
Shield section 3												
Material	C + B_4C	C + B_4C	$ZrH_{1.6}$	$ZrH_{1.6}$	NA(c)	NA(c)	NA(c)	C + B_4C	C + B_4C	NA(c)	C + B_4C	$ZrH_{1.6}$
Maximum o.d. (cm)	15.0	15.0	15.0	15.0	NA(c)	NA(c)	NA(c)	17.2	14.0	NA(c)	17.2	17.2
Minimum i.d. (cm)	7.0	7.0	7.0	7.0	NA(c)	NA(c)	NA(c)	10.0	10.0	NA(c)	11.0	11.0
Length (cm)	7.0	7.0	7.0	7.0	NA(c)	NA(c)	NA(c)	5.0	12.0	NA(c)	27.0	27.0

(a) Relative to reference fuel element design (case 1).

(b) B_4C in carbon; 20% natural boron by weight in mixture.

(c) Shield section removed or not applicable.

TABLE 8-2
SUMMARY OF GRID PLATE DAMAGE CALCULATIONS FOR MAJOR CASES STUDIED

	Case											
	1	2	3	4	5	6	7	8	9	10	11	12
Configuration (see Fig. 8-2)	Ref	Ref	Ref	Ref	MOD 1	MOD 2	MOD 2	MOD 3	Ref	MOD 1	MOD 4	MOD 4
Shield material	$C + B_4C$	$C + B_4C$	$ZrH_{1.6}$	$ZrH_{1.6}$	$C + B_4C$	$C + B_4C$	$C + B_4C$	$C + B_4C$	$C + B_4C$	$C + B_4C$	$C + B_4C$	$C + B_4C$ and $ZrH_{1.6}$
Quadrature	100 angles, asymmetric(a)	S_8, symmetric(b)	100 angles, asymmetric	100 angles, asymmetric	S_8, symmetric	S_8, symmetric	S_8, symmetric	S_8, symmetric	S_8, symmetric	S_8, symmetric	S_8, symmetric	S_8, symmetric
Total flux $[(n/cm^2\text{-sec}) \times 10^{-13}]$	4.1	4.1	3.2	3.1	3.1	1.7	2.0	1.7	2.6	2.1	1.6	1.7
Total fluence $[(n/cm^2) \times 10^{-22}]$	3.1	3.1	2.5	2.4	2.4	1.3	1.5	1.3	2.0	1.6	1.2	1.3
% damage response due to												
E > 1.0 MeV flux	4	4	3	4	2	3	6	4	4	2	5	5
1.0 MeV > E > 0.1 MeV flux	61	60	47	48	57	51	52	48	53	52	53	54
0.1 MeV > E > 1.0 KeV flux	35	36	29	26	39	46	42	48	43	46	42	41
E < 2.38 eV flux	∿0	∿0	21	22	∿0	∿0	∿0	∿0	∿0	∿0	∿0	∿0
Fluence limit for 10% RTE $[(n/cm^2) \times 10^{-22}]$												
Nominal	4.9	5.1	6.2	6.2	6.0	7.3	5.9	7.1	6.3	7.0	5.7	5.3
Lower bound	2.5	2.6	2.4	2.4	2.8	3.3	2.9	3.3	3.0	3.2	2.8	2.7
Time to reach 10% RTE (EPY)(c)												
Nominal(d)	48	50	76	78	76	169	118	165	97	130		121
Conservative(e)	12	13	15	15	18	38	29	38	23	30	35	30
Core element length change (cm)(f)	0	0	0	0	5.4	5.4	0	5.4	25.4	25.4	18.4	8.4

(a) Asymmetric quadrature (76 forward and 24 backward angles).

(b) S_8 symmetric quadrature.

(c) EPY = years at 0.8 load factor.

(d) Based on nominal fluence limit with no margin on calculated fluence.

(e) Based on upper-bound fluence limit with a factor of 2 margin on calculated fluence.

(f) Relative to reference fuel element design (case 1).

but the angular peaking decreases with decreasing energy, and only moderate peaking is exhibited near 10 KeV.

For the reference shield configuration with C + B_4C shield material (case 1), the total flux incident on the bottom surface of the grid plate (for all cases studied, the maximum damage occurs at the grid plate bottom surface) was calculated to be 4.1×10^{13} n/cm^2-sec, or a total 30-EPY fluence of 3.1×10^{22} n/cm^2. The spectrum impinging on the grid plate was found to be very similar to that emerging from the axial blanket, with about 90% of the flux between 1.0 KeV and 1.0 MeV and 37% of the total having $E > 0.1$ MeV. The lower-bound fluence limit for 10% RTE for this spectrum is 2.5×10^{22} n/cm^2. The conservative estimate of the time required to reach 10% RTE is 12 yr at a load factor of 0.8; the nominal estimate is 48 yr. A factor of two difference between the conservative and the nominal estimate results from the assumed margin in the calculated fluence. The other factor of two difference is due to the uncertainty of the energy dependence of the damage functions. Based on the nominal damage function, 75% of the damage response is due to fast ($E > 0.1$ MeV) flux, and 25% of the damage is due to the moderate energy flux between 1.0 KeV and 0.1 MeV. Based on the upper-bound damage function, 65% of the damage response is due to the fast flux, and the fraction attributed to the moderate energy flux increases to 35%, which is caused by the greater uncertainty of the energy dependence of the damage function over the lower-energy range. Neutrons with $E > 1.0$ MeV contribute only 4% to 5% of the total damage. It is evident that it is important to shield for the total flux consisting primarily of scattering neutrons rather than just the high-energy streaming component. The thermal flux remains small with the C + B_4C shield, and therefore helium production contributes negligible to grid plate embrittlement.

For the initial calculation with the reference C + B_4C shield (case 1), an asymmetric quadrature with 76 forward angles and 24 backward angles was used to enhance the accuracy of the treatment of the axially streaming neutrons. The calculation was repeated using a symmetric S_8 quadrature (case 2), and the results agreed within a few percent for a flux below about 1.0 MeV. For a flux above 1.0 MeV, which contributes little to grid plate damage, the difference was less than 20%. It was concluded that the S_8 calculation provided not only an accurate treatment of the streaming over the important spectral range, but also a considerable reduction in computation time.

The calculation was then performed for the reference shield with $ZrH_{1.6}$ replacing the $C + B_4C$ (case 3). This resulted in a 20% reduction in total fluence, from 3.1×10^{22} n/cm^2 to 2.5×10^{22} n/cm^2, and a similar increase in the conservative estimate of the time to reach 10% RTE, from 12 to 15 EPY. The lower-bound fluence limit for 10% RTE, however, remained about the same because the decrease in the damaging effectiveness of the spectrum due to increased moderation with $ZrH_{1.6}$ is compensated for by an increase in the damaging effectiveness due to a large thermal flux. The thermal flux for this case contributes over 20% of the damage response.

The next calculation used $ZrH_{1.6}$ as the shield material for the reference configuration, and the central shield section 2 was removed (case 4). This resulted in a slight decrease in the total fluence at the bottom of the grid plate compared with the case in which the central shield was included (case 3). This indicates that the central shield provides a scattering center for neutrons which would otherwise stream upward through the grid plate.

One-dimensional slab calculations indicated that 16 cm of $C + B_4C$ shield was required to attain the 10% RTE at 30 yr. Modified configuration 1 (case 5) represents a two-piece shield which provides about this amount of material. The time to reach 10% RTE is 18 EPY, which indicates the overall effect of streaming in the grid plate shield region.

Examination of the angular flux near the bottom of the grid plate revealed a reasonably isotropic flux distribution over much of the spectral range which contributes the majority of the damage (i.e., 1.0 KeV to 1.0

MeV). This indicated that as much shield material as possible should be placed in the local vicinity of maximum damage response. The shielding effectiveness of such locally placed material is not reduced by streaming effects. Modified configuration 2 is identical to modified configuration 1 except that the shield section attached to the duct wall (section 1) is extended several centimeters above the bottom of the grid plate to provide a locally protective collar. Comparing case 6 with case 5 (Table 8-2), it is seen that this thin collar increases the time necessary to reach 10% RTE by more than a factor of two, i.e., from 18 to 38 EPY.

Case 7 is for modified configuration 2 in which the central shield section located just above the flow manifold (section 2) was removed. The result is a 24% decrease in the time required to reach 10% RTE, from 38 to 29 EPY. The central shield is thus far less effective than the collar shield placed locally at the bottom of the grid plate.

Modified configuration 3 is similar to configuration 2 except that the shield section attached to the duct wall is divided into two pieces in a manner which complicates the streaming paths. Comparing case 8 for configuration 3 with case 6 for configuration 2 (Table 8-2), it is seen that both cases result in 38 EPY to reach 10% RTE. This further substantiates that direct ray streaming between the shield section and to the grid plate is not as important as the global or integrated effect of streaming of the diffuse, scattered flux component.

Cases 9 and 10 are lengthened versions of the reference configuration and modified configuration 1, respectively. Clearly, substantial lengthening of the fuel element (at least 25.4 cm) is required in order to attain the 30-EPY design life with either of these grid plate shield configurations.

From the results presented thus far, it is clear that modified configuration 2 with the central shield removed (case 7) (Tables 8-1 and 8-2) is the best alternative because the shield material is most strategically placed. However, three mechanical considerations preclude the incorporation of this modified shield without some alterations. These are

1. An acceptable helium pressure drop across the shield region.
2. Compatibility with the control element design.
3. Compatibility with the PES design.

The most effective placement of the shield material is attachment to the duct wall above and below the grid plate bottom. This scheme tends to maximize the shield volume at the expense of the helium flow area. The control rod drive tube, a hexagonal duct 6 cm across the flat, further reduces the available flow area in the control elements. Since it is desirable that the shield components for the 27 control elements be identical to those for the fuel elements, the flow requirements are determined by the control element. It should be noted that some additional grid plate shielding is provided by the control rods in the control elements since the absorber section of a withdrawn control rod extends from about 15 cm above the core - axial blanket interface to above the bottom of the grid plate.

Modified configuration 4 (Fig. 8-2) represents a compromise between the mechanical considerations and the shielding requirements. Note the gradual taper of the shield below the grid plate, which tends to minimize the expansion pressure loss. The shielding attached to the duct wall is thinner for configuration 4 than for configurations 1 to 3 to allow more flow area between the shielding and the control rod drive tube. Finally, note the gap in the shielding just below the grid plate which is for the PES vent connection; gases leave the fuel and blanket elements through vent connections to passages drilled through the grid plate.

Two cases were considered for configuration 4. The first used only C + B_4C as the shield material (case 11), and the second used a combination of C + B_4C and $ZrH_{1.6}$ shield sections (case 12). For case 12, the $ZrH_{1.6}$ is contained in the lower tapered section of the shield, and the C + B_4C is in the collar adjacent to the grid plate. The times required to reach 10%

RTE are 35 and 30 yr for cases 11 and 12, respectively. Approximately 4 cm of fuel element length is saved by employing both shield materials.

Evaluation of the results indicates that an improved understanding has been gained of the effect of streaming in the GCFR on the shielding of vital out-of-core structural components. The neutron source external to the blanket is primarily in the 1.0 KeV to 1.0 MeV energy range, where the flux is sufficiently diffuse so that direct ray streaming is not a dominant effect. Global, or integral, streaming of the scattered flux is important, however, and reduces the effectiveness of shielding. These studies show that where possible, an integumental shield configuration is the most effective means of protecting critical locations. For the grid plate, this means shielding of the grid plate and not the source emerging from the blanket. It is better to allow the flux to stream and disperse above the grid plate than to be intercepted and scattered to the grid plate. Allowing the neutrons to stream results in a larger source for the upper cavity. However, permanent shielding may be locally applied to protect the PCRV liner and the ducts leading to the circulators at less expense than additional grid plate shielding. This is because the grid plate shielding must be replaced with the fuel element. Modified configuration 4 represents an improved design which assures a grid plate design life of 30 EPY.

8.2. REVISED UPPER AXIAL SHIELD

Analysis of a revised upper axial shield was initiated during this quarter. Since the two-dimensional transport calculations were completed near the end of this quarter, this section only briefly reviews the revised upper axial shield and the model developed for calculations. The reference configuration of the upper axial shield is described in Ref. 8-5. As explained in Ref. 8-5, the upper shield provides radiation attenuation to protect the bottom portions of the reactor cavity closure, limit neutron streaming in the coolant inlet cross ducts and the subsequent activation of the main helium circulators, and limit the rate of heat deposition in the concrete above the outlet coolant ducts. The configuration of the reference shield shown in Fig. 8-3 is a central disc which forms the inner boundary

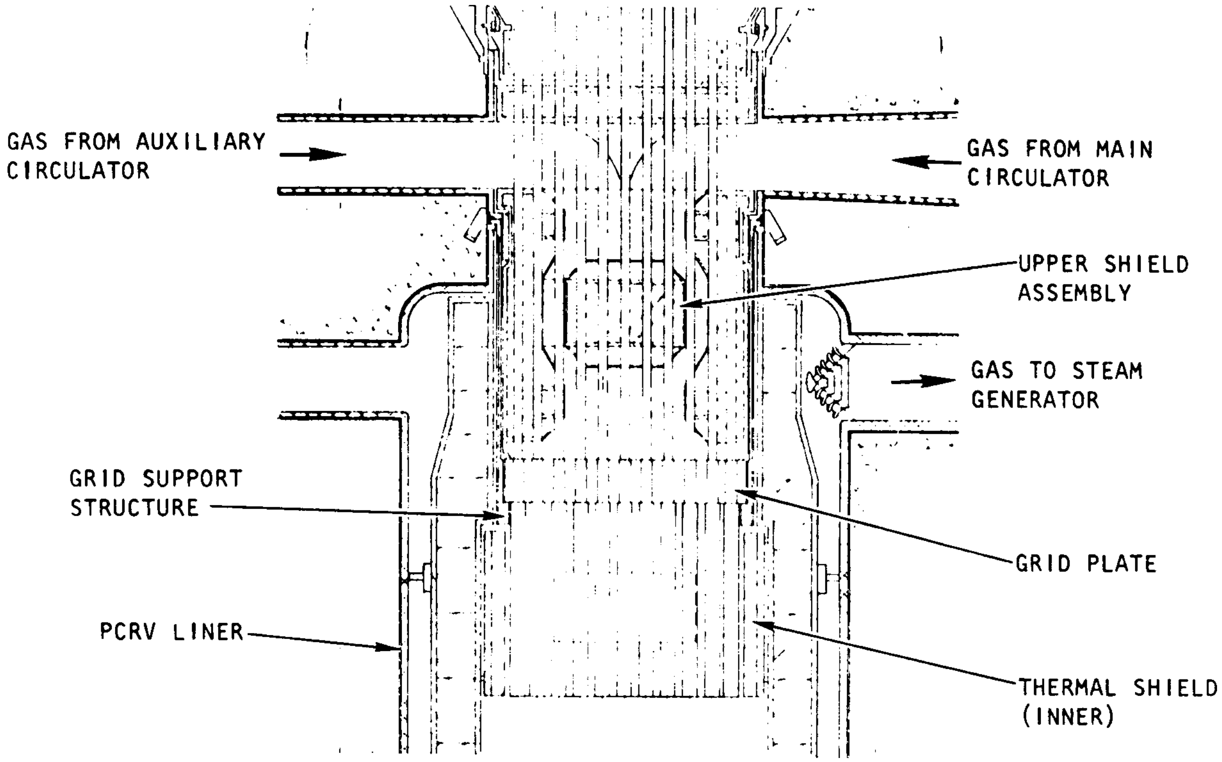

Fig. 8-3. Configuration of axisymmetric shield

of the annular coolant passage and an annular toroid with an o.d. of about 12 ft which forms the outer boundary of the coolant passage. These two shield masses are made of graphite and stainless steel and have a minimum thickness of 2 ft along any ray emanating from the upper surface of the grid plate. The graphite and steel are contained in a welded steel shell which is vented for pressure equalization. The flow passage is contoured to assure at least two scattering collisions for neutrons escaping through the duct and to minimize flow area variations and thus ensure minimum pressure losses in the transition from the three main helium cross ducts (and the three auxiliary loop ducts) to the contoured annulus. The third component of the upper shield is a flat disc-shaped section covering the lower face of the reactor cavity closure.

The reference upper shield assembly is penetrated by 265 mechanism guide tubes. To accommodate these tubes, the graphite components of the shield are fitted in welded steel shells containing holes for the guide tubes. The weight of the centrally located member of the upper shield assembly is supported by radially oriented vanes attached to the surrounding annular shield member. The entire weight of the assembly is carried by the grid plate support structure; the weight of the disc-shaped assembly is carried by the reactor cavity closure to which it is attached.

The revised upper plenum region is shown in Fig. 8-4. In this revised configuration, the fuel element locking mechanism extensions and the central plug of the upper shield assembly have been removed. This revised configuration provides the physical advantage of reducing the pressure drop in this region and is less difficult to analyze, but it still requires extensive two- and three-dimensional transport calculations. The shield materials shown in Fig. 8-4 are stainless steel and graphite. B_4C may be required in critical areas which may be revealed in the initial two-dimensional calculations. The seven penetrations from above are access ports for the fuel locking mechanism. Each sleeve contains shielding material plugs which remain in place during reactor operation.

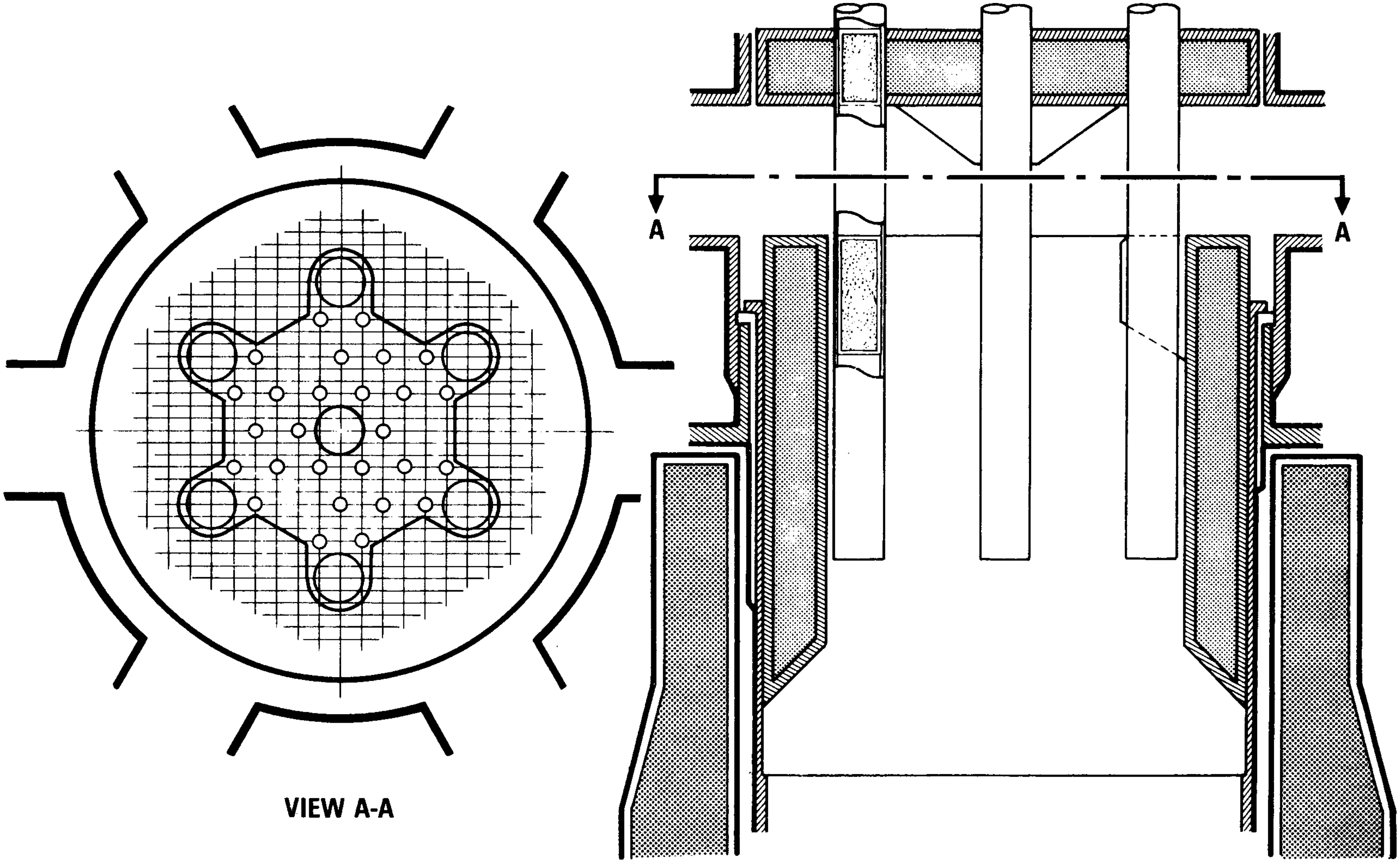

VIEW A-A

Fig. 8-4. Revised upper axial shield for 300-MW(e) GCFR

Given the proposed upper shield assembly shown in Fig. 8-4, the next step in the analysis is to develop a model for calculational purposes. The model initially used is shown in R-Z two-dimensional geometry in Fig. 8-5. Only the central penetration of the seven locking mechanism penetrations can be handled, and the radial shield at the lower level of the inlet ducts must be made continuous. At the level of the inlet ducts, the total area open to the six ducts is about equal to the closed area of the cavity wall between the ducts. Therefore, an open configuration was used at the level of the ducts in the R-Z calculations in order to obtain the upper bound on the streaming neutron flux source for use in subsequent duct streaming calculations.

A source is needed for the neutrons which stream up through the grid plate openings into the upper cavity plenum. This source was generated from one of the grid plate shielding configurations described in Section 8.1. The actual configuration used was close to MOD 4 of Fig. 8-2 without the control rod guide tube. Starting with the S_8 cylindrical angular fluxes at each radial interval along the top of the grid plate, the fluxes were averaged in space at each angle for a central angular source (only the fluxes directed toward the upper axial shield are needed for the surface source). Since using the central flux as a constant surface source along the entire radius at the top of the grid plate would have been much too conservative for the upper axial shielding studies, a radial dependence of the source was approximated. This was done by scaling the variation in the neutron flux calculated by ORNL at the level of the grid plate in their two-dimensional calculations of the GCFR reactor cavity. In all, eight scale factors were used between $r = 0$ and $r = 212.5$ cm.

The transport calculations were performed in symmetric S_8 angular quadrature and P_3 anisotropic scattering. The problem is also being calculated in two parts: part one covers the transport between $z = 0$ in Fig. 8-5 to $z = 420$ cm; part two, to be calculated during the next quarter, will cover the region between $z \sim 400$ cm to $z \sim 600$ cm. When completed, the neutron spectrum at critical areas in the upper plenum will be used as

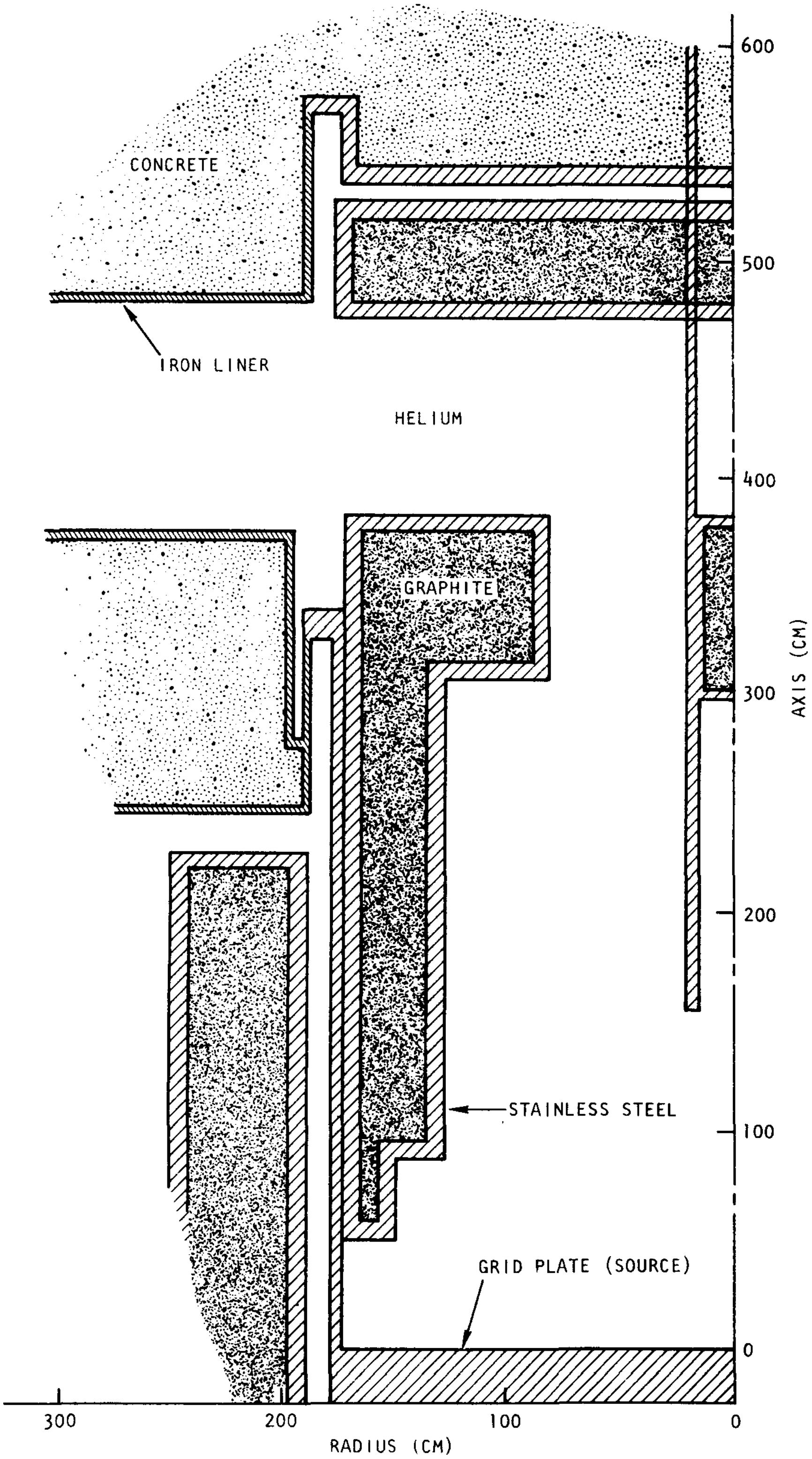

Fig. 8-5. Configuration of upper axial shield

a source for approximate one-dimensional calculations for local optimum shielding studies. More details will be presented in a future topical report.

REFERENCES

8-1. Nuclear Systems Materials Handbook, v. I, II, Hanford Engineering Development Laboratory (TID-2666).

8-2. "Gas-Cooled Fast Breeder Reactor Quarterly Progress Report for the Period February 1, 1976 Through April 30, 1976," ERDA Report GA-A13868, General Atomic, May 31, 1976.

8-3. Soo, P., "Type 304 and 316 Stainless Steel Data for High Temperature Design," USAEC Report WARD-3045T2C-3, Westinghouse Electric, November 1972.

8-4. Mathews, D. R., et al., "GGC-5, A Computer Program for Calculating Neutron Spectra and Group Constants," Gulf General Atomic, private data.

8-5. "300-MW(e) Gas-Cooled Fast Breeder Reactor Demonstration Plant," General Atomic Report GA-A13045, July 15, 1974.

9. REACTOR SYSTEMS ENGINEERING (189a No. SU019)

Under this task, reactor system development activities are being defined and carried out; analytical methods and models applicable to the assessment of thermal-hydraulic performance of the GCFR reactor core are being developed and utilized to define operating strategies; methods and materials behavior models are being evaluated to assess the capability of the PCRV internal structures to serve as a postaccident fuel containment (PAFC); and GCFR plant control systems are being developed, including establishment of the interface requirements between these control systems, the plant protection system, the operational protection system, and the plant operator.

9.1. CORE THERMAL-HYDRAULIC PERFORMANCE

Activities in this subtask are devoted to the development of accurate computer models for the evaluation of core thermal-hydraulic performance. In addition, the requirements for and methods of core temperature monitoring are being investigated.

During the previous quarter, the document describing the computer code GACOOL was prepared. During this quarter, documentation efforts continued and refinements in the computer program models were made; some additional results are presented. The evaluation of alternate core temperature monitoring systems was also continued, and the functional design criteria for the system underwent a thorough review.

9.1.1. GACOOL Development

GACOOL development activities continued, although at a lower level than during previous quarters. Slight improvements which streamline the calculational logic sequence were made to GACOOL, and it was extensively used to verify its accuracy and versatility over a wide range of boundary conditions. The main thrust of the development activity was twofold: (1) to verify the modeling of the radial blanket described in Ref. 9-1 and (2) to assure that the pressure drop model included all the effects necessary to correctly model the core over the 25% to 100% flow range. The primary consideration for the pressure drop model was to include the correct functional expressions for Reynolds number dependence for all pressure drop components.

The radial blanket element model in GACOOL was verified by hand calculations and extensive comparisons with the results of the more detailed COBRA subchannel analysis program. The hot spot factors used by GACOOL in its average channel approach should be different from those used in a subchannel analysis to account for the edge channel spacing and the actual flow distribution within the fuel rod bundle. Comparison shows that the channel and film hot spot factors used in GACOOL should be about 10% higher for the radial blanket than those used in COBRA. The blanket pressure drop calculated by GACOOL is close to that calculated by COBRA.

The previously constant fuel rod spacer pressure loss coefficient was modified to make it a function of Reynolds number; this function is based on preliminary data from the EIR. An investigation was initiated on the possibility of making GACOOL operational for low flow ranges, where laminar flow prevails and buoyancy effects may become important. This included a literature search for better heat transfer and friction factor data for laminar flow in tube bundles for the higher pitch/diameter (p/d) ratios encountered in the new, lower pressure drop core configuration (Ref. 9-2).

If GACOOL is modified to allow investigation of low flow conditions, a great deal of interaction with subchannel analysis programs will be required to provide information to and assure the accuracy of GACOOL under these conditions. However, such a modification would be of great utility since GACOOL has advantages over subchannel analysis programs because it is able to treat the entire reactor, core, and radial blanket and to consider the effects of orificing.

The HOLS1Z subroutine, which is based on American Society of Mechanical Engineers (ASME) orifice correlations and used in GACOOL to size orifices and predict orifice performance, was modified so that it can be used as an independent program. This program is being used to determine whether extrapolations beyond the range of the ASME correlations are valid and to study orifice performance at low flows.

9.1.2. Preliminary Core Performance and Orificing Results

Preliminary power-to-flow studies for the 300-MW(e) core over the 25% to 100% power range were completed using GACOOL. These studies were performed for the lower pressure drop core configuration described in Ref. 9-2. The design values for this core are

Pressure drop = 0.155 MPa (22.5 psi)
Reactor inlet pressure = 8.88 MPa (1288 psia)
Reactor inlet temperature = 351°C (663°F)
Reactor outlet temperature = 544°C (1011°F)
Coolant mass flow rate = 2.99×10^6 kg/hr (6.59×10^6 lbm/hr)

These studies included analysis of the core and radial blanket regions and the effects of orificing. Reynolds number dependence for the friction factor and the heat transfer multipliers in the roughened region of the core were based on preliminary EIR data. A Reynolds number dependence was also assumed for fuel rod spacer loss coefficient using EIR data.

The GACOOL off-design-point option which allows core performance to be determined for the case of specified orifice sizes and a specified maximum midwall hot spot cladding temperature was used to perform the power-to-flow studies. At off-design-point power levels, this option calculates the pressure drop, total core flow rate, and in turn, the upper limit of the power-to-flow ratio necessary to cool the core consistent with the specified cladding limit. This is accomplished by first determining the flow rate required to cool each element based on inlet conditions, element power level, and a midwall cladding hot spot temperature limit. The pressure drop is then calculated for each element, and the maximum pressure drop is determined. After determining the maximum pressure drop, the flow in all other elements is adjusted to match the maximum pressure drop.

Figure 9-1(a) shows a plot of the power-to-flow ratio as a function of power for a 700°C (1292°F) maximum cladding midwall hot spot temperature while holding the reactor inlet conditions constant at their design values. Under these conditions, the power-to-flow ratio is 1.0 down to approximately 40% power and reduces to 0.984 at 30% power. This analysis of the entire core with constant inlet conditions agrees closely with the subchannel power-to-flow analysis of one fuel element with constant reactor inlet conditions reported in Ref. 9-3.

Although the above study of the power-to-flow ratio as a function of power is of interest, holding the reactor inlet conditions constant at the design value is arbitrary and does not really represent plant part-load performance. Of greater importance is whether the core will be adequately cooled [maximum cladding midwall hot spot temperature of 700°C (1292°F)] under off-design conditions using the actual reactor inlet and flow conditions produced by the plant control system. Table 9-1 shows the inlet conditions obtained from the plant performance program COMB for one possible plant control system in which the main turbine throttle pressure and the steam generator outlet temperature and pressure are controlled.

Using the reactor inlet conditions shown in Table 9-1 and a maximum cladding midwall hot spot temperature of 700°C (1292°F), GACOOL analyses were used to predict the minimum flow required to cool the core. The helium flow actually being circulated through the primary system as determined by the plant control system programmed in COMB is 2% to 7% greater than the minimum flow required to cool the core over the 25% to 100% power range. These two cases are expressed as power-to-flow ratio versus power level in Fig. 9-1(b). The plant part-load operating line in Fig. 9-1(b) is determined by COMB for the present control system, whereas the limiting line is based on the minimum required coolant flow as calculated by GACOOL.

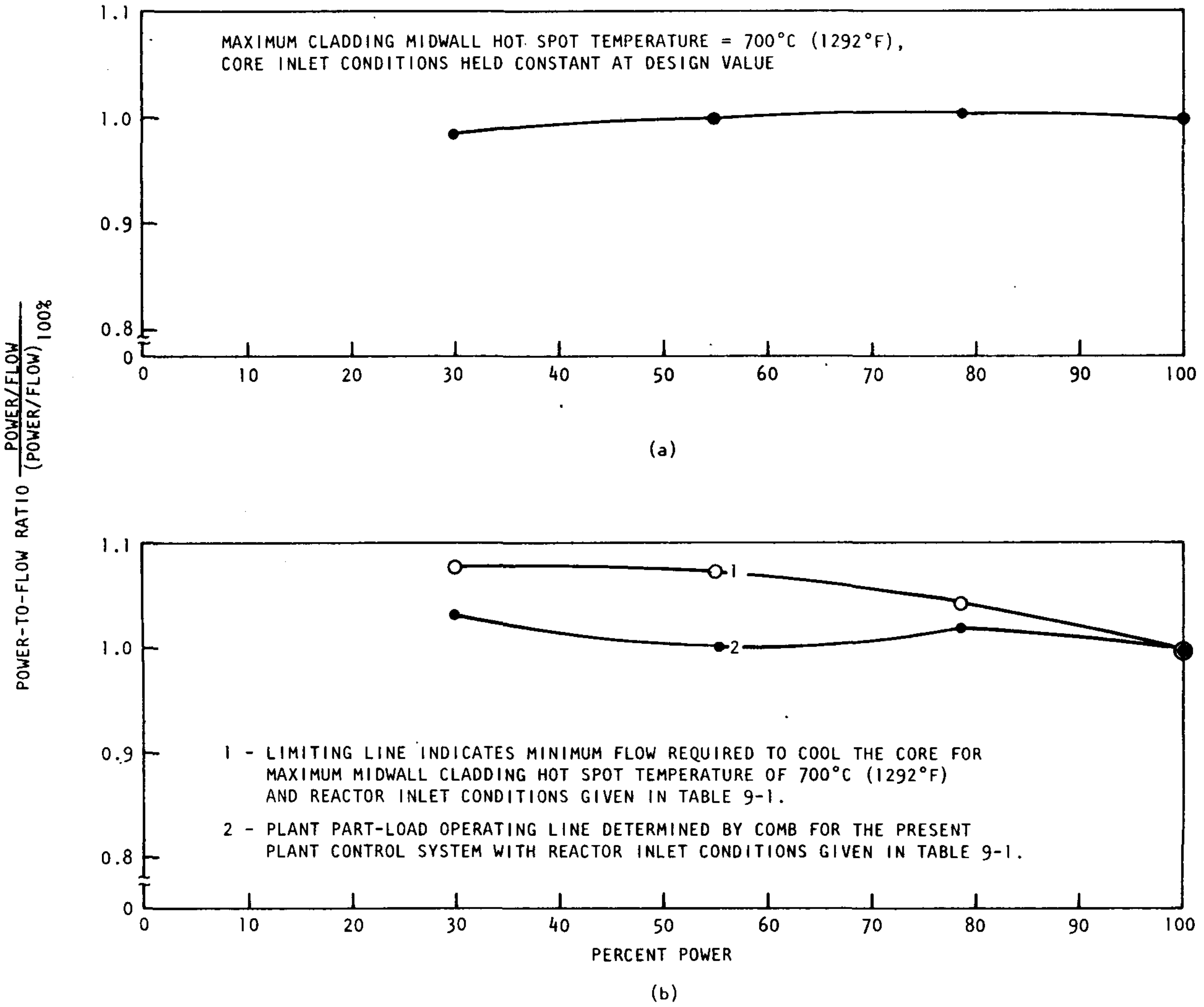

Fig. 9-1. Variation of power-to-flow ratio with percent of full power

TABLE 9-1
PART-LOAD REACTOR INLET CONDITIONS FOR PRESENT GCFR PLANT CONTROL SYSTEM(a)

Reactor Power Level (% of Design)	Reactor Inlet Temperature [°C (°F)]	Reactor Inlet Pressure [MPa (psia)]
100	350.8 (663.4)	8.881 (1288.1)
78.6	337.1 (638.8)	8.778 (1273.2)
55.2	328.3 (623.0)	8.702 (1262.2)
29.7	316.8 (602.2)	8.642 (1253.5)

(a)Main turbine throttle pressure and steam generator outlet pressure and temperature are controlled.

Power-to-flow ratio versus power level is used to show the minimum core cooling requirements and plant operating line because it is generally the calculated value which will be used to signal that the plant is operating within acceptable limits. However, Fig. 9-2 shows the minimum core cooling requirements and plant operating line in terms of power versus flow. From this figure, it is more easily seen that for a given power level, the current plant control system delivers a larger flow than is required to cool the core, and conversely, at a given flow rate, the core power level of the plant operating line is less than the core power which the given flow rate will cool.

Based on the above power-to-flow information, the following general trends can be considered requirements for the plant control system: (1) since the power-to-flow ratio required to maintain the maximum midwall cladding temperature at 700°C (1292°F) is close to 1.0 when the reactor inlet conditions are held constant at the design value, if the reactor inlet temperature increases from the design value or remains constant, the power-to-flow ratio produced by the plant control system must be less than 1.0; (2) a power-to-flow ratio slightly greater than 1.0 is allowable under part-load conditions if the reactor inlet temperature is reduced enough to maintain the maximum cladding hot spot temperature at or below limit, as the current control system does.

Core pressure drop characteristics as a function of flow rate were also determined, but such information is a function of reactor inlet condition, cladding temperature limit, and reactor power level. Figure 9-3 shows the core pressure drop characteristics as a function of flow rate, holding the reactor inlet conditions constant at the design value of 8.881 MPa (1288.1 psia) and 350.8°C (663.4°F) and varying the power level to maintain a maximum cladding temperature of 700°C (1292°F). The reactor power level for the given flow rate is also shown in Fig. 9-3. The core pressure drop characteristics for the operating and limiting lines shown in Fig. 9-1(b) also closely approximate Fig. 9-3. This is true even through for a given flow rate these cases would have slightly different power levels and average core conditions than those used in determining Fig. 9-3.

1 - LIMITING LINE INDICATES MINIMUM FLOW REQUIRED TO COOL THE CORE FOR MAXIMUM MIDWALL CLADDING HOT SPOT TEMPERATURE OF 700°C (1292°F) AND REACTOR INLET CONDITIONS GIVEN IN TABLE 9-1.

2 - PLANT PART-LOAD OPERATING LINE DETERMINED BY COMB FOR THE PRESENT PLANT CONTROL SYSTEM WITH REACTOR INLET CONDITIONS GIVEN IN TABLE 9-1.

3 - POWER VS FLOW FOR MAXIMUM MIDWALL CLADDING HOT SPOT TEMPERATURE OF 700°C (1292°F) AND REACTOR INLET CONDITIONS HELD CONSTANT AT DESIGN VALUES.

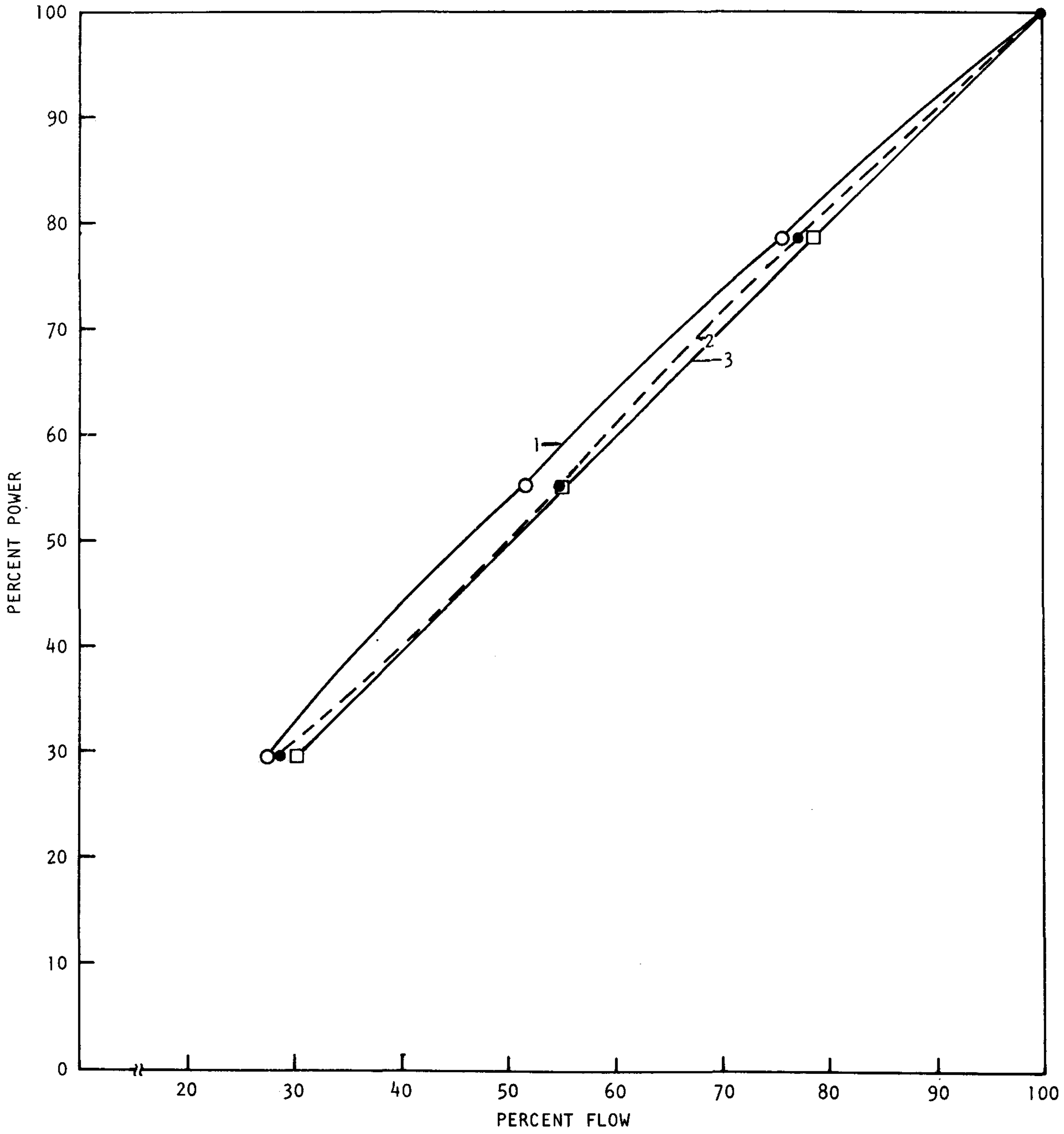

Fig. 9-2. Reactor power vs flow

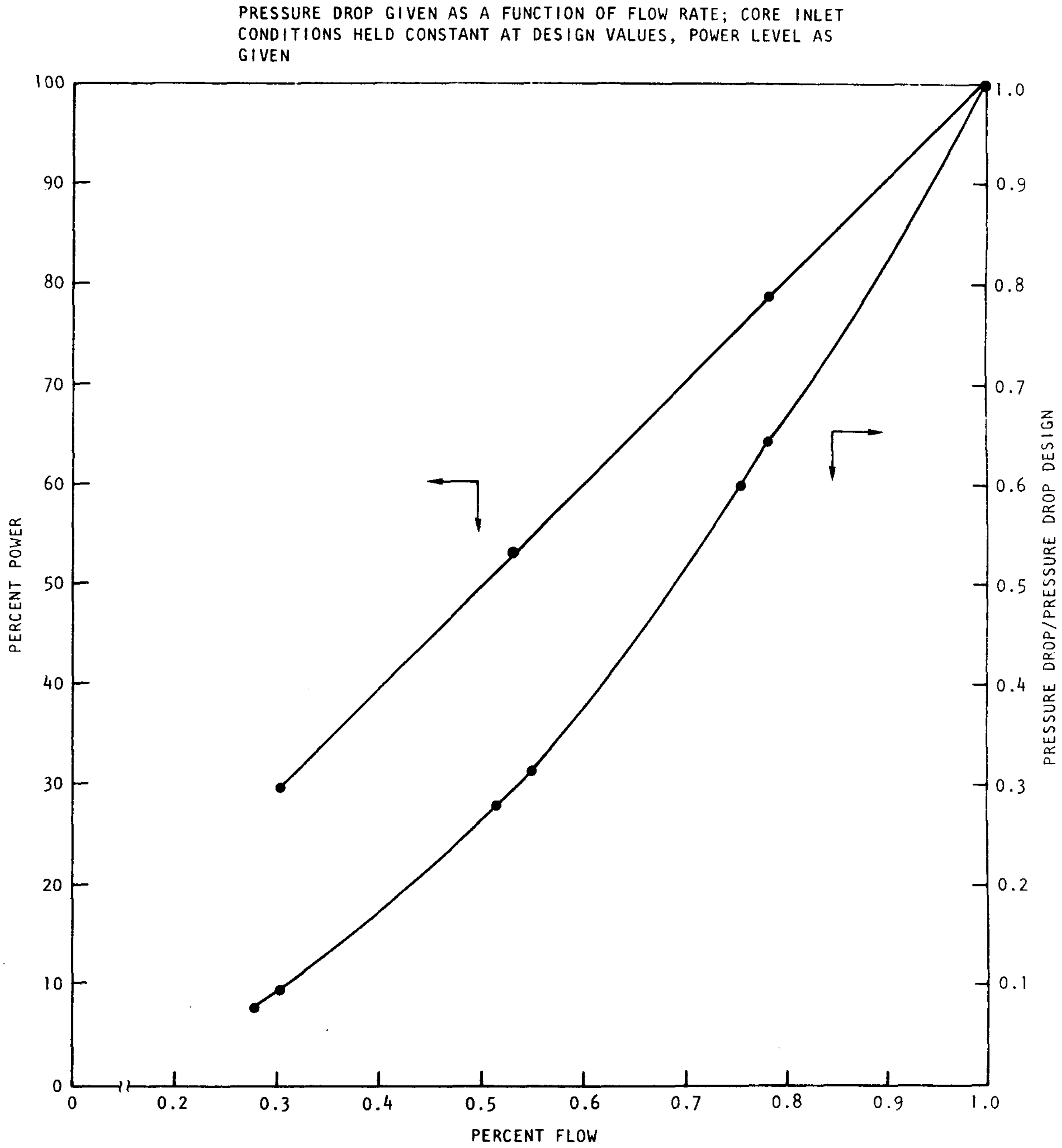

Fig. 9-3. Core pressure drop characteristics as a function of flow rate

The power levels at given flow rates for all three cases can be seen in Fig. 9-2.

During the power-to-flow studies, the total end-of-cycle reactor flow distribution to the core and radial blanket as a function of power level was also determined. Table 9-2 gives the flow distribution information for the following cases: (1) the maximum cladding midwall hot spot temperature of 700°C (1292°F), holding reactor inlet conditions constant at the design value, and (2) the limiting line in Fig. 9-1(b), which is based on a cladding limit of 700°C (1292°F) and the reactor inlet conditions shown in Table 9-1. As can be seen, the flow distribution is nearly identical for both cases, with total reactor flow in the radial blanket varying from 6% at 100% power to 6.2% at 30% power. This information was not determined for the plant operating line, although it should virtually be the same as for the limiting line.

Another independent investigation conducted during the quarter has shown that orificing uncertainties will primarily arise from uncertainties associated with orifice calibrations (i.e., flow coefficient) as opposed to dimensional tolerance uncertainties. An investigation is under way to estimate orifice performance uncertainties based on typical ASME orifice calibration data for inclusion in core hot spot/hot channel factor calculations.

9.1.3. Alternate Core Temperature Monitoring Concepts

Consideration of alternate core temperature monitoring concepts included a thorough review of the functional design requirements for this system. This review took into account overall reactor system requirements, precedents established within the light water reactor (LWR) industry, and the approach adopted for the Clinch River breeder reactor. The goal was to establish the design criteria for the GCFR temperature monitoring system independent of any specific hardware design considerations. One of the primary motivations for this review was the close relationship between the core temperature monitoring requirements and the core element locking

TABLE 9-2
TOTAL END-OF-CYCLE REACTOR FLOW DISTRIBUTION AS A FUNCTION OF POWER LEVEL

Reactor Power Level (% of Design)	Radial Blanket Flow/ Total Reactor Flow	
	Case 1[(a)]	Case 2[(b)]
100	0.0600	0.0600
78.6	0.0615	0.0614
55.2	0.0615	0.0614
29.7	0.0620	0.0619

(a) Case 1: cladding temperature limit = 700°C (1292°F), reactor inlet conditions held constant at the design value.

(b) Case 2: cladding temperature limit = 700°C (1292°F), reactor inlet conditions given in Table 9-1.

mechanism concept, which is also undergoing reevaluation. Resolution of some of the significant questions surrounding core temperature monitoring may have a significant impact on the design configuration in the upper plenum and the fuel element.

The primary conclusion of this review is that the requirement for having core temperature monitoring is well founded. The system will allow on-line verification of whole-core thermal-hydraulic performance and will provide the special assurance necessary for a first-of-a-kind plant that predicted and actual performance are in close agreement. An additional function for the system which has been discussed in previous quarterly reports is verification of fuel and orifice loading patterns. Although the temperature monitoring system may be able to at least partially perform this task, there are other simpler methods (visual or mechanical) which may be utilized; this function, therefore, does not constitute a basis for requiring individual element temperature monitoring. The core performance verification function is compatible with the precedents established within the LWR and the current approach adopted for the Clinch River breeder reactor. With this temperature monitoring philosophy, the system does not perform a safety function. Outlet temperature readings will be displayed, and abnormal readings will annunciate alarms; however, by design, the system will not have the capability of initiating any automatic plant protective action.

Other alternate core temperature monitoring activities were studied during this quarter. An overall feasibility study of infrared temperature monitoring in a GCFR was planned and the work initiated. This short-term, low-budget study is intended to evaluate the overall feasibility of this concept and thus contribute to a development decision during the next quarter. The initial studies deal with the optics-related problems of viewing the core element outlet temperatures from the bottom of the outlet plenum. The second phase of the study will focus on questions of mechanical and materials feasibility. Of particular concern are the problems of provision of a pressure-bearing window penetration in the PCRV through which an optical signal may be transmitted and the durability of an optical system in the GCFR temperature, flow, and radiation environment. The final phase is intended to estimate overall system accuracy and performance.

In addition to infrared techniques, the development status of noise power thermometry has been under review for potential application in the GCFR. A workshop sponsored by the Instrumentation and Controls Division of ORNL was attended for this purpose. Because noise power thermometers are similar to thermocouples in size and need for electrical leads, they could conceivably be substituted for thermocouples in the current reference design with little or no impact on the overall design effort. The decision to do so would be based on demonstrated performance in planned irradiation programs at ORNL and elsewhere. Developments of noise power thermometers will continue to be monitored.

9.2. POSTACCIDENT FUEL CONTAINMENT

The objectives of this subtask are (1) to assess the capability of the structures within the reactor cavity of the PCRV to contain the core debris associated with a postulated core melt-down arising from a series of very low probability failures and (2) to define the analytical and experimental studies needed to verify the thermal and chemical processes associated with core debris containment.

In the previous quarterly report (Ref. 9-1), results were reported for the study of upward heat removal by natural helium circulation at depressurized conditions. During this quarter, work has been completed on two downward heat removal cases: (1) with a variable thermal barrier thickness and (2) without helium and cavity liner cooling.

9.2.1. Effect of Thermal Barrier Thickness on Downward Heat Removal

The heat transfer behavior of the lower thermal shield using a variable thermal barrier thickness was studied under core melt-down conditions. A full core melt-down of the 300-MW(e) plant was assumed for the present analysis. Owing to ANL's findings (Ref. 9-4) that molten fuel flows freely in gaps larger than 2 mm (0.08 in.), the preshield was assumed to float atop the molten fuel layer at the time of accident initiation. Penetration of molten fuel into gaps in the lower main shield was not considered. For further simplicity, the top steel casing of the lower main shield was assumed to be combined with the preshield. The other initial and boundary conditions were the same as those of the previous analysis (Ref. 9-5). Numerical results were obtained using the NUTAP computer program.

The temperature history of the cavity liner versus the thermal barrier (SiO_2) thickness is shown in Fig. 9-4. It can be seen that for thinner thermal barriers, higher liner temperatures are reached within a shorter time. The effects of varying thermal barrier thickness on maximum temperatures and heat fluxes is more clearly seen in Fig. 9-5. Figure 9-5 shows the maximum temperature of the lower graphite-steel interface. Without a thermal barrier, the maximum temperature is 630°C (1166°F), and it starts rising with increased thermal barrier thickness until it reaches the melting point of steel when the thermal barrier thickness exceeds 50 mm (2 in.). From Fig. 9-5 it can be seen that the maximum liner temperature as well as the maximum downward heat flux increase with decreasing thermal barrier thickness. The upward heat flux, also shown in Fig. 9-5, is not strongly affected.

From the results of this analysis, it appears advantageous to have a thinner thermal barrier in order that the lower shield temperature can be kept low enough so that the steel casing below the graphite blocks do not melt; thus, floatation of graphite blocks could be prevented by fastening them to the steel casing. However, the maximum temperature and the maximum heat flux at the cavity liner will increase, which could require an increase of the liner cooling capacity. In addition, the possibility of liner buckling due to excessive thermal stresses must be considered. The thickness of the thermal barrier must be adequate to serve as a good thermal insulator during normal plant operating conditions. Thus, to satisfy these opposing requirements, an optimum thermal barrier thickness must be determined by a detailed design of the lower shield and cavity liner. The present analysis has shown that to satisfy PAFC considerations, a thermal

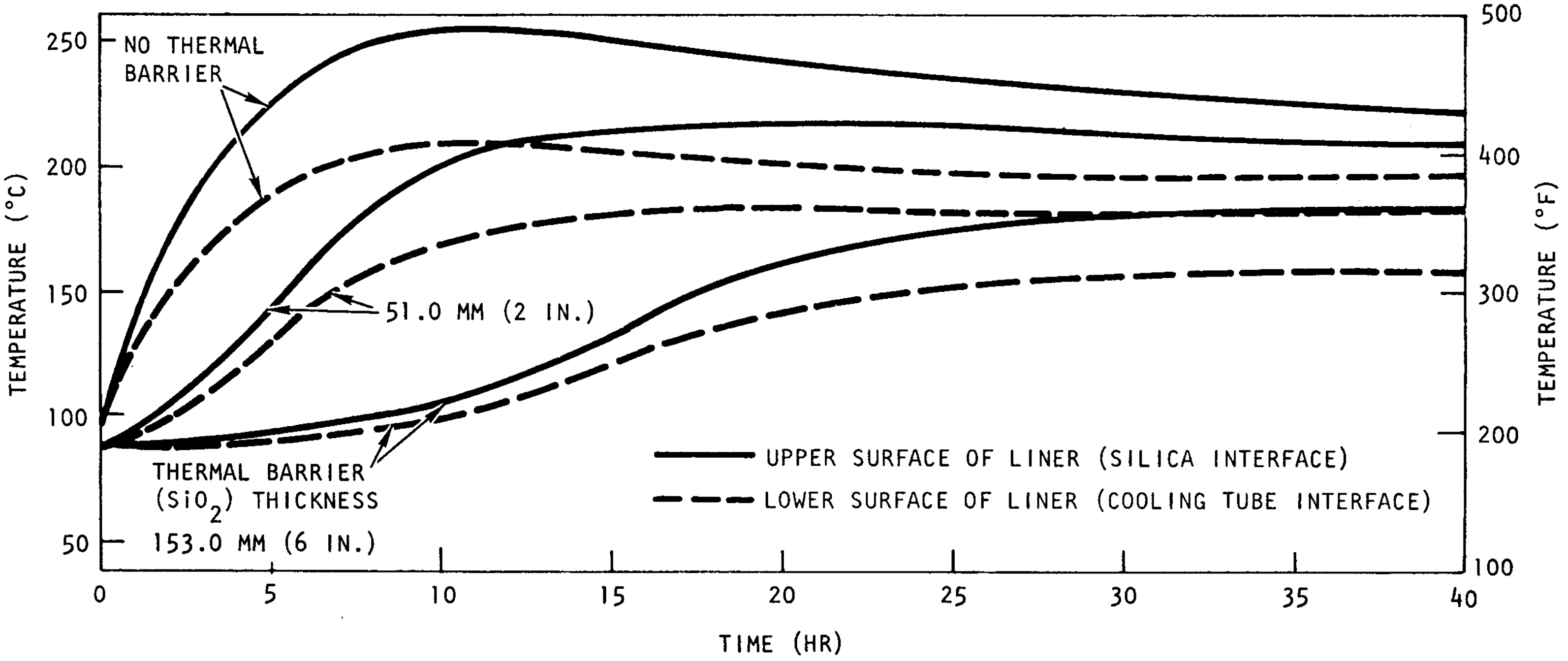

Fig. 9-4. Temperature history for cavity liner vs thermal barrier (SiO_2) thickness

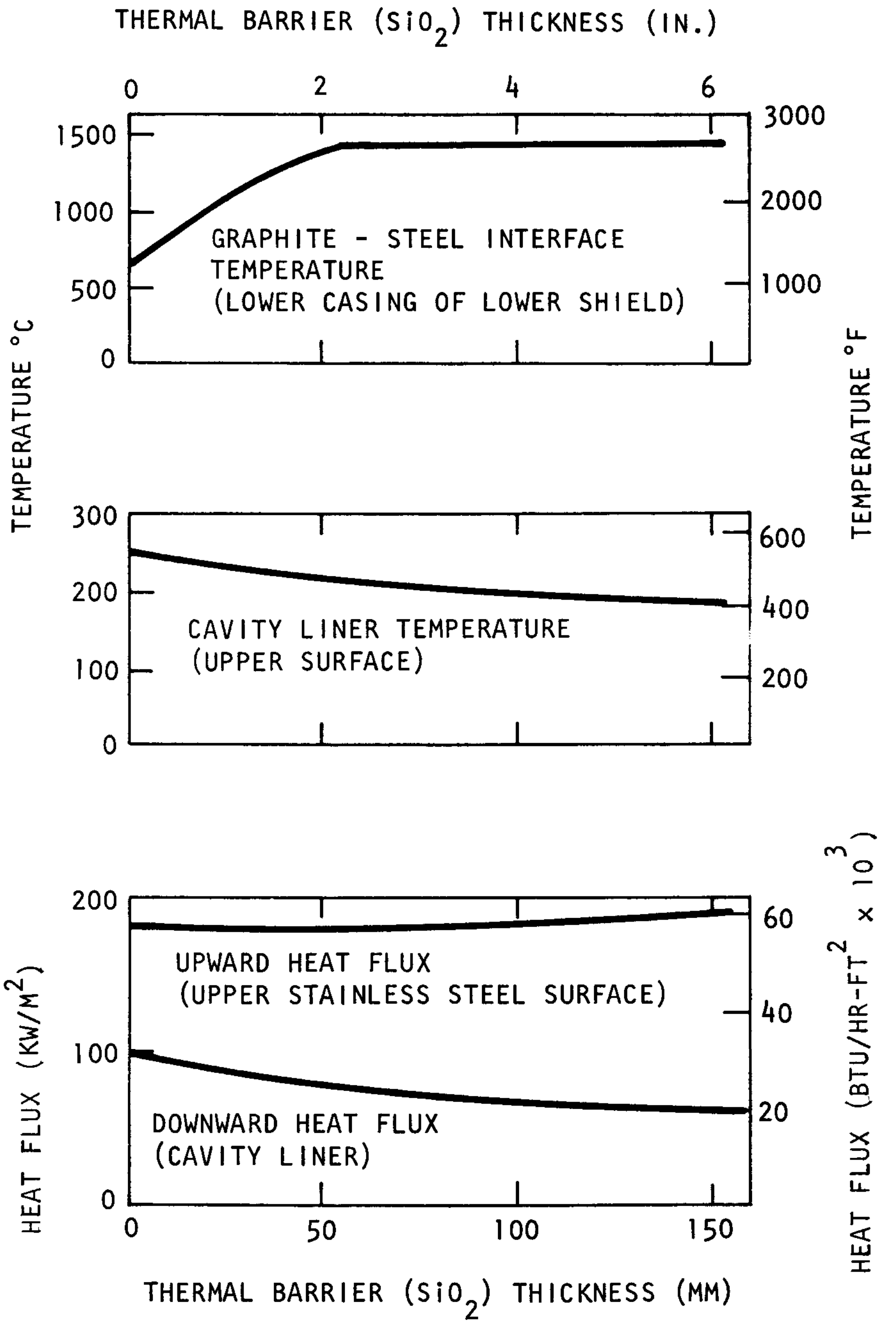

Fig. 9-5. Effect of thermal barrier (SiO_2) thickness on temperature and heat flux

barrier thickness of 50 mm (2 in.) SiO_2 (or any similar material with an equivalent thermal resistance) appears to be adequate.

9.2.2. Heat Transfer Behavior of the Lower Reactor Cavity Following a Core Melt-Down Accident Without Cooling

The heat transfer behavior of the lower end of the reactor cavity has been studied under core melt-down conditions for the case without any cooling. In the analysis, the PCRV liner cooling system and the core auxiliary cooling system were assumed to be nonoperational. Other conditions were the same as those given in Ref. 9-5 except that the preshield and the top steel casing of the lower main shield were assumed to float above the molten fuel layer at the time of accident initiation. In addition, heat conduction to the concrete was also neglected. The NUTAP computer program was used for the numerical analysis.

The cavity liner temperature history is shown on the lower curve of Fig. 9-6. It can be seen that the cavity liner reaches its melting point about 7 hr after the accident. However, buckling of the liner due to excess thermal stresses could occur at temperatures much lower than the melting point. Thus, the actual time required to breach the cavity liner may be shorter. This time is also influenced by the actual melting process through the lower shield assembly. For instance, with the model used in the previous analysis, stainless steel from the lower shield was assumed to float above the molten fuel layer only after it melted; hence, a large amount of downward heat is absorbed by the stainless steel during its change of phase, so that the melt-through time is delayed, whereas this time is comparatively shorter for the present, more conservative model because downward heat is stored in the lower shield mostly in the form of sensible heat.

The maximum fuel temperature is shown on the upper curve of Fig. 9-6. Its trend appears to be completely different from that of the cavity liner temperature. It reaches its maximum value (with respect to time) about 4 hr after the accident and then decreases throughout the remainder of the

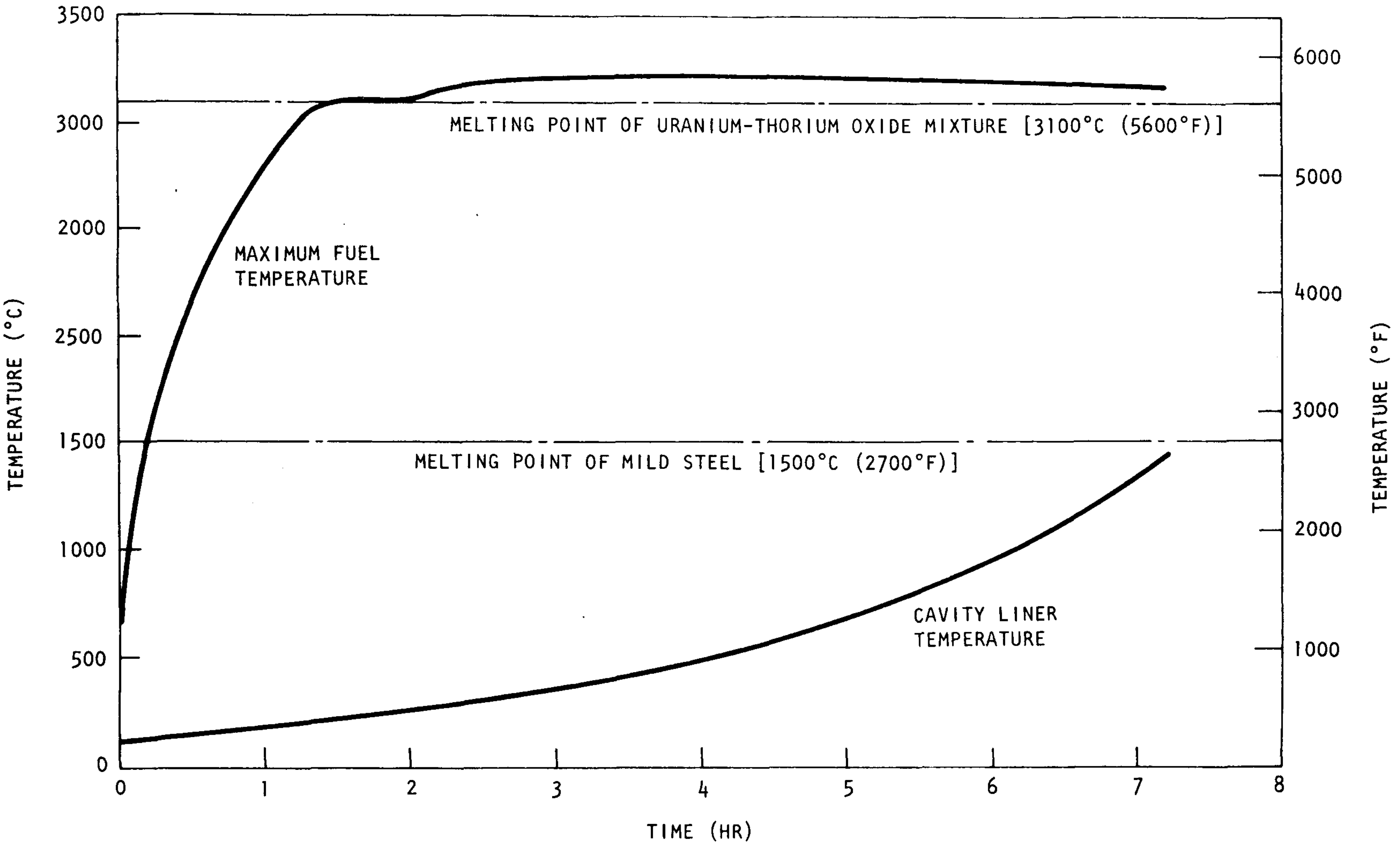

Fig. 9-6. Temperature history for molten fuel and cavity liner following a postulated core melt-down without lower thermal shield cooling

analysis because of the decreasing rate of decay heat. Since there is no cooling, this temperature must rise again after a certain length of time. However, it was found that until the cavity liner melt-through is completed, the maximum fuel temperature is just slightly above the melting point of mixed uranium - thorium oxide [3100°C (5600°F)], but far below the boiling point [4000°C (7230°F)]. This behavior of the maximum fuel temperature can be explained in Fig. 9-7. It can be seen that there is a solid fuel crust at the upper and lower fuel boundary. These crusts are formed owing to the high melting point and low thermal conductivity of the oxide fuel and the much lower initial temperature inside the reactor cavity. Before complete melting of the crust layers, it can be expected that the maximum fuel temperature will not be much different from the fuel melting point. Therefore fuel boiling is not expected as long as a solid fuel crust is calculated to exist. Furthermore, because of the very high melting temperature of the fuel, a large amount of heat is stored in the form of sensible heat (which means a temperature increase) in the lower shield assembly. These two combined effects are likely to cause either melt-through or mechanical failure of the cavity liner before boiling of the fuel. After the cavity liner fails, molten fuel as well as molten steel will be in contact with the concrete of the PCRV. Endothermic chemical reactions such as fuel-concrete and steel-concrete reactions are expected to occur at elevated temperatures. As compared with the lower shield assembly, the large quantity of concrete from the PCRV serves as an even bigger heat sink which further prevents the fuel from boiling.

In conclusion, it appears that boiling of fuel is unlikely to occur even in the absence of any cooling. However, the problem of hydrogen release accompanying the chemical reactions seems to be important and demands further attention.

9.3. CONTROL SYSTEMS

Digital coding and model checkout and tuning continued during this quarter, and it became evident that the data for the circulator-turbine unit required considerable manipulation to determine the desired curve

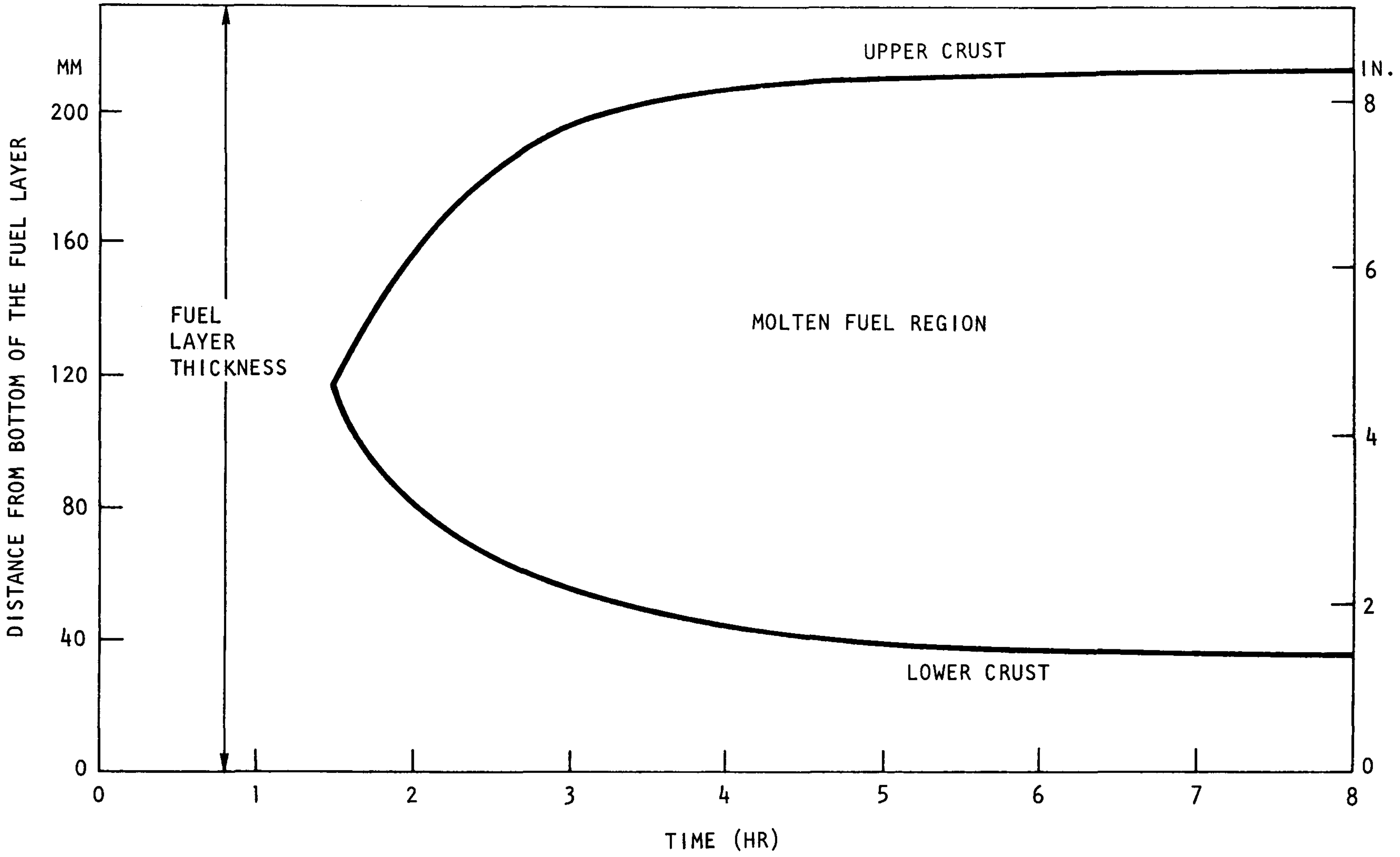

Fig. 9-7. Fuel melting history following a postulated core melt-down without lower thermal shield cooling

fitting functions for input into the simulation. Work was begun on reformulation of the model so that it will be able to use input data in a more readily available form. Documentation of the model development was started beginning with the steam generator model.

Coding for the three principal steam cycle valve controllers and the control rod controller was added to the detailed nonlinear plant model to be used for comparison with control system simulation results. This coding was generalized so that various control variable and set-point combinations could be examined. The valve controllers are of the position-integral-derivative (PID) type, and the control rod controller combines an adjustable dead band and hysterisis configuration to provide on-off control signals to the control rod drive motors. All coding has been checked out with the exception of the derivative portion of the PID controllers. Some modifications must be made to the derivative algorithm to minimize the effects of computational noise.

REFERENCES

9-1. "Gas-Cooled Fast Breeder Reactor Quarterly Progress Report for the Period February 1, 1970 Through April 30, 1976," ERDA Report GA-A13868, General Atomic, May 31, 1976, p. 9-6.

9-2. Ibid, p. 9-7.

9-3. Ibid., p. 2-11.

9-4. Johnson, T. R., et al., "Postaccident Heat Removal -- Preliminary Report on the First Large-Scale Molten Fuel-Sodium Interaction Experiment," Argonne National Laboratory Report ANL/RAS 73-6, April 1973, p. 6.

9-5. Menzel, H. F., and C. S. Kang, "Status of Post-Accident Fuel Containment Studies for a 300-MW(e) GCFR Demonstration Plant," General Atomic Report GA-A13734, December 18, 1975.

10. COMPONENT DEVELOPMENT (189a No. SU025)

10.1. REACTOR VESSEL

The scope of this subtask is to assure that the design of the PCRV and the related components which contribute to the integrity of the pressure boundary is satisfactory and to test critical component configurations to make certain that they attain the design objectives. This subtask will demonstrate by analyses and tests that the PCRV and its penetrations and closures meet the design criteria. It will also provide assurance that the design of the thermal barrier satisfactorily protects the liner and PCRV from the effects of high temperatures and the flow restrictors for the large penetrations can be developed to limit the flow of helium from the primary coolant systems to acceptable levels in the event of structural failure of a penetration or closure component.

Work accomplished during the previous quarter included revision of the model of the three-dimensional finite-element computer code to include the liners in the cavities and penetrations. In coordination with the Mechanisms Branch, layouts were prepared for the updated PCRV reactor cavity closure configuration which has 27 penetrations for the control rod drive mechanisms and 7 penetrations for the proposed remote handling machine to latch or unlatch the core elements. Drawings of alternate PCRV configurations were prepared for the primary coolant loops with low pressure drop using redesigned primary system components, including a steam generator without resuperheat.

In order to coordinate the PCRV closure test effort being conducted by ORNL, a drawing was prepared for a prototype configuration of the reactor cavity closure (Fig. 10-1). The structural adequacy of the prototype configuration was confirmed by computer analysis using a two-dimensional

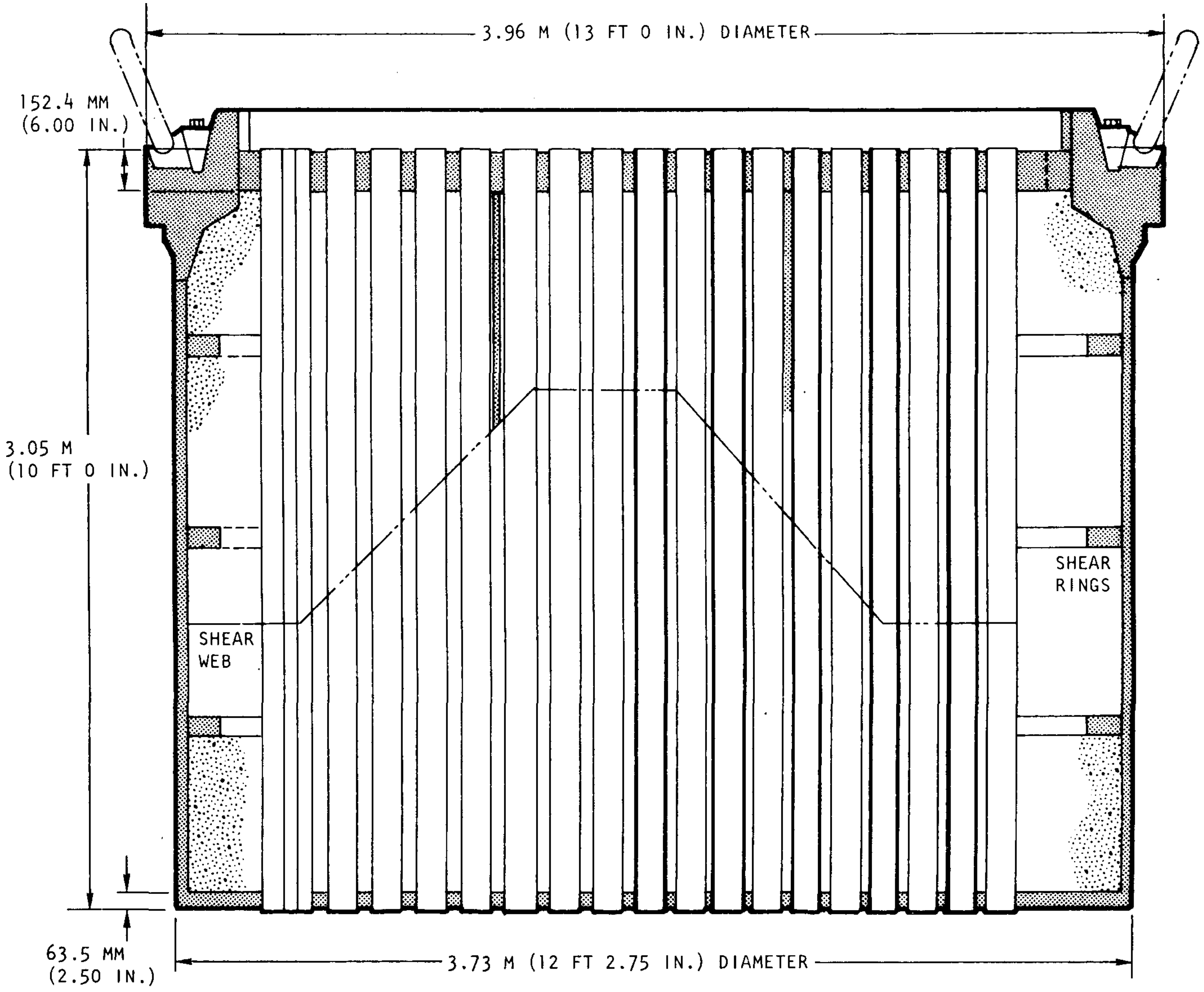

Fig. 10-1. Prototype configuration of reactor cavity closure

finite-element model which included modeling of the closure hold-down system. The stress distribution resulting from subjection of the closure to the maximum cavity pressure loading showed in general that the stress levels were within the allowable limits of the ASME Pressure Vessel Code, Section III, except in the region of the perforations. In this region, modeling was done using modified elastic constants and an axisymmetric solution. This neglects the effect of the pressure in the holes, which is expected to be beneficial in that it prestresses the ligaments in compression. Although this is helpful in the top center where bending is maximum, it is not sufficient to overcome the shear effects at the periphery of the perforated region. For this reason, shear webs have been added to the design. The webs are capable of carrying the entire shear load and should not be susceptible to buckling because of the presence of the concrete. The analysis showed that the shear rings on the cylindrical walls were adequate for transferring the coolant pressure force on the bottom of the closure through the concrete to the hold-down toggles. Copies of the closure configuration were sent to ORNL for guidance in the preparation of the 1/15-scale test models.

Layout drawings have been prepared for PCRV configurations for updated nuclear steam supply (NSS) system arrangements with low pressure drops in the primary coolant loops. The PCRV geometries were determined by preliminary sizing calculations necessary to contain the updated core configuration and primary coolant components. Hydrodynamic analyses of the PCRV ducts and plenums have been conducted to assure that the pressure drops are within the allocated values. These PCRV concepts incorporated engineering features, a ring PCRV pedestal support for better seismic resistance, and piping chases through the PCRV for the liner cooling system in order to simplify routing of the pipes. Basically, two concepts are being investigated: one concept has the helium circulator in the steam generator cavity, and the other concept has the helium circulator in a separate cavity. These studies determine the space requirements necessary for placement of the components for the helium purification system and the pressure relief systems.

A preliminary structural analysis has been initiated on the PCRV to determine the adequacy of the reference design. The primary analytical tool employed at GA to perform the analysis of the PCRV is the finite-element method. There are basically two types of analyses required, viz., elastic and inelastic analysis. Elastic analysis is used for determining the stresses resulting from the prestress, thermal, and pressure loads up to maximum cavity pressure. Inelastic, or nonlinear, analysis is used to determine the overall response of the PCRV to a hypothetical overpressurization.

For the structural analysis of the GCFR PCRV, a three-dimensional finite-element computer code is employed. This code can be used for analyzing elastic and inelastic behavior of concrete structures. The mathematical model treats an element as a 20-node brick with 3 deg of displacement per node for the series of strain-displacement equations. The PCRV was modeled as a 30-deg segment for which the boundary conditions are sufficiently known because of symmetry. A schematic of the model is shown in Fig. 10-2. Analyses were made for preload and pressure effects.

The resulting distribution of the stresses obtained from the finite-element computer program shows that the overall PCRV structural response is generally satisfactory. However, a detailed review of the computer analysis showed that the highest stress zone was that of the bottom head. To reduce the magnitude of the stresses caused by the fuel handling penetrations, a stress relief sleeve was proposed for the central penetration. The stresses were recalculated, and the levels were shown to be less than the maximum allowable values. The results of the recalculations are presented in Figs. 10-3 through 10-6. Figure 10-2 shows the elevations through the bottom head at which the calculations were performed. Figures 10-3 and 10-4 present the hoop and radial stress for the initial prestress condition. Figures 10-5 and 10-6 show the stresses for the prestress condition combined with the maximum cavity pressure at the end of reactor life. Additional analyses will be made at local areas of interest, such as the cavity haunches. In an effort to optimize the circumferential prestressing system, the loadings within the computer program will be

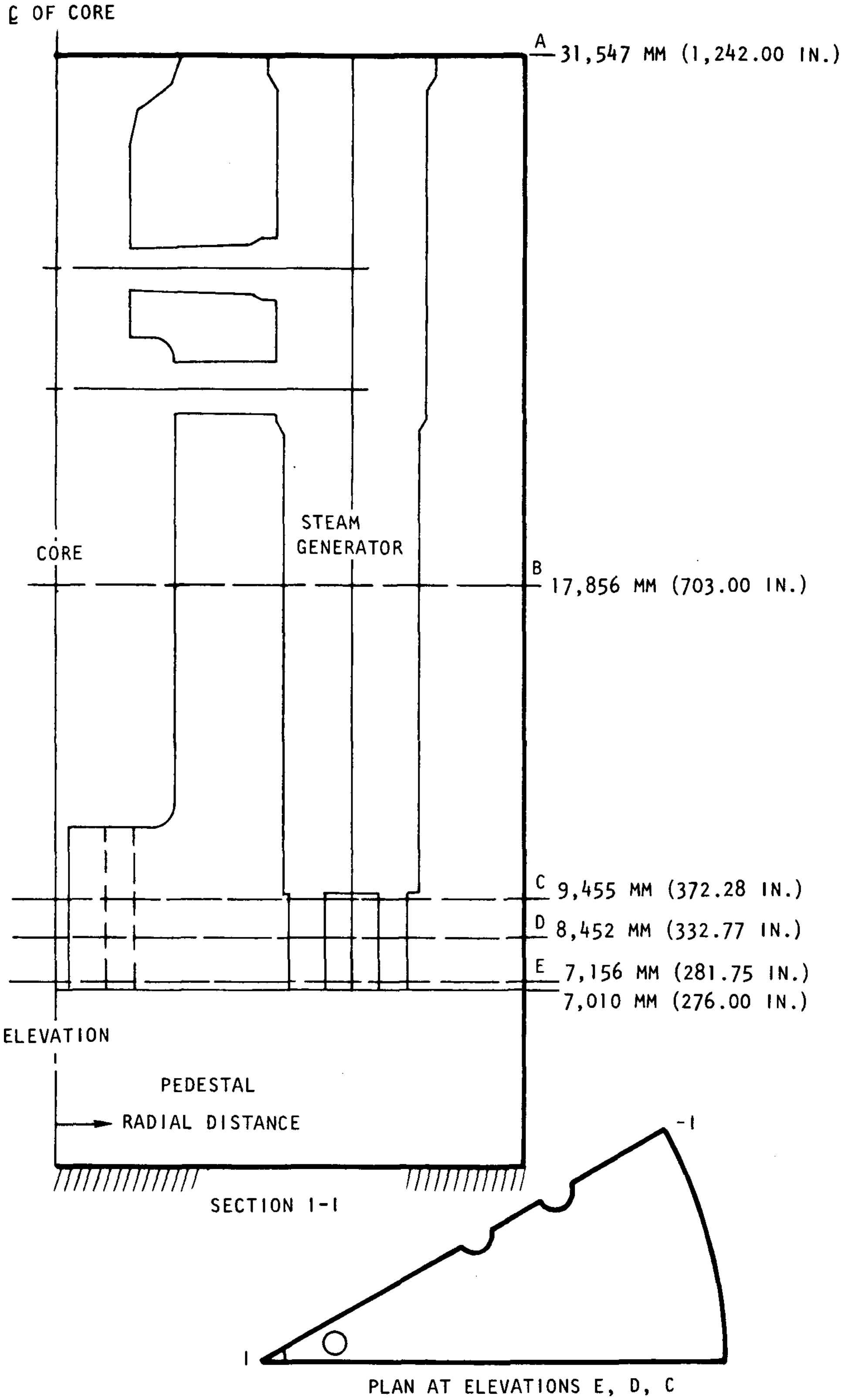

Fig. 10-2. PCRV sections

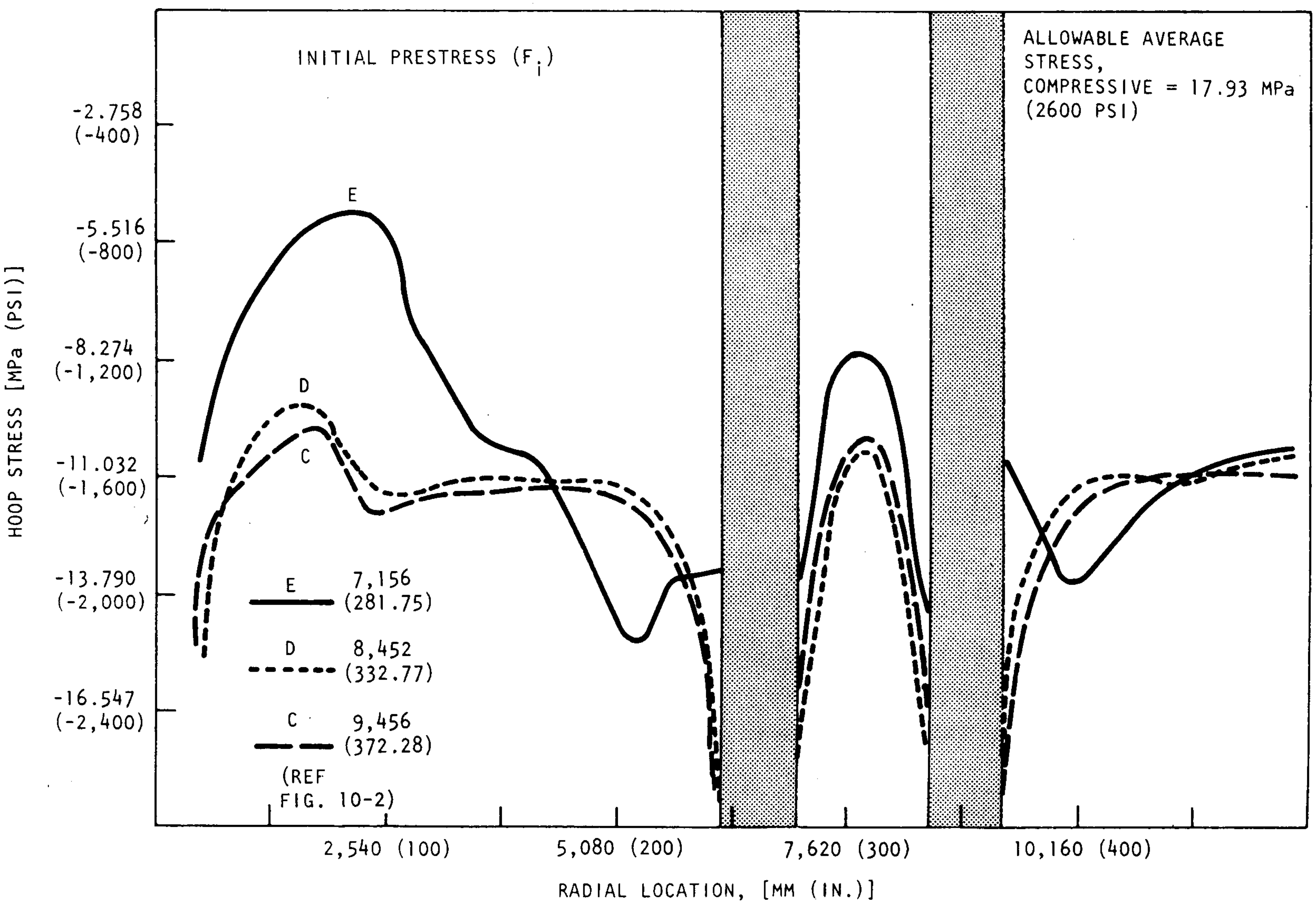

Fig. 10-3. Hoop stresses in bottom head (F_i)

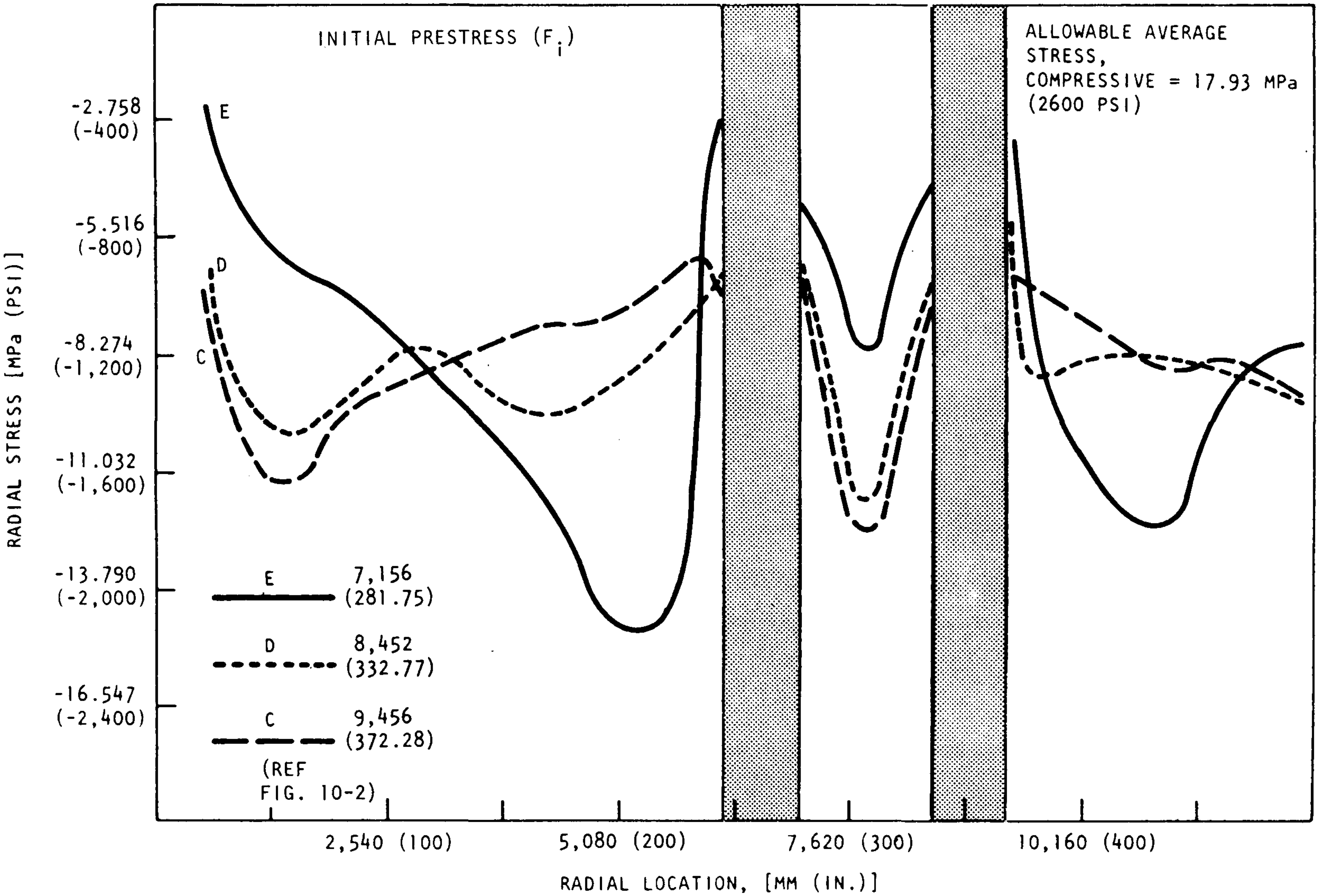

Fig. 10-4. Radial stresses in bottom head (F_i)

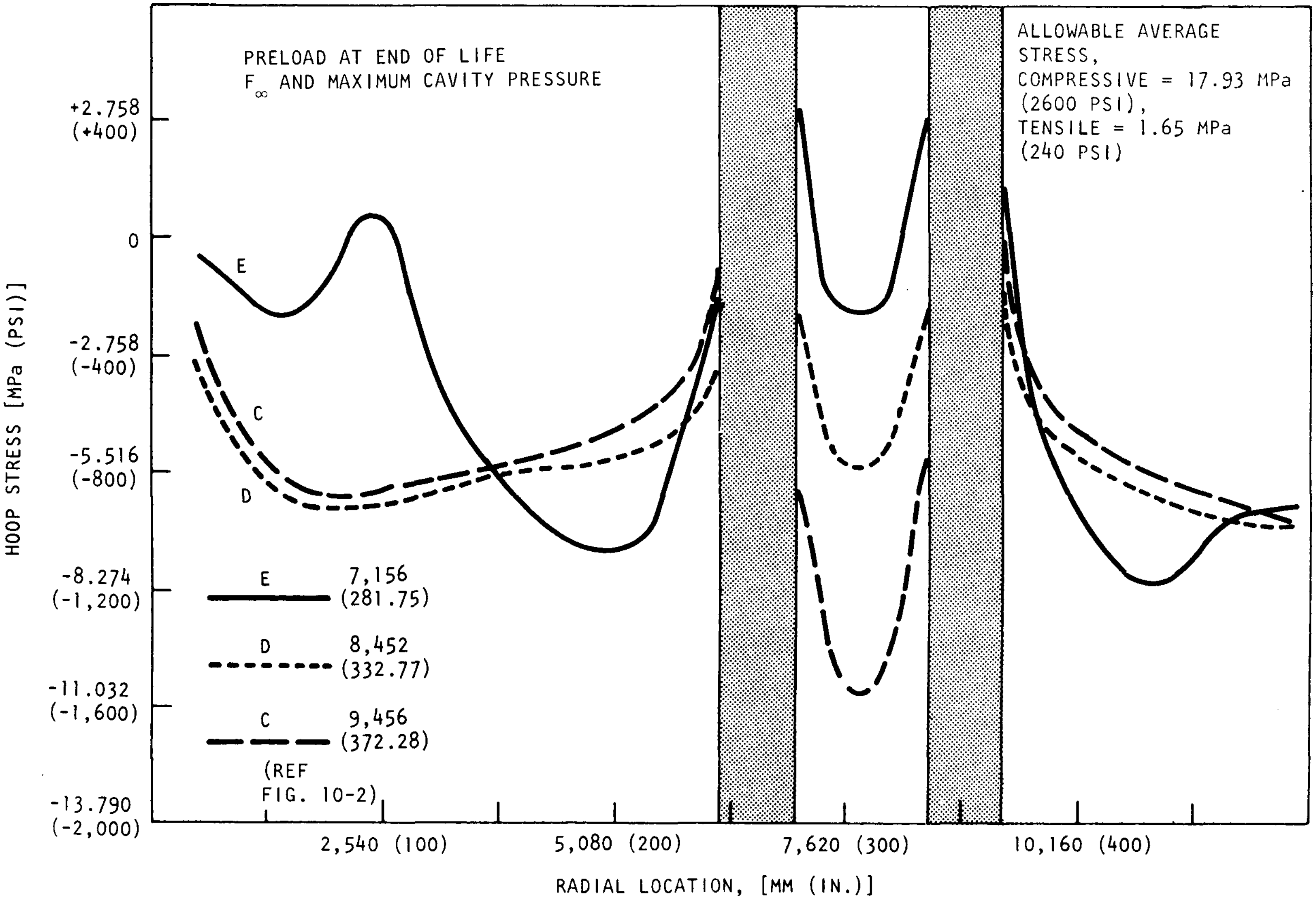

Fig. 10-5. Hoop stresses in bottom head (F_∞ + maximum cavity pressure)

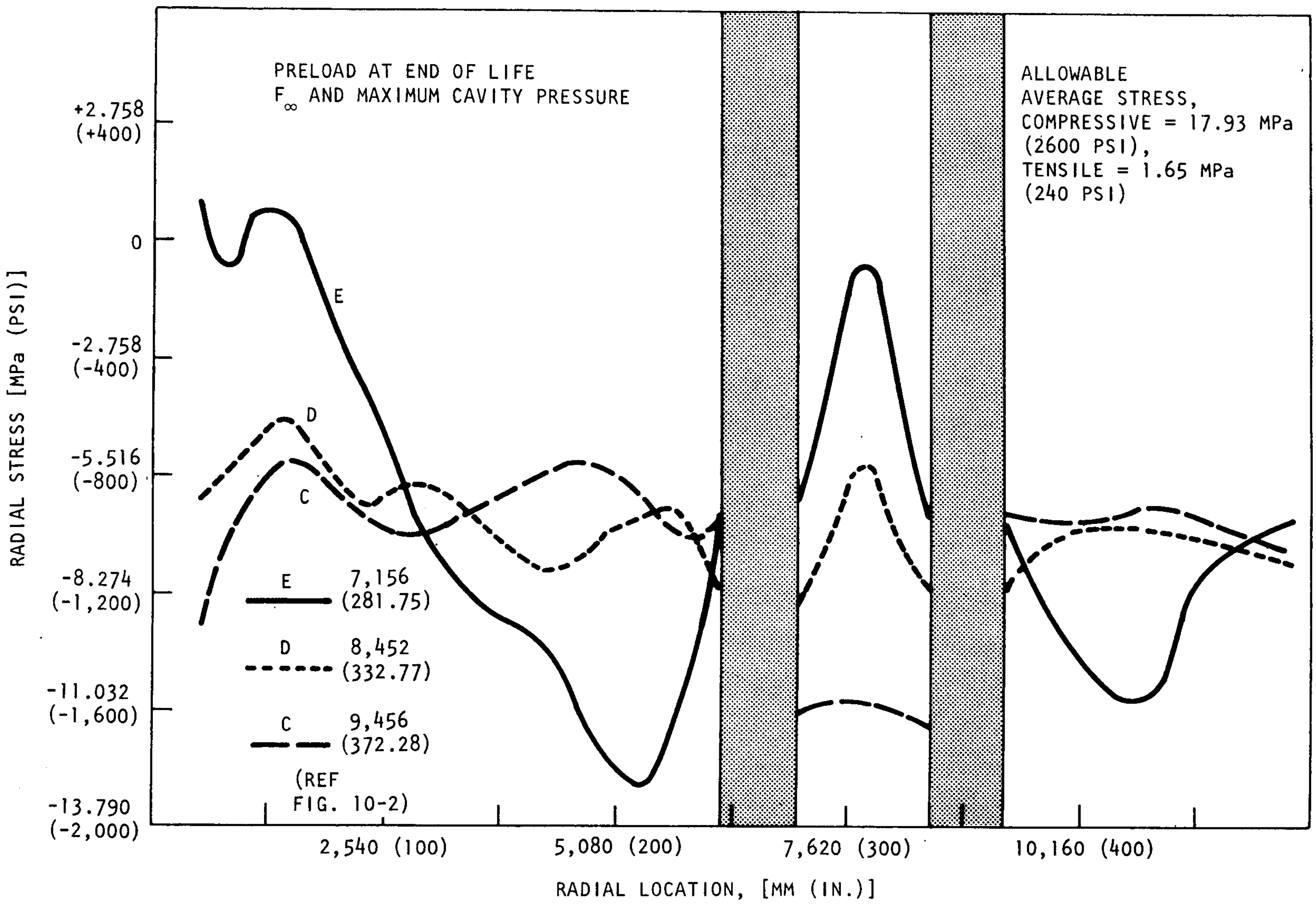

Fig. 10-6. Radial stresses in bottom head (F_∞ + maximum cavity pressure)

varied to produce bands of prestress for the top and bottom head regions and the barrel section.

10.2. CONTROL AND LOCKING MECHANISMS

The scope of this task covers the preparation of a development plan for the core element control and locking mechanisms for a 300-MW(e) GCFR demonstration plant. During this quarter, all written and illustrative material for the plan was completed in draft form for internal review issuance.

10.3. FUEL HANDLING DEVELOPMENT

10.3.1. Conceptual Studies and System Optimization

Significant recommendations for system improvement were made during this quarter and were included in the final stages of this subtask effort, which consists of summarizing in report form the various alternative refueling schemes studied during the fiscal year. The latest recommendations are concerned with improving the structural conditions of the PCRV and the containment building by reducing the PCRV support height and the containment building height. The recommendations consist of several points:

1. Reduction of containment building height and PCRV support structure height by 3.5 m (11.5 ft).
2. Reduction of the access hatch opening diameter from 6.1 m (20 ft) to 4.9 m (16 ft).
3. Reduction of the lean concrete fill thickness above the containment base mat to 0.9 m (3 ft).

4. Establishment of firm space envelope requirements for the refueling system in the area under the PCRV and in the containment building.

These structural modifications would result in a 35% reduction in height, thereby improving the response conditions due to potential seismic-induced loads. Reducing the access opening by 9.3 m^2 (100 ft^2) also reduces the primary and secondary containment building sealing surface area. In addition, the internal containment building net volume is reduced 1812 m^3 (64,000 ft^3), and the amount of lean concrete is reduced by 65%. These results together with results of other concurrent studies of equipment external to the vessel such as transfer casks and transfer cars led to the conclusion that only 5 m (16.5 ft) under the PCRV was necessary for refueling access purposes. This was the basis for establishing dimensional clearance envelope requirements. Obviously, the corresponding reduction in demonstration plant construction costs is significant, especially considering the structural and lean concrete in-place costs alone. It is believed that these recommendations are a major step toward achieving refueling system concept optimization.

The summary report for this subtask topic was outlined and drafted. This report is scheduled for issue during the transition quarter. To ensure that a fair evaluation is given to this topic, the report is arranged such that the historical aspects as well as the reference design are discussed and compared with the various alternative schemes studied. The discussion section includes

1. Early or previous system concepts.
2. Current reference design system concept.
3. Criteria for system optimization.
4. Alternative transfer concepts investigation.
5. Summary of recent system improvement recommendations.

This is followed by a description of the recommended baseline system design concept.

With respect to the component aspects of the conceptual design studies, certain equipment outside the vessel has undergone a preliminary feasibility study with respect to system improvement. For example, as opposed to the concept of two separate vehicles, the auxiliary transfer cask car and the fuel transfer cask can be combined with respect to the main support structure and main transfer drive system. This results in a separate self-contained fuel transfer cask which can be carried on the transfer car in the same manner as the auxiliary transfer cask, but not at the same time.

In-vessel component conceptual design studies of the fuel transfer machine continued during this quarter. Efforts were concentrated on the lower portion of the equipment, which incorporates three main functional units (as presently conceived):

1. Main housing. This unit mates with the central refueling penetration of the PCRV and supports the loads generated during functional operation of the fuel transfer machine. The housing also incorporates a lifting mechanism which extends the machine from its storage position into its operational position by raising the telescoping housing. The mechanism is driven by a brushless torque motor through a planetary gear set and four ball screws.

2. Telescoping housing. This unit is contained within the main housing during storage and is raised to the top of the main housing after the machine is installed. In this operational position, the telescoping housing has to be firmly locked to the main housing in order to relieve the main drive from loads generated during operation. This is accomplished by 12 precompressed heavy springs arranged around the periphery of the telescoping housing. These springs compress the telescoping housing against the main housing, enabling the telescoping housing to counteract any overturning moments as well as vertical

and horizontal forces. The telescoping housing incorporates all the mechanisms required to enable fuel element handling.

3. Arm linkage drive. This unit controls the horizontal translational motion of the fuel element. The kinematics of the linkage is quite significant since the velocities close to the centerline of the core determine the controllability of the horizontal motion. The related calculations as well as those which determine the forces acting on the linkage were performed in detail using computer-assisted methods.

It is believed that the feasibility of the fuel transfer machine mechanism functions is close to verification. Technical problems related to reducing the main housing diameter with respect to PCRV interfaces will be identified during the transition quarter.

10.3.2. Postirradiation Examination Facility Evaluations

Preliminary input data confirming most of the parameters contemplated for inspection were received during this quarter. These data are awaiting further review and follow-up action.

10.3.3. Spent Fuel Shipping Studies

There were no reportable results for this subtask topic during this quarter.

10.4. CORE SUPPORT STRUCTURE

The purpose of this subtask is to assure the availability of the structural analysis methods and materials mechanical behavior required to assess the structural integrity of the GCFR core support structure under all anticipated operational and safety-related loading conditions in the GCFR environment.

In previous quarterly reports (Refs. 10-1, 10-2), determination of the effect of thickness on grid plate displacement using the isotropic elasticity theory was reported along with analytical solutions of the grid plate using anisotropic elastic body theory. The results of the free-vibration test of the grid plate model and single core elements were also reported.

During this quarter, several tasks were performed. The Core Support Structure Development Plan was completed and is being issued. An outline for the Core Support Structure Static Test Report has been written. The free-vibration determinations were completed, and a simplified seismic response test of the core support model was continued. The method of assessing the effect of pressure on the behavior of the core support structure was also completed.

10.4.1. Structural Analysis

A comparison study on the effect of the pressure load on the GCFR core support structure was made using different theories. The difference as well as the similarities between the results are plotted and discussed in the following sections.

The geometric dimensions, elastic constants, and loadings for a transversely isotropic elastic body analysis of the brid plate are

Outside radius r_o = 1.6986 m (66.875 in.)
Thickness h = 0.6096 m (24.0 in.)
Pressure loading p = 290 kPa (42.0 psi)
In-plane Young's modulus E = 6.1 GPa (0.885×10^6 psi)
Axial Young's modulus E' = 39.85 GPa (0.578×10^7 psi)
Axial shear modulus G' = 7.943 GPa (0.1152×10^7 psi)
In-plane Poisson's ratio ν = 0.743
Axial Poisson's ratio ν' = 0.3

All the elastic constants are the effective elastic constants calculated according to Refs. 10-3 and 10-4.

The isotropic elastic body behavior can be obtained from the transversely isotropic model by letting all the elastic constants be the same as those in the in-plane direction; i.e.,

$$E = E' = 6.10 \text{ GPa } (0.885 \times 10^6 \text{ psi}) \quad ,$$

$$G = G' = 7.943 \text{ GPa } (0.1152 \times 10^7 \text{ psi}) \quad ,$$

$$\nu = \nu' = 0.743 \quad .$$

The other parameters remain unchanged. This set of data was also used for the thin plate theory analysis.

The computed results show that the radial and tangential stresses among the transversely isotropic elastic body, isotropic elastic body, and thin plate theory analyses of the grid plate are almost identical. The axial stress and transverse shear distribution along the thickness of the grid plate between the transversely isotropic elastic body and isotropic elastic body analyses are also very close. The prediction of the displacements, however, is much more sensitive to the method used than the stress. The radial displacement versus the radial coordinate plot of the transversely isotropic solution (Fig. 10-7) is quite different from that for the isotropic case. The maximum radial displacement for the transversely isotropic solution is -0.120 m (-4.71×10^{-3} in.) at r = 1.397 m (55 in.); the isotropic case is -81.28 µm (-3.2×10^{-3} in.) at r = 1.2573 m (49.5 in.). Comparison of the axial displacement at the center of the grid plate for the transversely isotropic elastic solution, the isotropic elastic solution, and the thin plate theory is most significant. The center axial displacement at the middle surface of the grid plate (Fig. 10-8) for the transversely isotropic solution is equal to 52.8 mm (2.08 in.). The prediction made by the isotropic elastic body solution for the displacement at the center of the grid plate is 64.0 mm (2.52 in.). The thin plate theory

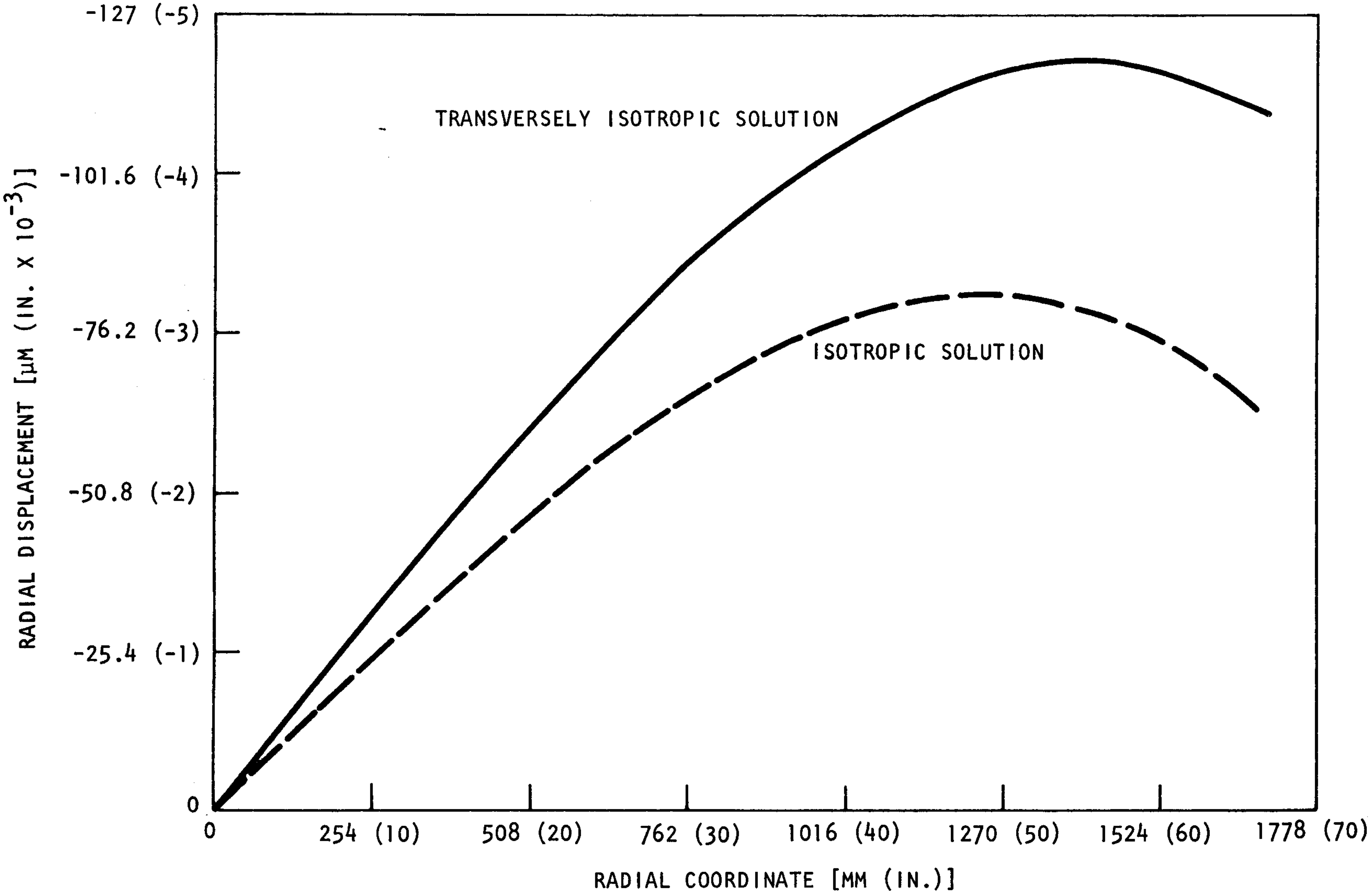

Fig. 10-7. Comparison of transversely isotropic and isotropic solutions: radial displacement vs radial coordinate of grid plate at top surface of grid plate

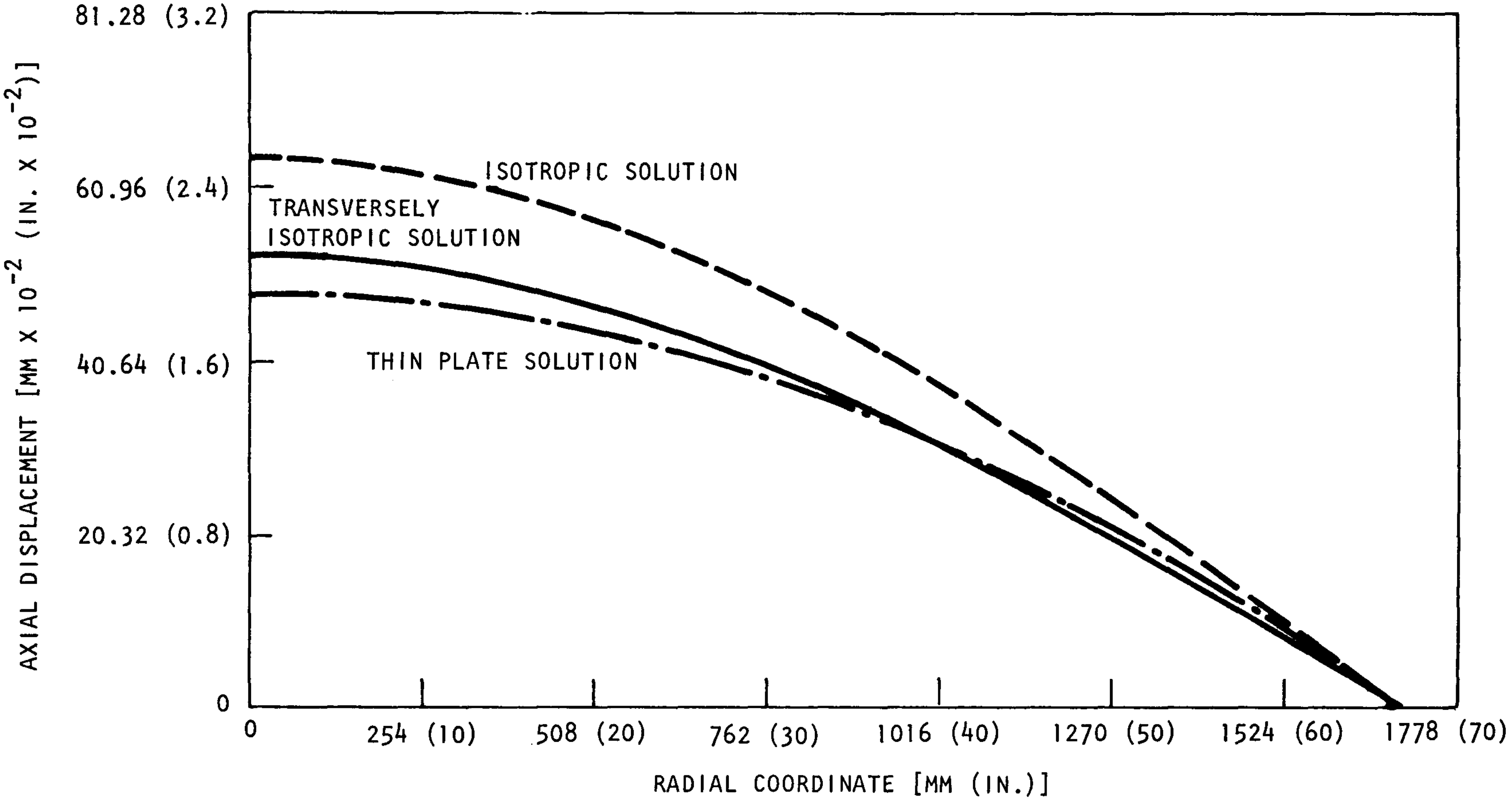

Fig. 10-8. Comparison of transversely isotropic, isotropic, and thin plate solutions: axial displacement vs radial coordinate of grid plate at middle surface of grid plate

gives the center displacement as 48.3 mm (1.90 in.). The inputs for the isotropic elastic theory and the thin plate theory solutions are identical. Therefore, the 32.6% difference for the axial displacement at the center of the grid plate is due to the effect of transverse shear and normal stress. The difference in the displacement at the center of the grid plate between the transversely isotropic and the isotropic solutions amounts to 21%. Both solutions take the transverse shear and normal stress into consideration. However, the transversely isotropic elastic body solution considers the axial direction elastic modulus, which is much higher than the in-plane direction. This higher elastic constant plus the different Poisson's ratio contribute to the difference in the displacement.

10.4.2. Core Support Structure Dynamic Model Test

Free-vibration and simulated seismic excitation tests of the grid plate model containing 267 core elements were performed. Figure 10-9 illustrates the general test setup. The core support structure was excited by a shaker in the horizontal direction; acoustic excitation was also used for one frequency in the vertical direction. Figure 10-9 also indicates some of the intrumentation. Ultralight accelerometers and special capacitors were used to measure frequencies, accelerations, and relative displacements. Figure 10-10 shows the grid plate model with the core elements. In this figure, some of the wiring to the accelerometers and capacitors is visible. The natural frequencies and mode shapes of the core system were found using deterministic excitation. Based on the previously calculated frequencies, by combining analytical and computer methods and applying the scale laws of models, it can be seen that the measured frequencies confirm the theoretical predictions. A simplified form of the El Centro earthquake spectrum was also applied to the simulated seismic excitation of the core model. A review of the test shows that although most of the core elements move in phase, some are out of phase owing to variations in their fundamental frequencies. A series of high-speed photographs were made to illustrate the motion of the core model. To complete this phase of the test program, some additional data reduction is required.

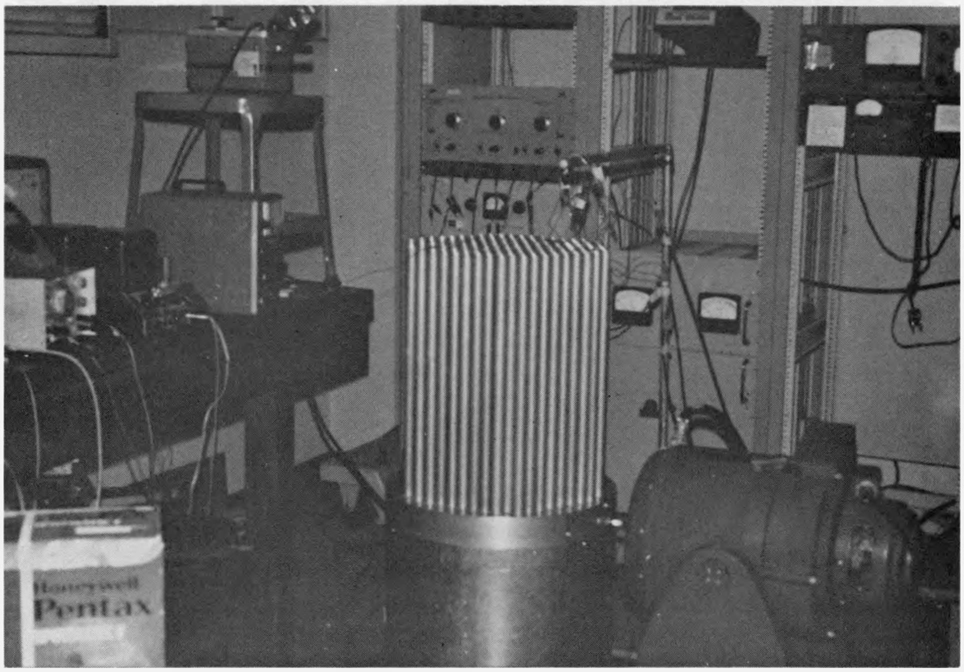

Fig. 10-9. General test setup

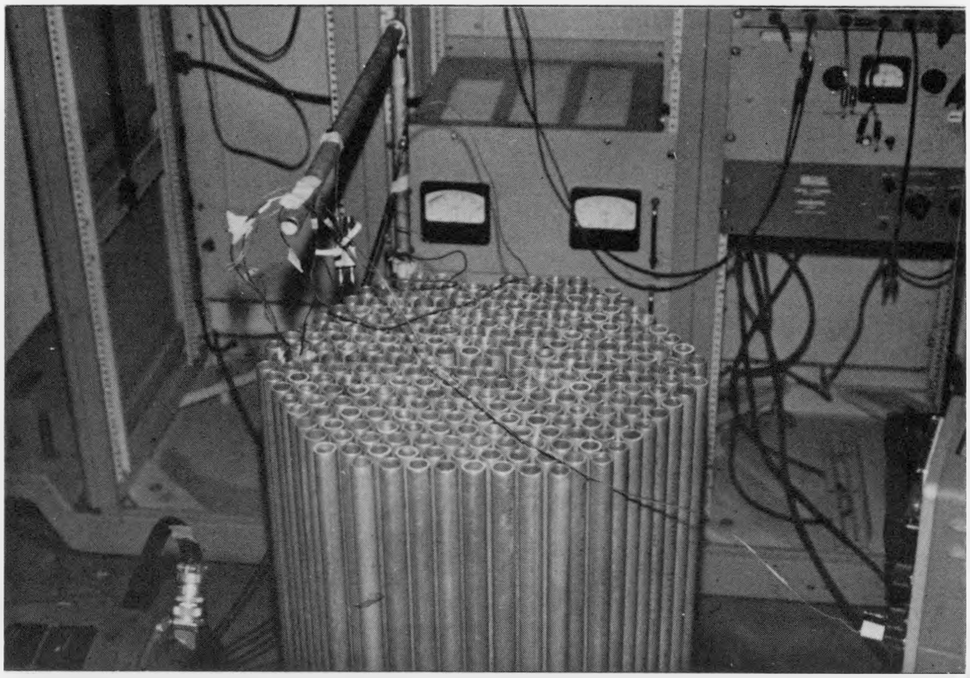

Fig. 10-10. Grid plate model with core elements

10.5. REACTOR SHIELDING ASSEMBLIES

The purpose of this task is to develop analytical methods and experimental programs to evaluate the reference design of the reactor shields. This evaluation considers heating and cooling of the shields, materials evaluation, seismic effects, need for flow tests, and structural analysis. The evaluation also includes alternate shield configurations as necessary to develop a satisfactory design.

During the previous quarter, the reference shield design was studied and compared with alternate shield configurations, and the effect of several proposed designs on the pressure drop was studied. An assessment of problem areas for the shield design was also made, and during this quarter, an intermediate report was written on the analytical methods used for the shield assembly, including structural analysis methods, temperature and pressure drop calculations, and an outline of a model pressure drop test.

10.6. MAIN HELIUM CIRCULATOR, VALVE AND SERVICE SYSTEM

The objective of this task is to prepare a topical report evaluating alternative main loop isolation valve conceptual designs. The purpose is to develop components for the main helium circulator valve and service system and to demonstrate performance and reliability by testing under anticipated operating conditions.

The basic function of the main loop isolation valve is to limit the reverse flow of primary coolant through a shutdown circulator. The performance requirements of the valve are such that the valve shall perform reliably under normal, upset, emergency, and faulted conditions. Since the last reporting period, the criteria for evaluating the conceptual designs have been prepared, and several valve configurations and actuating system concepts have been developed and evaluated. The criteria include the functional, performance, design, safety maintenance test, and in-service inspection requirements.

One of the criteria for the design requirements for the valve is the establishment of flow and leakage limits through an opened and closed valve in accordance with normal and accident requirements. The leakage limits include leakages through all the valve components associated with the main circulator, including the valve, the valve actuator, and the indicating devices. The evaluation of the alternate valve design concepts will also address the design diversity between the main and auxiliary valves. The topical report is approximately 30% complete, and its preparation is continuing.

10.7. STEAM GENERATOR

The purpose of this task is to develop a steam generator which meets the operational, performance, and safety requirements of the GCFR. During this fiscal year, several steam generator designs will be analyzed and evaluated, and the merits of each design will be compared.

Since the last reporting period, the updated cycle for the reference design with a 0.27-MPa (40-psi) helium pressure drop has been modified to incorporate revised main turbine performance characteristics. Using the conditions of this cycle, helical coil and straight tube steam generators without a resuperheater were sized as shown in Tables 10-1 and 10-2, respectively. The resulting units were slightly shorter than those designed for the previous updated cycle.

Table 10-1 shows the characteristics of helical coil steam generators with bundle diameters of 2.6 (8.5), 2.7 (9.0), and 3.0 m (10 ft) using Incoloy alloy 800H tubing and 2-1/4 Cr - 1 Mo steel as an alternate material. It can be seen that for the same bundle diameter, the bundle length is less for Incoloy alloy 800H than for 2-1/4 Cr - 1 Mo. Because of the greater required tube wall thickness, the 2-1/4 Cr - 1 Mo unit has more tubes in parallel but correspondingly less tube length. For either tube material, the required tube length, surface area, and weight remain virtually constant for the range of bundle diameters shown. Although the required surface area for 2-1/4 Cr - 1 Mo tubing is only about 10% greater

TABLE 10-1
300-MW(e) GCFR STEAM GENERATOR CHARACTERISTICS (HELICAL)[a]

Bundle Diameter [m (ft)]	Bundle Length [m (ft)]	No. of Tubes	Spacing, Transverse [cm (in.)]	Spacing, Longitudinal [cm (in.)]	Superheater Diameter x Thickness [cm (in.)]	Evaporator Diameter x Thickness [cm (in.)]	Economizer Diameter x Thickness [cm (in.)]	Material	Length [m (ft)]	Surface Area [m^2 (ft^2)]	Tube Material Volume [m^2 (ft^2)]	Tube Material Density [kg/m^3 (lb/ft^3)]	Tube Weight [kg (lb)]
3.0 (10)	6.4 (21)	180	3.5 (1.38)	3.8/3.2 (1.5/1.25)	2.5 x 0.17 (1 x 0.0676)	2.5 x 0.17 (1 x 0.0676)	1.9 x 0.12 (0.75 x 0.047)	Incoloy 800H	194.2 (637.2)	2,422 (26,065)	3.34 (118.1)	31.2 (501)	26,894 (59,168)
2.7 (9)	9.8 (32)	178	4.3 (1.71)	3.8/3.2 (1.5/1.25)	2.5 x 0.17 (1 x 0.0676)	2.5 x 0.17 (1 x 0.0676)	1.9 x 0.12 (0.75 x 0.047)	Incoloy 800H	190.8 (625.9)	2,364 (25,434)	3.27 (115.6)	31.2 (501)	26,325 (57,915)
2.6 (8.5)	12.8 (42)	176	5.1 (2.02)	3.8/3.2 (1.5/1.25)	2.5 x 0.17 (1 x 0.0676)	2.5 x 0.17 (1 x 0.0676)	1.9 x 0.12 (0.75 x 0.047)	Incoloy 800H	188.4 (617.9)	2,306 (24,813)	3.20 (112.9)	31.2 (501)	25,710 (56,563)
3.0 (10)	7.3 (24)	260	3.6 (1.43)	3.8/3.2 (1.5/1.25)	2.5 x 0.44 (1 x 0.172)	2.5 x 0.22 (1 x 0.0864)	1.9 x 0.18) (0.75 x 0.0715)	2-1/4 Cr - 1 Mo	144.9 (475.2)	2,674 (28,774)	6.65 (234.6)	30.5 (489.5)	52,202 (114,846)
2.7 (9)	11.3 (37)	260	4.6 (1.80)	3.8/3.2 (1.5/1.25)	2.5 x 0.44 (1 x 0.172)	2.5 x 0.22 (1 x 0.0864)	1.9 x 0.18 (0.75 x 0.0715)	2-1/4 Cr - 1 Mo	143.5 (470.6)	2,602 (27,995)	6.51 (229.7)	30.5 (489.5)	51,112 (112,448)
2.6 (8.5)	15.5 (51)	260	5.6 (2.20)	3.8/3.2 (1.5/1.25)	2.5 x 0.44 (1 x 0.172)	2.5 x 0.22 (1 x 0.0864)	1.9 x 0.18 (0.75 x 0.0715)	2-1/4 Cr - 1 Mo	141.0 (462.4)	2,557 (27,510)	6.40 (225.8)	30.5 (489.5)	50,244 (110,538)

[a] Updated reference design cycle: helium temperature = 543°C (1010°F) in, 342°C (648°F) out; water temperature = 208°C (406°F) in, 513°C (955°F) out; steam generator ΔP helium = 0.058 MPa (8.5 psi), total water = 1.89 MPa (275 psi); tube wall thickness based on ΔP; heat duty = 291 MW(t) (per unit).

TABLE 10-2

300-MW(e) GCFR STEAM GENERATOR CHARACTERISTICS (STRAIGHT)(a)

Bundle Diameter [m (ft)]	Bundle Length [m (ft)]	No. of Tubes	Tube Pitch [cm (in.)]	Tube Diameter x Thickness [cm (in.)]	Material	Surface Area [m^2 (ft^2)]	Tube Material Volume [m^3 (ft^3)]	Tube Material Density [kg/m^3 (lb/ft^3)]	Tube Weight [kg (lb)]
1.96 (6.45)	18.0 (59.05)	5429	2.5 (1.0)	1.6 x 0.10 (0.625 x 0.040)	Incoloy 800H	4,875 (52,452)	4.65 (164.1)	31.2 (501)	37,370 (82,214)
1.93 (6.35)	16.8 (55.2)	5262	2.5 (1.0)	1.6 x 0.32 (0.625 x 0.127)	2-1/4 Cr - 1 Mo	4,418 (47,529)	11.36 (400.8)	30.5 (489.5)	89,177 (96,191)

(a) Updated reference design cycle: helium temperature = 543°C (1010°F) in, 342°C (648°F) out; water temperature = 208°C (406°F) in, 513°C (955°F) out; steam generator ΔP helium = 0.058 MPa (8.5 psi), total water = 0.083 MPa (∿12 psi); tube wall thickness based on ΔP; heat duty = 291 MW(t) (per unit).

than that for Incoloy alloy 800H, the tubing weight is about twice as great. If it is assumed that the cost per pound of 2-1/4 Cr - 1 Mo tubing is about 30% of that for Incoloy alloy 800H, then the cost for the required 2-1/4 Cr - 1 Mo tubing will be about 60% of that of Incoloy alloy 800H. On the other hand, in addition to its demonstrated low permeability to tritium in the clean and oxidized states, Incoloy alloy 800H possesses the advantage, with regard to water boiling stability, of having a greater fraction (44% to 23% for 2-1/4 Cr - 1 Mo) of the total steam generator pressure drop in the all-liquid (economizer) section.

Table 10-2 shows the characteristics of straight tube steam generators for the updated cycle conditions. The overall bundle length [about 17.4 m (57 ft)] is comparable to the helical coil unit using a 2.6-m (8.5-ft) bundle diameter; however, the straight tube bundle diameter is only about 2.0 m (6.4 ft). The units shown are based on the closest practical tube spacing, i.e., 2.54-cm (1-in.) triangular pitch for the 1.6-cm (5/8-in.) diameter tubes, and as such represent the shortest possible length. In contrast to the helical units, the straight tube unit using 2-1/4 Cr - 1 Mo steel is slightly shorter than the unit using Incoloy alloy 800H because the latter unit has much greater water-side flow area and hence a lower water-side heat transfer coefficient.

Because a uniform tube wall thickness is used throughout, based on the highest temperature, the tube weight for 2-1/4 Cr - 1 Mo steel is about two and one-half times as great as that for Incoloy alloy 800H even though the latter unit has a slightly greater surface area. However, the cost of tubing for the 2-1/4 Cr - 1 Mo unit would be about 70% of that for the Incoloy alloy 800H unit.

The first draft of the steam generator topical report is 50% complete and includes sections on nuclear power plant steam generator operating experience, thermal-hydraulic analysis, comparison of straight tube and helical coil steam generators, materials, and critical heat flux. With respect to the critical heat flux behavior of water, an examination of the literature indicates that significant differences exist between a straight tube and a helical coil tube. These differences and their possible effect on low-flow boiling stability are discussed in the topical report.

10.8. AUXILIARY CIRCULATOR, VALVE AND SERVICE SYSTEM

The general objective of this task is to prepare and issue a core auxiliary cooling system (CACS) component development plan document. The purposes are to develop components for the CACS system to meet the reliability and safety criteria and to demonstrate the performance and reliability of critical components by testing under anticipated operating conditions. The draft copy of the CACS component development plan has been completed and is being reviewed for approval.

REFERENCES

10-1. "Gas-Cooled Fast Breeder Reactor Quarterly Progress Report for the Period May 1, 1975 Through July 31, 1975," ERDA Report GA-A13565, General Atomic, October 2, 1975.

10-2. "Gas-Cooled Fast Breeder Reactor Quarterly Progress Report for the Period August 1, 1975 Through October 31, 1975, ERDA Report GA-A13766, General Atomic, January 5, 1976.

10-3. Slot, T., "Stress Analysis of Thick Perforated Plates," PhD thesis, University of Technology, Delft, The Netherlands, September 1972.

10-4. "ASME Boiler and Pressure Vessel Code," Section III, Article A-8000 (ASME 111/2).

11. HELIUM CIRCULATOR TEST FACILITY (189a No. SU046)

The objective of this task is to develop a test facility for qualification testing of the GCFR main helium circulator. The scope of this task involves (1) evaluation of alternative test facility concepts in terms of technical feasibility and cost, (2) identification of the most promising test facility concept, (3) an architect/engineer preliminary design study, and (4) final design, construction, and checkout of the facility.

The final draft of the topical report describing the full-power (100%) helium circulator test facility concept scoping and cost evaluation study is in final review prior to publication. The 25%-power helium circulator test facility scoping study is complete and documented in a topical report which was submitted for internal GA review during the last quarter.

At the request of ERDA, an updated and expanded Schedule 44 Construction Project Data Sheet was prepared. The test facility construction cost was increased from $17,900,000 to $18,200,000 to reflect equipment cost changes since the last submittal in September 1975. The circulator test facility cost schedule was revised to reflect the anticipated changes for the remainder of FY 76 and the transition period.

12. REACTOR SAFETY (189a No. SU021)

The purpose of this task is to study the reactor safety aspects of the GCFR. Logical probabilistic methods are employed to determine the probabilities associated with various accident initiation and progression sequences and to identify potential design modifications which would help reduce risks. The thermal behavior of the fuel element duct walls under conditions of loss of shutdown heat removal is studied to determine the relative timing of duct wall melting and fuel melting. Scoping studies are performed to determine test requirements for duct melting experiments. This task also includes liaison between GA and the ERDA-funded GCFR safety task at ANL.

12.1. ACCIDENT INITIATION AND PROGRESSION STUDIES

Applying the accident initiation and progression analysis (AIPA) techniques developed in FY 74, work is being directed toward the probabilistic analysis of potential accident sequences leading to low-probability, high-consequence sequences of events; this is also under study at ANL under the task "GCFR Safety Aspects on Fuel and Core." The principal AIPA effort is directed at the 300-MW(e) demonstration plant, with scoping-type analyses to be performed for larger plant sizes. The three principal accident classes under investigation are loss of flow (LOF) with shutdown, LOF with failure to shut down, and transient overpower (TOP). The objective of this work is to provide a best-estimate assessment of accident sequences within each of these classes. This assessment will be reported in a year-end report covering activities through June 1976. This report will include work performed during this quarter.

12.2. SAFETY-RELATED ANALYTICAL AND EXPERIMENTAL STUDIES

During this quarter, analyses have been completed to assess the change in the fuel rod cladding thickness from 0.48 mm (19 in.) to 0.38 mm (15 in.) on the duct and fuel melting sequence in the control fuel element. With a reduced cladding thickness, duct and fuel melting occur earlier, but the difference between the time of duct melting and the time of fuel melting increases.

Detailed analyses of the duct melting sequence in an in-pile experiment in a GRIST-type facility were completed, and the results compared with the duct melting sequence in a core element under accident conditions. The results confirmed earlier scoping analyses (Ref. 12-1) and indicated that duct melting at the duct midflat can be well simulated in such an experiment. However, a separate experiment would be required to correctly simulate duct corner melting. Furthermore, the fuel temperatures in the experiment are lower than those anticipated in an accident.

12.2.1. Effect of Reduced Cladding Thickness on Duct Melting Sequence

In a previous quarterly progress report (Ref. 12-1), the results of detailed thermal analyses of circumferential duct melting in a standard fuel element were presented. These results were based on a fuel pin cladding thickness of 0.48 mm (0.019 in.) and a fuel pin pitch of 9.80 mm (0.386 in.). In the interim, the actual cladding thickness has been reduced to 0.38 mm (0.015 in.), holding the fuel rod outer diameter constant. The effect of this change on the duct and fuel melting sequence was assessed by modifying the fuel element model discussed in Refs. 12-1 and 12-2. The results are summarized in Table 12-1.

The reduced cladding thickness results in earlier melting of all components because less heat is required to melt the steel components. However, the difference between melting of the last duct section and the first fuel section increases by 6 s because (1) the duct wall is exposed to the

TABLE 12-1

CALCULATED DUCT AND FUEL MELTING TIMES IN THE CENTRAL FUEL ELEMENT AT THE AXIAL CORE MIDPLANE FOLLOWING A TOTAL LOSS OF FLOW IN TWO SECONDS(a)

	Cladding Thickness (mm)	
	0.48	0.38
Melting times (s)(b)		
First cladding	40	28
Last cladding	120	106
First tie rod section	149	140
Last tie rod section	170	159
First duct wall section	127	115
Last duct wall section	185	174
First fuel	198	193

(a) See Refs. 12-1 and 12-2 for details of fuel element model.

(b) The melting times are defined as the 50% heat of fusion condition.

high temperature of the unclad fuel rods at an earlier time and (2) the fuel cross section and its heat capacitance are increased. Figure 12-1 shows the heat-up transient in the fuel and the duct wall for the two cases. It is concluded that the reduced cladding thickness has the desirable effect of increasing the duct-to-fuel-melting time lag.

12.2.2. Duct Melting Sequence in an In-Pile Test Configuration

Consideration has been given to the usefulness of an in-pile test to verify the calculated sequence of duct and fuel melting during an LOF accident in the shutdown reactor. As compared with out-of-pile tests, the primary advantage of an in-pile test would be the use of prototypical fuel and nuclear heating. The disadvantages of an in-pile test are the difficulty of instrumentation and observation, the complicated circumstances of a post-test examination, and the high cost of large in-pile tests. Analysis of a duct melting test in the conceptual GRIST 1 facility using the SCSF fuel position in the engineering test reactor (ETR) has been completed. For this analysis, a fuel configuration with an increased fuel rod pitch of 10.8 mm (0.433 in.), which is being considered for the GCFR, has been chosen because it places more stringent limitations on the maximum bundle size which can be accommodated in the fixed-size test space. The design of a double-section test assembly which was chosen for the analysis is discussed in Ref. 12-3.

The analytical model of a quarter-section of the double-section test assembly is shown in Fig. 12-2. The principal dimensions of the model are summarized in Table 12-2. The model consists of all or part of 19 fuel pins and 2 unfueled corner support rods, the corresponding section of duct wall, and an insulated boundary on two sides. The boundaries on the other two sides are adiabatic. Each fuel pin is divided into six 60-deg pie-shaped sections (the two fuel pins along the midflat boundary are divided into two 60-deg and two 30-deg sections). Each section is modeled by five nodes, three material nodes and two surface nodes. The outer material node consists of 20% of the fuel and all the cladding, and each of the other fuel nodes includes 40% of the fuel. Conduction in the radial and angular

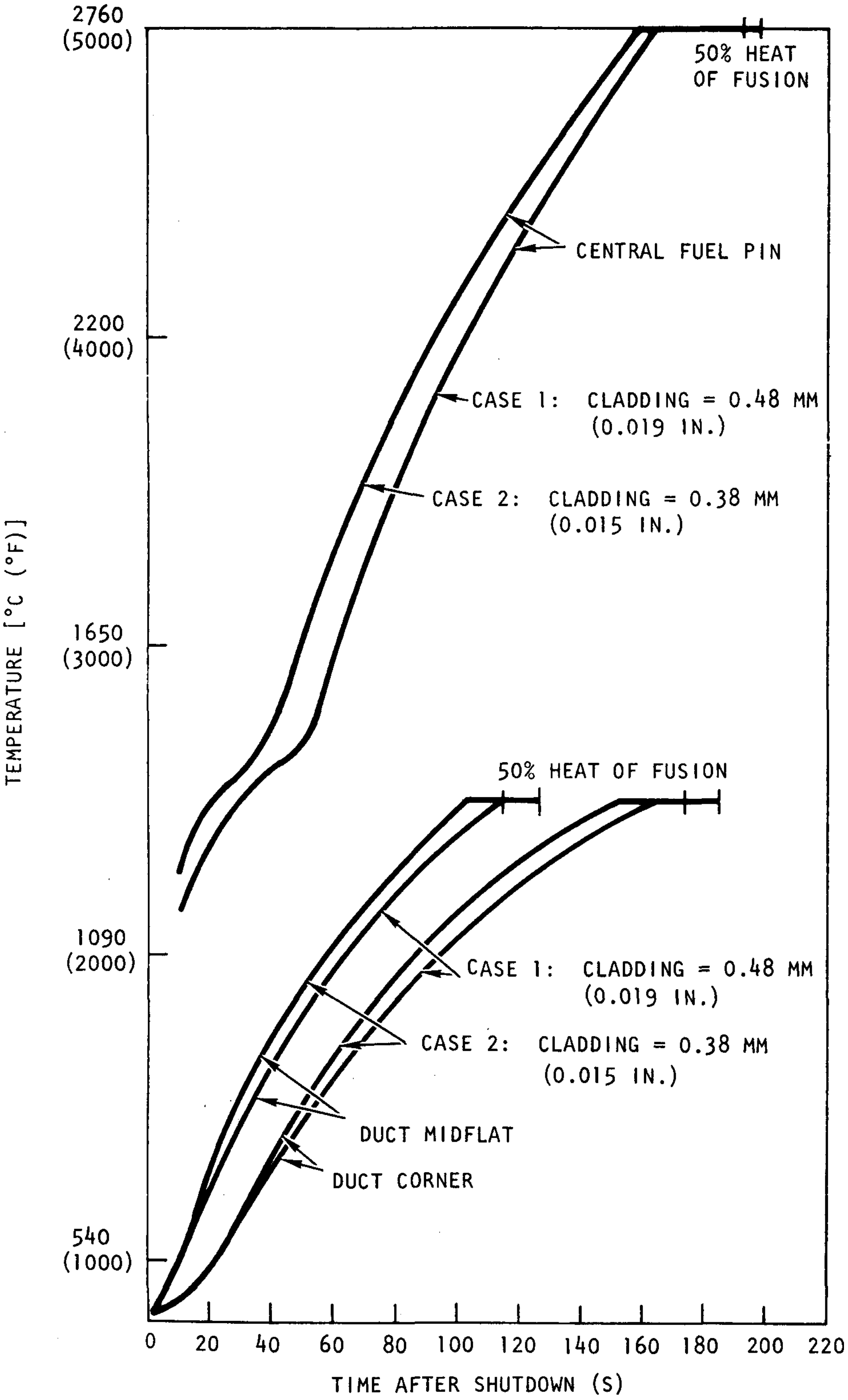

Fig. 12-1. Peak duct midflat and corner temperatures vs time

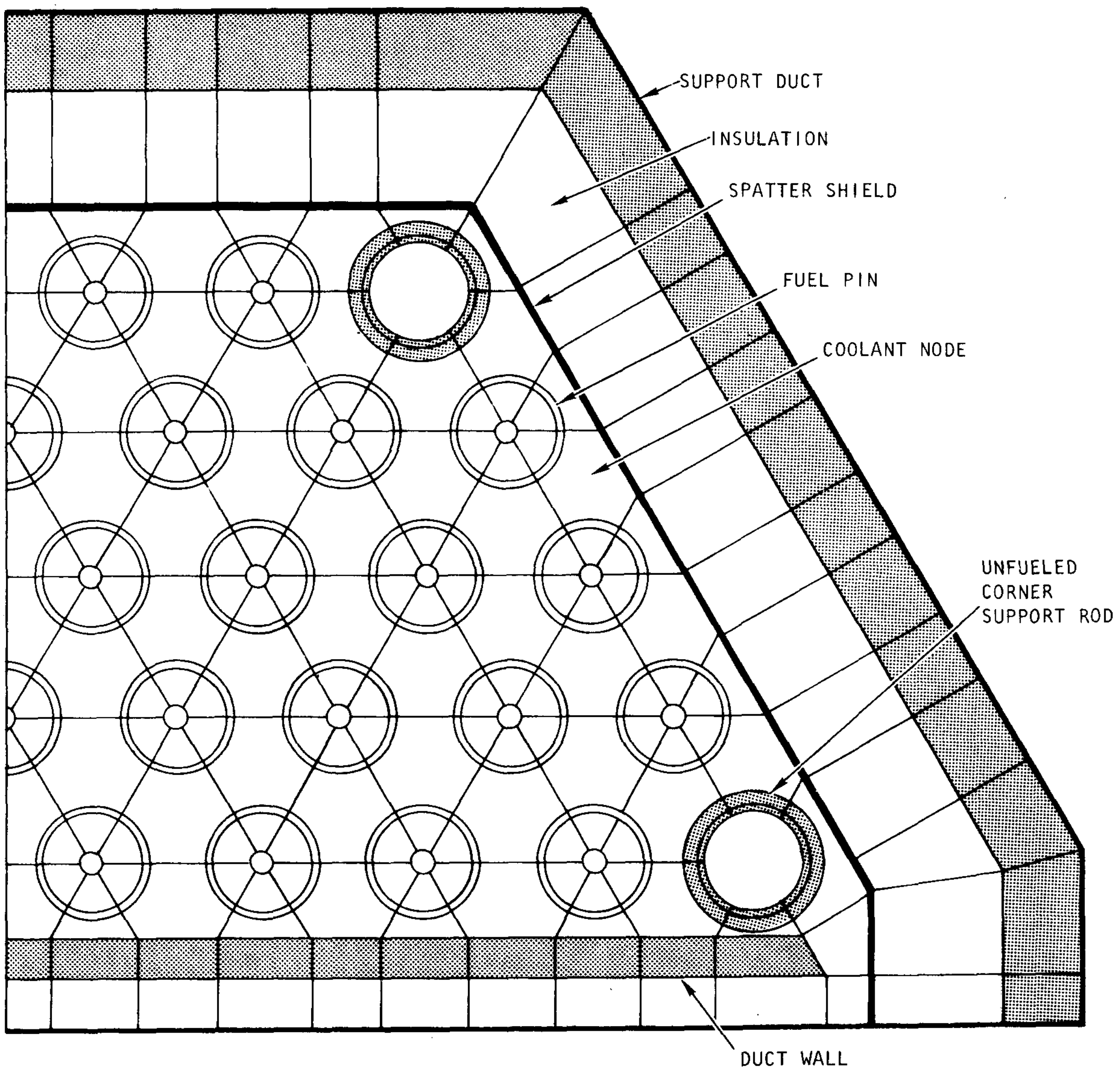

Fig. 12-2. Thermal model of GRIST test assembly

TABLE 12-2
PRINCIPAL DIMENSIONS OF GRIST TEST ASSEMBLY MODEL

Fuel pellet diameter [mm (in.)]	6.29 (0.248)
Cladding thickness [mm (in.)]	0.38 (0.015)
Fuel rod o.d. [mm (in.)]	7.2 (0.283)
Fuel rod pitch [mm (in.)]	10.8 (0.425)
Edge channel gap (% of fuel rod spacing)	40
Duct wall thickness [mm (in.)]	2.5 (0.098)
Spatter shield thickness [mm (in.)]	0.5 (0.020)
Insulation thickness [mm (in.)]	8.0 (0.315)
Support duct thickness [mm (in.)]	5.0 (0.197)
Corner support rod i.d. [mm (in.)]	6.2 (0.244)
Corner support rod o.d. [mm (in.)]	10.0 (0.394)

directions is modeled for each material node and for the outer surface nodes. A gap conductance is included in the conductance term joining the outer two material nodes to their corresponding surface nodes. Radiation across the fuel pin center holes is included in all fuel pins.

Each unfueled corner rod is divided into six 60-deg sections. Each section is modeled by two material nodes and four surface nodes. Angular and radial conduction is included. Radiation across the center hole and across the gap between the concentric rods which make up an unfueled corner rod is also included together with a gap conductance. Energy exchange through the coolant channels is represented by conduction in stagnant helium and by radiation and reflection between adjacent surface nodes.

The insulated boundary consists of a molybdenum spatter shield, a high-temperature insulation which is thermally represented by stagnant helium, and a stainless steel support duct. On the outside, the support duct is coupled to a constant boundary temperature of 440°C (826°F) through a convection coefficient.

The duct wall is divided into ten material nodes (Fig. 12-1). Surface nodes are provided on each side of the duct. Conduction between the material nodes and their corresponding surface nodes is included in the model along with conduction between adjacent material nodes.

When melting of a duct wall or an unfueled corner rod node occurs, its properties are changed to helium, and any existing radiation connections are set to zero. When a cladding node melts, the portion of the outer fuel pin material node which consists of cladding is modified so that the correct heat capacitance and resistance are used. When either a cladding node or an unfueled corner rod node melts, the view factor matrix is corrected to account for the geometric change.

The GRIST model is based on a cladding thickness of 0.38 mm (0.015 in.) and a fuel pin pitch of 10.8 mm (0.425 in.). To provide a fuel element model for comparison, this model was modified by making the top boundary at the spatter shield adiabatic, splitting the fuel pins and unfueled corner rods along the diagonal boundary, and making the new boundary adiabatic.

Table 12-3 presents the results of two consistent calculations, one simulating the GRIST experiment model and the other simulating a fuel element with the modified GRIST model. Comparison shows that a GRIST test assembly could accurately model the midflat duct melting time and thus confirm earlier scoping studies reported in Ref. 12-1. However, duct corner melting in the test assembly is significantly delayed and would thus lead to an exaggerated degree of axial duct melting prior to complete lateral duct melting in the experiment. Improved corner melting characteristics could be achieved by including in the test model a corner support rod with only half the heat capacity of an actual support rod. Alternatively, a triple-section test assembly (Ref. 12-3) specifically designed to simulate duct corner melting would be required. Figure 12-3 shows the fuel and duct temperature transients for the two cases. The fuel temperature transient indicates the inability of a test assembly of the size considered to simulate expected fuel temperatures during an accident; this agrees with the conclusions from the earlier scoping study (Ref. 12-1).

Although these analyses have been aimed at a detailed assessment of the performance of an in-pile experiment to simulate the important features of the heat-up and melting sequence for the duct wall and the fuel during an LOF accident in the shutdown reactor, the conclusions apply equally well to out-of-pile simulation tests with an equivalent-size test assembly. Therefore, out-of-pile tests, which in principal are not subject to such stringent limitations on the test assembly design, are considered to have a major advantage, and consideration of large test configurations should be included early in the development of the out-of-pile test program which has been initiated at Los Alamos Scientific Laboratory (LASL).

TABLE 12-3
CALCULATED MELTING TIMES IN A GRIST EXPERIMENT ASSEMBLY AND IN A SIMULATED FUEL ELEMENT AT THE AXIAL MIDPLANE FOLLOWING A LOSS OF FLOW TWO SECONDS AFTER SHUTDOWN

	Melting Time (s)	
	GRIST Experiment	Fuel Element
First cladding	26	24[a]
Last cladding	124	106
First tie rod section	169	126
Last tie rod section	204	157
First duct wall section	112	111
Last duct wall section	221	176
First fuel	--	183[a]

(a)Approximate melting time based on an adiabatic fuel pin.

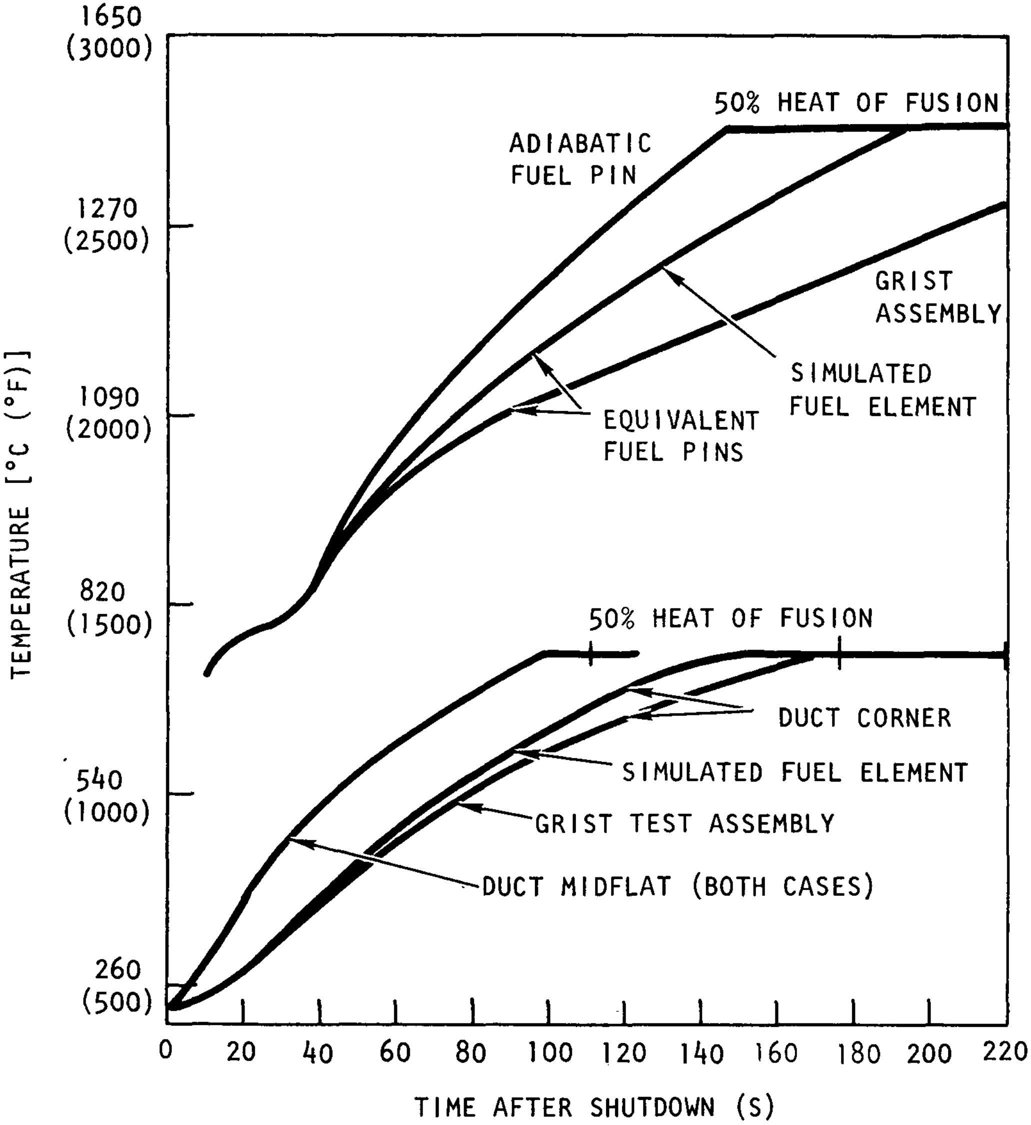

Fig. 12-3. Duct and fuel pin temperatures as a function of time for GRIST test assembly and simulated fuel element

12.3. SAFETY RESEARCH AND DEVELOPMENT LIAISON

During this quarter, safety R&D liaison was maintained with ERDA and the national laboratories involved in the national GCFR safety program [primarily ANL, Aerojet Nuclear Corporation (ANC), and LASL]. On May 4, 1976, GA personnel visited LASL (1) to discuss the basic requirements for out-of-pile tests to simulate fuel element duct melting and dropout during an LOF accident in the shutdown reactor and (2) to evaluate the LASL experimental facilities available for such a test program. The visit resulted in a recommendation for LASL funding of a test program. A GCFR Safety Program Review Committee (GSPRC) meeting was held at LASL on May 18, 1976. The major items of business were

1. GSPRC recommended that a Schedule 44 for the GRIST 1 test facility at the ETR not be submitted as a safety test facility for FY 77 owing to the higher priority assigned to a test program based on a test facility with overpower capability.

2. GSPRC reviewed the LASL proposal of a test program for simulation of duct melting and dropout during an LOF in the shutdown reactor and recommended implementation of the program. ERDA funding of this test program has been initiated for the FY 76 transition quarter.

3. At the request of ERDA, GA prepared a set of test facility requirements for a transient overpower safety test facility (GRIST 2), shown in Table 12-4. Test requirements for such a facility were discussed, and the proposed requirements were adopted, with the exception that a 37-rod bundle was recommended as the maximum test bundle size rather than a 19-rod bundle. ANC prepared an initial evaluation of transient test facilities and was directed to implement the test facility requirements into its evaluation.

TABLE 12-4
PRELIMINARY REQUIREMENTS FOR A GCFR TRANSIENT IN-PILE SAFETY TEST FACILITY (GRIST 2)

	Type of Test		
	Loss of Flow Without Scram	Loss of Pressure Without Scram	Reactivity Insertion Without Scram
Test objective	Cladding and fuel disposition, fuel dispersal mode	Cladding and fuel disposition, fuel dispersal mode	Fuel failure mechanism and threshold, fuel disposition (sweep-out or blockage)
No. of fuel rods			
Minimum	1	1	1
Maximum	19 or 7 plus heated wall	19 or 7 plus heated wall	19 or 7 plus heated wall
Length of fuel rods			
Minimum(a)	100-cm (39-in.) core, 45-cm (19-in.) upper and lower axial blankets	100-cm (39-in.) core, 45-cm (19-in.) upper and lower axial blankets	Upper axial blanket not needed, otherwise the same
Maximum(b)	150-cm (59-in.) core, 60-cm (24-in.) upper and lower axial blankets	150-cm (59-in.) core, 60-cm (24-in.) upper and lower axial blankets	
Maximum heating rate	From ANL	From ANL	~1500°C/s (~2700°F/s)
Maximum initial temperature	2000°C (3600°F),(c) 1400°C (2550°F)	2000°C (3600°F),(c) 1400°C (2550°F)	2000°C (3600°F),(c) 1400°C (2550°F)
Range of flow rates	0 to 0.08 lb/s-rod (0.036 kg/s-rod)(d)	Up to 0.08 lb/s-rod (0.036 kg/s-rod)(e)	0.04 to 0.08 lb/s-rod (0.018 to 0.036 kg/s-rod)
Flow time interval(f)	From ANL	From ANL	Up to 3 min
Fuel preirradiated	Yes and no	Yes and no	Yes and no
Fuel restructured	Yes, if not preirradiated	Yes, if not preirradiated	Yes, if not preirradiated
Steady-state capability	No, except for preheat phase	No, except for preheat phase	No, except for preheat phase
Test data desired	Cladding, fuel motipn, and refreezing	Cladding, fuel motion, and refreezing	Cladding failure location and time, fuel motion and disposition
Post-transient examination	Yes	Yes	Yes
Neutron spectrum	Hard spectrum preferred to avoid radial flux depression within rods	Hard spectrum preferred to avoid radial flux depression within rods	Hard spectrum preferred to avoid radial flux depression within rods
Gamma heat source	No special emphasis if similar to GCFR	No special emphasis if similar to GCFR	No special emphasis if similar to GCFR

(a) Based on demonstration plant core; shorter lead tests may be useful.

(b) Based on commercial plant fuel element size.

(c) Peak fuel temperature, including hot spot factors, at full power = 2000°C (3600°F); averaged over the fuel rod cross section, the maximum temperature is 1400°C (2550°F).

(d) At constant helium pressure of 85 atm (1250 psia).

(e) Cooling pressure decreasing from 85 atm (1250 psia).

(f) Reactivity insertion case is likely to be limiting for combination of flow rate and flow time.

Under private funding, a one-week meeting between GA staff and representation of KWU and Interatom was held in Germany to discuss the reliability analyses performed by both parties on the 300-MW(e) GCFR demonstration plant. At GA, the GCFR reliability work is sponsored by ERDA. The meeting resulted in principal agreement in all major areas of reliability analyses. In particular, agreement was reached on (1) adopting a common reliability data base, (2) using reliability data for analyses, and (3) including common mode failure effects in the analyses.

REFERENCES

12-1. "Gas-Cooled Fast Breeder Reactor Quarterly Progress Report for the Period November 1, 1975 Through January 31, 1976," ERDA Report GA-A13815, General Atomic, March 22, 1976.

12-2. "Gas-Cooled Fast Breeder Reactor Quarterly Progress Report for the Period August 1, 1975 Through October 31, 1975," ERDA Report GA-A13766, General Atomic, January 5, 1976.

12-3. "Gas-Cooled Fast Breeder Reactor Quarterly Progress Report for the Period February 1, 1976 Through April 30, 1976," ERDA Report GA-A13868, General Atomic, May 31, 1976.

13. IN-PILE SAFETY TEST PROGRAM GRIST (189a No. SU015)

13.1. INTRODUCTION

The GRIST program is being evaluated by ERDA, ANL, ANC, and GA as a potential follow-on to analytical and experimental programs being conducted under the LMFBR and GCFR programs. Important data for the design basis of the GCFR demonstration plant will be provided by in-pile endurance testing of the 12-rod GCFR test assemblies in the BR-2 reactor in Mol, Belgium, and out-of-pile testing with the CFTL, described in Section 4. The GRIST program has the objective of going beyond the design basis accidents, in particular, investigating the behavior of melted cladding and fuel. In addition, in order to provide information that would be of importance in improving the performance of commercial plants, less severe transients of core power, coolant flow, and coolant pressure were included to investigate the effects of upset, emergency, and faulted conditions on the GCFR fuel assemblies. However, during this quarter, the GSPRC reached the consensus that GCFR fuel tests in a transient facility are urgently needed. Acting on this recommendation, ERDA has directed that work commence on a transient GCFR loop program (to be known as GRIST-2). This program will largely displace work previously scheduled for the steady-state GCFR loop program in the ETR (GRIST-1).

Therefore, during this quarter, efforts were devoted to the completion and documentation of the GRIST-1 multisection test assembly conceptual designs which were in progress to ensure that GRIST-1 information already developed was properly reported. The multisection test assemblies being considered were designed to prototypically simulate duct wall behavior during temperature excursions which cause duct wall melting.

13.2. CONCEPTUAL TEST DESIGN STUDIES FOR DUCT WALL MELTING TESTS (GRIST 1)

In-pile duct wall melting tests were considered to experimentally verify and demonstrate that during severe accidents (loss of flow, loss of coolant) involving melting of cladding, flow ducts, and fuel, the lower portion of the GCFR fuel assembly will drop out of the core prior to gross fuel melting. Previous analyses and conceptual design considerations have indicated that duct wall melting tests with multisection test assemblies could only demonstrate and verify certain aspects of the dropping hypothesis. For example, phenomena which may be separately tested are the melt-through rate and melting progression of (1) the flat sections of the flow ducts and (2) the corner sections behind the unfueled spacer support rods. The results of these tests may be employed to check calculational methods and analytical approaches to the dropping phenomenon.

Two multisection test assembly designs were prepared at GA. Both designs evolved from the 37-rod fuel test assembly design (developed earlier) and were developed in order to include localized duct melting as a part of the test program. The two test assembly designs are the double-section design shown in Figs. 13-1 and 13-2 and the triple-section design shown in Fig. 13-3. Consistent with the GCFR fuel design concept, both designs incorporate hexagonally patterned rod bundles and flow ducts with a cylindrical section above the manifold grid. The overall configuration of the test assemblies and the deviations from the GCFR fuel design concept were determined by (1) the spacer grid and support, (2) the pressure equalization and fuel vent system, (3) the flow duct geometry, and (4) the instrument leads and connectors.

13.2.1. Double-Section Test Assembly

Two design versions of the double-section test assembly were developed to study melting of the flat wall portions of the hexagonal duct walls. Analysis of the first design revealed that unacceptable duct bowing would occur during testing. A cross section of the double-section design (test

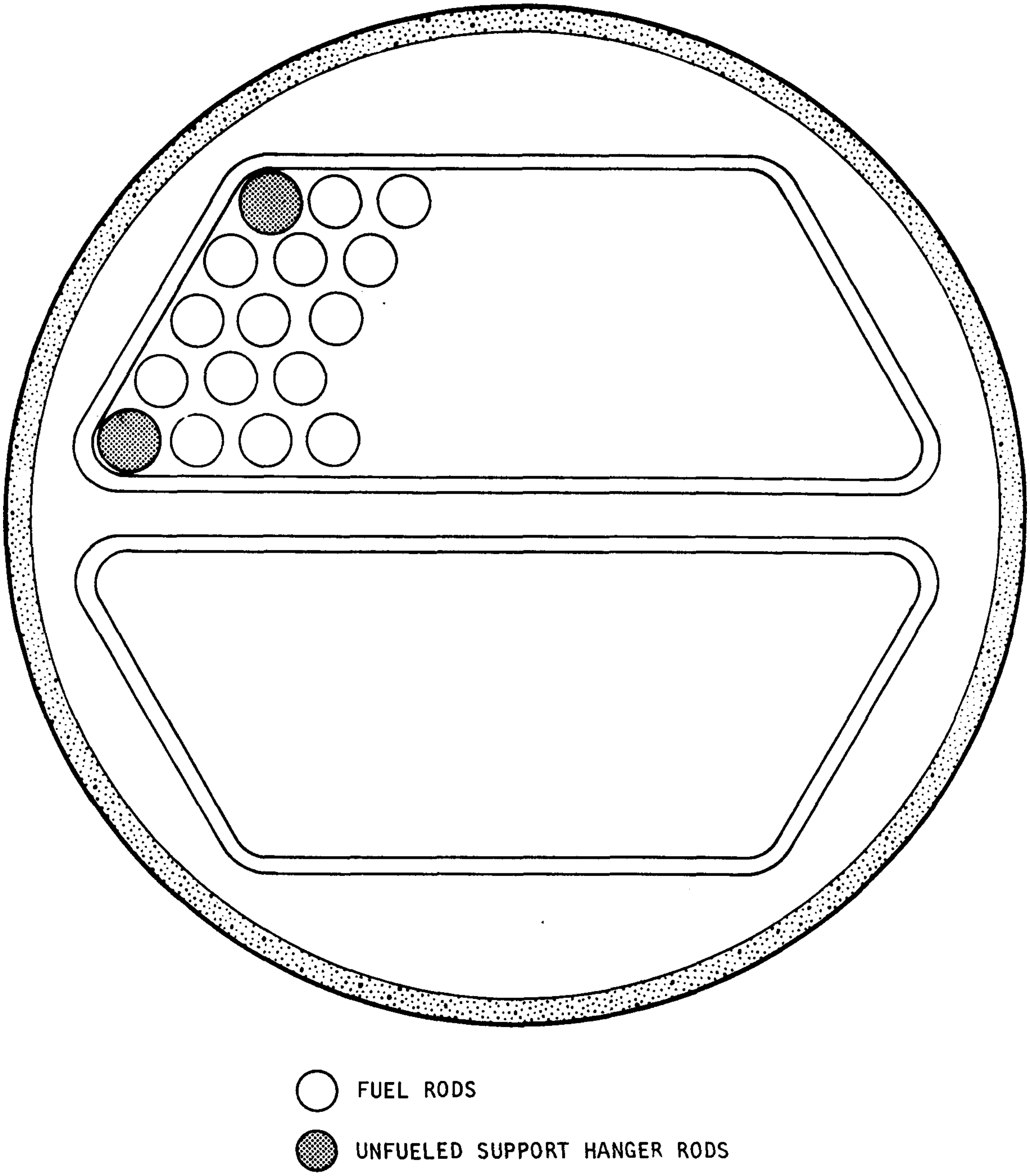

Fig. 13-1. Cross section of double-section test assembly No. 1

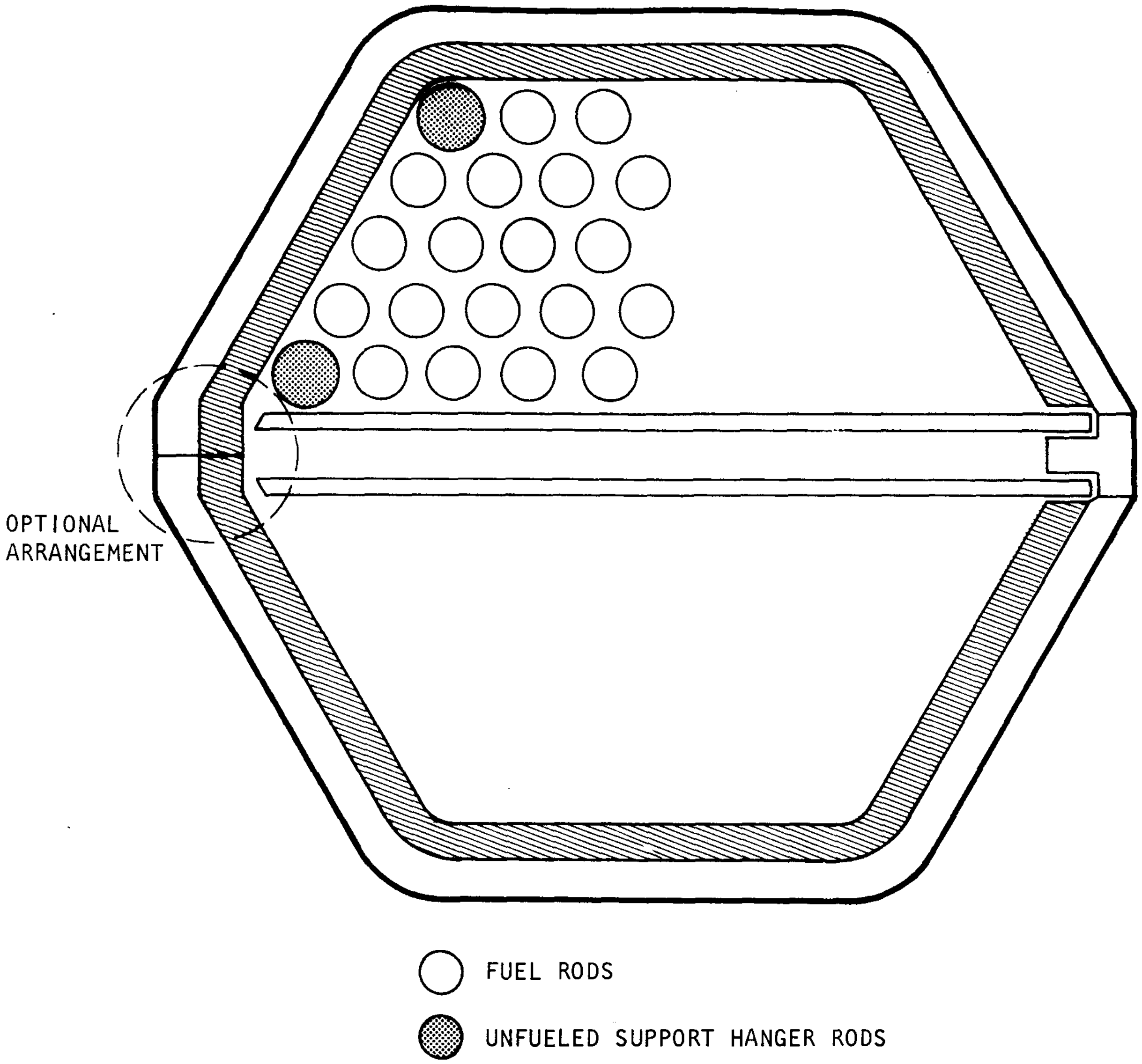

Fig. 13-2. Cross section of double-section test assembly No. 2

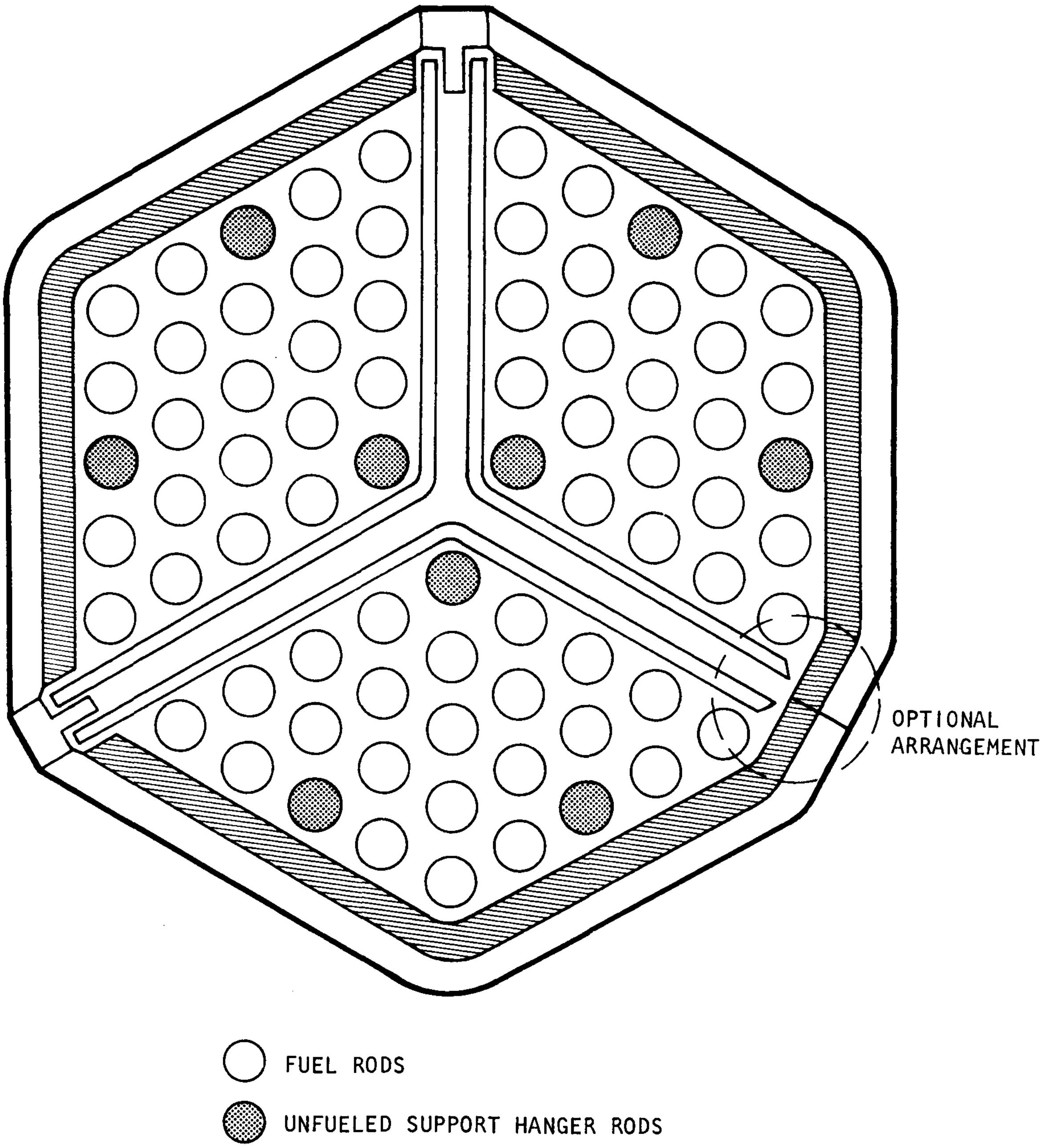

Fig. 13-3. Cross section of triple-section test assembly

assembly No. 1) is shown in Fig. 13-1. As shown in this figure, the fuel rod bundles were separated into two groups, with each group contained in its own duct. The analysis of thermal expansion of the two ducts containing the bundles showed that the central duct walls expanded (lengthened) more than the outer duct walls, and consequently each duct bowed outward from the center plane. To eliminate the duct bowing problem (but still retain the capability to conduct this localized duct melting test program), the two-duct design version was modified to the design shown in Fig. 13-2 (test assembly No. 2). In this design, the two complete ducts containing the fuel rod bundles were replaced by two duct walls separating the two fuel rod bundles. The center plane location of the duct walls was retained, but the bowing associated with the initial two-duct version was eliminated by physical separation of the two portions of the flow duct. This design permits a large axial expansion of the center duct section without yielding the duct bowing effect.

13.2.2. Triple-Section Test Assembly

The triple-section design was developed to investigate melting in the duct wall corners behind the unfueled support hanger rods. The triple-section design evolved from the double-section (test assembly No. 2) design effort, and its design is quite similar to the double-section assembly No. 2 design. As shown in Fig. 13-3, the center plane duct wall features of the double-section design mentioned above were retained, but the duct walls were modified in order to provide a duct corner geometry corresponding to the GCFR fuel assembly duct corners.

The flow duct is a single-wall structure which is bolted to its support member at the top and can be removed for interim examination. It was designed for ease of disassembly and reassembly in a hot cell. The three rod bundles are completely separate, and their individual flow duct walls (and attached insulation) may be removed, allowing easy access to the rod bundles and the central duct walls. A layer of thermal insulation protected by thin metal plates is located between the fuel rods and the outer duct wall. The purposes of the insulation is to protect the outer duct wall, to reduce the temperature gradient across the fuel rod bundle, and to reduce the heat flow into the duct wall during transients. Prototypical duct wall corner conditions will be experienced by the duct walls in the center of the assembly. These duct walls are firmly anchored in the upper blanket area and are laterally supported in the fueled and lower blanket areas. An optional arrangement in which these central duct walls are not laterally restrained in the fueled area is also presented in Fig. 13-3. The relatively cold attemperation flow which flows downward past the in-pile tube provides proper cooling to the in-pile tube wall and assures that its temperature is maintained at reasonably low levels during high-temperature tests.